University of Padua

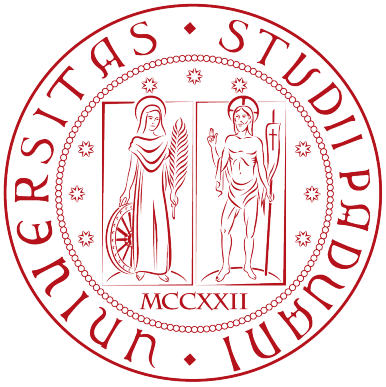


Department of Physics and Astronomy "Galileo Galilei"

---

Ph. D. course in Physics

# Towards the development of the ferromagnetic axion haloscope

Candidate:
Nicolò Crescini

Supervisors:
Prof. Giovanni Carugno
Dr. Giuseppe Ruoso

Cycle XXXII
December 2019

*"That the powerful play goes on, and you may contribute a verse."*
Walt Whitman

*A mio padre.*

**Abstract**

The axion is an hypothetical beyond the Standard Model particle, first introduced in the seventies as a consequence of the strong CP problem of QCD. Axions can be the main constituents of the galactic Dark Matter halos. Their experimental search can be carried out with Earth-based instruments immersed in the Milky Way's halo, which are therefore called "haloscopes". Nowadays haloscopes rely on the inverse Primakoff effect to detect axion-induced excesses of photons in a microwave cavity under a static magnetic field.

This thesis describes the process leading to the successful operation of a ferromagnetic axion haloscope, which does not exploit the axion-to-photon conversion but its interaction with the electron spin. The study of the axion-spin interaction and of the Dark Matter halo properties yields the features of the axionic signal, and is fundamental to devise a proper detector. A scheme of a realistic ferromagnetic haloscope is drawn to realize the challenges of its development. It emerges that there are a number of requirements for a this setup to get to the sensitivity needed for a QCD-axion search. These are kept in mind when designing the prototypes, to overcome the problems without compromising other requirements. A state-of-the-art sensitivity to rf signals allows for the detection of extremely weak signals as the axionic one. The number of monitored spins is necessarily large to increase the exposure of the setup, thus its scalability is a key part of the design process.

A ferromagnetic haloscope consists in a transducer of the axionic signal, which is then measured by a suitable detector. The transducer is a hybrid system formed by a magnetic material coupled to a microwave cavity through a static magnetic field. Its two parts are separately studied to find the materials which match the detection conditions imposed by the axion-signal. The detector is an amplifier, an HEMT or a JPA, reading out the power from the hybrid system collected by an antenna coupled to the cavity. A particular attention is given to the measurement of the noise temperature of the amplifier. As it measures variation in the magnetization of the sample, the ferromagnetic haloscope is configured as a spin-magnetometer.

Three different prototypes of increasing sensitivity make up the part of the thesis dedicated to physics results, namely limits on the axionic Dark Matter field. For every prototype it is verified that larger sample dimensions do not compromise the signal transduction or increase the noise. The working temperature of the haloscope ranges from the 300 K of the first device, to 90 mK of the last one. In every step the noise temperature is also decreased. The final prototype reached the sensitivity limit imposed by

quantum mechanics, the Standard Quantum Limit, and can be improved only by quantum technologies like single photon counters. The haloscope embodies a large quantity of magnetic material, i. e. ten 2 mm YIG spheres, and is designed to be further up-scaled. The quantum-limited ultra cryogenic prototype meets the expectations, and, to present knowledge, is the most sensitive rf spin-magnetometer existing. The minimum detectable field results in $5.5 \times 10^{-19}$ T for 8 h integration, and corresponds to a limit on the axion-electron coupling constant $g_{aee} \leq 1.7 \times 10^{-11}$. This result is the best limit on the DM-axions coupling to electron spins in a frequency span of about 150 MHz, corresponding to an axion mass range from 42.4 $\mu$eV to 43.1 $\mu$eV.

The efforts to enhance the haloscope sensitivity include improvements in both the hybrid system and the detector. The deposited axion power can be increased by means of a larger material volume, possibly with a narrower linewidth. To overcome the standard quantum limit of linear amplifiers one must rely on quantum counters. Novel studies on microwave photon counters, together with some preliminary results, are reported. Other possible usages of the spin-magnetometer are eventually discussed.

## Sommario

L'assione è un'ipotetica particella oltre il Modello Standard, introdotta originariamente negli anni settanta come conseguenza di un problema di cromodinamica quantistica chiamato "problema della CP forte". L'assione può essere uno dei principali costituenti dell'alone di Materia Oscura galattico. La ricerca sperimentale di assioni può quindi essere fatta da esperimenti terrestri immersi nell'alone della Via Lattea, e chiamati di conseguenza "aloscopi". Ad oggi, gli aloscopi usano l'effetto Primakoff inverso per rivelare eccessi di fotoni indotti da assioni in una cavità a microonde sotto un campo magnetico statico.

Questa tesi descrive il processo che ha portato alla messa in funzione di un aloscopio ferromagnetico per assioni, che non usa la conversione dell'assione in fotone, ma il suo accoppiamento con lo spin dell'elettrone. Lo studio dell'interazione spin-assione e delle proprietà dell'alone di Materia Oscura dà le caratteristiche del segnale assionico, ed è fondamentale per progettare un rivelatore adeguato. Quello che emerge da un realistico schema di aloscopio, è che sono presenti diversi requisiti da soddisfare per arrivare alla sensibilità utile ad una ricerca di assioni di QCD. Una sensibilità allo stato dell'arte per i segnali rf permette di rivelare segnali estremamente deboli, come quello assionico. Il numero di spin controllati deve essere grande per aumentare l'esposizione dell'apparato, quindi la scalabilità è una parte chiave della progettazione.

Un aloscopio ferromagnetico consiste in un trasduttore del segnale assionico, che viene poi misurato da un rivelatore. Il trasduttore è un sistema ibrido formato da un materiale magnetico accoppiato ad una cavità risonante attraverso un campo magnetico. Le sue due parti sono studiate separatamente per trovare i materiali che meglio soddisfano le condizioni imposte dal segnale assionico. Il rivelatore è un amplificatore, HEMT o JPA, che legge la potenza uscente dal sistema ibrido e raccolta da un'antenna accoppiata criticamente alla cavità. Una particolare attenzione è riservata alla misura della temperatura di rumore dell'amplificatore. Dal momento che misura una variazione di magnetizzazione, un aloscopio ferromagnetico è uno uno spin-magnetometro.

Tre diversi prototipi di crescente sensibilità costituiscono la parte di questa tesi dedicata ai risultati di fisica, ossia dei limiti sul campo assionico di Materia Oscura. Per ogni prototipo è stato verificato che maggiori dimensioni del campione non compromettono la trasduzione del segnale o incrementano il rumore. La temperatura di lavoro dell'aloscopio va dai 300 K del primo ai 90 mK dell'ultimo. In ogni step anche la temperatura

di rumore viene ridotta. Il prototipo finale raggiunge il limite di sensibilità imposto dalla meccanica quantistica, il limite quantistico standard, e può essere migliorata solo usando tecnologie quantistiche come i contatori di fotoni. L'aloscopio incorpora una grande quantità di materiale magnetico, dieci sfere di YIG di 2 mm, ed è progettato per essere ulteriormente scalato. Questo prototipo ultra criogenico e limitato quantisticamente risulta come era atteso, ed è il più sensibile spin-magnetometro rf esistente. Il minimo campo rivelabile è stato $5.5 \times 10^{-19}$ T con un tempo di integrazione di 8 ore, che corrisponde ad un limite sull'accoppiamento assione-elettrone di $g_{aee} \leq 1.7 \times 10^{-11}$. Questo risultato è il miglior limite sull'accoppiamento tra assioni di Materia Oscura e spin elettronici in un range di frequenza di circa 150 MHz, corrispondente ad un intervallo di masse tra 42.4 $\mu$eV to 43.1 $\mu$eV.

I miglioramenti della sensibilità dell'aloscopio riguardano sia il sistema ibrido, che il rivelatore. La potenza depositata dall'assione può essere aumentata con un maggior volume di materiale con una minor larghezza di riga. Per superare il limite quantistico degli amplificatori sarà necessario utilizzare un contatore di fotoni. Sono riportati nuovi studi sui contatori quantistici e alcuni risultati preliminari. Infine sono discussi altri possibili usi dello spin-magnetometro.

## Acknowledgments

All this work would have never been possible without the help of a lot of people. My gratitude goes to all of them, so there are a lot of "to" coming. To my family for the constant support they gave me. In particular to my mother Daniela and to my grandparents Luigi and Antonietta. You have been the examples I always followed, and gave me all the best you had. To my friends, you have been the brothers and sisters I never had, and more. Davide and Riccardo, we know each other since we remember something, we grew up in Volargne together, and here we are, after 27 years and counting! We shared everything, we can always rely on each other and there is nothing to give in exchange: "noialtri semo sempre a posto". I am lucky I can tell the same about all the wonderful persons who entered our lives: Giulia, Manuel, Debora, Elisa, Chiara and Enrico. To the Valpolicella crew: Matteo (my favourite yes-man), Alice, Ilaria, Daniele, Sonia, Andrea, Nicola, and so on. After all these years we still have a constant wish to hang out together, it must be because we always have a great time! To my room and flatmates of these years, Mattia, Dimitri, Giulia, Andrea, Giulia and Martina, we have always been more than just friends, the huge amount of time we shared was never wasted and our flat has always been home to me. To my university mates, Alessandro, Rita, Marco, Giulio and Chiara, our mutual support was the key for survival, and somehow we also managed to make it fun! I really miss the years spent in Padova with all of you.

These years at LNL were filled by a lot of wonderful people which I want to thank. To the best laboratory mates one can desire, Federico Chiossi, Marco Guarise and Sebastiano Gallo: the "Gianni's Angels". Your dedication, passion and cleverness make you "people who get things done", you have my full esteem. I would be lucky to work with you again in the future, and I really hope so. In that case, we should probably limit the drinks.

All the other people of the group who were constantly a source of new challenges and ideas, including but not limited to Caterina Braggio, David Alesini, Sergey Vasyukov, Paolo Falferi, Claudio Gatti, Antonello Ortolan, Raffaele Divora, Luca Taffarello and Clive Speake.

What is written hereafter is the scientific part which I think can be interesting to somebody, but it is actually just the top of an iceberg. What is not written is all the hard work necessary to make this happen, and I want to thank all the technicians and engineers who helped in the realization of this. To Fulvio Calaon, who can fix everything from the kitchen fridge to a dilution refrigeration unit, and whose competence spared a close to infinite amount of time to us all. To Enrico Berto, who is a true artist when

using the lathe, there is no single mechanical piece of the apparatuses which was not improved by one of his ideas. To Mario Tessaro, who somehow knows exactly how everything works, have a deep physics insight and a true willingness to help. You really know the difference between what can and can not be done, and I learned as much as I could from you in the countless hours spent wiring the electronics, refurbishing that old delfridge or figuring out why things did not work.

I would like to thank the many people I had the pleasure to visit and the relative groups: Aaron Chou, Daniel Bowring, Andrew Sonnenschein at Fermilab, Gianpaolo Carosi at Livermore and Berkeley, Yasunobu Nakamura, Koji Usami, Yutaka Tabuchi and Yutaka Shikano at Tokyo, Leonid Kuzmin and Andrey Pankratov at Nizhny Novgorod, Riccardo Barbieri at Scuola Normale of Pisa, Tim Duty and Simon Mitchinson in Sweden, and David Marsh, Mazhar Ali and Erik Lentz in Göttingen. In particular Mike Romalis and his collaborators, it was great to work with you and be part of your team even if just for some months. I also want to acknowledge all the scientists who came to LNL or Padua, and I had the chance to discuss with: Pierre Sikivie, Christian Enss, GP again, Evgeny Stadnik, Andrew Geraci, Wei-Tou Ni, Martin Weidess, Motohiko Yoshimura, Noboru Sasao, and many more.

Above all, my deep gratitude goes to Pino Ruoso and Gianni Carugno. You were a constant inspiration, guiding me when I needed to be guided and letting me free when trying something new. Most of my motivation comes from the true passion you have for your work and which I think I feel too. I am truly grateful for these years and for all the possibilities you gave me, I hope to always remain as curious as you still are.

# Contents


**1 Introduction** **1**
- 1.1 Axions, Dark Matter, and BSM physics . . . 1
  - 1.1.1 Axion parameter-space and axion-like particles . . . 12
- 1.2 Experimental axion searches . . . 15
  - 1.2.1 Searches of astrophysical and cosmological axions . . . 16
  - 1.2.2 Pure laboratory searches . . . 18
- 1.3 Thesis overview . . . 19

**2 Concept of the ferromagnetic haloscope** **21**
- 2.1 Axion-fermion interaction . . . 21
  - 2.1.1 Axion-electron interaction and the BCFV scheme . . . 22
  - 2.1.2 Axion-nucleon interaction . . . 26
- 2.2 Spin-based experimental searches . . . 27
  - 2.2.1 The QUAX proposal . . . 28

**3 Modelization and experimental techniques** **35**
- 3.1 Photon-magnon hybrid systems . . . 35
  - 3.1.1 Microwave resonant cavities . . . 38
  - 3.1.2 Electron spin resonance materials . . . 42
- 3.2 Modelization of an hybrid system . . . 45
  - 3.2.1 Second quantization model . . . 46
  - 3.2.2 Haloscope tuning range . . . 48
  - 3.2.3 Electrical circuit representation . . . 52
- 3.3 Precision power measurement . . . 62
  - 3.3.1 HEMT amplifiers . . . 63
  - 3.3.2 Josephson parametric amplifiers . . . 64

**4 Haloscope prototypes** **71**
- 4.1 Room temperature single-sample prototype . . . 72

4.1.1 YIG and copper cavity . . . 73
4.1.2 Rf-electronic chain . . . 73
4.1.3 Preliminary results . . . 74
4.2 Cryogenic multi-samples prototype . . . 75
4.2.1 Multiple YIG spheres in a single copper cavity . . . 77
4.2.2 Cryogenic rf electronics and data acquisition . . . 81
4.2.3 First limits on the axion-electron coupling . . . 85
4.3 Ultracryogenic quantum-limited prototype . . . 89
4.3.1 Coherent couping between material and cavity . . . 95
4.3.2 Operation of the Josephson Parametric Converter . . . 103
4.3.3 Data acquisition and analysis . . . 108
4.3.4 Final results . . . 111

**5 Further developments** **115**
5.1 Maximizing the axion-deposited power . . . 116
5.1.1 Increased material volume and number of cavities . . . 116
5.2 Overcoming the standard quantum limit . . . 119
5.2.1 Microwave single photon counters . . . 120
5.3 Detecting the QCD axion . . . 122

**6 Conclusions** **125**

**Appendices** **131**

**Appendix A Versatility of the ferromagnetic haloscope** **131**
A.1 Neutrino induced spin-flips . . . 131
A.2 A GHz gravitational waves detector? . . . 134
A.3 Electron EDM measurements . . . 136
A.3.1 Sensitivity test . . . 139

**Appendix B Longitudinal axion detection** **141**

**Appendix C A testbed for Dicke superradiance?** **143**

# Chapter 1

# Introduction

This first chapter introduces the reader to some well-known physics needed to properly understand the rest of the work. The device described in this thesis aims to detect dark matter in the form of axions, thus the fundamental concepts related to these two topics will be treated. The different techniques proposed to detect the axion are briefly reviewed to frame the ferromagnetic haloscope in the context of present axion searches.

Most of this work uses Einstein notation, where Latin indexes denote the spatial components taking on values 1, 2, 3 and Greek ones are used for space and time, and take on values 0, 1, 2, 3.

## 1.1 Axions, Dark Matter, and BSM physics

A long-standing puzzle of beyond the Standard Model (BSM) physics consists in the dark matter (DM) problem. In 1933 Fritz Zwicky used two different techniques to estimate the mass of the Coma and Virgo clusters, one was based on the luminosity of the galaxies in the clusters while the other used the velocity dispersion of individual galaxies. These two independent estimations did not agree by orders of magnitude [1]. It is only in the seventies that this discrepancy started to be studied systematically. In particular, Vera Rubin studied the rotation curves of spiral galaxies and observed a violation of the second Kepler's law: the outer stars of the galaxies were moving as quickly as those close to the center [2, 3]. These studies first showed that spiral galaxies should not be stable objects if their mass was constituted only by luminous matter. Since the rotation curve can be explained assuming that the mass profile does not vanish beyond the stars, this was an early indication that spiral galaxies could be surrounded by an

halo of DM, as shown in Fig. 1.1. Other evidences of the existence of DM are related to gravitational lensing: DM is far more abundant than ordinary matter in the Universe, and its mass would bend the spacetime which is crossed by the light. By using the data of galaxy surveys it is possible to map the dark matter density as is shown in Fig. 1.1 [4–7]. The simplest

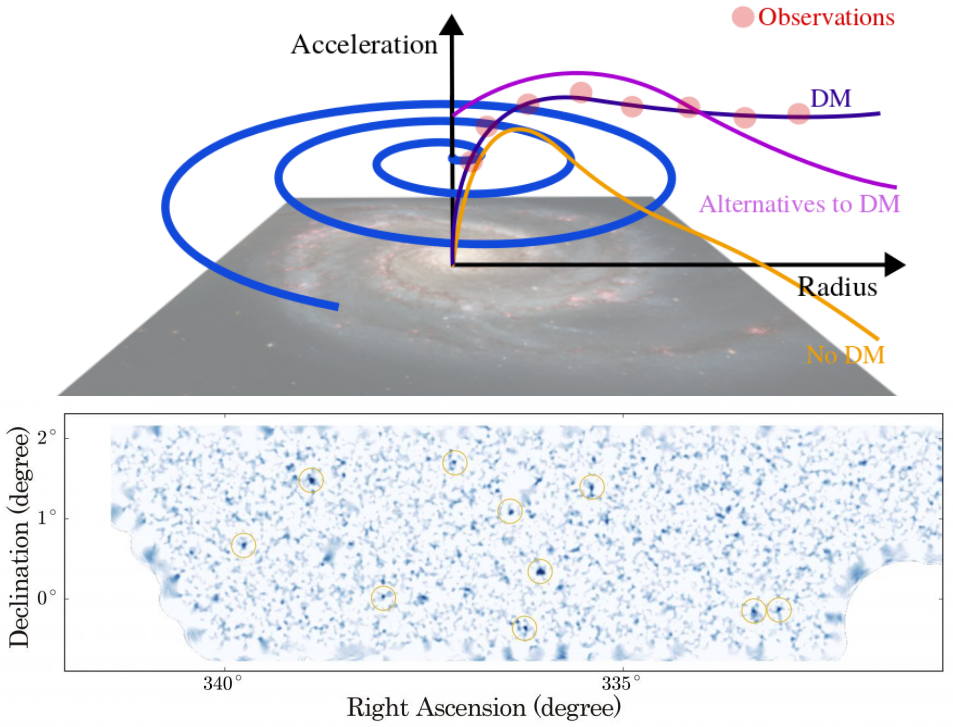


Figure 1.1: *Upper* - Stellar acceleration as a function of radius in a spiral galaxy. Reproduced from Di Paolo et al. [8]. *Lower* - DM distribution map of a region of the Universe. The orange circles are around the regions with a higher DM concentration identified by gravitational lensing. Credits: NAOJ/University of Tokyo [6, 7].

model to account for present observations assumes that General Relativity is correct and contains dark energy (related to the cosmological constant $\Lambda$), cold dark matter (CDM) and ordinary matter. A parametrization of the Big Bang cosmological model, the so-called $\Lambda$-CDM model, predicts the properties of the Cosmic Microwave Background (CMB), of the large-scale structure in the distribution of galaxies, of the elements abundance in the Universe and its accelerated expansion. The evolution of the Universe is

influenced differently by ordinary and dark matter, allowing to indirectly probe the presence of DM by fitting the Λ-CDM model to the CMB spectrum [9, 10]. CMB experimental data collected by COBE, BOOMERanG, WMAP, and more recently by Planck, strongly support the existence of DM. Other observations supporting the Λ-CDM are the study of the Lyman-$\alpha$ forest, the structure formation, and the existence of peculiar objects such as the Bullet Cluster [11–14]. Besides DM, modified Newtonian gravity (MOND) theories were proposed to explain different observations. However, MONDs are not as well suited as DM to explain the mentioned phenomena, and are failing even in the description of galaxy rotation curves [8] (see Fig.1.1).

Despite all these evidences, the nature of DM is still unknown. Its possible composition could be baryonic or non-baryonic. The former considers matter similar to the one already known, while the latter comprehends hypothetical particles of beyond the Standard Model (BSM) physics:

- baryonic DM: astronomical objects such as black holes, neutron stars or brown dwarfs are heavy and have weak electromagnetic interactions, and are therefore known as massive compact halo objects (MACHOs). However, there are multiple evidences that the majority of DM is not made of baryons, even if in principle MACHOs could account for it [15–17];

- non-baryonic DM: includes particles outside the Standard Model (SM), such as axions, sterile neutrinos, weakly interacting massive particles (WIMPs) and gravitationally interacting massive particles (GIMPs). Most of the particles in this category are theoretically well motivated and their detection is a tough but feasible experimental challenge.

The case of a non-baryonic DM is where cosmology meets particle physics. Approaching this problem, physicists glimpse the possibility of merging different questions which are apparently uncorrelated. New theories, remarkably supersymmetric DM [18], triggered experimental searches in different forms and with various techniques. Low-background laboratory experiments aim at a direct detection [19], accelerators could produce such particles and observe their missing energy and momentum [20], while indirect evidences are based on their decay or annihilation [21]. No conclusive signal has been found so far.

The detection of BSM particles would shed light on fundamental question like DM or the unification of all forces. Up to now the results of the LHC and experiments therein showed no evidence of new physics up to the 10 TeV scale. On the other hand, there are significant hints for physics at

the sub-eV scale, like neutrino oscillation or the vacuum energy density of the Universe [22]. The physics case of weakly interacting sub-eV particles (WISPs) is motivated by the fact that any theory introducing a high-energy global symmetry breaking implies a light particle by the Nambu-Goldstone theorem [23]. Examples of WISPs are the scalars arising from string compactification or chameleons [22].

Among other WISPs, the axion appears as a well-motivated BSM particle. Originally introduced to account for a fine-tuning issue in the SM known as the "strong CP problem" of quantum chromodynamics (QCD), it quickly became a prominent DM candidate. The existence of axions is a very attractive perspective, since its addition to the SM (see Fig. 1.2) would solve two major problems of modern physics in a single shot [24]. QCD is

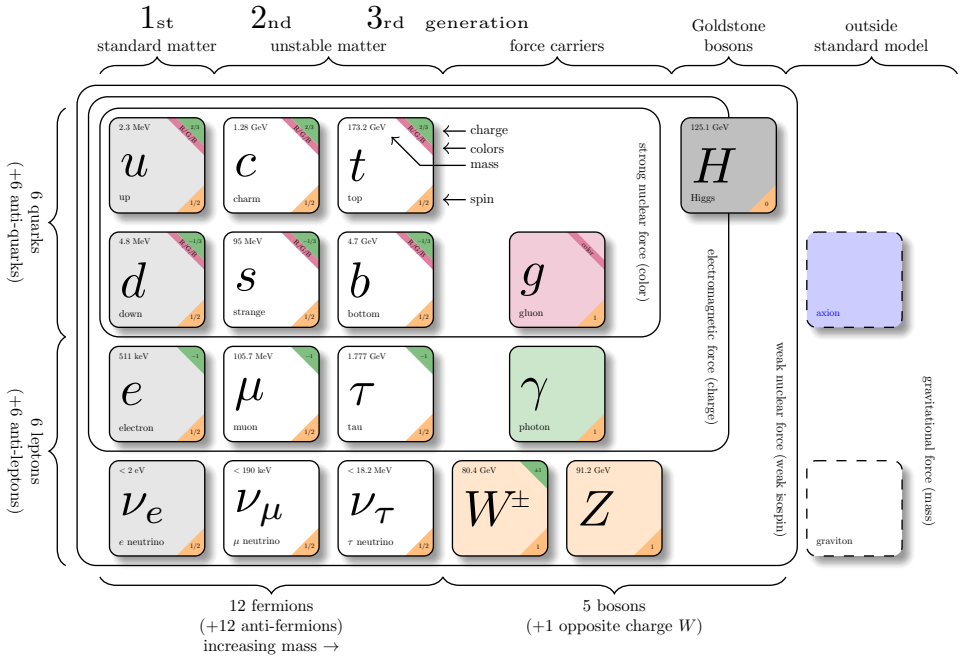


Figure 1.2: The Standard Model of particle physics.

a non-Abelian $SU(3)_c$ gauge theory which describes the strong interactions. Its Lagrangian $\mathcal{L}_{\text{QCD}}$ contains a CP-violating term which is compatible with all symmetries of the SM gauge group. However, an unnatural suppression of this term is needed, since there is no experimental sign of CP violation in strong interactions. The first $SU(3)_c$ theory was proposed as CP-conserving to agree with experimental observations, but had an issue at low energy

known as Weinberg's $U(1)_A$ missing meson problem. The strong CP problem arises following the solution of the missing meson problem proposed by t'Hooft[1].

A simplified QCD Lagrangian can be written by using two quarks flavours $q = (u, d)$ with masses $m_q$, the gluon field strength tensor $G^a_{\mu\nu}$, and a common phase $\theta_Y$

$$\mathcal{L}_2 = -\frac{1}{4} G^a_{\mu\nu} G^{\mu\nu}_a + i\bar{q}\not{D}q - (\bar{q}_L m_q e^{i\theta_Y} q_R + \text{h.c.}), \tag{1.1}$$

where $\not{D} = \gamma_\mu D^\mu$ and $\gamma_\mu$ is the Dirac matrices vector. The quark phase transformation has four parameters $(\alpha_0, \alpha_1, \alpha_2, \alpha_3)$

$$q \to e^{i\gamma_5(\alpha_0 + \alpha_i \sigma^i)} q, \tag{1.2}$$

where $\sigma_i$ is the vector of Pauli matrices and $\gamma_5 = i\gamma_0\gamma_1\gamma_2\gamma_3$. In the $m_q \to 0$ limit it is a $U(2)_A = U(1)_A \otimes SU(2)_A$ symmetry of the Langrangian. The U(1) and SU(2) are respectively a flavour-independent and flavour-dependent phase shifts, and the first can be used to reabsorb $\theta_Y$ which should have no observable effects. The symmetry is explicitly violated by the quark masses, but this is a perturbation since $m_q$ are much smaller than the QCD energy scales. At low energies the symmetry is spontaneously broken by the quark condensate $\langle \bar{u}u \rangle = \langle \bar{d}d \rangle = -v^3$. By the Goldstone theorem, a symmetry breaking produces a Nambu-Goldstone boson (NGB) in the low-energy effective field theory. If the symmetry is exact the bosons are massless, but since $U(2)_A$ is already broken by $m_q$ the result of the Goldstone theorem are massive pseudo-NGBs. A 4-parameters symmetry produces 4 bosons, and their mass can be computed by promoting the phases of the symmetry to fields

$$\alpha_0 \to \frac{\Pi_0(x^\mu)}{f_0} = \theta_0(x^\mu), \quad \alpha_i \to \frac{\Pi_i(x^\mu)}{f_\pi} = \theta_i(x^\mu), \tag{1.3}$$

where $f_0$ and $f_\pi$ are energy scales related to $\Lambda_{\text{QCD}}$. The Goldstone-less quarks thus become

$$q = e^{i\gamma_5(\theta_0 + \theta_i \sigma^i)/2)} \tilde{q}. \tag{1.4}$$

In the light of this redefinition, recasting the quark mass term in the charged

[1] The following derivation relies on [25] by J. Redondo; lecture notes can be found at http://webtheory.sns.it/ggilectures2019.

$\theta^{\pm} = (\theta_1 \pm i\theta_2)/2$ sector yields

$$\begin{aligned}\tilde{q}_L m_q q_R + \text{h.c.} \to &- (m_u + m_d)v^3 \cos\left(\sqrt{\theta_- \theta_+}\right) \\ =&(m_u + m_d)v^3 + \frac{(m_u + m_d)v^3}{2f_\pi^2}\Pi^-\Pi^+ + \dots\end{aligned} \tag{1.5}$$

The mass term of the charged pion results in $m^2_{\pi^+} = (m_u + m_d)v^3/f_\pi^2$. The mass of the neutral sector bosons ($\pi_0$ and $\eta'$) can be obtained similarly. The relation between the masses of the charged and neutral sector is $m^2_{\eta'} + m^2_{\pi^0} = m^2_{\pi^+}[1 + (f_\pi/f_0)^2]$. The observed meson masses are $m_{\pi^+} :: m_{\pi^0} :: m_{\eta'} = 134.9766(6)\,\text{MeV} :: 139.57018(35)\,\text{MeV} :: 957.78(6)\,\text{MeV}$, yielding $(f_\pi/f_0)^2 \simeq m^2_{\eta'}/m^2_\pi \simeq 50$. Since QCD confinement does not distinguish between flavours one expects $f_0 \sim f_\pi$ and value of their ratio close to the unity. Experimentally, there is no trace of a neutral meson with mass close to the one of the $\pi^0$, which is known as Weinberg's missing meson [26]. The inclusion of the strange quark produces a theory with three neutral mesons that have to be associated with $\pi^0$, $\eta$ and $\eta'$, but the problem remains.

The current associated to $\mathrm{U}(1)_A$ by Noether's theorem is $j^\mu_A = \bar{u}\gamma^\mu\gamma_5 u + \bar{d}\gamma^\mu\gamma_5 d$, and its quadridivergence results

$$\partial_\mu j^\mu_A = -2im_u\bar{u}\gamma_5 u - 2im_d\bar{d}\gamma_5 d + 4\frac{\alpha_s}{8\pi}G^a_{\mu\nu}\tilde{G}^{\mu\nu}_a, \tag{1.6}$$

with $\tilde{G}^{\mu\nu}_a = \epsilon^{\mu\nu\varrho\sigma}G_{\varrho\sigma,a}/2$. Eq. (1.6) gets contributions from the quark masses which explicitly violate the symmetry, but also from the triangle loop diagram. The effect of $G\tilde{G}$ was initially neglected as it is a quadridivergence, but then t'Hooft showed that there are topologically non-trivial field configurations that do not vanish at infinity and thus contribute to the term. These are called instantons and are related to the structure of QCD vacuum [27, 28]. The $G\tilde{G}$ term violates P and T and thus CP, and have to be included in the QCD Lagrangian

$$\mathcal{L}_{\text{QCD}} = -\frac{1}{4}G^a_{\mu\nu}G^{\mu\nu}_a + i\bar{q}\not{D}q - (\bar{q}_L m_q e^{i\theta_\lambda}q_R + \text{h.c.}) - \theta_{\text{QCD}}\frac{\alpha_s}{8\pi}G^a_{\mu\nu}\tilde{G}^{\mu\nu}_a, \tag{1.7}$$

where $\theta_{\text{QCD}}$ is a parameter that determines the QCD vacua. The last term of Eq. (1.7) explicitly violates $\mathrm{U}(1)_A$, so it should generate a mass term for $\Pi_0$. An infinitesimal $\mathrm{U}(1)_A$ transformation like Eq. 1.2 adds a term in the Lagrangian

$$\delta\mathcal{L} = \alpha\partial_\mu j^\mu_A = -2i\alpha m_u\bar{u}\gamma_5 u - 2i\alpha m_d\bar{d}\gamma_5 d + 4\alpha\frac{\alpha_s}{8\pi}G^a_{\mu\nu}\tilde{G}^{\mu\nu}_a, \tag{1.8}$$

which is a variation of the quark masses phase and a redefinition of $\theta_{\text{QCD}}$. The phases can be rotated to get a single physical parameter

$$\bar{\theta} = \theta_{\text{QCD}} + 2\theta_Y \tag{1.9}$$

which multiplies the $G\tilde{G}$ term, making QCD a CP violating theory. The two angles $\theta_Y$ and $\theta_{\text{QCD}}$ are related to the Yukawa couplings and to the QCD vacuum respectively, so in principle $\bar{\theta}$ is expected to be $O(1)$.

The $G\tilde{G}$ term solves the missing meson problem thanks to its contribution to the meson potential. Only some field configuration like instantons contribute to the spacetime integral of the $G\tilde{G}$ term, which results

$$\int \mathrm{d}^4x \frac{\alpha_s}{8\pi} G^a_{\mu\nu}\tilde{G}^{\mu\nu}_a = n \in \mathbb{Z}. \tag{1.10}$$

The quantities which depends on $\bar{\theta}$ must have a $2\pi$ periodicity, in particular the effective potential path integral,

$$e^{-\int \mathrm{d}^4x_E V[\theta]} = \int \mathcal{D}A_{a\mu} e^{-S_E[A_{a\mu}] - i\theta \int \mathrm{d}^4x_E \frac{\alpha_s}{8\pi} G^a_{\mu\nu}\tilde{G}^{\mu\nu}_a} \tag{1.11}$$

will satisfy $V(\theta) = V(\theta + 2\pi)$. It also has an absolute minimum for $\theta = 0$

$$\begin{aligned} e^{-\int \mathrm{d}^4x_E V[\theta]} &= \left| \int \mathcal{D}A_{a\mu} e^{-S_E[A_{a\mu}] - i\theta \int d^4x_E \frac{\alpha_s}{8\pi} G^a_{\mu\nu}\tilde{G}^{\mu\nu}_a} \right| \\ &\leq \int \mathcal{D}A_{a\mu} e^{-S_E[A_{a\mu}]} \left| e^{-i\theta \int d^4x_E \frac{\alpha_s}{8\pi} G^a_{\mu\nu}\tilde{G}^{\mu\nu}_a} \right| \\ &\leq \int \mathcal{D}A_{a\mu} e^{-S_E[A_{a\mu}]} = e^{-\int \mathrm{d}^4x_E V[0]}. \end{aligned} \tag{1.12}$$

The definition of the Goldstone-less quarks produces a term in the Lagrangian

$$\frac{\theta_0}{2}\partial_\mu j^\mu_A \ni 2\theta_0 \frac{\alpha_s}{8\pi} G^a_{\mu\nu}\tilde{G}^{\mu\nu}_a \tag{1.13}$$

which adds $2\theta_0(x)$ to the theta-angle [29]. The meson potential have to be parametrized according to the previous consideration: it must have a minimum for $2\theta_0 - \bar{\theta}$, a non-null second derivative to give mass to the $\eta'$ and a periodicity of $2\pi$ in $2\theta_0 - \bar{\theta}$. The simplest choice is a cosine, yielding

$$V \simeq -m_u v^3 \cos(\theta_0 + \theta_3) - m_d v^3 \cos(\theta_0 + \theta_3) - \Lambda^4 \cos\big(2\theta_0 + \bar{\theta}\big), \tag{1.14}$$

where $\Lambda$ is an energy scale of non-perturbative QCD, from which the $\eta'$ get its mass

$$m^2_{\eta'} \simeq 4\Lambda^4 + O(m_q v^3). \tag{1.15}$$

So, while the pions get their mass from the chiral symmetry breaking, the $\eta'$ takes it from the $G\tilde{G}$ term. It was shown that the solution of the missing meson problem brings on CP violation in QCD, which is parametrized by $\bar{\theta}$. To conserve CP either $\bar{\theta}$ should be zero or one of the quarks should be massless. There is no trace of a massless quark in nature, but the up and down quarks have small masses so CP-violating observables are slightly suppressed. The minimization of the potential yields $2\theta_0 - \bar{\theta} = 0$, but the quark mass terms forbids it, so this suppression just acts up to a certain level.

Among the measurable observables containing $\bar{\theta}$ and thus CP violation, the neutron electric dipole moment (nEDM) results [30–32]

$$d_n = \frac{g_{\pi NN}\bar{g}_{\pi NN}}{4\pi^2 m_N} \log\left(\frac{m_N}{m_\pi}\right) \simeq 4.5 \times 10^{-15}\, e\,\mathrm{cm}, \tag{1.16}$$

where $g_{\pi NN}$ and $\bar{g}_{\pi NN}$ are the pion-nucleon couplings and $m_N$ is the nucleon mass. The angle $\bar{\theta}$ enters linearly in the product of the couplings and it can be constrained by a measurement of $d_n$. The first experimental tests were performed by Smith, Purcell and Ramsay, resulting in $\bar{\theta} \lesssim 10^{-4}$. More recent results by the nEDM collaboration constrain the parameter even more $\bar{\theta} \lesssim 10^{-10}$ [33–35]. Since it is unlikely that nature chose very small $\theta_Y$ and $\theta_{\mathrm{QCD}}$ or a fine tuning among them, a naturalness problem arises. It is normally denoted as the strong CP problem, which is an important hint of BSM physics.

By looking at Eq. (1.14) it can be noticed that the potential has three terms but only two degrees of freedom, so the minimization is compromised. But what if also $\bar{\theta}$ was a field? This will add a new meson-like degree of freedom similarly to the chiral anomaly. This was realized, albeit in a different way, by Peccei and Quinn [36], who introduced a new $\mathrm{U}(1)_{\mathrm{PQ}}$ symmetry to the SM to dynamically interpret $\bar{\theta}$. The idea was further developed by, among others, Weinberg and Wilczek [37–41], who realized that it implies the existence of a new light pseudo-NGB which was called axion. The minimization of the potential $\partial_{\theta_0} V = \partial_{\theta_3} V = \partial_{\theta_\phi} V = 0$ gives $\theta_0 + \theta_3 = \theta_0 - \theta_3 = 2\theta_0 + \theta_\phi - \bar{\theta} = 0$, and adjusts the axion vacuum expectation value to cancel any effect of CP violation. By defining the CP-violating phase in terms of a scalar field $\phi$, it becomes $\theta_\phi(x) = \phi/f_\phi$. The axion field is $\phi$ and $f_\phi$ is its decay constant. The axion Lagrangian results

$$\mathcal{L}_\phi = \frac{1}{2}\partial_\mu\phi\partial^\mu\phi + \frac{\alpha_s}{8\pi} G^a_{\mu\nu}\tilde{G}^{\mu\nu}_a \frac{\phi}{f_\phi}, \tag{1.17}$$

and its mass eigenstate can then be computed as

$$m_a^2 \simeq \frac{m_u m_d v^3}{(m_u + m_d) F_a} = \frac{m_u m_d}{(m_u + m_d)^2} \frac{m_\pi^2 f_\pi^2}{F_a^2}, \tag{1.18}$$

where $F_a = f_\phi$, and $a$ will be used to indicate the axion mass eigenstate. The energy scale $F_a$ is the PQ-symmetry breaking scale, and as the axion is the pseudo-NGB arising from this process, its mass and couplings are proportional to $F_a^{-1}$ making it very light and weakly-interacting. Originally it was assumed that $F_a \simeq \Lambda_{\text{weak}} = (\sqrt{2} G_F)^{-1/2} = 247\,\text{GeV}$, but these first axion models were quickly ruled out by accelerators [42]. If $F_a \gg \Lambda_{\text{weak}}$ the so-called "invisible-axion models" still hold, since they evade current experimental limits [43]. There are two main classes of invisible axions whose archetype are the Kim-Shifman-Vainshtein-Zakharov (KSVZ) and Dine-Fischler-Srednicki-Zhitnitsky (DFSZ) models [39, 41, 44–46]. The former introduces new electrically neutral heavy quarks, which carries the $\text{U}(1)_{\text{PQ}}$ charge and leaves the SM quarks and leptons without tree-level axion couplings. The latter includes two Higgs doublets and ordinary quarks and leptons carry PQ charge. Both of them have at least one electroweak singlet scalar that acquires a vacuum expectation value and breaks the PQ symmetry. In supersymmetric models, both heavy quarks and Higgs doublets carry PQ charge and predict a spin-0 saxon and a spin-1 axino with suppressed SM-couplings and large masses.

The Lagrangian which includes the interaction with fermions and with light results

$$\begin{aligned} \mathcal{L} \supseteq & -\frac{1}{2}\partial_\mu a \partial^\mu a - m_a^2 a^2, \\ & - \frac{g_{a\gamma\gamma}}{4} a F_{\mu\nu} \tilde{F}^{\mu\nu} - \frac{i}{2} g_d a \bar{N} \sigma_{\mu\nu} \gamma_5 N F^{\mu\nu} \\ & + \frac{g_{aNN}}{2m_N} \partial_\mu a (\bar{N} \gamma^\mu \gamma_5 N) + \frac{g_{aee}}{2m_e} \partial_\mu a (\bar{e} \gamma^\mu \gamma_5 e) - V(a), \end{aligned} \tag{1.19}$$

where $F^{\mu\nu}$ is the electromagnetic (em) field tensor, $N$ and $e$ are the nucleon and lepton fields and $m$ and $g$ are their masses and couplings. The couplings of axions to the SM particles generally depend on the specific model. For example the axion-fermion coupling is suppressed in the KSVZ but not in the DFSZ or in more recent models [47–51].

It is now possible to analyze the axion as a constituent of DM. Cold DM particles must be present in the Universe in a sufficient quantity to account for the observed DM abundance and they have to be effectively collisionless, i. e. to have only significant long-range gravitational interactions. The

axion satisfies both these criteria. Even if it is very light, the axion population is non-relativistic since it is produced out of equilibrium by vacuum realignment, string decay or domain wall decay [46, 52–58]. Different temperatures can be defined to understand the processes that can lead to axion production. If $k_B$ is Boltzmann constant, let's define the following temperatures: $T_{\rm PQ} = F_a/k_B$ the temperature at which the PQ symmetry breaks, $T_R$ the inflationary reheating temperature, and $T_1 \simeq 1\,\text{GeV}$ the temperature of the Universe at the time $t_1 \simeq 1/m_a$, when the axion mass becomes important [59].

For a Universe temperature $T \gg T_{\rm PQ}$ the PQ symmetry is not broken, but when $T$ approaches $T_{\rm PQ}$ the symmetry breaks spontaneously and the axion field may acquire any value. The phase of the complex scalar field varies of order one from one horizon to the next and axion strings appear as topological defects. If $T_{\rm PQ} > T_R$ the string density is diluted by inflation and these mechanisms do not contribute to the cold DM energy density. If $T_{\rm PQ} < T_R$ string and domain wall decay contribute to the axion energy density, and when $T \sim T_1$ the axion strings become the boundaries of the domain walls.

Vacuum realignment always gives a contribution to the cold axion DM population independently on $T_R$, for this reason it is treated in some detail. A toy axion model with a single complex scalar field $\phi(x)$ has a potential

$$V(\phi) = \frac{\lambda}{4}(|\phi|^2 - F_\phi^2)^2. \tag{1.20}$$

When $T \sim T_{\rm PQ} \sim F_\phi$, the vacuum expectation value of $\phi$ results

$$\langle\phi\rangle = F_\phi \exp(i\theta(x)), \tag{1.21}$$

where the axion field $a(x) \equiv F_\phi\theta(x)$, and $F_\phi \equiv F_a$ becomes the axion decay constant. When the temperature falls below $T \sim \Lambda$ an effective potential

$$\tilde{V}(\theta) = m_a^2(T)F_a^2(1 - \cos\theta) \tag{1.22}$$

is produced. At this temperature non-perturbative QCD effects give the axion a mass due to the curvature of the potential at its minimum. The mass inherits a time dependence from the potential temperature dependence, thus in a Friedmann-Robertson-Walker Universe the equation of motion of $\theta$ is

$$\ddot{\theta} + 3H(t)\dot{\theta} - \frac{1}{S^2(t)}\nabla^2\theta + m_a^2(t)\sin(\theta) = 0, \tag{1.23}$$

where $H(t)$ is the Hubble constant at the time $t$, and $S^2(t)$ is the scale factor. For $T_{\rm PQ} > T_R$ the field $\theta(x)$ is homogeneous, thus Eq. (1.23) becomes the one of a damped harmonic oscillator (HO)

$$\ddot{\theta} + 3H(t)\dot{\theta} + m_a^2(t)\theta = 0, \tag{1.24}$$

since for small angles $\sin\theta \simeq \theta$. At the time $t_1 \simeq 2\times10^{-7}(F_a/10^{12}\,\text{GeV})^{1/3}\,\text{s}$ the temperature approaches $T_1 \simeq 1\,(10^{12}\,\text{GeV}/F_a)^{1/6}\,\text{GeV}$ and the field begins to oscillate in its potential. The momentum $p_a$ of a $\phi$-quantum cannot realign faster than allowed by causality, thus

$$p_a(t_1) \simeq 10^{-3}\left(\frac{2\times10^{-7}\,\text{s}}{t_1}\right)\mu\text{eV}. \tag{1.25}$$

Since for $F_a \simeq 10^{12}\,\text{GeV}$ the axion mass is $6\,\mu$eV by Eq. (1.18), the DM population is non-relativistic or cold. The energy density of $\phi$ around its potential minimum is

$$\varrho = \frac{F_a^2}{2}\left(\dot{\theta}^2 + m_a^2(t)\theta^2\right), \tag{1.26}$$

and by the Virial theorem

$$\langle\dot{\theta}^2\rangle = m_a^2\langle\theta^2\rangle = \frac{\varrho}{F_a^2}. \tag{1.27}$$

If $m_a$ varies adiabatically the axion density per comoving volume is conserved, as $\varrho \propto m_a(t)/S^3(t)$ for cold and decoupled particles. The initial energy density $\varrho_1 = \varrho(t_1)$ is

$$\varrho_1 = \frac{1}{2}F_a^2 m_a^2(t_1)\theta_1^2, \tag{1.28}$$

where $\theta_1$ is the initial misalignment angle. Today's axion density results

$$\varrho_0 \simeq \varrho_1\frac{m_a(t_0)}{m_a(t_1)}\frac{S^3(t_1)}{S^3(t_0)} = \frac{1}{2}\left(\frac{S^3(t_1)}{S^3(t_0)}\right)^3\frac{m_a F_a^2}{t_1}\theta_1^2, \tag{1.29}$$

implying an axion energy density

$$\Omega_a \simeq 0.15\left(\frac{F_a}{10^{12}\,\text{GeV}}\right)^{7/6}\theta_1^2. \tag{1.30}$$

If $T_{\rm PQ} < T_R$ the axion field varies by $F_a$ over horizon scales, and one needs to consider zero and higher-momentum modes. The zero-momentum modes are calculated as above with $\langle\theta_1^2\rangle \simeq 1$. The higher-momentum modes' density

is $\varrho_{\rm hm} \sim (\nabla a)^2$. Their energy density can be estimated by integrating $\varrho_{\rm hm}$ over the momenta between $1/t_1$ and infinite [60]. The result is that the two contribute the same order of magnitude to the axion energy density. The extremely weak axion coupling allows these coherent oscillations not to decay, and the axion to be a candidate for the cold DM of the Universe.

String and domain wall decay mechanisms of DM production also yield $\Omega_a^{\rm string}$ and $\Omega_a^{\rm wall}$ proportional to $F_a^{7/6}$. For further details see for example Ref.s [60, 61].

### 1.1.1 Axion parameter-space and axion-like particles

The axion has to be framed in the context of present physical theories, since one can wonder if the presence of light scalars may influence the behavior of already studied physical systems. Several constraints come from fitting the axion theory into astrophysical and cosmological observations. As other weakly interacting low-mass particles, they can contribute to the cooling of stars and be produced in astrophysical plasmas [62–64]. Such phenomena can constrain the axion parameter-space by including the axion theory into present models as reported in Fig. 1.3. In the Sun axions are produced via the Primakoff effect $\gamma + Ze \to Ze + a$, and since the photon luminosity is fixed the axion losses require enhanced nuclear energy. This produces enhanced neutrino fluxes which can be measured by neutrino observatories like SNO, constraining the axion-photon coupling constant in an interval of mass values. Combining solar neutrinos results with helioseismology yields even more restrictive limits. The axion must also affect stellar evolution, which is specifically studied in globular-cluster stars. The axion losses accelerate the consumption of helium, reducing the lifetime of stars in the horizontal branch of the color-magnitude diagram. The comparison between these stars and red giants, which are not affected by Primakoff losses, excludes a wide mass range through the axion-photon coupling [65, 66]. Other limits can be obtained from the axion-electron coupling (only for the DFSZ models). Using this coupling, the evolution of red giants and the luminosity of white dwarfs can put stringent limits to the axion mass, roughly stating that $m_a \lesssim 10\,\text{meV}$ [67–70]. From the supernova SN-1987A burst duration and energy loss due to nucleon bremsstrahlung $N + N \to N + N + a$, one can obtain a minimum mass close to the one previously described [62, 71]. It is also possible to search for hints of axions which may cause some unexpected phenomena. An astrophysical hint is the surprisingly fast cooling of the neutron star in the Cassiopea A supernova remnant, measured from its surface temperature, which could be explained with an axionic energy loss

due to the axion-neutron coupling [72–74].

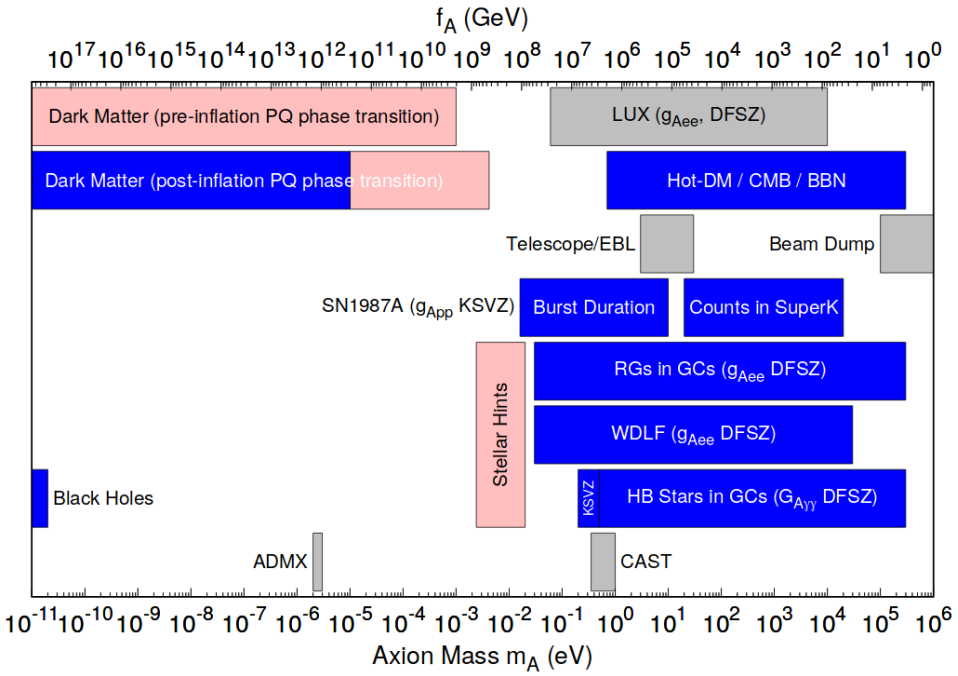


Figure 1.3: Astrophysical and cosmological limits on the axion mass. In gray are reported existing experimental exclusion bands, the mass constraints at low masses are cosmological, while the high mass limits are given by both cosmological and astrophysical considerations. The plot was taken from [43], see text for further details.

The cosmological bounds for high masses are related to the axion production after color confinement by the process $\pi + \pi \leftrightarrow \pi + a$ [75]. The constraints on the hot DM fraction results in $m_a \lesssim 1\,\mathrm{eV}$, this number will be improved by future data of a EUCLID-like survey combined with Planck CMB data. For $m_a \gtrsim 20\,\mathrm{eV}$ an excess radiation would have been injected by a fast axion decay, extending the studies to higher masses [76–78]. Lower limits on the axion mass come from the production of DM-axions in the early Universe [52, 79–87]. Peccei-Quinn spontaneous symmetry breaking (SSB) occurs when the PQ-particles temperature falls below the energy scale $F_a$ [48, 61]. The study of the axion DM abundance can be divided in two distinct scenarios, depending whether the SSB happens during the ordinary thermal evolution of the Universe or before/during inflation, as discussed in Sec. 1.1. In the pre-inflationary SSB scenario near the QCD epoch, instan-

tons explicitly break the PQ symmetry exciting coherent oscillations of the axion field that represent a condensate of cold DM. The fractional cosmic mass density created by this realignment mechanism of Eq. (1.30) can be written as [59–61]

$$\Omega_a^{\rm vr} h^2 \simeq 0.12 \left(\frac{6\,\mu{\rm eV}}{m_a}\right)^{1.165} F_i \Theta_i^2, \tag{1.31}$$

where $h$ is the current Hubble-expansion parameter in $\mathrm{km\,s^{-1}Mpc^{-1}}$, $-\pi \leq \Theta_i \leq \pi$ is the initial misalignment angle, and $F_i$ is a factor accounting for anharmonicities in the axion potential. For $F_i\Theta_i^2 = O(1)$ the axion mass must be higher than $6\,\mu$eV to avoid the overclosure problem, i. e. an axion density exceeding the observed DM density. Lighter masses are still possible if $F_i\Theta_i^2 < 1$, the so-called "anthropic axion window". In the post-inflationary SSB scenario, the average contribution of $\Theta_i$ results

$$\Omega_a^{\rm vr} h^2 \simeq 0.12 \left(\frac{30\,\mu{\rm eV}}{m_a}\right)^{1.165}. \tag{1.32}$$

Cosmic strings and domain walls change the population of cold-DM axions and several prevision of the axion mass were proposed by different groups [88–90]. The exponent of Eq.s (1.31) and (1.32) comes from the temperature dependence of topological susceptibility $\chi(T) = m_a^2(T)F_a^2$, which allows its calculation in lattice-QCD and is remarkably similar to the dilute instanton gas approximation [91–96]

$$m_a = 5.70(7) \left(\frac{10^9\,{\rm GeV}}{F_a}\right) \mu{\rm eV}. \tag{1.33}$$

For a fixed $\Theta_i$, lattice-QCD estimations of the axion mass are compatible with the previous prediction [e. g. Eq. (1.18)] within a factor $O(1)$.

A general case of BSM particles are the so-called "axion-like particles" (ALPs). Let's consider a theory adding a global symmetry to the SM symmetry group $\mathrm{SU(3)}_c \times \mathrm{SU(2)}_L \times \mathrm{U(1)}_h$, as it was shown, its spontaneous breaking implies the existence of a NGB or pseudo-NGB. For example, family and lepton number symmetries yield the familion and the majoron, respectively. The interest in ALPs relies on the fact that its mass and coupling constants can be unrelated (other than for axions), thus they do not necessarily solve the strong-CP problem but still can account for the whole DM density of the Universe [97]. Any experimental search not reaching the axion sensitivity is still a probe of ALPs.

## 1.2 Experimental axion searches

Low-energy measurements, precisely testing known physical laws, are a powerful probe of BSM physics, mainly complementary to accelerator physics. As shown in Fig. 1.4, thanks to Nambu-Goldstone theorem, extremely high energy scales can be explored by measuring faint effects at the limit of present technology. Eventually, new instruments and devices can be built to push the current technological limits to new levels and hopefully help not only fundamental physics but many other fields. In the last decades

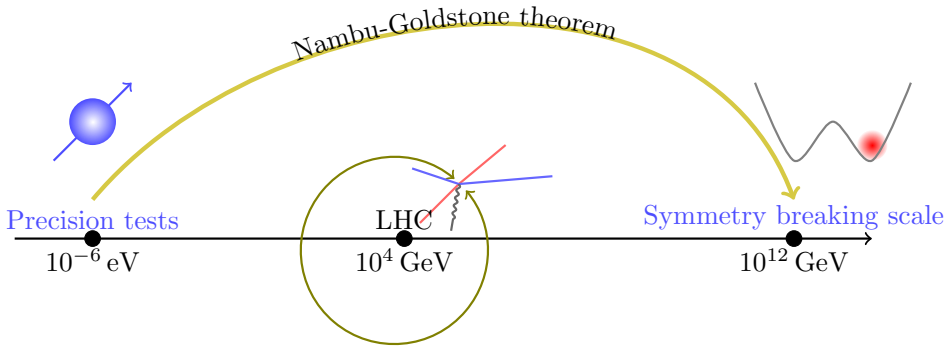


Figure 1.4: The usage of Nambu-Goldstone theorem to infer on physics at energy scales inaccessible to accelerators.

several experimental techniques have been proposed to detect axions and ALPs [22, 98]. This section gives an overview of the different ideas that people have proposed and realized. Most experiments do not reach the axion-required sensitivity. The physics result of these measurements is to limit the ALPs parameter space. The most tested effects of axions are related to their coupling to photons, being this one the strongest and thus most accessible parameter. Fig. 1.5 shows the most recent limits on the axion-photon coupling in the classic axion window. These limits mostly rely on the inverse Primakoff effect: in a strong static magnetic field it is possible to convert an itinerant axion into a photon that can be detected. These and other limits are discussed in the next two sections by dividing them in searches of axions from cosmological and astrophysical sources, and into pure laboratory searches, where axions and ALPs effects are independent from external sources.

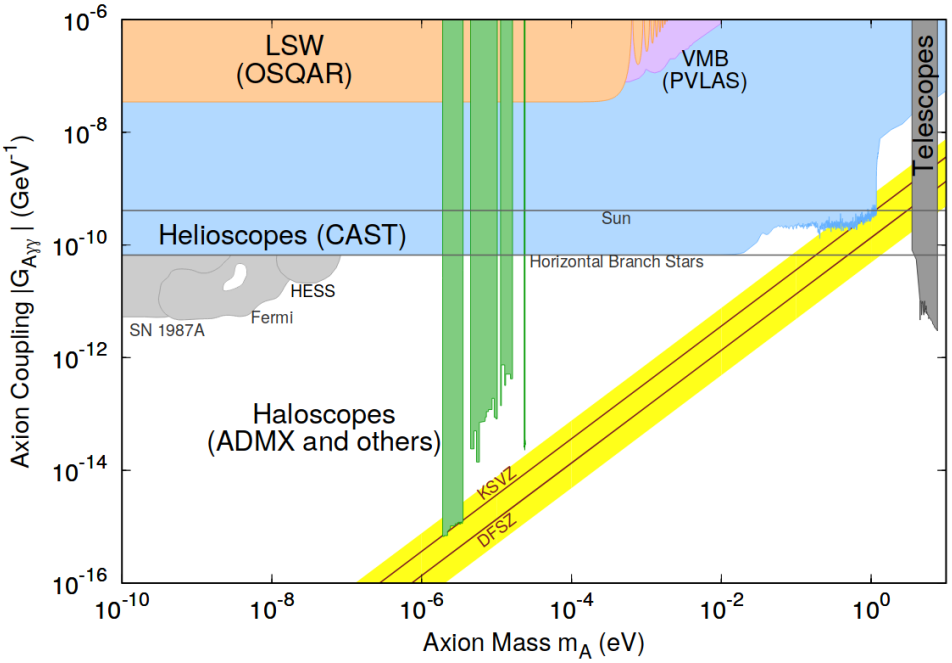


Figure 1.5: Experimental limits on the axion-photon coupling. The plot was taken from [43] and the different limits are discussed in the text.

### 1.2.1 Searches of astrophysical and cosmological axions

As previously explained axions may be produced in stars and contribute to their cooling, it is thus possible to search directly for these axion fluxes on Earth. The Sun is a powerful source of axions and ALPs. The axion-em interaction of Eq. (1.19) yields the Primakoff effect, a two photon vertex which converts photons to axions and vice versa. The same effect can be exploited in terrestrial laboratories by using strong magnetic fields to convert sun-produced axions to x-ray photons, with an average energy 4.2 keV. The first helioscope was operated at Brookhaven [99], it used a iron core dipole magnet, a proportional chamber for x-ray detection and had a measurement window of 15 minutes per day. The Tokyo axion helioscope used a superconducting magnet to convert solar axions into photon which were detected with PIN-photodiodes. By tracking the Sun the collaboration reported a limit $g_{a\gamma\gamma} < 6 \times 10^{-10}\,\mathrm{GeV}^{-1}$ for $m_a < 0.3\,\mathrm{eV}$ at 95% CL [100]. The most recently operated helioscope is the CERN axion solar telescope (CAST), which used a decommissioned LHC magnet on a mount following

the Sun. The x-ray detectors are grazing-incidence optics with solid-state detectors, and a novel x-ray Micromegas position-sensitive gas detectors. The best results are reported in Fig. 1.5 [101, 102]. The axio-electric effect is the axionic analogue of the photoelectric effect. It can be exploited to search for solar axions in large noble gas detectors used for direct DM searches like EDELWEISS-II, LUX or XENON100 [103–108]. The most stringent limits are reported in [109] and results in $g_{aee} < 3.5 \times 10^{-12}\,\mathrm{GeV}^{-1}$ al 90% CL, excluding DFSZ axions heavier than 0.12 eV. The Primakoff effect may also

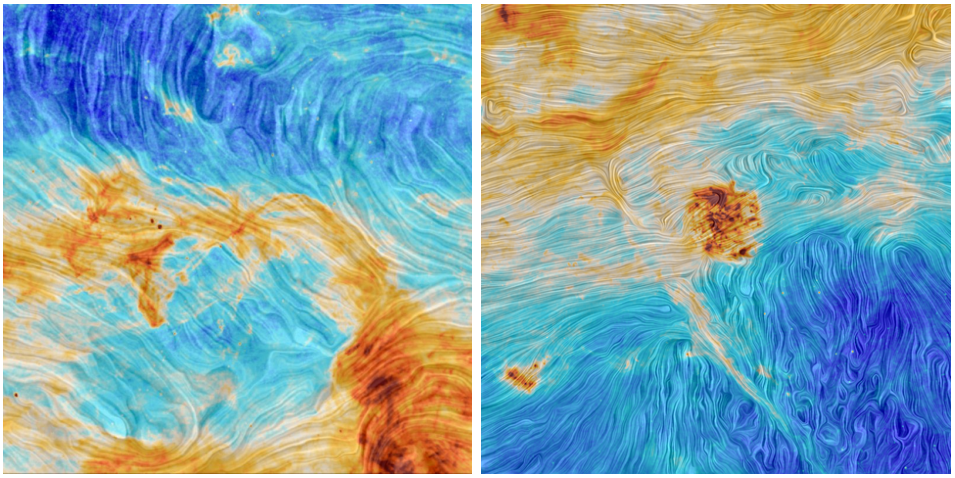

Figure 1.6: Planck maps of the magnetic field on the Magellanic Clouds and of the Spider in the Loop, as revealed by starlight and sub-millimeter polarization. The relief lines laced across this image show the average direction of the Milky Way's magnetic field in the region containing the object.

be exploited considering the effect of astrophysical scales magnetic field on photons or axions propagation. Photon fluxes can be modified by the axion dynamics causing frequency-depending dimming. This can be due to modified polarization or avoided absorption of photons which travel in the form of axions. Polarization measurements of photons from supernovae, white dwarfs or quasars can provide limits on $g_{a\gamma\gamma}$ for low axion masses [110]. A remarkable observation is that the Universe could be too transparent to TeV $\gamma$-rays. This can be explained by the fact that a photon could convert into axion (or ALP) in an interstellar magnetic field, the axion then travels unaffected by pair-production on extragalactic background light and is eventually converted back to a TeV photon [111–115]. An example of these fields is the galactic field, Fig. 1.6 shows a map of the magnetic field on

different cosmic structures as mapped by the Planck satellite. The typical field magnitude is of the order of the nT. Another probe is related to the superradiant mechanism that can affect the dynamics of rapidly rotating black holes, and thus their emission of gravitational waves [116].

As already discussed axions may constitute DM, and if existing at least a fraction of DM have to be composed of axions. DM is an interesting source of axions and triggered multiple experimental searches. Optical telescopes are sensitive to photons and thus to eV axion masses. Their searches include quasi-monochromatic emission lines from galaxies and galaxy-clusters, these limits [117–119] are reported in Fig. 1.5. The same holds for low-mass axions producing radio lines [120]. Instruments searching for DM-axions composing the Milky Way's halo are called haloscopes. Haloscopes are particularly interesting in the scope of this work, which is devoted to the study of a ferromagnetic one. In 1983, Sikivie proposed new ways to detect the axion by resonantly converting them into microwave photons inside a high quality factor ($Q$) cavity under a static magnetic field [121]. The resonance condition implies that the apparatus is sensitive to axions in a very narrow frequency range. The frequency of the axion signal is related to its mass and its width depends on the virial DM velocities in the galaxy. These kinds of experiments need to change resonant frequency to scan for different masses. The Axion Dark Matter eXperiment (ADMX) reached the sensitivity of KSVZ axions in the range $1.9\,\mu\text{eV} - 3.3\,\mu\text{eV}$ [122, 123] assuming virialized axions composing the whole DM density $\varrho_{\text{DM}} = 0.45\,\text{GeV/cm}^3$. The setup was improved by using SQUID amplifiers [124], and then reached the line of the DFSZ model [125]. The HAYSTAC experiment searched for heavier axions by operating a setup similar to the ADMX one but using a Josephson Parametric Amplifier (JPA), and achieving quantum limited sensitivity [126]. The collaborations UF and RBF also reached remarkable limits, and the ORGAN experiment operated a pathfinding haloscope at $110\,\mu\text{eV}$ [127, 128]. All these results are reported in Fig. 1.5. Several new concepts have been proposed to search for DM axions with next-generation haloscopes based not only on the Primakoff effect but also on axion-induced electric dipole moments (EDM) or on the axion-spin interaction [129–136].

### 1.2.2 Pure laboratory searches

The idea of pure laboratory experiments is to detect ALPs or axions independently from any astrophysical or cosmological source. The Primakoff effect can be used to create an axion beam by a laser of frequency $\omega_{\text{lsw}}$ traversing a dipole magnet of length $L$. The photons can be blocked and the resulting

pure axion beam is coherent if $m_a^2 L/2\omega_{\rm lsw} < 2\pi$. Then it can be regenerated back to photons by using the magnetic field $B$ of another magnet, the total conversion probability results $P(\gamma \to a \to \gamma) \simeq (g_{a\gamma\gamma}BL)^4/16$. The best limits of such experiments, called "light shining through walls" (LSW), was obtained by the OSQAR and ALPS collaborations [138, 139]. An important improvement is foreseen by using a resonant axion regeneration scheme [140–142]. The use of a laser beam to search for axions can be exploited also by studying its polarization in an external field. The production of real axions causes dichroism, while the mixing of virtual axions manifests as a birefringence. Considering linearly polarized light these effects result in a polarization rotation or an elliptical polarization, respectively. They have been extensively studied by the PVLAS collaboration, obtaining limits on axion-photon coupling close to the ones of LSW experiments [143, 144].

New light bosons also mediate fifth forces [98, 145]. The lower the mass the longer the force range, as it is the Compton wavelength of the mediator. The presence of such forces have been tested in many different ways and are thus severely constrained [146–155]. Among the best limits obtained for spin-mass coupling, the one of QUAX-$g_p g_s$ was measured in parallel with the work described in this thesis [156]. It was obtained by using a dc-SQUID monitoring the magnetization of a paramagnetic crystal, modulated in time by a force with wavelength $\sim 2\,$cm sourced by rotating lead masses. A new measurement is on the way, which includes larger samples and a better magnetic field sensitivity. The expected improvement is of about two orders of magnitude, and could be possibly enhanced.

## 1.3 Thesis overview

This chapter gives an introduction to some basic aspects useful to understand and motivate the rest of the work. Chapter 2 describes in detail the axion-spin coupling and the theoretical aspects needed to properly design a ferromagnetic haloscope. The Barbieri Cerdonio Fiorentini Vitale (BCFV) scheme is explained together with other similar proposals to get a clear picture of what an experiment should ideally look like. The aim of Chapter 3 is to introduce the reader to the experimental systems and techniques studied to operate the device. A photon-magnon hybrid system (HS), consisting in a resonant cavity coupled to a magnetized material is at the heart of the haloscope, thus its behavior was extensively studied in different conditions. Since the readout limits the precision of the measurement, a description of the different amplifiers is provided. Chapter 4 reports the different develop-

ment stages of the ferromagnetic haloscope, from a simple room-temperature apparatus to a 100 mK quantum-limited one, close to what a DFSZ-sensitive experiment should be. For every stage the HS, electronic readout and data analysis are considered. Chapter number 5 is focused on how to further improve the experiment to eventually get to the DFSZ axion line. These improvements include the usage of a much larger scale apparatus and a sensitivity beyond the quantum limit. Clearly, being this a pathfinder run, all the conditions can be relaxed depending on what is the easier way to get to the goal of QCD. Chapter 6 is the executive summary of this work. In Appendix A are listed other possible usages of the haloscope. Being a rf-spin magnetometer, it can be used for measurements other than axion searches. Appendix **??** introduces a scheme that uses a ferromagnetic haloscope to switch the axion effect from a power deposition to a frequency modulation, which is an exciting possibility for future axion searches. Eventually, Appendix C shows that the HS system used in the haloscope could be a natural testbed to probe solid superradiant phenomena.

In the rest of the thesis, if not explicitly specified, the term "axion" is used generically to indicate both the QCD-axion and axion-like particles.

# Chapter 2

# Concept of the ferromagnetic haloscope

Many proposals of how to search for the invisible axion were presented after its first introduction. The most successful is still the Sikivie haloscope, which converts axions to photons thanks to an intense magnetic field and detects this excess of photons in a microwave (mw) cavity. Here a new type of haloscope is conceptually described, namely the ferromagnetic haloscope. Such instrument aims to detect magnetization oscillations induced by DM-axions, which are then converted into photons deposited in a mw cavity. Since it is based on the interaction between the axion and the spin of an electron, this will be derived and described in details starting from the interaction with fermions. Afterwords, different fermion-based detection schemes are introduced to eventually focus on the QUAX proposal to search for DM with the axion-electron interaction.

## 2.1 Axion-fermion interaction

Section 1.1 derives the axion Lagrangian resulting in Eq. (1.19), which comprehends the interaction with em-fields, nucleons and electrons. Generically, the derivative interaction with fermions is invariant under a shift of the axion field $a \to a + a_0$ and reads

$$\mathcal{L}_\psi = \frac{C_\psi}{2F_a}\bar{\psi}\gamma^\mu\gamma_5\psi\partial_\mu a \tag{2.1}$$

where $\psi$ is the spinor field of a fermion of mass $m_\psi$, and $C_\psi$ is a model-dependent coefficient. The dimensionless couplings can be defined as

$$g_{a\psi\psi} = C_\psi m_\psi / F_a \tag{2.2}$$

and play the role of Yukawa couplings, while the fine structure constant of the interaction is $\alpha_{a\psi\psi} = g^2_{a\psi\psi}/4\pi$. Let's consider the DFSZ model and the different couplings that it can have with the standard model fermions. The tree-level coupling coefficient to the electrons of the DFSZ model is [44, 45]

$$C_e = \frac{\cos^2\beta'}{3}, \tag{2.3}$$

where $\tan\beta' = v_d/v_u$, the ratio of the vacuum expectation values of the Higgs field giving mass to the down-type quarks and to the up-type quarks. The use of $\beta'$ is to avoid confusion with the Higgs literature which uses $\tan\beta = \cot\beta' = v_u/v_d$, here $\beta' \simeq 1$. For nucleons the tree-level coupling coefficients are related to axial-vector current matrix elements by Goldberger-Treiman relations

$$\begin{aligned} C_p &= (C_u - \eta)\Delta u + (C_d - \eta z)\Delta d + (C_s - \eta w)\Delta s \\ C_n &= (C_u - \eta)\Delta d + (C_d - \eta z)\Delta u + (C_s - \eta w)\Delta s. \end{aligned} \tag{2.4}$$

Here, $\eta = (1 + z + w)^{-1}$, with $z = m_u/m_d$ and $w = m_u/m_s \ll z$ and the $\Delta q$ are given by the axial vector current matrix element $\Delta q S_\mu = \langle p|\bar{q}\gamma_\mu\gamma_5 q|p\rangle$ with $S_\mu$ the proton spin. Present experimental results give $\Delta u = 0.84 \pm 0.02$, $\Delta d = -0.43 \pm 0.02$ and $\Delta s = -0.09 \pm 0.02$, similar to what is used in the axion literature [157, 158]. As for the uncertainties, the ones on axion-nucleon couplings are mainly due to $z \simeq 0.38 \div 0.58$. In KSVZ models $C_{u,d,s} = 0$, and while $C_p$ is not vanishing within a plausible $z$ range, $C_n$ could also be zero. In the DFSZ models $C_u = \sin^2\beta'/3$ and $C_d = \cos^2\beta'/3$, so $C_{p,n}$ as functions of $\beta'$ and $z$ do not vanish simultaneously.

### 2.1.1 Axion-electron interaction and the BCFV scheme

The coupling between axions and electron spins can be used for axion detection as an alternative to the coupling to photons [159–162]. Being it weaker than the axion-photon coupling it was not immediately exploited, but recently new experimental schemes were presented. Besides the axion discovery, the axion-electron coupling is interesting for distinguishing between different axion models. The possibility of detecting galactic axions by means of converting them into collective excitations of the magnetization

(magnons) was considered by Barbieri *et al.* in [159], laying the foundations to the Barbieri Cerdonio Fiorentini Vitale (BCFV) scheme and to the following experimental proposal. The original idea is to use the large de Broglie wavelength of the galactic axions to detect the coherent interaction between the axion DM cloud and the homogeneous magnetization of a macroscopic sample. To couple a single magnetization mode to the axion field, the sample is inserted in a static magnetic field. The interaction yields a conversion rate of axions to magnons which can be measured by monitoring the power spectrum of the magnetization. The form of the interaction is calculated hereafter in terms of an effective magnetic field. Such a field is the searched-for signal. Its features are derived and characterized as follows.

The axion-fermion derivative part of the interaction can be generically expressed as

$$\mathcal{L}_\psi = \frac{g_{a\psi\psi}}{2m_\psi}\partial_\mu a(x)\big(\bar{\psi}(x)\gamma^\mu\gamma_5\psi(x)\big) \simeq -ig_{a\psi\psi}a(x)\bar{\psi}(x)\gamma_5\psi(x), \tag{2.5}$$

where the last term is an equivalent Lagrangian obtained by using Dirac equation and neglecting quadridivergences. The Feynman diagram of this interaction is reported in Fig. 2.1 and suggests how the process happens: an axion is absorbed and causes the fermion to flip its spin, and the macroscopic effect is a change in the magnetization of the sample containing the spin. By

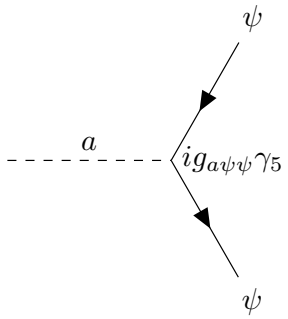


Figure 2.1: Feynman diagrams of the axion-fermion interaction, showing how the effect of the axion is to be absorbed and cause the spin flip of the fermion. The corresponding interaction Lagrangian is reported in Eq. (2.5).

taking the non-relativistic limit of the Euler–Lagrange equation, the time evolution of a spin 1/2 particle can be described by the usual Schroedinger equation

$$i\hbar\frac{\partial\varphi}{\partial t} = \Big(-\frac{\hbar^2}{2m_\psi}\nabla^2 - \frac{g_{a\psi\psi}\hbar}{2m_\psi}\boldsymbol{\sigma}_\psi\cdot\nabla a\Big)\varphi, \tag{2.6}$$

where $\sigma_\psi$ is the Pauli matrices spin vector. The first term on the right side of Eq. (2.6) is the usual kinetic energy of the particle, while the second one is analogous to the interaction between a spin and a magnetic field. One can notice that

$$-\frac{g_{a\psi\psi}\hbar}{2m_\psi}\boldsymbol{\sigma}_\psi\cdot\nabla a \equiv -2\frac{e\hbar}{2m_\psi}\boldsymbol{\sigma}_\psi\cdot\left(\frac{g_{a\psi\psi}}{2e}\right)\nabla a = -2\mu_\psi\boldsymbol{\sigma}_\psi\cdot\left(\frac{g_{a\psi\psi}}{2e}\right)\nabla a, \quad (2.7)$$

since $\mu_\psi$ is the magnetic moment of the particle, it can be both Bohr magneton or a nuclear magneton, depending on the considered fermion. From Eq. (2.7) it is clear that the effect of the axion is the one of a magnetic field, but since it does not respect Maxwell's equations it is an effective magnetic field

$$\mathbf{B}_a \equiv \left(\frac{g_{a\psi\psi}}{2e}\right)\nabla a. \quad (2.8)$$

This definition is useful to quantify the performances of a ferromagnetic haloscope in terms of usual magnetometers sensitivity. In the BCFV case, the signal is given by the electrons' magnetization. An intuitive connection between the macroscopic magnetization and the spin is given by $M \propto \mu_B N_S$ where $N_S$ is the number of spins which take part to the magnetic mode [163]. In such a way, the spin-flip can be classically considered a variation of the magnetization at a frequency given by the axion field.

It is now necessary to understand which are the features of $B_a$ to design a proper detector. The isothermal model of the Milky Way's DM halo predict a local density of $\varrho_{\mathrm{DM}} \simeq 0.45\,\mathrm{GeV/cm^3}$ [9]. An Earth-based laboratory is thus subjected to an axion-wind with a speed $v_a \simeq 300\,\mathrm{km/s}$, that is the relative speed of Earth through the Milky Way. Using the vector notation, the value of $v_a^i$ can be calculated from the speed of the galactic rest frame. The speed on Earth $v_E^i$ is given by the sum of $v_S^i$, $v_O^i$ and $v_R^i$, which are respectively the Sun velocity in the galactic rest frame (magnitude 230 km/s), the Earth's orbital velocity around the Sun (magnitude 29.8 km/s), and the Earth's rotational velocity (magnitude 0.46 km/s). The observed axion velocity is then $v_a^i = -v_E^i$. The velocities follow a Maxwell-Boltzmann distribution, its calculations in the Galactic and Earth frames are shown in Fig. 2.2. As will be shown hereafter, the effect of this motion is a non-zero value of the axion gradient, and a modulation of the signal with a periodicity of one sidereal day and one sidereal year [64, 164, 165].

The numeric axion density in the DM halo depends on the axion mass and results $n_a \simeq 3\times10^{12}\,(10^{-4}\,\mathrm{eV}/m_a)\,\mathrm{cm^{-3}}$. The coherence length of the axion field is related to the de Broglie wavelength of the particles, which is

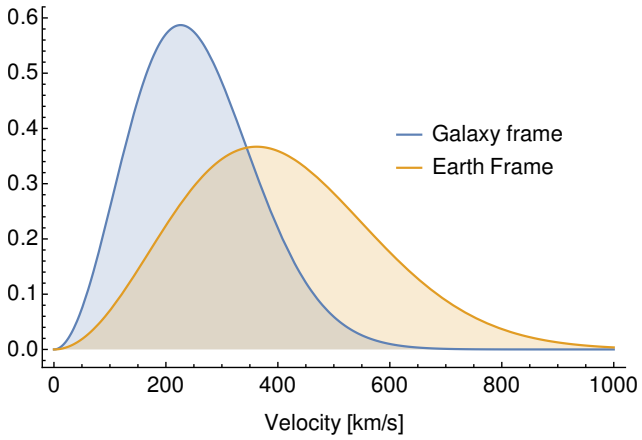


Figure 2.2: Velocity distribution of DM-axions in the Galaxy frame and in the Earth frame. Vertical units are arbitrary.

given by

$$\lambda_a = \frac{h}{m_a v_a} \simeq 14 \left(\frac{10^{-4}\,\mathrm{eV}}{m_a}\right) \mathrm{m}. \tag{2.9}$$

Such wavelength allows for the use of macroscopic samples to detect the variation of the magnetization. The large occupation number $n_a$, coherence length $\lambda_a$, and $\beta_a = v_a/c \simeq 10^{-3}$ permit to treat $B_a$ as a classical field[1]. The coherent interaction of $a(x)$ with fermions has a mean value

$$a(x) = a_0 e^{i p_a^\mu x_\mu} = a_0 e^{i(p_a^0 t - p_a^i x_i)}, \tag{2.10}$$

where $p_a^i = m_a v_E^i$ and $p_a^0 = \sqrt{m_a^2 + |p_a^i|^2} \simeq m_a + |p_a^i|^2/(2m_a)$. The production of DM axions is discussed in Sec. 1.1, where it is shown that they are indeed cold DM since their momentum is orders of magnitude smaller than the mass. The axion kinetic energy is expected to be distributed according to a Maxwell-Boltzmann distribution, with a mean relative to the rest mass of $7\times10^{-7}$ and a dispersion about the mean of $\sigma_{\mathrm{MB}} \simeq 5\times10^{-7}$ [64,164,166]. The effect of the mean is a negligible shift of the resonance frequency with respect to the axion mass. The consequence of the dispersion on the effective magnetic field is a natural figure of merit

$$Q_a = \frac{1}{\sigma_{\mathrm{MB}}} \simeq \left(\frac{m_a}{\langle p_a^i \rangle}\right)^2 = \frac{1}{\beta_a^2} \simeq 2\times10^6. \tag{2.11}$$

[1] The average speed $v_a \ll c$ also justifies the approximation of Eq. (2.6), i. e. the use of the non-relativistic limit of Euler-Lagrange equations.

To calculate the field amplitude $a_0$, the momentum density of the axion field is equated to the mean DM momentum density yielding

$$a_0^2 p_1^0 p_a^i = n_a \langle p_a^i \rangle = n_a m_a v_a \quad \Rightarrow \quad a_0 = \sqrt{n_a/m_a}\,. \tag{2.12}$$

For calculation purposes natural units are dropped and the Planck constant $\hbar$ and speed of light $c$ are restored. The effective magnetic field associated to the mean axion field reads

$$B_a^i = \frac{g_{a\psi\psi}}{2e}\left(\frac{n_a \hbar}{m_a c}\right)^{1/2} p_a^i \sin\left(\frac{p_a^0 ct + p_a^i x_i}{\hbar}\right). \tag{2.13}$$

From Eq. (2.13), the frequency and amplitude of the axionic field interacting with electrons result

$$\begin{aligned} B_a =& \frac{g_{aee}}{2e}\left(\frac{n_a \hbar}{m_a c}\right)^{1/2} m_a v_a \simeq 5 \times 10^{-23} \left(\frac{m_a}{50\,\mu\text{eV}}\right) \text{T}, \\ \frac{\omega_a}{2\pi} \simeq& \frac{c p_a^0}{\hbar} = \frac{m_a c^2}{\hbar} \simeq 12 \left(\frac{m_a}{50\,\mu\text{eV}}\right) \text{GHz}. \end{aligned} \tag{2.14}$$

As the equivalent magnetic field is not directly associated to the axion field but to its gradient, the corresponding correlation length and coherence time must be corrected to [134]

$$\begin{aligned} \lambda_{\nabla a} \simeq& 0.74\,\lambda_a = 0.74 \frac{\hbar}{m_a v_a} \simeq 20 \left(\frac{50\,\mu\text{eV}}{m_a}\right) \text{m}; \\ \tau_{\nabla a} \simeq& 0.68\,\tau_a = 0.68 \frac{2\pi\hbar}{m_a v_a^2} \simeq 46 \left(\frac{50\,\mu\text{eV}}{m_a}\right)\left(\frac{Q_a}{1.9 \times 10^6}\right) \mu\text{s}. \end{aligned} \tag{2.15}$$

The nature of the DM axion signal is now well-defined: an effective magnetic field of amplitude $B_a$, frequency $f_a = \omega_a/2\pi$, and quality factor $Q_a$ with values defined by Eq.s (2.14) and (2.15).

### 2.1.2 Axion-nucleon interaction

Most of the calculations in Sec. 2.1.1 are valid for both electrons and nucleons. In particular the considerations are the same in the two cases until Eq. (2.13), which can be used also for nucleons. The coupling constant $g_{aNN}$ follows from Eq. (2.2) and since $C_\psi = O(1)$ its value is $m_N/m_e \sim 10^3$ times stronger than $g_{aee}$. A nuclear axion-wind detector benefits from a larger coupling constant, thus in principle is more suitable for axion searches [167]. The experimental differences between a nuclear scheme and the BCFV one are discussed in Sec. 2.2.

The interaction with gluons of Eq. (1.17) is in some sense the reason why the axion was originally introduced. The corresponding term in Eq. (1.19) describes a coupling with the spins and with an electric field. The Hamiltonian can be written more intuitively as

$$\mathcal{H}_d = d_N \sigma_N^i E_i, \tag{2.16}$$

where $\sigma_N^i$ represents the spin, and $E_i$ is an electric field [167]. As for $d_N$, it is an oscillating electric dipole induced by axions of magnitude $d_N \simeq 10^{-16}\,(a/F_a)\,e\,\mathrm{cm}$. Both these terms of the Lagrangian can be the base of experimental searches exploiting nuclear magnetic resonance (NMR) techniques and, as is described in the next section, are a perfect probe for light and ultra-light ALPs.

## 2.2 Spin-based experimental searches

Referring to Chapter 1, the first strong constraints on $\bar{\theta}$ come from the measurements of EDM, in particular the one of the neutron. It is mentioned in Sec 1.1 that the nEDM collaboration reports $|d_n| < 3.0 \times 10^{-26}\,e\,\mathrm{cm}$ at 90% CL [33–35], which limits $\bar{\theta} \leq 10^{-10}$.

As a matter of fact, EDMs and axion physics are related by CP violation and so are the experimental searches. The search for EDM appears as a natural choice to test the axion by means, for example, of the oscillating EDM of Eq. (2.16). To reach axionic-relevant sensitivity one needs to work on some resonant phenomenon, as it is done by the CASPEr collaboration [131, 132, 168, 169]. These schemes work at typical NMR frequencies, which are mainly related to light axions. In their case the axion-gluon coupling gives an oscillating nuclear dipole

$$d_N = g_d \frac{\sqrt{2\varrho_{\mathrm{DM}}}}{\omega_a} \cos(\omega_a t). \tag{2.17}$$

The CASPEr-Electric scheme makes use of a static magnetic field to tune the resonance frequency of nuclear spins to axion masses below a $\mu$eV. Depending on the nucleon gyromagnetic ratio $\gamma_N$, hundreds of MHz can be reached by using $B$-fields up to 20 T. A static electric field perpendicular to the magnetic field is used to remove the electric dipole degeneration and stimulate the on-resonance axion absorption. It has been discussed whether axions induce an EDM also on electrons [170, 171], and it is worth wondering if a resonant absorption may be used also in this case [172]. When trying

to boost the signal[2] using an electric field, an anomaly factor arises which limits the achievable sensitivity [174].

A resonant detection of the DM-wind can be exploited much like is proposed by the BCFV scheme. This is the purpose of CASPEr-Wind [131,132], namely the detection of an effective axion field which reads

$$B_a^{(N)} = g_{aNN} \frac{\sqrt{2\varrho_{\rm DM}}}{\gamma_N} v_a, \tag{2.18}$$

by using precision measurements of NMRs. The signal-to-noise ratio (SNR) on-resonance is given by

$$\mathrm{SNR}_N = \gamma_N^2 \frac{\varrho_N P_N B_a}{S_B(f)} \tau_N^{3/2}, \tag{2.19}$$

where $\varrho_N$ is the nuclear-spin density, $P_N$ is their polarization fraction and $S_B(f) \simeq \mathrm{fT\,Hz^{-1/2}}$ is the field sensitivity of a SQUID or a spin-exchange-relaxation-free (SERF) magnetometer. The coherence time $\tau_N$ is the nuclear-spin relaxation time, which (in the limit of $\tau_N < \tau_a$) also limits the maximum integration time. For low-mass axions the coherence time $\tau_a$ is typically much longer then any other timescale involved in the measurement. Interestingly , it was recently pointed out [175] that present limits on low-mass ALPs may have to be relaxed due to the stochastic nature of the signal.

Nuclear axion-wind haloscopes are typically sensitive to light axions since it is difficult to reach GHz-range NMR, corresponding to the usual QCD-axion window. These frequencies are typical of electron-spin-resonance (ESR) measurements, since the electron gyromagnetic ratio $\gamma_e$ is roughly $10^3$ times larger than $\gamma_N$. A suitable magnetometer could measure magnetization oscillations of electrons even at tens of GHz frequencies and probe $g_{aee}$. Unfortunately radiation damping is limiting the sensitivity of such experiments, as it is reported in the following Section, thus the scheme has to be changed to overcome it.

### 2.2.1 The QUAX proposal

The QUAX ("QUaerere AXion" or "QUest for AXions") proposal aims at the implementation of the BCFV scheme to build an haloscope sensitive to the axion-electron spin coupling [133, 134]. A viable experimental

[2] To get an order-of-magnitude estimation of experimental sensitivity one may take e. g. the electron EDM measurement by the ACME collaboration, which obtained $|d_e| < 1.1 \times 10^{-29}\, e\,\mathrm{cm}$ at 90% CL [173].

scheme must be designed to detect the field $B_a^i$, whose features are defined by Eq.s (2.14) and (2.15). In principle the same NMR scheme described in Sec. 2.2 can be exploited switching from NMR to ESR, since the working frequencies corresponding to the QCD-axion window are tens of GHz. A magnetic sample with a high spin density $n_S$ and a narrow linewidth $\gamma_m = 2\pi/T_2$ (i. e. long spin-spin relaxation time $T_2$) can be used as a detector. The magnetic field $B_a$ drives a coherent oscillation of the magnetization over a maximum volume of scale $\lambda_{\nabla a}$. The sensitivity increases with the sample volume $V_s$ up to $(\lambda_{\nabla a})^3$.

For electrons $\gamma_e \simeq (2\pi)28\,\mathrm{GHz/T}$, so the corresponding magnetic field $B_0$ is of order 1 T and experimentally easily obtainable. The electrons' spins of a magnetic sample under a uniform and constant magnetic field result in a magnetization $\mathbf{M}(\mathbf{x}, t)$ that can be divided in magnetostatic modes. The space-independent mode of uniform precession is called Kittel mode. A sample in a magnetic field directed along $\hat{z}$, the $\hat{x}$ and $\hat{y}$ component of the Kittel mode are oscillating, while the $\hat{z}$ component is constant [176]. Its dynamics is described by Bloch equations in terms of $\mathbf{M} = (M_x, M_y, M_0)$,

$$\begin{aligned} \frac{\mathrm{d}M_{x,y}}{\mathrm{d}t} &= \gamma_e(\mathbf{M}\times\mathbf{B})_{x,y} - \frac{M_{x,y}}{T_2} - \frac{M_{x,y}M_0}{M\tau_r}, \\ \frac{\mathrm{d}M_0}{\mathrm{d}t} &= \gamma_e(\mathbf{M}\times\mathbf{B})_z - \frac{M-M_0}{T_1} - \frac{M_x^2+M_y^2}{M\tau_r}, \end{aligned} \tag{2.20}$$

where $M = |\mathbf{M}|$, $T_1$ is the spin-lattice relaxation time, and $\tau_r$ is the radiation damping (RD) time. The axionic field couples to the components of $\mathbf{M}$ transverse to the external field, depositing power in the material. More power is deposited if the axion field is coherent with the Kittel mode for a longer time. The best-case scenario is a material with a quality factor $Q_m = \gamma_e B_0/\gamma_m$ which matches $Q_a$, so that the coherent interaction between spins and DM-axions lasts for $\tau_{\nabla a}$. For this reason the magnetic field uniformity over the sample must be $\leq 1/Q_m$ to avoid inhomogeneous broadening of the ESR. The high working frequency does not allow to use magnetometers as rf-SQUIDs, which works up to roughly 1 GHz. A detection scheme may consist in a coil coupled to an high-frequency amplifier, like an high electron mobility transistor (HEMT), to measure the sample magnetization fluctuations. However, the limit of this design is not the amplifier noise but a short coherence time. In fact at such high frequency the rate of dipole emission $1/\tau_r$ becomes higher than the intrinsic material dissipation since

$$\tau_r = \frac{c^3}{\omega_m^3}\frac{4\pi}{\mu_0\gamma_e M_0 V_s}, \tag{2.21}$$

where $\omega_m = \gamma_e B_0$ is the electron's Larmor frequency, $\mu_0$ is vacuum magnetic permeability [177–179].

Since RD is related to the sample dipole emission, a possible way to reduce its contribution is to limit the phase-space of the radiated light by working in a controlled environment like a resonant cavity. This possibility is considered in the following calculation. A small sample of magnetic material is embedded in a mw cavity under a constant field $B_0$. If the cavity rf field is $\mu H_x$ the total field results $\mathbf{B} = (\mu H_x, 0, B_0)$, where $\mu$ is the material magnetic permeability. The magnetization of the sample interacts with the cavity electromagnetic field, modifying the dynamics described by Eq.s (2.20). Since the cavity can be represented by an electrical resonator [180,181] with resistance $R$, inductance $L$ and capacity $C$, an equation can be added to the system in Eq. (2.20) to account for its presence. The resulting equation system is immune to radiation damping and reads

$$\begin{aligned} \frac{\mathrm{d}M_{x,y}}{\mathrm{d}t} &= \gamma_e(\mathbf{M}\times\mathbf{B})_{x,y} - \frac{M_{x,y}}{T_2}, \\ \frac{\mathrm{d}M_0}{\mathrm{d}t} &= \gamma_e(\mathbf{M}\times\mathbf{B})_z - \frac{M-M_0}{T_1}, \\ -\mathcal{K}\frac{\mathrm{d}M_x}{\mathrm{d}t} + L\frac{\mathrm{d}I}{\mathrm{d}t} + RI + \frac{1}{C}\int I\mathrm{d}t &= V_{\mathrm{rlc}}. \end{aligned} \tag{2.22}$$

The current $I = \mathcal{K}' H_x$ is related to the rf field, $\mathcal{K}$ and $\mathcal{K}'$ are geometrical factors of dimension 1/m, and $V_{\mathrm{rlc}} = v_{\mathrm{rlc}}\sin(\omega_{\mathrm{rlc}}t)$ is the driving potential of frequency $\omega_{\mathrm{rlc}}$. The spins process along $\hat{z}$, so $\mathrm{d}M_0/\mathrm{d}t \simeq 0$, and if the rf field is small compared to the external field, $M \simeq M_0$. Under these approximations Eq.s (2.22) describe a hybrid system of two coupled harmonic oscillators [182]. The factor $\mathcal{K}$ of Eq.s (2.22) describes the coupling between cavity and material; it depends on the superposition between the cavity mode and the sample volume. If the resonant frequencies of the two HOs are tuned to be equal, the cavity and Kittel mode are in full hybridization, the radiation damping is avoided [177]. The steady state solution of the system in Eq.s (2.22) under the effect of a driving field $B_1$ is

$$M_{x,y}(\omega) = M_0 \frac{(\omega-\omega_m)\tau_h^2}{1+\left[(\omega-\omega_m)\tau_h\right]^2}\gamma_e B_1, \tag{2.23}$$

where $\tau_h$ is the average of the cavity and material relaxation times. The RD-free scheme preserves the sensitivity of the apparatus. A measurement of the RD linewidth broadening and of its removal is reported in Fig. 2.3, where a Yttrium Iron Garnet (YIG) sphere is coupled to different mw cavities at

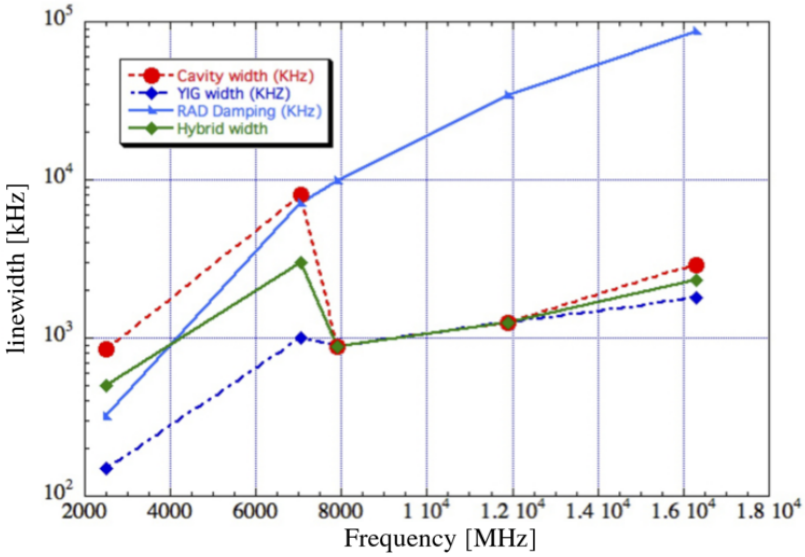


Figure 2.3: Measurement of the RD broadening and of its limitation. The red and purple points are the linewidths of resonant cavities and material resonances, respectively. The calculated free-field linewidth of the ESR is reported in light-blue and is affected by RD, while the green points represent the coupled material-cavity linewidths, immune from RD.

increasing frequencies. More details on cavity-material hybrid systems are given in the dedicated Section 3.1. The axion field, like $B_1$ in Eq. (2.23), drives the magnetization on a plane perpendicular to the static field. Such resonant magnetization results

$$M_a(t) = \gamma_e \mu_B B_a n_s \tau_{\min} \cos(\omega_a t), \tag{2.24}$$

where $\tau_{\min} = \min(\tau_{\nabla a}, \tau_h)$. The axion deposited power can be calculated as

$$P_{\text{in}} = \mu_0 H_{a,i} \frac{\mathrm{d}M_a^i}{\mathrm{d}t} V_s = B_a \frac{\mathrm{d}M_a}{\mathrm{d}t} V_s = \gamma_e \mu_B N_S \omega_a B_a^2 \tau_{\min}. \tag{2.25}$$

In a steady-state, power balance ensures that half of the power can be collected as rf radiation by an antenna critically coupled to the hybrid mode, thus $P_{\text{out}} = P_{\text{in}}/2$ [178]. Using Eq. (2.25), the power released by a DFSZ-

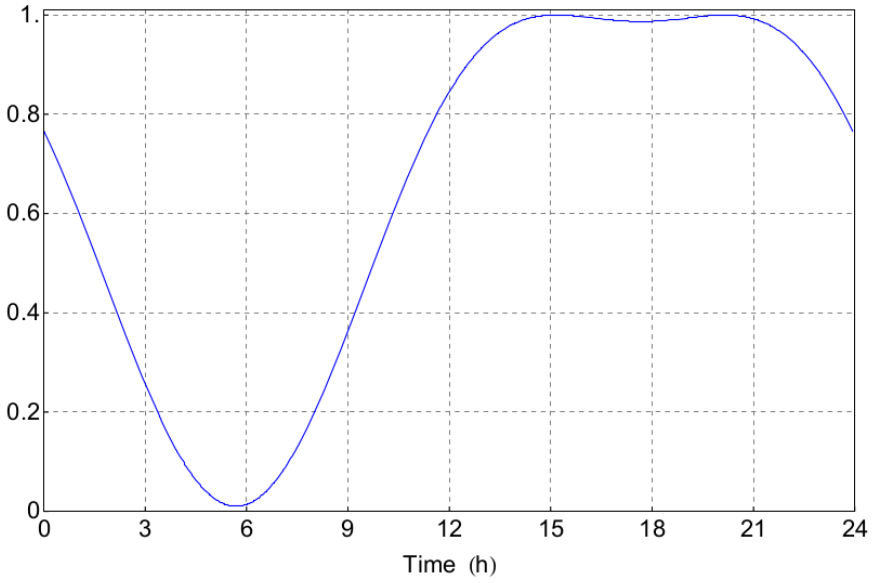


Figure 2.4: Daily modulation of the axion wind signal for the QUAX detector, located at Legnaro (Padua, Italy) and with $B_0$ along the horizontal plane and oriented north-south.

axion wind in 100 cc of YIG with a practicable linewidth is

$$P_{\text{out}} = \frac{P_{\text{in}}}{2} = 5.9 \times 10^{-28} \left(\frac{m_a}{50\,\mu\text{eV}}\right)^3 \times \\ \times \left(\frac{n_s}{2 \cdot 10^{28}/\text{m}^3}\right) \left(\frac{V_s}{100\,\text{cc}}\right) \left(\frac{\tau_{\min}}{2\,\mu\text{s}}\right) \text{W}, \tag{2.26}$$

corresponding to a rate $r_a \sim 10^{-6}$ Hz of 12 GHz photons. It can be shown that to actually detect this excess of photons one needs to rely on a single photon counter rather than on an amplifier [183].

As seen in Sec. 2.1.1, due to Earth rotation the direction of the static magnetic field $B_0$ changes with respect to the direction of the axion wind (Vega in Cygnus). The full daily modulation is shown in Fig. 2.4. Considering a preliminary setup with a power sensitivity $\Sigma_P$, the 95% C. L. two-sigma limit on the axion-electron coupling in the case of non-detection is

$$g_{aee} \leq \frac{e}{\pi m_a v_a} \sqrt{\frac{2\Sigma_P}{\gamma_e c \mu_B n_a N_s \tau_{\min}}}. \tag{2.27}$$

where usually $\tau_{\min} = \tau_h$, and $\Sigma_P$ is essentially given by the noise fluctuations. The noises affecting the measurement are different depending on the readout. Considering a noiseless detector, the fundamental noise of the scheme is Johnson noise

$$\mathrm{d}P_J = k_B T \mathrm{d}f, \tag{2.28}$$

where $T$ is the thermodynamic temperature of cavity and material, and $\int_{\mathrm{RBW}} \mathrm{d}f = \Delta f$ is the resolution bandwidth. The case of a real detector with a noise temperature $T_n$ can be treated by replacing $T$ of Eq. (2.28) with an effective system temperature $T_s = T + T_n$. These considerations hold as long as the temperature is high with respect to the quantum scale of the HO under study [184]. One may consider the crossing point between the thermodynamic and quantum regimes

$$k_B T_q = \hbar\omega, \tag{2.29}$$

which gives $T_q \simeq 0.5\,(\omega/10\,\mathrm{GHz})\,\mathrm{K}$. This temperature corresponds roughly to the standard quantum limit of a linear amplifier working at the frequency $\omega$. Such limit is essentially given by the zero-point fluctuations of a quantum HO. For example, the mode of a resonant cavity with frequency $\omega_{\mathrm{ho}}$ have an average stored energy $(\langle n\rangle + 1/2)\hbar\omega_{\mathrm{ho}}$, where $\langle n\rangle$ is the average occupation number given by a Bose-Einstein distribution

$$\langle n\rangle = \frac{1}{e^{\hbar\omega_{\mathrm{ho}}/k_B T} - 1}. \tag{2.30}$$

Simple calculations show that for temperatures lower than $T_q$, in the stored energy the $\hbar\omega_{\mathrm{ho}}/2$ term dominates, and gives the standard quantum limit (SQL). This noise arises because linear amplifiers measure simultaneously energy and time, and are thus subjected to Heisenberg uncertainty principle. A device which drops one of these two quantities to measure just the other should not be subjected to the SQL. For example, a single photon counter [183] may be a switching detector yielding no information about the energy of the detected photon and just measuring a rate (i. e. time). Being such device only sensitive to real thermal photons, the readout of a 10 GHz oscillator with 1 $\mu$s relaxation time kept at 50 mK, will exhibit a noise counting rate $r_n = \langle n\rangle|_{T=50\,\mathrm{mK}}/1\,\mu\mathrm{s} = 70\,\mathrm{Hz}$. Since the axion-electron interaction strength grows with frequency while the noise decreases, it is desirable to work at higher frequencies.

The described detector is a ferromagnetic axion haloscope, but it is actually sensitive to any effect which somehow modulates the magnetization of the sample, configuring it as a spin-magnetometer. Therefore,

throughout the text the ferromagnetic haloscope is also referred to as spin-magnetometer. For example, in nuclei like holmium, it should be possible to have NMRs at GHz frequencies with relatively small magnetic fields [185] by polarizing the electrons which consequently polarize the nucleons. This particular feature may allow the use of the QUAX scheme for probing axion-nucleon interaction in microwave cavities. Some of the other possible usages of this device are discussed in Appendix A.

# Chapter 3

# Modelization and experimental techniques

This chapter explains the two main branches to be considered when building an haloscope. These are somehow complementary and consist in the maximization of the axionic signal and in the improvement of power sensitivity of the detector. Sec. 3.1 details the HS composed by a mw cavity and magnetic materials. Sec. 3.2 is devoted to understand and optimize the absorption and transduction of the axionic signal, which is measured using the devices described in Sec. 3.3.

## 3.1 Photon-magnon hybrid systems

As seen in the previous Chapter, it is possible to effectively remove radiation damping by embedding the sample in a mw cavity and tuning the magnetic field such that $\omega_m = \gamma_e B_0 \simeq \omega_c$, where $\omega_c$ is the resonance frequency of a cavity mode. The first theoretical analysis of such systems was given by Charles Kittel [186, 187] in 1947. The HS dynamics was completed by Bloembergen and Pound in 1954 [177], and an exact description of the system is given by the Tavis-Cummings model [188]. This last one discusses the interaction of $N_S$ two-level systems with a single mw mode, and predicts a scaling of the cavity-material coupling strength $g_{cm} \propto \sqrt{N_S}$. The single-spin coupling is

$$g_s = \frac{\gamma_e}{2\pi}\sqrt{\frac{\mu_0 \hbar \omega_m}{\xi V_c}}\,, \tag{3.1}$$

where $V_c$ is the cavity volume and $\xi$ a mode-dependent form factor [189], with this relation $g_{cm} = g_s\sqrt{N_S}$. Such scaling has been verified experimentally down to mK temperatures for an increasing number of spins $N_S$ [189, 190]. For a quantity of material such that $g_{cm} \gg 1\,\text{MHz}$, the single cavity mode splits into two hybrid modes with frequencies $\omega_+$, $\omega_-$ and $g_{cm} = \omega_+ - \omega_-$. For $\omega_m = \omega_c$ the linewidths of the hybrid modes are the average of the cavity mode linewidth $\gamma_c$ and of the material one $\gamma_m$, namely $\gamma_h = (\gamma_c + \gamma_m)/2$. The coupling $g_{cm}$ is in fact a conversion rate of the material magnetization quanta (magnons) to cavity photons and viceversa. If $g_{cm} > \gamma_h$ the system is in the strong-coupling regime, meaning that for a magnon (photon) it is more likely to be converted than to be dissipated.

When close to their resonant frequencies, coherent systems such as a microwave cavity normal mode or the electron spin resonance (ESR) of a magnetized material, can be described as HOs. A scheme of the considered HS is reported in Fig. 3.1, where the HOs and the couplings are represented by three spheres and two springs, respectively. This intuitive scheme is the

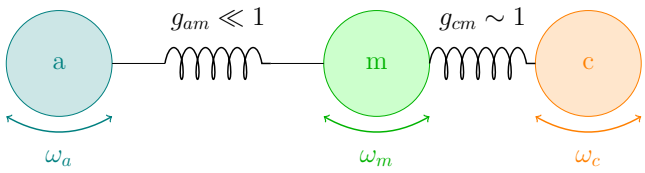


Figure 3.1: The coupled harmonic oscillators are reported in orange, green and blue for cavity $c$, material $m$ and axion $a$ respectively. The uncoupled normal-modes frequencies of the HOs are $\omega_c$, $\omega_m$ and $\omega_a$ and the couplings are $g_{am}$ and $g_{cm}$, represented by springs.

base of the two models of Sec.s 3.2.1 and 3.2.3. The resonant cavity and the magnetic material, the two HO which form the HS, are described in Sec.s 3.1.1 and 3.1.2. A practical realization of an HS is a ferrimagnetic YIG sphere placed on the maximum of the magnetic rf field mode of a copper resonant cavity. A static field is used to vary the YIG electrons' Larmor frequency, while a transfer function $S_{21}$ is measured. As can be seen in Fig. 3.2, the result of this procedure is an anticrossing curve. The avoided mode crossing is a well-known phenomenon for coupled oscillators [176]. The condition $\omega_m = \omega_c$ minimizes the distance between the two hybrid modes. In this state, the linewidth of the hybrid modes should be equal. However, experimentally this is not necessarily verified so the modes linewidths are labeled $\gamma_-$ and $\gamma_+$, taking into account possible asymmetries of the system.

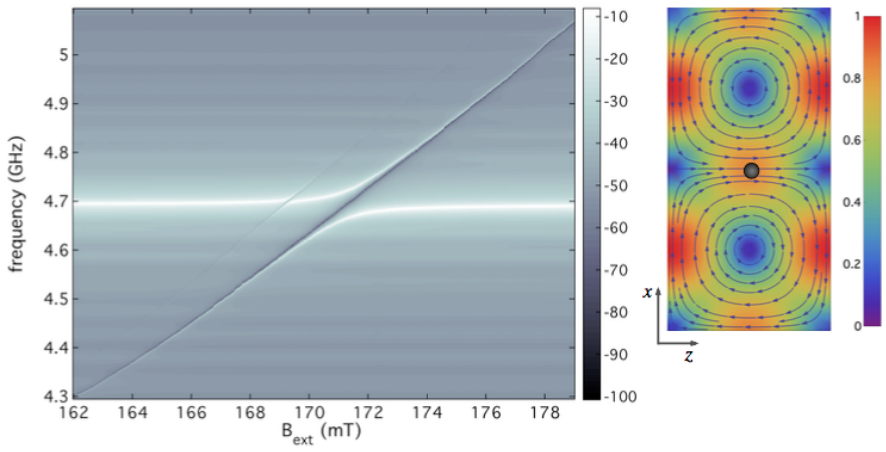


Figure 3.2: Anticrossing curve of an HS (*left*) consisting in the TE102 mode of a rectangular cavity (*right*) with a YIG sphere at its center. The sphere is magnetized with a static field, and the curve is obtained by varying it and acquiring $S_{21}$ spectra. The grayscale is in dB and the colorscale is the normalized amplitude of the cavity rf $B$-field.

### Quantum information and precision physics

Photon-magnon HSs are widely used in different fields of physics. Towards the development of quantum computers, different groups [189–196] are coherently coupling spin ensembles, microwave cavities and superconducting quantum circuits to create, for example, quantum memories [197–199]. Quantum technology is an incredibly fast-growing field, hybrid quantum systems based on magnonics offer opportunities to develop microwave-to-optical quantum transducers for quantum information processing [200, 201] and quantum-enhanced detection of magnons for magnon spintronics [202].

The usage of HSs in quantum technology and in precision physics can mutually benefit. However, even if the experimental techniques are similar, the aims are quite different, and it is not always possible to exploit this possibility. For example, single photon counters or single spin-flip detectors have been developed for quantum information purposes. These devices can not be directly deployed into an haloscope to detect a low rate of photons or magnons, due to their low duty cycle. This specific topic is treated in Sec. 5.2.1, and for a complete and interesting review the reader is referred to [203].

### 3.1.1 Microwave resonant cavities

The photonic oscillators of photon-magnon hybrid systems are typically mw resonant cavities. In resonant axion searches, copper cavities are widely used since they show the highest quality factors in strong magnetic fields [121–128]. The axion-to-photon conversion rate increases with the cavity volume, which is larger at low frequencies. For higher frequencies (i. e. above 5 GHz) several experimental limitations occur due to small volumes and lowering quality factors of copper resonant cavities. In the case of a ferromagnetic haloscope a resonant cavity and a material with a high quality factor are necessary to match $\tau_h$ with $\tau_{\nabla a}$. A resonant cavity exhibits several normal modes of the electromagnetic fields. Depending on the type of haloscope, a specific mode can be chosen to optimize the measurement of the axion-photon or axion-electron interaction.

When building a haloscope, copper cavities are a satisfying choice since their quality factor is rather high $\gtrsim 10^4$ and copper has almost no magnetic interaction. A static magnetic field does not affect the resonant frequency and penetrates the cavity walls, allowing the conversion of axions to photons in the cavity volume. This property needs to be preserved in the new concepts of haloscope cavities. The literature includes several designs of high-$Q$ cavities, but none of them has all the requested features. For example, natural choices are superconducting (SC) cavities, which are widely studied for their application in accelerator physics [204]. In axion searches, these are operated in a strong magnetic field that weakens superconductivity and is screened by the SC material.

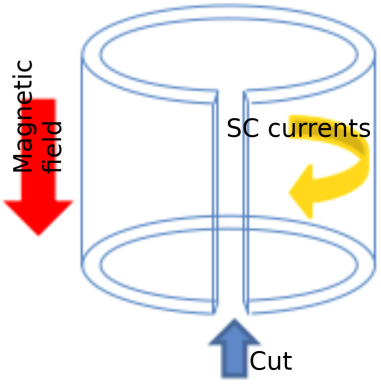


Figure 3.3: Scheme of the SC cavity walls and of the supercurrent block.

In this thesis work, to overcome both limitations, a cylindrical cavity is designed divided in two halves, each composed by a type II SC body and copper end caps. Type II superconductors are in fact known to have a reduced sensitivity to the applied magnetic field. Moreover, magnetic field penetration in the inner cavity volume is allowed by the interruption of SC surface as shown in Fig. 3.3. In the practical realization, the screening supercurrents are blocked with the insertion of a 30 $\mu$m-thick copper layer between the two halves. The built cavity is shown

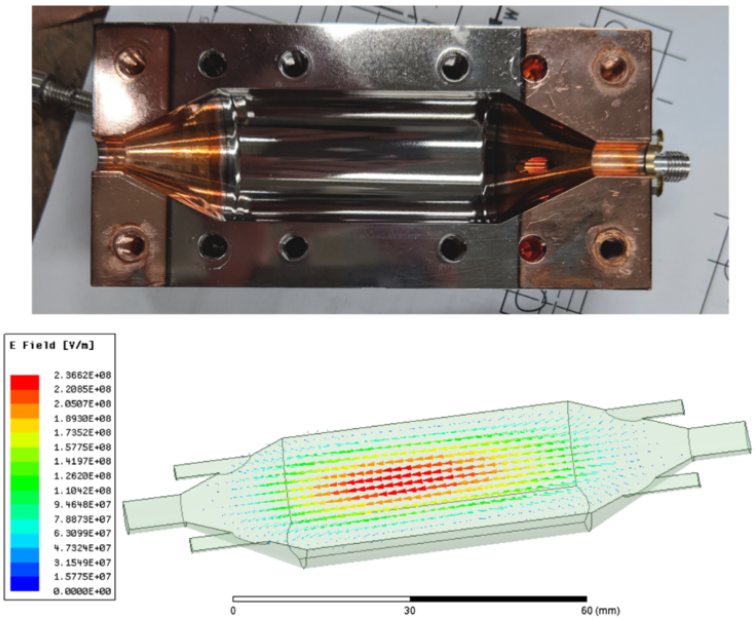


Figure 3.4: *Upper* - Picture of one half of the hybrid cavity described in the text. *Lower* - Electric field profile of the 9.08 GHz TM010 mode used to measure the axion-photon interaction.

in the upper part of Fig. 3.4, and features a structure of two copper semicells with a cylindrical body and conical endcaps to reduce current dissipation at interfaces. The cylindrical body is 50 mm long with diameter 26.1 mm, while the cones are 19.5 mm long. The inner cylindrical part of the cavity is coated by means of a 10 cm planar magnetron equipped with a NbTi target. The estimated coating thickness ranges between 3 to 4 $\mu$m. For the detection of axions through its interaction with the electron spin, part of the cylinder was flattened to break the angular symmetry and remove the degeneration of the chosen mode TM110, resonating at 14 GHz. Because of this hybrid geometry, the quality factor is expressed as

$$\frac{1}{Q_0} = \frac{R_s^{\text{cyl}}}{G^{\text{cyl}}} + \frac{R_s^{\text{cones}}}{G^{\text{cones}}}. \tag{3.2}$$

$R_s$ are the surface resistances and a finite element calculation yields $G^{\text{cones}} \simeq 6270.11\,\Omega$ and $G^{\text{cyl}} \simeq 482.10\,\Omega$. Around 10 GHz and 4 K temperature, the surface resistance for copper is $R_s^{\text{Cu}} \simeq 4.9\,\text{m}\Omega$ [205]. A pure copper cavity with this geometry would have $Q_0^{\text{Cu}} \simeq 9 \times 10^4$, while an hybrid cavity with

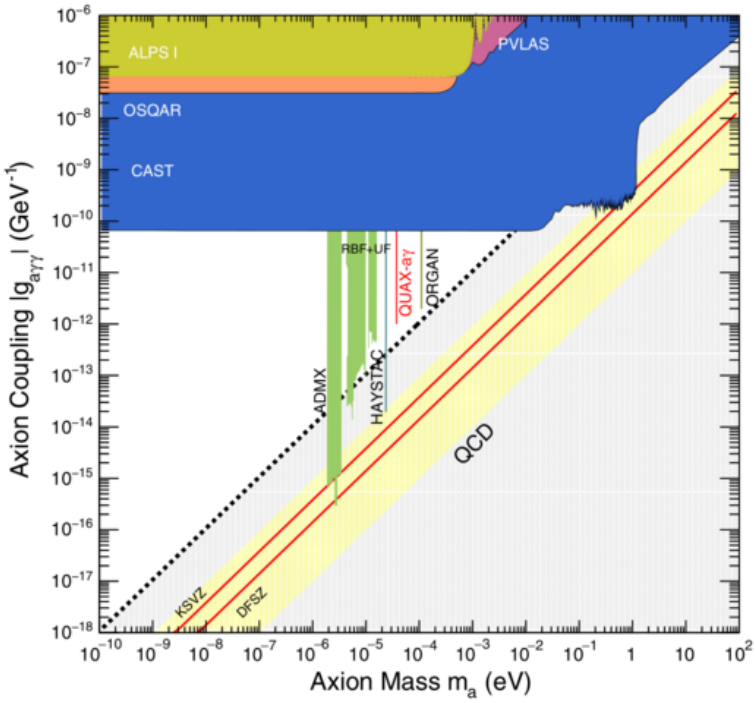


Figure 3.5: Exclusion plot of the axion-photon coupling constant with the result of QUAX-$a\gamma$ reported in red. The grey area indicates the prediction from other hadronic axions models [206].

copper cones and no losses on the cylindrical surface would have $Q_{\max} = G_{\text{cones}}/R_s^{\text{Cu}} \simeq 1.3 \times 10^6$. To test these promising simulations, the cavity is cooled down and studied in a variable magnetic field. The cavity shows a quality factor at zero-field of $1.2 \times 10^6$, which is probably limited by the copper cones, and decreases when applying an external magnetic field. A YIG sphere is inserted in the cavity to test the magnetic field penetration, and the expected hybridization is obtained, showing that the field is entering almost unaltered in the cavity volume. In fact, since the relation $\gamma_h = (\gamma_c + \gamma_m)/2$ is found to be valid, there is no evidence of non-uniformed of the $B$-field over the YIG down to roughly one part in $10^4$.

The TM010 mode of the described cavity is used to set a preliminary limit on the axion-photon coupling (see Fig. 3.4). A setup similar to the one described in Sec. 4.2 is used to search for extra power deposited in the cavity by DM-axions and collected by a critically coupled antenna. Such

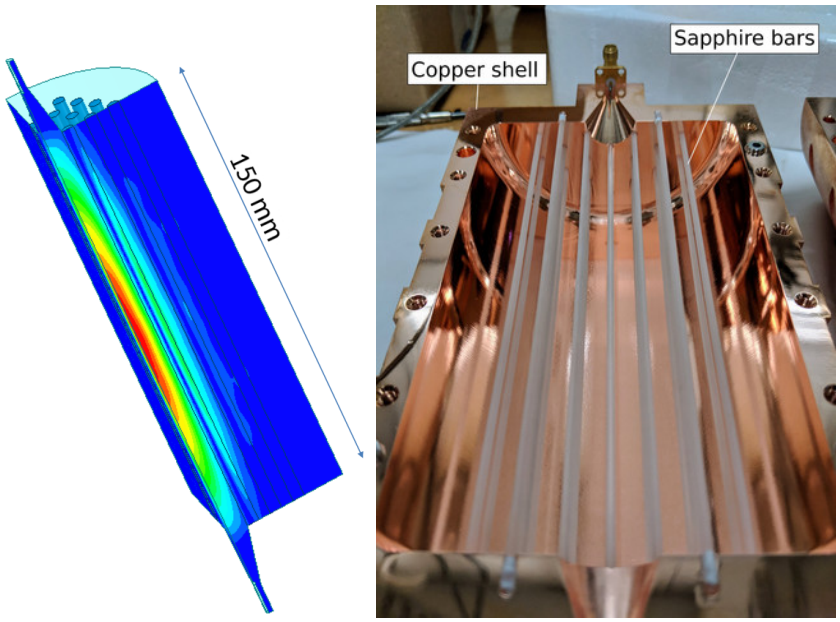


Figure 3.6: Design (*E*-field, *left*) and realization (*right*) of the photonic cavity with sapphire bars. The TM010 mode is confined by the sapphire roads and by the conic endcaps.

power results

$$P_{a\gamma\gamma} = \frac{g_{a\gamma\gamma}^2 \varrho_a}{2} \omega_c B_0^2 C_{\rm c}^{(g_{a\gamma\gamma})} V_{\rm c}^{(g_{a\gamma\gamma})} Q_L^{(g_{a\gamma\gamma})}, \tag{3.3}$$

where $Q_L^{(g_{a\gamma\gamma})}$ is the loaded quality factor of the cavity in the magnetic field $B_0$. The measured and simulated resonant frequencies are compatible and results $f_c \simeq 9.07\,\text{GHz}$, the volume is $V_{\rm c}^{(g_{a\gamma\gamma})} \simeq 36.4\,\text{cm}^3$ and the simulated field profile of Fig. 3.4 gives a mode volume coefficient $C_{\rm c}^{(g_{a\gamma\gamma})} = 0.59$ [207]. The expected axion-induced power in this system results

$$P_{a\gamma\gamma} = 1.85 \times 10^{-25} \left(\frac{\omega_c/(2\pi)}{9.07\,\text{GHz}}\right) \left(\frac{B_0}{2\,\text{T}}\right)^2 \left(\frac{C_{\rm c}^{(g_{a\gamma\gamma})}}{0.59}\right) \left(\frac{V_{\rm c}^{(g_{a\gamma\gamma})}}{36.4\,\text{cm}^3}\right) \left(\frac{Q_L^{(g_{a\gamma\gamma})}}{2 \times 10^5}\right) \text{W}, \tag{3.4}$$

which, thanks to an integrated power sensitivity of $\sim 5 \times 10^{-22}\,\text{W}$, allows to put an upper limit $g_{a\gamma\gamma} \leq 1.03 \times 10^{-12}\,\text{GeV}^{-1}$ in a narrow frequency band of 45 kHz at the cavity frequency, corresponding to $m_a \simeq 37.5\,\mu\text{eV}$. The measurement of the limit, shown in the exclusion plot of Fig. 3.5, and a comprehensive study of the NbTi cavity are reported in [205, 208].

Other designs of high-$Q$ cavities are being tested. Remarkably good results were obtained with photonic-bandgap sapphire cavities like the one of Fig. 3.6. Such cavity was fabricated and tested, showing a room temperature quality factor of 170000 for the TM010 mode. Being composed of copper and sapphire, both are insensitive to the magnetic field, making this cavity an ideal candidate for haloscope searches. Liquid helium tests also showed an improvement of the $Q$, as expected from simulations. The limiting factor is the external copper holding the sapphire bars, but it is not necessary to further improve the quality factor since it almost matches the axion one. A novel sapphire cavity with tunable resonant frequency is in development and will be used to build a Primakoff haloscope.

### 3.1.2 Electron spin resonance materials

Two types of high-$Q$ cavities were discussed in the previous section and both are suitable to be mounted on a ferromagnetic haloscope. Since $\gamma_h = (\gamma_c + \gamma_m)/2$ the material needs to have a narrow linewidth too. In the search for the ideal material for building the haloscope, roughly a dozen different narrow-linewidth and high spin-density candidates were tested. Among the possible choices ferromagnetic insulators are the most suitable one, since they do not introduce extra losses in the cavity and have a large number of spin. To avoid geometric demagnetization and surface effects they are normally shaped as highly polished spheres. Here are reported only the most promising samples, which were studied at liquid helium temperature. The hybridization with a known resonant cavity is an ideal technique to measure the linewidth and spin-density of different materials, as $\gamma_h$ gives $\gamma_m$ and the splitting $g_{cm}$ gives the spin density. In this way the material is tested in the same configuration used for the experiment. The samples to test are placed in a dedicated cylindrical copper cavity equipped with two dipole antennas, one weakly coupled and one with variable coupling to the TM110 mode. The materials are held on the cavity axis, where lies the maximum of the magnetic rf field, by means of PTFE holders. A superconducting magnet is used to provide the static field, and all the different measurements are performed in the full hybridization regime, i. e. for $\omega_c = \omega_m \simeq 14\,\mathrm{GHz}$. A precise characterization of the cavity is essential for the measurement, this can be achieved by means of an $S_{21}$ transmission spectrum and with simulations:

- the $S_{21}$ spectrum of the resonant cavity with weakly coupled antennas gives a quality factor of 54000, yielding a linewidth of 0.26 MHz;

- finite element calculations give the value of the cavity magnetic field, which can be used to extract the overlapping factor $\xi$.

The overlapping factor is used to estimate the single spin coupling by using Eq. (3.1) and then to extract the spin density of the sample. Its calculation relies on the normalized magnetic field on the sample [189], and reads

$$\xi = \frac{(\vec{h}(\mathbf{r}) \cdot \hat{x})^2 + (\vec{h}(\mathbf{r}) \cdot \hat{y})^2}{\max\{|\vec{h}(\mathbf{r})|^2\}} \simeq \frac{\vec{h}(\mathbf{r}) \cdot \hat{x}}{\max\{\vec{h}(\mathbf{r}) \cdot \hat{x}\}}, \tag{3.5}$$

where $\vec{h}(\mathbf{r})$ is the magnetic field amplitude at the location $\mathbf{r}$ of the sample. The tested samples are mainly ferro/ferrimagnets and of spherical shape to reduce the geometric demagnetization. Among them the test on YIG, hyperpure-YIG (hp-YIG), LiFe (Lithium Ferrite), GaYIG (Gallium doped YIG), CvBIG (Calcium Vanadium Bismuth Iron Garnet) and BDPA ($\alpha$,$\gamma$-Bisdiphenylene-$\beta$-phenylallyl, a paramagnetic salt) are reported, as these are the most promising materials. Two example measurements are reported in Fig. 3.7. Among all, the Lithium Ferrite is the one with the higher

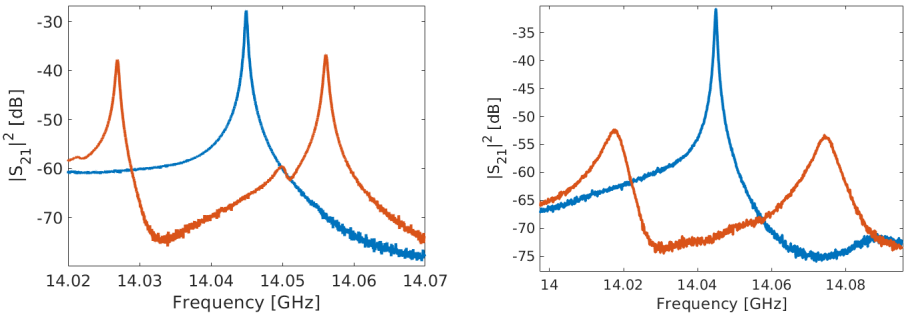


Figure 3.7: Transmission spectra of the hyperpure-YIG (*left*) and LiFe (*right*) samples. The blue curve is the zero-field spectrum while the orange one is for a magnetic field of about 0.5 T corresponding to the full hybridization.

spin-density resulting in $n_S^{\text{LiFe}} \simeq 4 \times 10^{28}\,\text{spins/m}^3$. However, its linewidth is not as narrow as the one of hp-YIG samples. Normal YIG in fact shows a broad linewidth at low temperatures, resulting from the presence of rare earth impurities at the level of ppm. The amount of impurities was measured with a dedicated instrument at Laboratori Nazionali del Gran Sasso (LNGS). Tab. 3.1 is a summary of the obtained results. No data are reported therein for the BDPA sample, since the measurement was performed only at 77 K

| | $\omega_-/2\pi$ | $\gamma_-/2\pi$ | $\omega_+/2\pi$ | $\gamma_+/\pi$ | $g_{cm}/2\pi$ | $\gamma_m/2\pi$ |
|---|---|---|---|---|---|---|
| YIG | 14004.9 | 6.5 | 14080.7 | 9.1 | 75.8 | 15.1 |
| hp-YIG | 14028.1 | 1.2 | 14056.7 | 1.3 | 28.7 | 2.0 |
| LiFe | 14017.7 | 5.2 | 14074.2 | 4.8 | 56.5 | 9.5 |
| CvBIG* | 14034.1 | 3.6 | 14055.8 | 2.6 | 21.7 | 5.9 |
| GaYIG | 14007.4 | 0.9 | 14079.6 | 1.2 | 72.2 | 1.8 |

Table 3.1: Results of the measurements of the different spheres reported in MHz. All the quantities are measured with one antenna critically coupled, except (*). The calculated $\gamma_m$ is obtained averaging $\gamma_\pm$, and the $g_{cm}$ can not be directly compared since the samples have different sizes.

and with a different cavity: for it $n_s^{\mathrm{BDPA}} \simeq 1.5\times10^{-27}\,\mathrm{spins/m^3}$ and $\gamma_M^{\mathrm{BDPA}} \simeq 2\,\mathrm{MHz}$. This material has the advantage of being in powder form, making it very easy to upscale.

Among all, hp-YIG and GaYIG samples result as the most suitable for axion-detection, thanks to their narrow linewidth $\gamma_m^{\mathrm{YIG,GaYIG}} \simeq 2\,\mathrm{MHz}$ and high spin-density $n_s^{\mathrm{YIG,GaYIG}} \simeq 2\times10^{28}\,\mathrm{spins/m^3}$. YIG is a synthetic garnet with chemical composition $Y_3Fe_5O_{12}$. The samples used are single-crystals carved to the shape of a sphere. The five iron ions occupy two octahedral and three tetrahedral sites, with the yttrium ions coordinated by eight oxygen ions in an irregular cube. The iron ions in the two coordination sites exhibit different spins, resulting in a magnetic behavior [209–215].

### On-site YIG spheres fabrication

Large YIG spheres are commercially available, but their delivery time is long and narrow linewidths are not guaranteed. On the other side, large single-crystals of YIG are readily available but can not be used due to their irregular shape, it is thus necessary to carve them into spheres. To this aim, different techniques are being used. In the following, the chosen one is described. First, the crystal is cut in cubes with a side of about 3 mm. The cubes are let free to bounce on a moving abrasive surface, in this way random jumps will remove material randomly on a $4\pi$ angle. For a large number of bounces the outcome is a sphere with a diameter smaller than the initial side of the cube. If the initial crystal size if it is much larger than the final sphere dimension the result is independent from the initial shape.

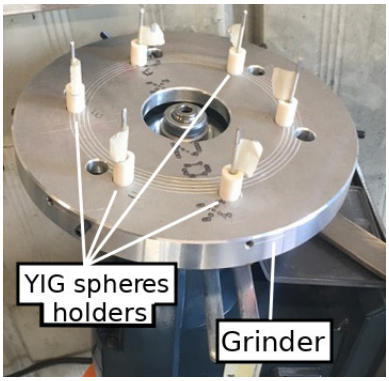


Figure 3.8: The instrument used to produce the spheres.

This procedure is realized by using a grinder and sand-paper of different grit sizes. The YIG sample is held in place while the disk rotates under it. The setup is shown in Fig. 3.8, where the disk of the grinder is under a steel cover used as a holder for the YIG samples. After some tests, the right amount of grinding time for each grit size is fixed, providing a systematic procedure to obtain spheres of the same diameter[1]. The lapping is done by using Alumina-based polishing suspension. The final spheres diameters are in the 2 mm range. Their shape and surface roughness are such that the linewidth is not dramatically increased by geometric demagnetization and surface effect. The measured linewidth is $\sim 2\,\mathrm{MHz}$, matching the best results obtained with commercial spheres reported in Tab. 3.1.

Gem-cutters are using a different technique. The irregular sample is rotated by two holding rods and the spherical shape is obtained by approaching a hollow cylinder with an abrasive inner surface to it [216]. The spherical shape depends on the cylinder, which can be easily manufactured with high precision. This technique is called tumbling.

## 3.2 Modelization of an hybrid system

A mathematical model is necessary to understand the physics of the system under study, and can be enlightening from the experimental point of view. This section includes two different ways to describe the HS. The first one (Sec. 3.2.1) is used to provide a quantum description of the physics, while the second (Sec. 3.2.3) is more intuitive and easy to compare to experimental observations. Both are used to understand the dynamics of a ferromagnetic haloscope and optimize its operation.

[1] As shown in Sec. 4.3.1, for coherent coupling between multiple spheres it is necessary to use spheres with the same diameter.

### 3.2.1 Second quantization model

A second quantization formalism, in natural units, is used to write the Hamiltonian of the two coupled oscillators, photon and magnon, and of an external field $a$ interacting only with the magnon (see Fig. 3.1)

$$\begin{aligned}\mathcal{H}_{\mathrm{cm}} =& \Big(\omega_m - \frac{i\gamma_m}{2}\Big)m^+m + \Big(\omega_c - \frac{i\gamma_c}{2}\Big)c^+c \\ &+ g_{cm}(mc^+ + m^+c)/2 + g_{am}\sqrt{N_a}(me^{-i\omega_a t} + m^+e^{i\omega_a t}),\end{aligned} \tag{3.6}$$

where $m$ ($m^+$), $c$ ($c^+$) are the destruction (creation) operators of magnons and photons, respectively. The constant $g_{am} \sim g_{aee}$ is the axion-magnon coupling, and $N_a$ is the axion number $N_a = \langle a^+a\rangle$. The axion interacts only with the magnon and its effect is to deposit energy in the form of spin-flips (i. e. magnons), which, at the rate $g_{cm}$, are converted into photons that can be collected as rf power.

The dynamics of this photon-magnon hybrid system affects the optimization of the spin-magnetometer. The aim of the calculation is to understand how to maximize the collected axion power by changing the system parameters, and calculate its useful bandwidth. Starting from the hamiltonian in Eq. (3.6), the evolution of the system can be derived with the Heisenberg-Langevin equations for the magnon

$$i\dot{m} = [m, H] = (\omega_m - i\gamma_m/2) + \frac{g_{cm}}{2}c + g_{am}\sqrt{N_a}e^{-i\omega_a t} \tag{3.7}$$

and for the photon

$$i\dot{c} = [c, H] = (\omega_c - i\gamma_c/2) + \frac{g_{cm}}{2}m, \tag{3.8}$$

which can be recast in terms of the operator $M = (m, c)$ in the matrix form

$$i\dot{M} = \begin{pmatrix}\omega_m - i\gamma_m/2 & g_{cm}/2 \\ g_{cm}/2 & \omega_c - i\gamma_c/2\end{pmatrix} M + g_{am}\sqrt{N_a}\,e^{-i\omega_a t}\begin{pmatrix}1\\0\end{pmatrix}. \tag{3.9}$$

If $M = A\exp(-i\omega_a t)$, then

$$\Big[\begin{pmatrix}\omega_a & 0\\ 0 & \omega_a\end{pmatrix} - \begin{pmatrix}\omega_m - i\gamma_m/2 & g_{cm}/2 \\ g_{cm}/2 & \omega_c - i\gamma_c/2\end{pmatrix}\Big] = KA = g_{am}\sqrt{N_a}\begin{pmatrix}1\\0\end{pmatrix}, \tag{3.10}$$

yielding

$$A = g_{am}\sqrt{N_a}K^{-1}\begin{pmatrix}1\\0\end{pmatrix} \tag{3.11}$$

from which it is possible to extract the term describing the coupling between the axion field and the cavity

$$\begin{aligned} A_2 =& g_{am}\sqrt{N_a}(K^{-1})_{21} \\ =& \frac{(g_{cm}/2)g_{am}\sqrt{N_a}}{(\omega_a-\omega_m+i\gamma_m/2)(\omega_a-\omega_c+i\gamma_c/2)-(g_{cm}/2)^2}. \end{aligned} \tag{3.12}$$

Since the observable is the power deposited in the resonant cavity, the operator $z$

$$z = \frac{1}{\sqrt{2\omega_c}}(c^+ + c) = \frac{1}{\sqrt{2\omega_c}}(A_2 e^{-i\omega_a t} + A_{21}^* e^{i\omega_a t}), \tag{3.13}$$

can be used to write it as

$$\begin{aligned} P_{ac} =& \frac{\gamma_c}{2}\langle \dot{z}^2\rangle = \frac{\gamma_c\omega_a^2}{4\omega_c}|A_{21}|^2 \\ =& \frac{\gamma_c\omega_a^2}{4\omega_c}\frac{(g_{cm}/2)^2 g_{am}^2 N_a}{|(\omega_a-\omega_m+i\gamma_m/2)(\omega_a-\omega_c+i\gamma_c/2)-(g_{cm}/2)^2|^2}. \end{aligned} \tag{3.14}$$

Eq. (3.14) describes the dynamics of the system and can be used to optimize the power to be collected, and thus the detection of axions with a ferromagnetic haloscope. It is interesting to consider the case of an axion field on resonance with one of the two hybrid modes of the system at frequencies

$$\omega_\pm = \frac{\omega_c+\omega_m}{2} \pm \sqrt{\left(\frac{\omega_c-\omega_m}{2}\right)^2 + \left(\frac{g_{cm}}{2}\right)^2}. \tag{3.15}$$

To calculate the bandwidth of the apparatus one needs to recast $\omega_m$ in terms of $\omega_\pm$ by inverting Eq. (3.15). Substituting the resulting expression into Eq. (3.14), $P_{ac}$ results

$$P_{ac}(\omega_\pm) = \frac{\gamma_c}{16}\frac{\omega_\pm^2}{\omega_c}\frac{g_{cm}^2 g_{am}^2 N_a}{\left|\left(\omega_\pm + \frac{i\gamma_c}{2} - \omega_c\right)\left(\omega_\pm + \frac{i\gamma_m}{2} - \frac{\omega_\pm^2-\omega_c\omega_\pm-(g_{cm}/2)^2}{\omega_\pm-\omega_c}\right) - \left(\frac{g_{cm}}{2}\right)^2\right|^2}. \tag{3.16}$$

The deposited power is pictured in Fig. 3.9 for a particular HS which is used in the following Section. For a fixed value of $\omega_m$ the useful bandwidth of the spin-magnetometer is limited to the linewidths of the hybrid modes. The red line in the plot shows the (left) axion-mass interval that can be scanned by varying $\omega_m$. It follows from the figure that the hybrid resonances allow the apparatus to work on two axion-mass intervals. These intervals, being more than one order of magnitude broader then the resonance linewidth, let the bandwidth of the spin-magnetometer increase thanks to a simple tuning of $\omega_m$ through the static field.

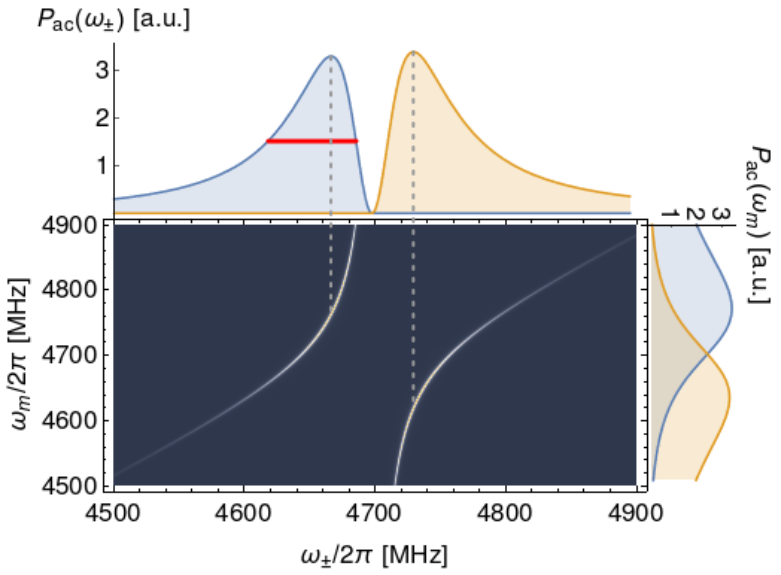


Bandwidth $\simeq 64\,\text{MHz}$

$\omega_c = (2\pi)\,4.7\,\text{GHz}$ $\quad g_{cm} = (2\pi)\,57\,\text{MHz}$
$\gamma_c = (2\pi)\,1.1\,\text{MHz}$ $\quad \gamma_m = (2\pi)\,3.5\,\text{MHz}$
$g_{am} = (2\pi)\,10^{-13}\,\text{MHz}$ $\quad N_a = 10^{24}$

Figure 3.9: Collected axion power as a function of the magnon and hybrid mode frequency. The main figure is the anticrossing plot of $P_{ac}(\omega_\pm, \omega_m)$ as given by Eq. (3.14), while the upper and right curves are the projections of the deposited power as a function of $\omega_\pm$ and $\omega_m$, respectively. The upper plot, representing $P_{ac}(\omega_\pm)$, shows the apparatus bandwidth in blue for $\omega_a = \omega_-$ and in orange for $\omega_a = \omega_+$. The bandwidth is calculated as the FWHM of the $\omega_-$ curve of $P_{ac}(\omega_\pm)$, and is reported in red. The experimental parameters used for the calculation are in black, while $g_{am}$ and $N_a$ are reported in blue and are chosen arbitrarily.

### 3.2.2 Haloscope tuning range

The calculation of Sec. 3.2.1 defines the bandwidth of the spin-magnetometer. An experimental verification is performed to test whether these considerations are correct and the full tuning range of the haloscope can be exploited for an axion search.

The experimental setup adds a magneto-optical effect to modify the magnetization of the sample without interacting with the cavity. The effect is induced by a short laser pulse hitting the magnetic sample inside the cavity. It is assumed that the magneto-optical effect can be described by a term analog to the last one of Eq. (3.6), and that the short laser pulse acts as a $\delta$ function in the time domain. Each pulse has a white spectrum in the Fourier domain and varies the sample magnetization. The system dynamics can thus be studied by considering the excitation as frequency-independent. The scheme of the apparatus is represented in Fig. 3.10. A 1064 nm Nd:$YVO_4$

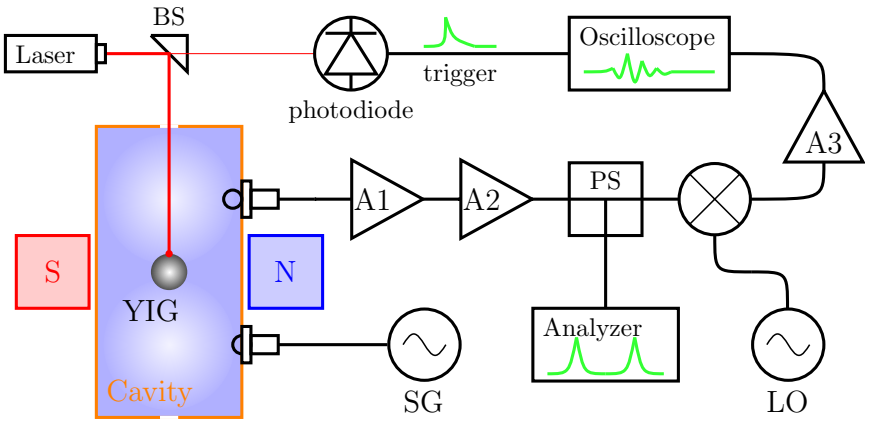


Figure 3.10: Scheme of the experimental setup for the characterization of the bandwidth of an haloscope. The YIG sphere is reported in black, the north and south poles of the magnet are reported in blue and red, respectively, while the color filling the cavity roughly outlines the profile of the mode magnetic field. The shape of the different signals are reported in green. Details on the electronics are given in the text.

mode-locking laser produced a train of short pulses, from which 7 ps isolated pulses are extracted by an acousto-optic modulator. The laser pulse illuminates the 2 mm YIG sphere, which at this wavelength is opaque. A small fraction of the beam is deviated by a beam-splitter (BS) and measured by a fast photodiode for triggering. The YIG sphere is coupled to the TE102 mode of a rectangular cavity as shown in Fig. 3.2. Its resonance frequency is $\omega_c \simeq (2\pi)\, 4.7\,\text{GHz}$ and the linewidth is $\gamma_c \simeq (2\pi)\, 1.1\,\text{MHz}$. The frequency of the Kittel mode can be tuned with the external magnetic field $\omega_m = \gamma_e B_0 \simeq (2\pi \times 28\,\text{GHz/T}) \times B_0$. By setting $B_0$ such that $\omega_c = \omega_m$ the coupling $g_{cm} \simeq 57\,\text{MHz}$ is measured. The factor $\gamma_m$ is derived from the hybrid mode linewidth $\gamma_h$ as $\gamma_m = 2\gamma_h - \gamma_c \simeq 3.5\,\text{MHz}$ (see the upper

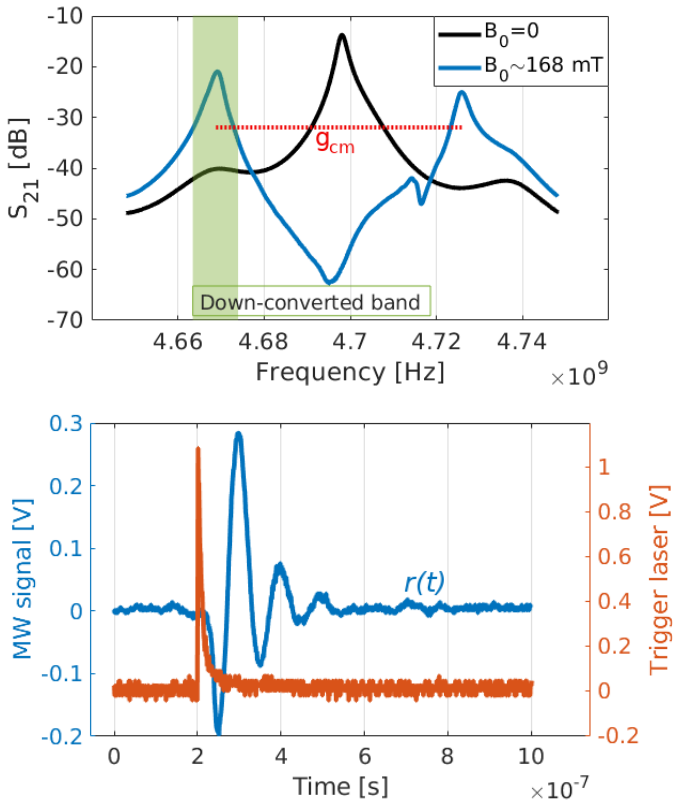


Figure 3.11: *Upper* - Transmission spectrum of the hybrid system for $B_0 = 0$ and for $B_0 = 168\,\mathrm{mT}$. The down-conversion band is colored in green. *Lower* - Acquisition laser trigger (orange) and corresponding down-converted microwave pulse $r(t)$. The duration of the laser pulse is given by the photodiode response time, and the frequency of the mw pulse is $\omega_{\mathrm{LO}} - \omega_{-}$.

plot in Fig. 3.11). Thanks to the strong coupling, laser-induced fluctuations of the sample magnetization are converted into cavity photons, as shown in the lower plot of Fig. 3.11. The mw radiation is collected by a critically coupled antenna, amplified by A1 and A2, and divided between a spectrum analyzer and a down-conversion mixer with a power-splitter (PS). The spectrum analyzer monitors the system, while the down-converted signal is further amplified by A3 before being acquired in coincidence with the laser trigger. A rf signal generator (SG) injects signals into the cavity for $S_{21}$ measurements, while the local oscillator (LO) sets the down conversion frequency $\omega_{\mathrm{LO}}$. The described setup can be used for different purposes. In

particular, since it can simulate an axionic signal, the characterization of a spin-magnetometer used as an axion haloscope can be performed. The magneto-optical effect which converts the laser pulse in a microwave signal is interesting by itself, and will be the subject of a forthcoming work. In principle, a well-characterized effect of this kind could be used for absolute calibration of the haloscope.

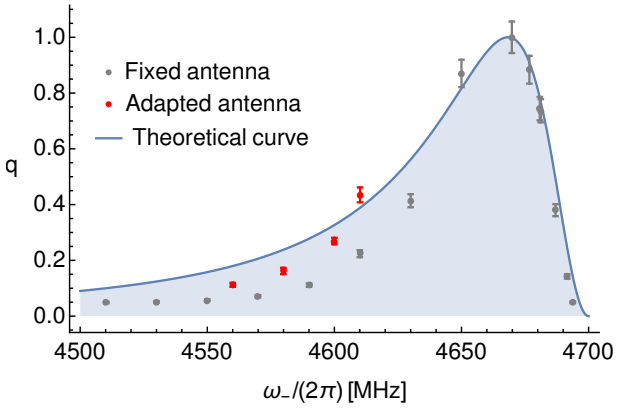


Figure 3.12: Theoretical curve and measured points. The blue curve is calculated with the parameters reported in Fig. 3.9 and normalized. The maximum measured signal is scaled to the unity and the other points are scaled consequently. The gray points are collected with a fixed antenna, while for the red ones the coupling is optimized. Theory and measurement are superimposed, no fit has been performed.

In Fig. 3.12 the results of the measurements are compared to the theoretical curve obtained in Sec. 3.2.1, which is the top-left the projection already reported in Fig. 3.9. Fig. 3.12 shows the normalized power is $q = P_{ac}(\omega)/\max(P_{ac})$ and experimental data are obtained as follows. By varying $B_0$ data-points are taken for different values of $\omega_-$. The laser-induced magnetization fluctuations generate a mw signal $r_\omega(t)$ (blue curve in the upper plot of Fig. 3.11). This signal is squared and integrated to get

$$q_r(\omega_-) = \int_{t_{\text{laser}}}^{t_{\text{laser}}+4\tau_h} |r_\omega(t)|^2 \mathrm{d}t, \tag{3.17}$$

where $t_{\text{laser}}$ is the starting time of the laser trigger (orange curve in the lower plot of Fig. 3.11). For every frequency $\omega_-$ roughly 1000 points $q_r(\omega_-)$ are collected, their normalized mean and standard deviation are reported in Fig. 3.12. There is a good agreement between theory and data for $\omega_- >$

4.65 GHz, but lower-frequency points show a discrepancy. Since the antenna coupling is not taken into account by the model, which assumes critical coupling, the differences can be due to a non-critical antenna. To verify this, more points were collected trying to maximize the extracted power by varying the antenna coupling, the corresponding data are shown in red in Fig. 3.12. Since these are closer to the theoretical curve the non-optimal antenna coupling is a viable explanation for the discrepancy. In conclusion, the measurement validates the model of Sec. 3.2, which will be used to estimate the bandwidth and the signal strength of the haloscope in Sec. 4.3.

### 3.2.3 Electrical circuit representation

HSs are described by many different models, among which the most used is input-output theory [217]. Here is reported a novel approach for their modelization, which yields more physical intuition than the one of Sec. 3.2.1 and can be used to closely reproduce and interpret different experimental observations.

An HO can be described by a linear $RLC$ electrical circuit obeying Kirchhoff's laws. The resonance frequency $\omega$ and quality factor $Q$ of the normal-mode of oscillation can be chosen by suitable values of resistance $R$, inductance $L$ and capacity $C$ [218]. Different HOs (e.g. 1 and 2) can be coupled through a mutual inductance $M_{12} = k_{12}\sqrt{L_1 L_2}$, where $k_{12}$ is the coupling constant and $L_{1,2}$ are the inductances of the two HOs. We consider three HOs accounting for the cavity $c$, the material $m$ and the axion field $a$. A voltage generator $v_{c,m,a}$ is added to every circuit loop to inject energy into the HO, and an antenna is inductively coupled to the cavity to account for the readout. The circuit is represented in Fig. 3.13 and is the electrical equivalent of Fig. 3.1. This modelization yields more physical intuition on the phenomena than the second quantization model of Sec. 3.2.1. A similar formalism can be found in [219], and is optimal to understand the behavior of the system. To solve this circuit it suffices to switch to the Laplace domain and write the complex impedance of the $\alpha^{\text{th}}$ resonant circuit

$$z_\alpha = R_\alpha + i\omega L_\alpha + \frac{1}{i\omega C_\alpha}, \quad \alpha = \{c, t, m, a\}, \tag{3.18}$$

where $i$ is the imaginary unit and $\omega$ is the angular frequency. Recasting this expression, the values of resonance frequency and unloaded quality factor of every circuit are

$$\omega_\alpha = \frac{1}{\sqrt{L_\alpha C_\alpha}}, \quad Q_\alpha = \frac{\omega_\alpha L_\alpha}{R_\alpha}. \tag{3.19}$$

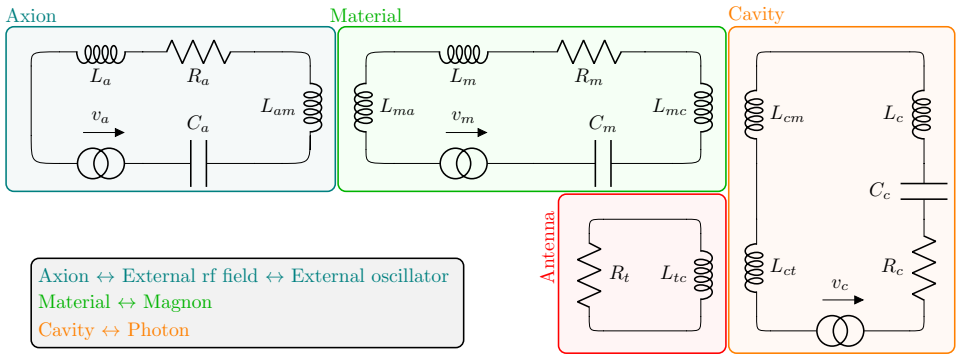


Figure 3.13: Lumped elements representation of the three HOs model: the first subscript of each lumped element stands for the oscillator to which the element belongs. The second subscript, if present, identifies the oscillator to which the element is coupled (e.g. $L_{tc}$ is the inductance of the antenna $t$ which couples to the cavity $c$).

In the frequency domain it is possible to write down the transfer matrix of a system of coupled oscillators and extract the transfer function of the whole system. If $V_\alpha(\omega) = (v_a(\omega), v_m(\omega), v_c(\omega), v_t(\omega))$ is the voltage vector[2] and $I_\alpha(\omega)$ is the current vector, then

$$V_\alpha(\omega) = T_{\alpha\beta}(\omega) I_\beta(\omega), \tag{3.20}$$

where $T_{\alpha\beta}(\omega)$ is the transfer function matrix. Using Eq.(3.18) $T_{\alpha\beta}(\omega)$ results

$$T_{\alpha\beta}(\omega) = i\omega \begin{pmatrix} z_c & z_{ct} & z_{cm} & z_{ca} \\ z_{tc} & z_t & z_{tm} & z_{ta} \\ z_{mc} & z_{mt} & z_m & z_{ma} \\ z_{ac} & z_{at} & z_{am} & z_a \end{pmatrix} = T_{\beta\alpha}(\omega), \tag{3.21}$$

where the diagonal terms are

$$\begin{cases} z_c = i\omega \left(L_c + L_{ct} + L_{cm}\right) + \frac{1}{i\omega C_c} + R_c \\ z_t = i\omega L_{tc} + R_t \\ z_m = i\omega \left(L_m + L_{ma} + L_{mc}\right) + \frac{1}{i\omega C_m} + R_m \\ z_a = i\omega \left(L_a + L_{am}\right) + \frac{1}{i\omega C_a} + R_a \end{cases}, \tag{3.22}$$

i.e. the complex impedances of the HO. The mutual inductances coupling

[2]Here $v_t$ is always zero, here is reported for completeness.

the oscillators $M_{\alpha\beta} = k_{\alpha\beta}\sqrt{L_{\alpha\beta}L_{\beta\alpha}}$ are the off-diagonal terms

$$\begin{cases} z_{ct} = i\omega M_{ct} = z_{tc} \\ z_{cm} = i\omega M_{cm} = z_{mc} \\ z_{ma} = i\omega M_{ma} = z_{am} \\ z_{ta} = z_{at} = z_{tm} = z_{mt} = z_{ca} = z_{ac} = 0. \end{cases} \tag{3.23}$$

This matrix completely describes the system, and allows us to define the transfer function $\tau(\omega) = \det(T_{\alpha\beta}(\omega))$. From this function it is possible to calculate poles and zeros of the system, which are the resonant frequencies and quality factors of the normal-modes of oscillation. The experimental observable is the power dissipated on an antenna coupled to the microwave cavity. The power spectral density of the signal in the antenna accounts for this readout. An orthonormal vector is substituted to the antenna row of Eq.(3.21) for every HO. For example, for the cavity this substitution yields

$$T^{(c)}_{\alpha\beta}(\omega) = i\omega \begin{pmatrix} z_c & z_{ct} & z_{cm} & z_{ca} \\ 1 & 0 & 0 & 0 \\ z_{mc} & z_{mt} & z_m & z_{ma} \\ z_{aa} & z_{at} & z_{am} & z_a \end{pmatrix}, \tag{3.24}$$

then, $\tau_c(\omega) = \det\left(T^{(c)}_{\alpha\beta}(\omega)\right)$ and $\tau_m(\omega) = \det\left(T^{(m)}_{\alpha\beta}(\omega)\right)$. This procedure is repeated to get $\tau_t(\omega)$ and $\tau_a(\omega)$. After noting that in this case the complex conjugate is $\tau^*(\omega) = \tau(-\omega)$, the power spectral density produced by each voltage generator $v_\alpha(\omega)$ reads

$$S_\alpha(\omega) = |v_\alpha(\omega)|^2 \frac{\tau_\alpha(\omega)\tau_\alpha(-\omega)}{\tau(\omega)\tau(-\omega)}, \quad \alpha = \{a, c, m, t\}. \tag{3.25}$$

The total signal collected by the antenna is obtained superimposing the four power spectral densities of Eq.(3.25)

$$S(\omega) = \sum_\alpha S_\alpha(\omega) = S_a(\omega) + S_m(\omega) + S_c(\omega), \tag{3.26}$$

since $v_t = 0 \Rightarrow S_t(\omega) = 0$. As for the quantization of the system, it suffices to substitute the voltage generators with the corresponding quantized expressions [184, 219]. These are functions of the creation and annihilation operators $\hat{q}^+_\alpha(\omega)$ and $\hat{q}_\alpha(\omega)$, which satisfy $[\hat{q}_\alpha(\omega), \hat{q}^+_\beta(\omega')] = \delta(\omega - \omega')\delta_{\alpha\beta}$. The substitution results

$$v_\alpha(\omega) \to \hat{v}_\alpha(\omega) = \sqrt{\frac{\hbar\omega R_\alpha}{2}}\,\hat{q}_\alpha(\omega), \quad v^*_\alpha(\omega) \to \hat{v}^+_\alpha(\omega) = \sqrt{\frac{\hbar\omega R_\alpha}{2}}\,\hat{q}^+_\alpha(\omega). \tag{3.27}$$

The quantum description is useful to understand how single quanta propagate into the HS, however for the purposes of this work the generators are only set to constant values.

To compare the results with experimental data $R_c$, $L_c$ and $C_c$ are such that $Q_c \simeq 3 \times 10^4$ and $\omega_c \simeq 14\,\text{GHz}$ (see Eq.(3.19)) to model a copper cavity at liquid helium temperature. With a suitable material and magnetic field, the electron spin resonance frequency (i.e. the electrons Larmor frequency) can be tuned to $\omega_m \simeq \omega_c$ to achieve the hybridization of the normal modes. The quality factor of the material $Q_m \simeq 7000$ depends on its linewidth $\gamma_m \simeq 2\,\text{MHz}$, which gives a relaxation time $T_2 \simeq 0.1\,\mu\text{s}$ typical of materials such as YIG. As for the axion oscillator, its resonance frequency is chosen to lie on the hybrid mode with lower frequency. The values of resistance, capacity and inductance used to obtain these characteristics of the three oscillators $c$, $m$ and $a$ are reported in Tab. 3.2, together with the values of the antenna lumped elements. As for the antenna, the resistance $R_t$ is added to account for the input impedance, which for a critically coupled antenna is $50\,\Omega$. This, in principle, holds as long as the antenna coupling constant $\beta_t$ is unitary. In the case of this model the antenna coupling is determined by a combination of $k_{ct}$ and $R_t$, thus a fixed $R_t = 50\,\Omega$ is used to tune the coupling only changing $k_{ct}$. This will result in a smaller signal amplitude, closer to experimental results, since the antenna acts as a high-pass filter (see Tab. 3.3).

| Cavity | Material | Axion | Antenna |
|---|---|---|---|
| $R_c = 1\,\text{m}\Omega$ | $R_m = 5\,\text{m}\Omega$ | $R_a = 20\,\mu\Omega$ | $R_t = 50\,\Omega$ |
| $L_c = 20\,\text{nH}$ | $L_m = 20\,\text{nH}$ | $L_a = 20.1\,\text{nH}$ | $L_t = 2\,\text{pH}$ |
| $C_c = 0.64\,\text{pF}$ | $C_m = 0.64\,\text{pF}$ | $C_a = 0.64\,\text{pF}$ | $C_t = 0\,\text{F}$ |

Table 3.2: Indicative values of resistance, capacity and inductance defining the resonance frequencies and quality factors of the oscillating circuits. The values set for the coupling constants and inductances are reported in Tab. 3.3.

To match experimental observations, the couplings between two oscillators do not have to affect its uncoupled frequency. For this reason the coupling inductances are fixed to values $\sim 100$ times smaller than the HO inductances. All these smaller inductances are equal, to ensure that the coupling strength is tuned only through the coupling constants. This value is also small enough not to affect the antenna impedance, $\omega L_{tc} \ll R_t$. The

value of $k_{cm}$ is set to match $g_{cm} \simeq 70\,\text{MHz}$, the coupling strength of a 1 mm YIG sphere hybridized with the cavity used in the measurements. The axion-material coupling is arbitrarily small $k_{ma} \ll k_{cm}$ and $k_{ct}$ is set to extract the maximum possible power from the hybrid modes. The coupling inductances $L_{\alpha\beta}$ and the coupling constants $k_{\alpha\beta}$ are reported in Tab. 3.3. If not explicitly specified, the values used to get a spectra are the ones reported in Tab. 3.2 and 3.3. The voltage generators included in every HO are used

| Cavity-antenna | Cavity-material | Material-axion |
|---|---|---|
| $k_{ct} = 3.4$ | $k_{cm} = 0.5$ | $k_{ma} = 10^{-4}$ |
| $L_{ct,tc} = 2\,\text{pH}$ | $L_{cm,mc} = 2\,\text{pH}$ | $L_{ma,am} = 2\,\text{pH}$ |

Table 3.3: Indicative values of the coupling constants and inductances used to couple the different oscillators. The values set for the other lumped elements are reported in Tab. 3.2.

to inject signals in the corresponding loop. They can be set to a constant value to represent a white signal, useful to evaluate transfer functions. Such a signal can be, for instance, the power sent to the cavity during a transmission measurement or thermal noise. In this section the axion oscillator will not be used, as it is not easily implemented in the experiment.

It is interesting to verify that the natural linewidth of a normal mode increases with the antenna coupling and, when its value is doubled, the extracted thermal power is maximized and the antenna is critically coupled to the mode [218]. The antenna is coupled to the cavity through the constant $k_{ct}$, and the cavity is decoupled from the other two HOs ($k_{cm} = 0$). For a value of $k_{ct}$ close to the unity the critical coupling is reached and the maximum extracted power corresponds to a mode linewidth $2\gamma_c$ as shown in Fig. 3.14a. The same procedure is repeated for the HS in the strong coupling regime, it is verified that the hybrid linewidth $\gamma_h$ becomes $2\gamma_h$ when critically coupled. As Fig. 3.14b shows, it results that $k_{ca}$ must be $\sim 3.4$ to extract the maximum power. Experimental measurements show that to reach the critical coupling with the hybrid mode, the antenna must be set in a position which would be over-critical for the cavity mode, as obtained with the model. For example, this suggests that the different antenna coupling not only depends on the geometry of the cavity rf fields, but also on the HS transmission function. The critical coupling is reached for both the hybrid resonances with the same value of $k_{ct}$, thus the coupling in this range results frequency independent. This fact is not experimentally verified, since

the antenna is not critically coupled to both modes in the same position. Hereafter, if not otherwise specified, the antenna will be critically coupled to the normal modes. The results shown in Fig. 3.14 are consistent with

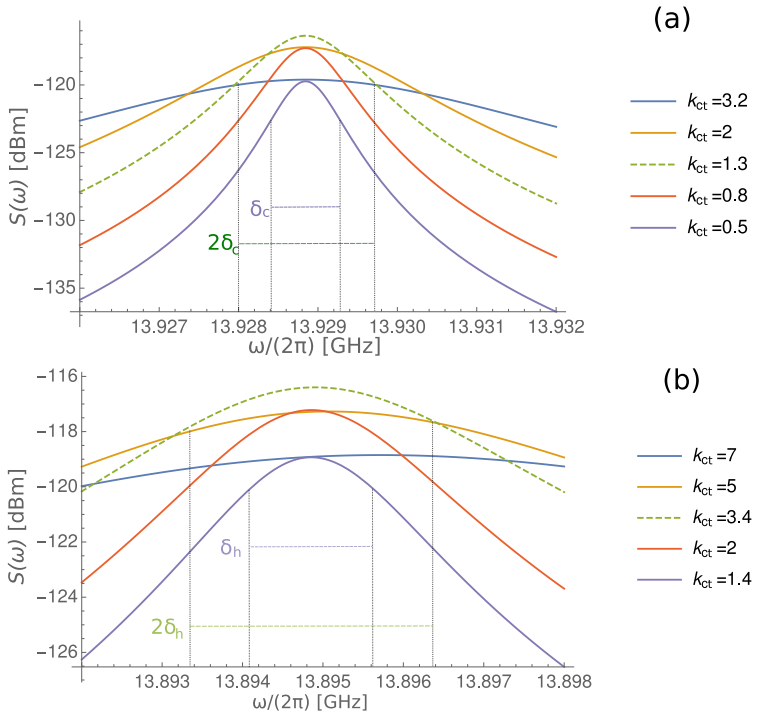


Figure 3.14: (a) Different couplings of the antenna to the cavity normal mode, the variation spans from weak to over-critical coupling. The dashed green line represents the resonance with a critically coupled antenna, the linewidth is doubled and the extracted power is -114 dBm. (b) The coupling is varied also in the case of a hybrid mode. The maximum power is -116 dBm, and is lower than the previous one because the hybrid linewidth increased with respect to the cavity one.

experimental observations. The same behavior can be obtained using an antenna with a variable coupling as an iris or a movable dipole.

The linewidths of the hybrid modes are the average between the linewidths of the two uncoupled resonances for $\omega_m = \omega_c$. This has been widely verified experimentally and is also obtained with our model. For non-minimum hybridization, i.e. $\omega_m \neq \omega_c$, the hybrid modes frequencies are either closer to $\omega_c$ or to $\omega_m$ and $\gamma_h \neq (\gamma_c + \gamma_m)/2$, as is correctly reproduced by the *RLC* model. The anticrossing curve of a photon-magnon HS is experimen-

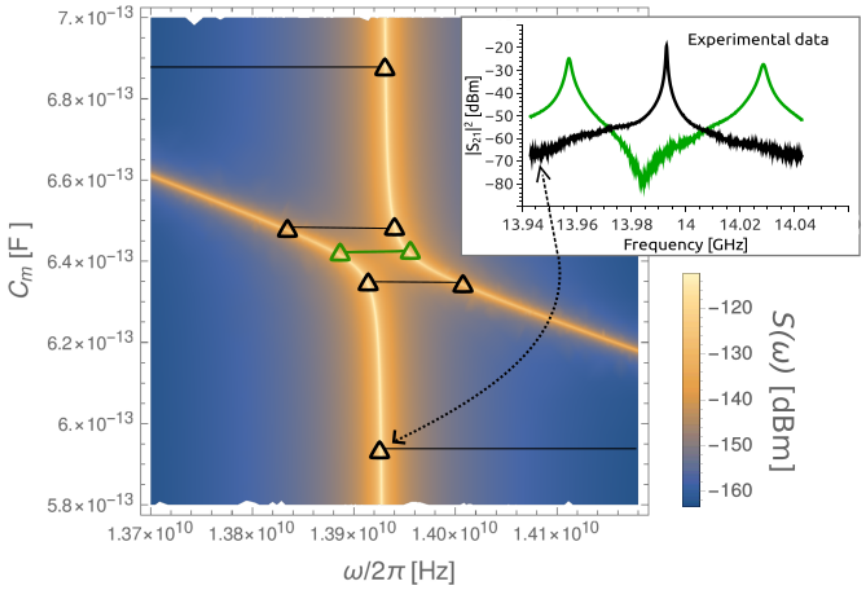


Figure 3.15: Anticrossing curve of the cavity and Kittel mode (blue to orange). The triangles are measures of the normal mode resonance frequencies, the green ones are for $\omega_m = \omega_c$, obtained with a field of 0.5 T. Two triangles connected by a line correspond to the same value of the magnetic field. The measured power spectra of the cavity and hybrid modes are shown as an inset. The experimental data are collected with a transmission measurement, while the model is evaluated for thermal noise. Since the resonance frequencies are not influenced by the signal amplitude the result is invariant.

tally obtained by varying the electrons Larmor frequency (i. e. changing the magnetic field) of a magnetic sample.

A YIG sphere [220, 221] embedded inside a copper cavity is used to realize a system to compare to the model. The ferromagnetic resonance of the material is set by a field of $\sim 0.5\,\mathrm{T}$, matching the cavity frequency of 13.9 GHz. In order to reproduce the splitting $g_{cm} \simeq 70\,\mathrm{MHz}$ due to the 1 mm YIG sphere, $k_{cm}$ is set to 0.5. To mimic the magnetic field variation $\omega_m$ is changed by means of the capacity of the material HO, $C_m$. The resulting curve is reported in Fig. 3.15 together with some measured points. There is a good agreement between the measurement and the calculation, when $\omega_c = \omega_m$ the value of $g_{cm}$ is 69 MHz. The model is then fitted to a spectrum collected with a transmission measurement of the hybrid system (see Fig. 3.16). To reproduce the transmission measurement with the *RLC*

model, the cavity generator is set to an arbitrary value, while the material generator is set to zero. This corresponds to the limit in which the power injected in the cavity, in this case from an antenna, is much higher than the one injected in the material (or equivalently, the cavity temperature is much higher than the material one). Effectively the difference is a marked minimum between the two resonances, not present with thermal noise, which is correctly reproduced in the calculated transmission spectra. The experi-

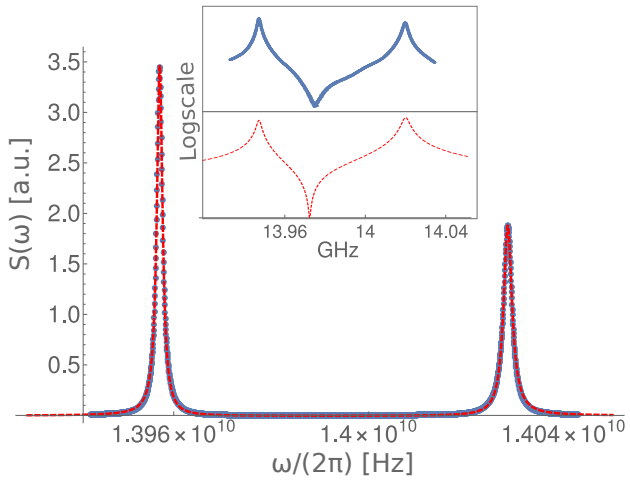


Figure 3.16: Fit of the model (red dashed line) on experimental data (blue points). The inset reports the data points and the model in logarithmic scale to show the shape of the two spectra. The antenna coupling to the hybrid system experimentally is not the same for both modes. As the model is not able to reproduce this, the fit is obtained for a non-minimum hybridization, allowing the modes to have different amplitudes. This suggests that for a given antenna, the coupling to the two hybrid modes is different because of the geometry of the rf fields.

mental data are closely reproduced by the model, the results of the fit can be used to describe the apparatus and get precise information about its behavior. However, since the system is linear, a complete identification is not possible. In general the number of free parameters is $2N_{\mathrm{HO}} - 1$, where $N_{\mathrm{HO}}$ is the number of coupled HOs. It is still possible to calibrate the system using a controlled source to get a calibration constant. See for instance [222] or Sec. 4.2, where a $50\,\Omega$ termination with a variable temperature is used for this aim. Large quantities of material and narrow linewidths increase the sensitivity of a spin-magnetometer. To design such detectors it is important

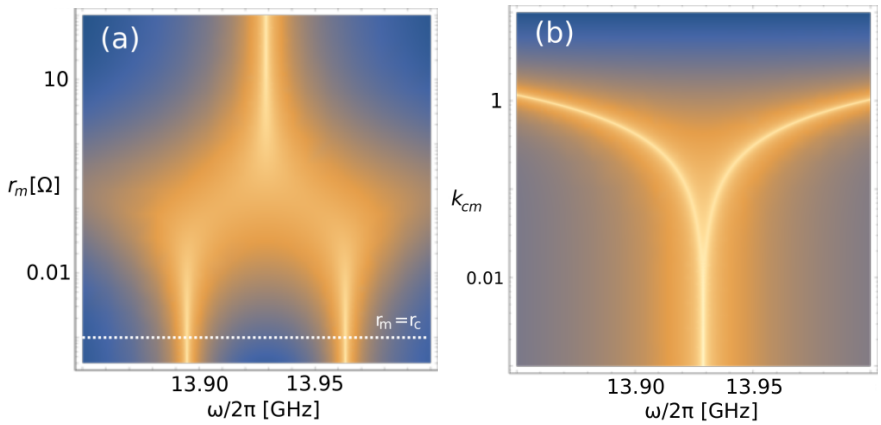


Figure 3.17: (a) Variation of the material resonance quality factor, for a cavity resistance $r_c = 1\,\mathrm{m}\Omega$. The two oscillators can be efficiently coupled only if the two linewidths have similar values. (b) Hybrid system spectra as a function of the material-cavity coupling. By increasing $k_{cm}$ any coupling strength can be reached, and the frequency difference $g_{cm}$ becomes asymptotically large for $k_{cm}$ close to the unity. Amplitude units are arbitrary.

to know whether any fundamental limitation is present on both these fronts. This model is thus used to understand the behavior of the HS if the material and cavity quality factor drastically differ. This is motivated by the fact that usually ESRs do not match the high quality factors of microwave cavities. As described in Sec. 3.1, two resonances with different linewidths can be coupled, resulting in a hybrid mode linewidth which is the average of the previous two. To test to what extent this is valid, the cavity linewidth is fixed while the one of the material is gradually increased, as reported in Fig. 3.17a. The coupling starts to decrease as the quality factors of the two resonances differ by more than one of magnitude. Moreover, if the material linewidth is even larger, the system gets back to the uncoupled cavity state. Therefore, for example, a material with a short $T_2$ can not be coupled to a high quality factor resonant cavity.

The *RLC* model can be used to describe both a strongly or a weakly coupled system, let's consider the case of a variable coupling strength. Fig. 3.17b. Any coupling can be reached by increasing $k_{cm}$, and that the value of the coupling does not affect the main features of the system, except the normal modes frequencies. This suggests that an arbitrarily large volume of material can be coupled to a cavity to increase the sensitivity of a spin-magnetometer. To optimize the system one can use the observ-

able $P$, which can be studied as a function of different parameters of the HS to extract information on how the transfer function is influencing the signal-to-noise ratio. The power $P$ is calculated as

$$P = \frac{1}{2\pi}\int_b \frac{S_a(\omega)S_n(\omega)}{S_a(\omega)+S_n(\omega)}\mathrm{d}\omega, \tag{3.28}$$

where $b$ is the system resolution bandwidth and $S_n(\omega) = S_m(\omega) + S_c(\omega)$ is the power spectral density of the additive noise. Under the hypothesis that the random signal and noise are orthogonal, $P$ is the output quantity that best matches the searched signal, minimizing the mean square error with $v_a$ [223]. The axionic signal has a natural figure of merit, yielding a

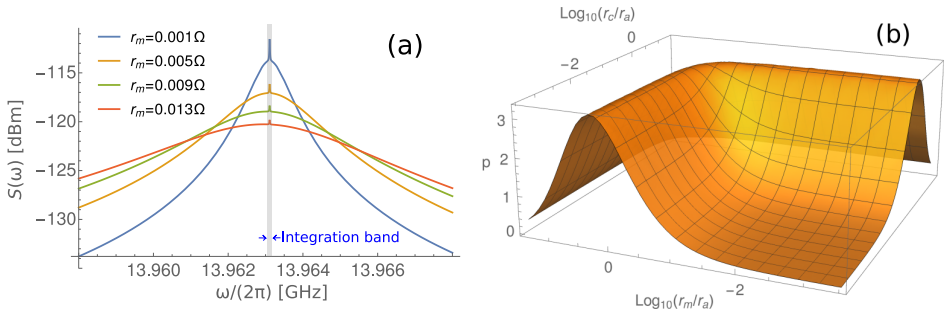


Figure 3.18: (a) Power spectrum of the hybrid resonance with axionic signal for different values of the resistance of the material HO (no differences has been found between varying $r_c$ or $r_m$). The sharp peak on the top of the resonant mode is the axionic oscillator signal, whose generator amplitude $v_a$ is not being changed. The gray band evidences the integration interval used to obtain the plot (b) of this figure. (b) The normalized observed power $p$ as a function of the resistances of the cavity and material HOs. The higher sensitivity is obtained for $\gamma_h \simeq \gamma_a$.

$Q_a \simeq 10^6$ (see Sec. 2.1.1), and unknown frequency $\omega_a$. Considering a signal on-resonance with one of the hybrid modes, the SNR is optimized with respect to the cavity and material linewidths. No limitations have been found for the coupling strength, which depends on the quantity of material, so the experiment can be upscaled to increase its sensitivity. The axion oscillator is used to inject the signal in the HS. Since $k_{ma}$ needs to be small, the generator amplitude $v_a$ is set to be 100 times higher than thermal noise and have a defined peak. The dependence of the transfer function on the resistance of the material HO is plotted in Fig. 3.18a. As expected a higher quality factor transfers the power from the axion oscillator more efficiently.

To get the optimal material and cavity linewidths to be used for an axion search we rely on the quantity $P$ defined in Eq. (3.28). $P$ is integrated over the axion bandwidth $b \simeq \gamma_a \simeq 7\,\mathrm{kHz}$ and scaled to get $p = P/10^{-22}\,\mathrm{W}$. The integration bandwidth $b$ is set equal to the axion bandwidth to collect all the possible power deposited by the dark matter axions. Fig. 3.18b shows the behavior of $p$ as a function of the two linewidths of cavity and material. It emerges that the axion resistance is a threshold above which there is no improvement on the signal-to-noise ratio: a hybrid mode quality factor higher than the one of the axion (i. e. $\gamma_h < \gamma_a$) reduces the sensitivity of the experiment for a fixed bandwidth. By matching $b$ with the hybrid linewidth, one can improve the SNR, given that the signal is large enough to be measured.

In a spin-magnetometer such as the one described in [222], the calibration constant does not account for the presence of an HS. The axionic signal is expected to modulate the sample magnetization, so a similar signal should be used to get an end-to-end calibration. Experimentally this is not simple, but could be achieved for example by means of magneto-optical effects [201] (see Sec. 3.2.2). Instead of using an external oscillator, another generator capable of injecting a signal with an arbitrary shape can be inserted in the material circuit. This can be useful, for example, to study a signal distributed according to a Maxwell-Boltzmann function, as could be the one of dark matter axions [164, 166].

## 3.3 Precision power measurement

The HS described previously in this Chapter acts as a transducer of the axionic signal. The power coming from the HS must be measured and acquired with a suitable detection chain, and, as it is extremely weak, needs to be amplified. The intrinsic noise of an haloscope is essentially related to the temperature of the setup, and since axionic and Johnson power have the same origin it is the ultimate limit of the SNR. The amplification process inevitably introduces a technical noise which, for these setups, is useful to quantify in terms of noise temperature $T_n$ to compare to the Johnson noise. This stage of the measurement is setting the overall sensitivity of the apparatus since, as shown hereafter, for very low working temperatures the noise temperature is higher than the thermodynamic one. Minimizing $T_n$ is a key part of the development of an haloscope, and is complementary to the maximization of the axion deposited power.

The mw amplifiers used for precision measurement are mostly high elec-

tron mobility transistors (HEMT), since they have high gain and low noise, of the order of 4 K. These are described in Sec. 3.3.1 and used for the first ferromagnetic haloscope prototypes. The most sensitive amplifier available is the Josephson parametric amplifier, which reaches the quantum noise limit and is described in Sec. 3.3.2. This is used in the ultra-cryogenic prototype, and its performances can be overcome only by using a photon counter.

### 3.3.1 HEMT amplifiers

Early mw amplifiers relied on klystrons, travelling-wave tubes, and tunnel or varactor diodes. Major improvements on solid-state technology allowed nowadays amplifiers to be mostly based on transistors [218]. These amplifiers can be used at frequencies in excess of 100 GHz, they are small, reliable, have a low noise figure and a broad bandwidth, making them ideal for precision mw measurements.

In particular, HEMT are field effect transistors based on an heterojunction, i. e. a PN junction of two materials with different band gaps [224]. In doped semiconductors, conduction is allowed by impurities which donates either electrons or holes. However, electrons are slowed down by collision with these same impurities. Heterojunctions generate high mobility electrons through a highly doped wide-bandgap n-type donor-supply layer like AlGaAs, and a non-doped narrow-bandgap channel layer with no dopant impurities, as GaAs. Different band-gap materials form a quantum well in the conduction band on the GaAs side where, since the GaAs layer is undoped, the electrons can move without colliding with any impurities and from which they cannot escape. The n-type layer is depleted by surface trapping of free electrons and by electron transfer into the undoped layer. Free electrons in the AlGaAs layer are transferred to the undoped GaAs due to its high electron affinity and form a two dimensional high mobility electron gas on the interface. This is a thin layer of highly concentrated and mobile conducting electrons, resulting in a low resistivity channel. The bias voltage applied to the gate formed as a Schottky barrier diode, and is used to modulate the number of electrons in the channel formed by the 2D electron gas and consecutively. This controls the conductivity of the device, while the width of the channel can be changed by the gate bias voltage. The proper doping profile and band alignment gives rise to extremely high electron mobilities, and thus to amplifiers which can have high gain and very low noise temperature, making them ideal for the detection of weak mw signals.

These devices can be calibrated by using a load with variable tempera-

ture as a source of Johnson noise [225]. The typical calibration procedure for a cryogenic HEMT-based detection chain is as follows. Referring to Fig. 3.19, the load $R_J$ can be heated to a temperature $T_r$ without significantly heating other parts of the apparatus, and the output noise power is measured in the temperature range $5 \div 25\,\mathrm{K}$. A scheme of the apparatus and

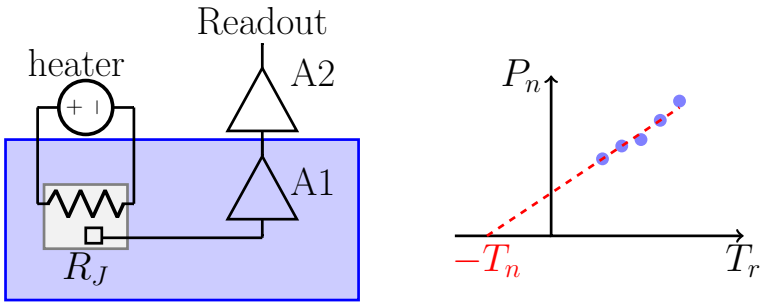


Figure 3.19: Apparatus and measurement to get the noise temperature of a HEMT-based detection chain. The left part is a scheme of the setup, where the blue rectangle encloses the parts that can be cooled down to cryogenic temperatures. The right part shows how the measurement is performed by collecting $P_n$ at different $T_r$ and fitting the data with a line. Both A1 and A2 are HEMT, but the contribution of A2 to the noise temperature is reduced by the gain of A1 resulting in $T_n^{(\mathrm{A2})}/G_{\mathrm{A1}}$.

of the measurement are reported in Fig. 3.19. The rf power from Eq. (2.28) is

$$P_n = k_B(T_r + T_n)\Delta f. \tag{3.29}$$

By gradually changing $T_r$ the measured power level of Eq. (3.29) is linearly increased to determine the noise temperature and gain of the electronics, similarly to what is usually obtained with the Y-factor method. The points are fitted with $q_c(T) = a_c T + b_c$ to obtain $T_n = -b_c/a_c$ and the total gain $G_{\mathrm{tot}} = a_c$. These two values completely characterize the whole electronic chain that can be used for the measurement of extra power injected in a system, for example, by DM-axions.

### 3.3.2 Josephson parametric amplifiers

Even if their noise temperature is low, HEMTs are not the most sensitive amplifiers available. As discussed before, at 10 GHz frequency the SQL of linear amplifiers is close to 0.5 K, which is about one order of magnitude lower than the $T_n$ of HEMTs. Such remarkably low $T_n$ is achieved by JPAs, resonant

amplifiers with a narrow bandwidth but with quantum-limited noise. This feature makes them the ideal tool to measure faint rf signals, and thus to be implemented in ferromagnetic or Primakoff haloscopes.

Quantum limited parametric amplification with a JPA was first demonstrated by Yurke in 1989 [226], and different other groups obtained remarkable results in the next years [227–232], including the measurement of the dynamical Casimir effect [233, 234]. Nowadays these devices are used in many researches involving precision rf measurements [126]. JPAs are essentially three-wave mixing devices which convert power among three mw fields, called signal, idler and pump. The non-linear mixing is given by a J-RLC circuit with a quadratic time-dependent Hamiltonian, which can be degenerate or non-degenerate depending on whether the signal and idler waves are at the same frequency or not [235]. A non-degenerate device consists in a three-modes, three-input circuit made of four Josephson junctions forming a Josephson ring modulator (see Fig. 3.20a). It effectively is a three-wave purely dispersive mixer which can be used for parametric amplification [236]. The hamiltonian of the three-oscillators system is

$$\frac{\mathcal{H}_3}{\hbar} = \omega_s s_3^+ s_3 + \omega_i i_3^+ i_3 + \omega_p p_3^+ p_3 + g_3\big(s_3^+ + s_3\big)\big(i_3^+ + i_3\big)\big(p_3^+ + p_3\big), \quad (3.30)$$

where $\omega_{s,i,p}$ are the signal, idler and pump frequencies, $\{s,i,p\}_3$ ($\{s,i,p\}_3^+$) are the destruction (creation) operators and $g_3$ is the trilinear coupling. The couplings to the ports are $\kappa_{s,i,p}$ and the frequency scale is such that $\omega_p \gg \omega_s > \omega_i \gg \kappa_p \gg \kappa_i \simeq \kappa_s \gg g_3$. Higher order terms of Eq. (3.30) are neglected and, considering coherent signals, the first order perturbation in $g_3$ does not offset the frequencies of the quadratic terms. In the regime where the pump mode is driven by a large coherent field $p_{03}e^{-i\Omega_3 t}$ the hamiltonian becomes

$$\frac{\mathcal{H}_3}{\hbar} \simeq \omega_s s_3^+ s_3 + \omega_i i_3^+ i_3 + 2g_{si}\big(s_3^+ + i_3\big)\big(i_3^+ + i_3\big)\cos(\Omega_3 t + \theta_3). \quad (3.31)$$

In the rotating wave approximation and for $\Omega_3 = \omega_s + \omega_i$, the fast rotating terms can be neglected and $\mathcal{H}_3$ reads

$$\frac{\mathcal{H}_3}{\hbar} \simeq \omega_s s_3^+ s_3 + \omega_i i_3^+ i_3 + \big(2g_{si} s_3 i_3 e^{i(\Omega_3 t+\theta_3)} + \text{h. c.}\big), \quad (3.32)$$

which is the hamiltonian of the non-degenerate parametric amplifier. In this simpler configuration the drive frequency is usually twice the resonance frequency of the amplified mode. Such device can be improved extending its working frequency range by adding four linear inductances cross-linking the

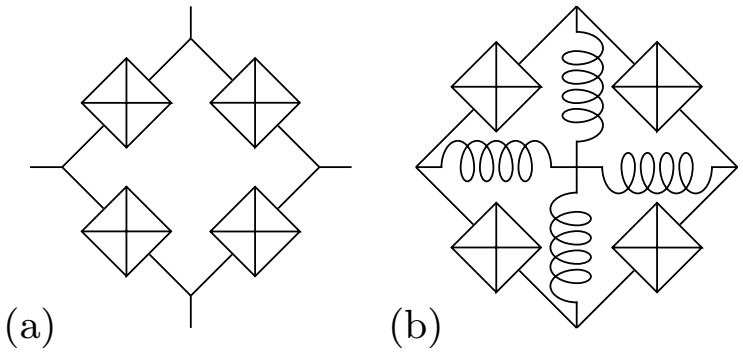


Figure 3.20: Josephson ring modulator in the standard configuration (a) and the widely tunable one (b), presented in [237].

ring modulator [237], as is shown in Fig. 3.20b. For large pump amplitudes and low pump depletion, the non-linear mixing process appears as a linear scattering, thus the JPA is a linear amplifier. As such, it is quantum limited and its noise temperature depends on the working frequency. The amplifier used in the last prototype described in Sec. 4.3 implements this type of Josephson parametric converter (JPC), its characterization is described hereafter.

The JPC is inside two concentric cans, the external one is made of Amuneal and the external is of aluminum. The first is useful to reduce the Earth magnetic field in which the SC parts (shields and junctions) undergo the transition, while the second screens from external disturbances. Everything is attached to the mixing chamber plate of a dilution refrigerator with a base temperature of about 90 mK. To use the amplifier in a wide frequency range, a bias field is applied to the ring and the resonance frequencies of the signal, idler and pump mode are tuned. This is achieved with a small SC coil placed below the ring, biased with a current $I_b$. The electronic scheme used to test the amplifier is reported in Fig. 3.21. The first measurements are performed with the pump, the readout and the aux lines, to verify the nominal working frequencies of the amplifier and test it both with transmission measurements and thermal noise. After the first tests a cylindrical cavity is added to the setup to operate it in a configuration closer to the one of an haloscope. The implementation of a tunable antenna gives an extra degree of freedom to the setup, which can be used for precisely control the coupling to the cavity mode and for calibration purposes (see Sec. 4.3). Let's consider the switch as turned in the cavity direction. To

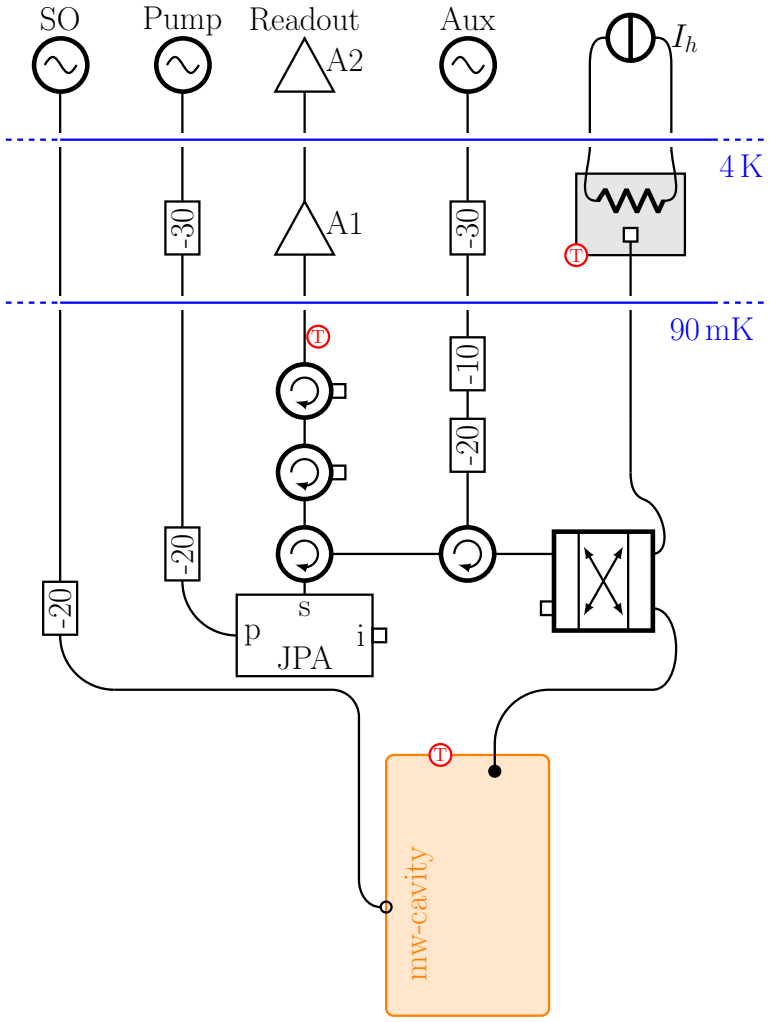


Figure 3.21: Electronic rf scheme of the apparatus used to test the JPC. The red circled $T$s are the thermometers, $I_h$ is the heater current source, and SO is a source oscillator connected to a weakly coupled antenna.

understand the working frequencies of the JPC it is useful to measure the effect of $I_b$ on the modes. To this aim multiple $S_{21}$ spectra of the ring are measured for different $I_b$, resulting in the plot in Fig. 3.22 (upper plot). The parametric amplification process occurs on the beginning and ending parts of the long lobes in Fig. 3.22 (upper plot). Here the derivative of the mode resonant frequency with respect to an external field is maximum, and thus

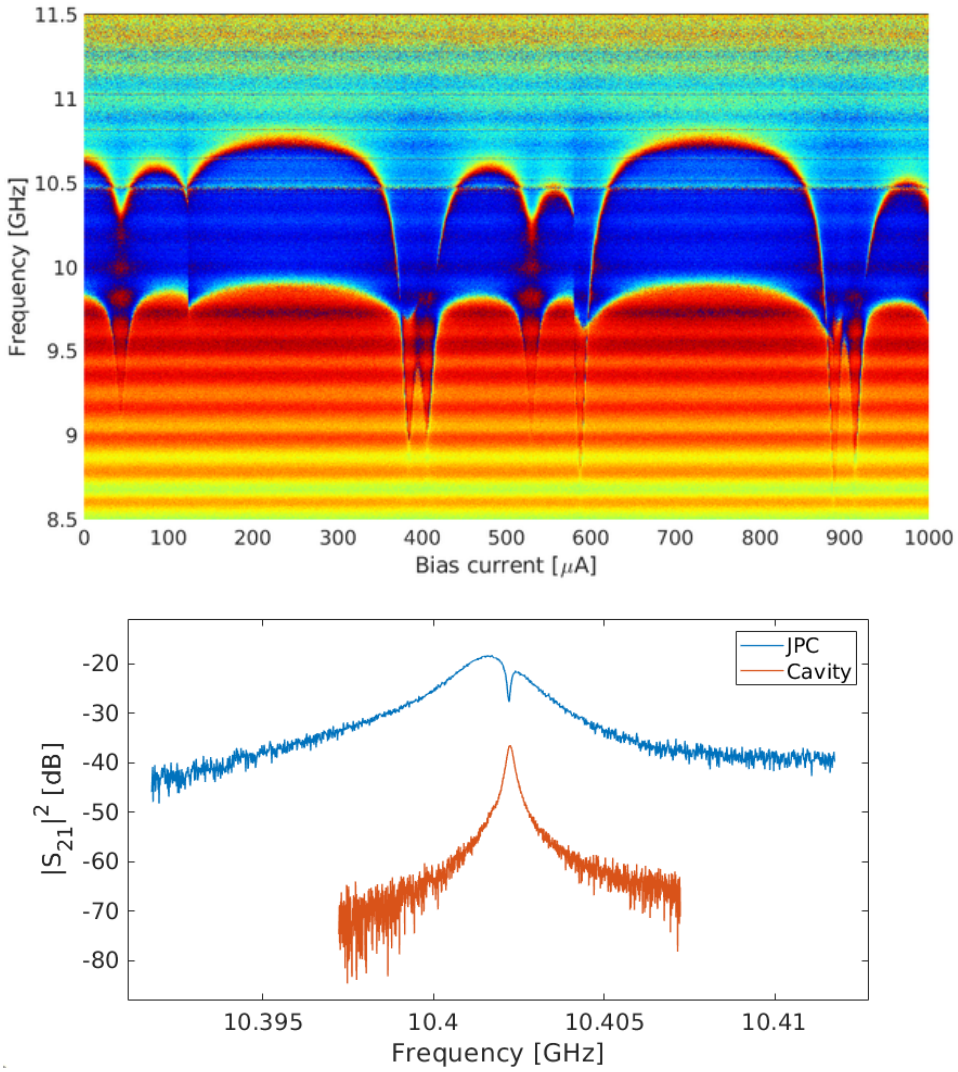


Figure 3.22: *Upper* - Phase-field characteristic in arbitrary units, obtained by varying the current $I_b$ of a superconducting coil located close to the ring modulator of the JPC. The color scale representing the phase is in arbitrary units. The horizontal line around 10.4 GHz is due to the cavity. *Lower* - $S_{21}$ spectral measurement of the cavity with a critically coupled antenna, and corresponding measurements with the JPC on. The signal used for the spectroscopic measurements is absorbed by the cavity at its resonance frequency, causing a steep decrease of power in the JPC spectrum.

the effect of the pump is to drive the parametric amplification. The lower plot in Fig. 3.22 shows a transmission measurement of the cavity with the SO line as input and the readout line as output (with JPC off) and the corresponding measurement with the JPC on with the aux line as input and the readout as output. The lower output power in correspondence to the cavity resonance is due to the fact that, with a critically coupled antenna, the probe signal gets absorbed on resonance and reflected elsewhere. The same effect should be measured in the case of thermal noise, but instead of the probe signal one has to rely on a hot load. This measurement is interesting for multiple reasons and is shown in Fig. 3.23. The deep in the

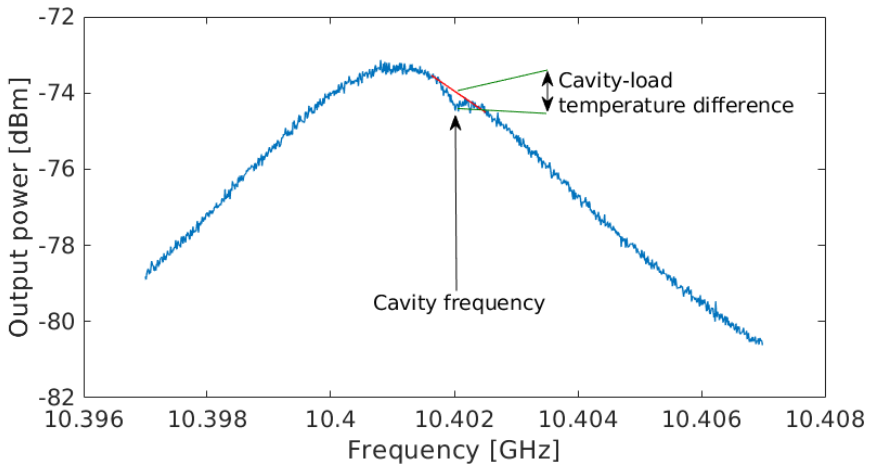


Figure 3.23: Thermal noise amplified by the JPC. The considered load is the one with higher temperature between the switch 50 Ω and the last attenuator of the aux line.

cavity spectrum is related to the temperature difference between the cavity and a load. In this case it means that the cavity has a lower temperature then the respective load, otherwise, other than a deep, the spectrum would show a bump at the same frequency, stating that the power coming from the cavity is higher than the one of the load. The cavity absorption profile is not as low as the one of Fig. 3.22 because the monochromatic probe signals act as an high effective temperature of the load. The difference between the expected power and the measured one (see Fig. 3.23) can thus be used for calibration, if the temperatures of cavity and load are precisely controlled.

Consider now the scheme of Fig. 3.21 with the switch directed on the variable-temperature 50 Ω. Ideally one could use the same technique de-

scribed in Sec. 3.3.1 to characterize the JPC, and get a proper noise calibration of the electronic chain. Unfortunately this is not possible because of the low dynamic range of the JPC when measuring white noise: the measurements show that a 4 K load largely saturates the amplifier. The same configuration with a lower temperature load could solve this problem, but in this setup would destabilize the system causing a heating of the mixing chamber and thus of the whole apparatus. Since in principle the measurement is effective if only the temperature of the 50 Ω changes, it is hardly usable for calibration purposes.

# Chapter 4

# Haloscope prototypes

Here are discussed the three development stages of the haloscope. The starting room temperature setup is a simple apparatus with a single YIG sphere in copper cavity and an HEMT amplifier. It is essentially limited by thermodynamic noise and the data are acquired with an high-frequency spectrum analyzer. The second prototype consists in a cylindrical cavity with five YIG spheres inside, is at liquid helium temperature and features a cryogenic HEMT. The amplifier and thermodynamic noises contribute almost equally to the system noise, while a dedicated system acquires and stores data. The last prototype works at ultra cryogenic temperatures, with 10 larger YIG spheres coherently coupled to a cylindrical copper cavity with a novel design. The readout is performed by a quantum limited JPA, which introduces almost the totality of the system noise. The acquisition system is the same of the previous prototype. The design of these prototypes is such that they can easily be scaled up to increase the volume of material. The

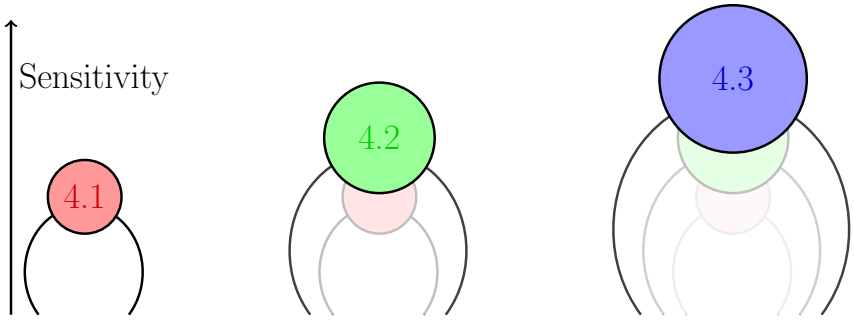


Figure 4.1: The three experimental setups described in this chapter, labelled with the corresponding section number.

description is organized as follows because the setups are embedded one in the other in a matryoshka-like design (see Fig. 4.1). This is convenient from the experimental point of view, since the "inner" parts on the apparatus are fully characterized and reliable. Every prototype is described in terms of the hybrid system and of the rf and low frequency electronics. The data storage and analysis are eventually described.

## 4.1 Room temperature single-sample prototype

This section describes the basic configuration of a spin-magnetometer and its preliminary operation. In this setup the directionality, scalability and data acquisition and storage are not considered. In this sense this first prototype is not configurable as an haloscope, but more as a proof-of-principle setup useful for the design of the following ones. The scheme of the device reported in Fig. 4.2 consists in a parallelepiped resonant cavity with $\omega_c/2\pi \simeq 5.16\,\text{GHz}$ and $\gamma_c/2\pi \simeq 2.4\,\text{MHz}$ and a 2 mm diameter YIG sphere. The hybrid system is at room temperature, the amplifier is at 77 K and an electromagnet is used to provide the external field [134].

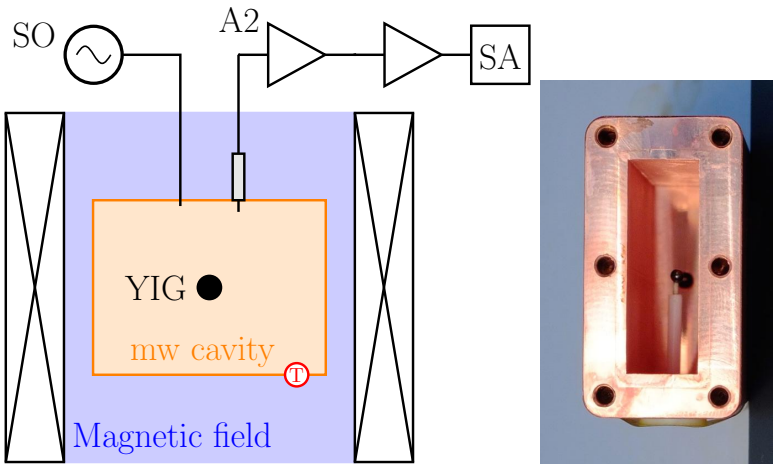


Figure 4.2: *Left* - scheme of the HS and electronics used for the first room temperature prototype. A2 is the HEMT amplifier (the name is used for consistency with the next electronic schemes), SA is the spectrum analyzer, and SO is a source oscillator used to perform transmission measurements of the system. *Right* - picture of the HS's cavity and YIG.

### 4.1.1 YIG and copper cavity

The microwave resonator used for this test is a copper cavity shaped in the form of a parallelepiped with dimensions along $x$ ,$y$ ,$z$ axes 85 mm, 40 mm and 10 mm, respectively. The resonance frequency of the selected TE102 mode is 5.15 GHz, with a total cavity linewidth $\gamma_c/2\pi \simeq 2.4$ MHz. The magnetic material is a sphere of YIG ($n_s \simeq 2 \times 10^{28}\,\mathrm{m}^{-3}$) of 2 mm diameter placed exactly at the center of the cavity. The sphere is glued to a cylindrical ceramic rod with its easy axis laying on the plane perpendicular to the rod axis. A PTFE support is used to block the rod and thus the sphere in a fixed position in the cavity. The system is studied by means of $S_{21}$ measurements from the SO to the second antenna, which can be tuned to weak coupling. The resonance frequency of the bare cavity is slightly changed by the presence of the sphere and support to $\omega_c/2\pi \simeq 5.16$ GHz, apart from this small change no other appreciable differences are present. The magnetizing field $B_0 = 0.19$ T along the $z$ direction of the cavity, i.e. orthogonal to the radio frequency magnetic field, is used to obtain the hybridization of the cavity and Kittel mode. When the system is hybridized, two peaks appear with a separation of about 80 MHz. The expected value is $g_{cm}/2\pi \simeq 90$ MHz. From the linewidth of the hybrid peak the material linewidth results $\gamma_m \simeq 1.0$ MHz, which corresponds to the natural linewidth of YIG associated with the spin-spin relaxation time $T_2 = 16\,\mu$s.

### 4.1.2 Rf-electronic chain

The mobile loop antenna is critically coupled to the cavity mode, and measures the power delivered by the cavity also in the absence of any input from SO. The residual emission is due to the thermal photons stored in the resonator. The antenna output is amplified by a cascade of two amplifiers, but the sensitivity is essentially fixed by the first one (A2). Its noise temperature is well below the cavity one and can be measured with the technique described in Sec. 3.3.1 with a load at 300 K and 77 K. The final output, amplified of about 69 dB, is then fed into a spectrum analyzer for recording. For calibration purposes a 50 Ω load is put at the input of the amplifying chain: this allows to check the gain versus frequency curve and the nominal input level. As can be seen from Fig. 4.3, the cavity peak power level corresponds to the Johnson noise of the load as expected. When the system is hybridized, the height of the two hybridized modes coincides again with the Johnson noise of the load and consequently of the empty cavity. This

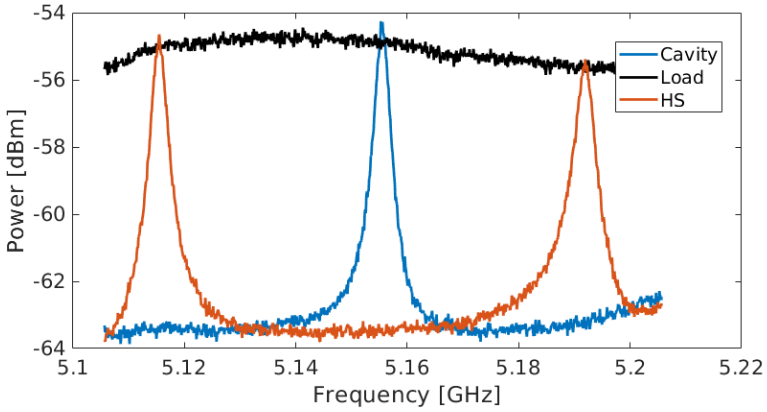


Figure 4.3: Measurement of the thermal noise output of a 50 Ω resistor, of the HS with zero applied field, and of the HS in the full hybridization regimes. These are reported for comparison in black, blue and orange respectively. The fact that all the peaks maxima are at the 50 Ω level is a proof that no extra noise is added to the system when hybridization occurs.

fact demonstrated that there is no added noise related to the HS and thus to the material. Checking this fact at different temperatures allows one to infer that thermal noise in a cavity filled with a magnetized sample is the same as in an empty cavity.

### 4.1.3 Preliminary results

As already discussed, a measurement of the sample magnetization can be extracted from the on-resonance power of one of the hybrid peaks. In the absence of a signal, a limit of the minimum detectable field can be extracted and corresponds to the sensitivity of the spin-magnetometer. By recasting Eq. (2.25) the field sensitivity of the apparatus for an integration time $T_{\text{in}}$ results

$$\sigma_B = \sqrt{\frac{\sigma_P}{2\gamma_e \mu_B N_s \omega_h \tau_h}} = \sqrt{\frac{k_B T_s \sqrt{\Delta f / T_{\text{int}}}}{2\gamma_e \mu_B N_s \omega_h \tau_h}}, \tag{4.1}$$

where the power sensitivity $\sigma_P$ is recast in terms of the Dicke radiometer equation. The stored data are the averaged hybrid resonance curve, and the power sensitivity $\sigma_P$ is estimated with the residuals of a Lorentzian fit over the data points. In the light of the BCFV scheme, a measurement of the hybrid resonance effectively produces a limit on the axion field. To get such

a limit, the optimal RBW $\Delta f$ to be used is the axion linewidth $\gamma_a$. Here the RBW which optimizes the SNR is $\Delta f = 3\,\mathrm{kHz}$, where the worst case scenario is the axionic power splitted in two adjacent bins. For a frequency of 5.1 GHz, a relaxation time of 80 ns, a volume of $18\,\mathrm{mm}^3$ and an integration time of one hour the limit on the magnetic field sensitivity results $\sigma_B^{(1)} \simeq 4 \times 10^{-16}\,\mathrm{T}$. There was no deviation from the expected $t^{-1/4}$ dependence of the power RMS on the integration time, thus the system long-term stability is more than one hour. The limit on the axion field is $B_m^{(1)} \lesssim \sqrt{2}\,\sigma_B^{(1)}$. This simple measurement can be compared to the expected axion effective field at this frequency, which from Eq. (2.14) results $B_a = 2.0 \times 10^{-23}\,\mathrm{T}$. While these values are far from the needed sensitivity, one needs to remember that this is a room temperature device with a very small magnetic sample.

## 4.2 Cryogenic multi-samples prototype

A setup with the characteristics of an actual haloscope is designed starting from the satisfying results obtained with the prototype described in the previous section. The meaning of this manifests essentially into two features: the possibility of performing long measurements storing the results, and the scalability of the setup. The first one can be implemented by using a standard heterodyne down-conversion scheme and a commercial ADC. The second one is important because to eventually detect an axionic signal it is necessary to largely increase the quantity of material, as calculated in Eq. (4.7). To this aim this setup uses a cylindrical cavity with 5 YIG spheres placed on its axis. This configuration can in principle be extended by means of a longer cavity roughly preserving the same resonant frequency. The symmetry is not broken also using a cylindrical sample, unfortunately these are hardly available and thus this possibility was not tested. More ideas to increase the sample volume are discussed in Sec. 5.1.1.

The apparatus is built as shown in the left part of Fig. 4.4. The cryogenic part of the setup is enclosed in a steel vacuum vessel which is first emptied by air and then filled with 10 mbar of exchange helium for thermalization. The electronics part constituting the LTE and HTE are shown in the right part of Fig. 4.4, which is the complete electronic scheme of the haloscope. The setup works at liquid helium temperature for different reasons. The Johnson noise is drastically reduced by the low temperature of the cavity and material, and it makes it possible to use cryogenic HEMT which has a noise temperature comparable with the thermodynamic one. Moreover, a liquid helium bath allows for the employment of a superconducting magnet

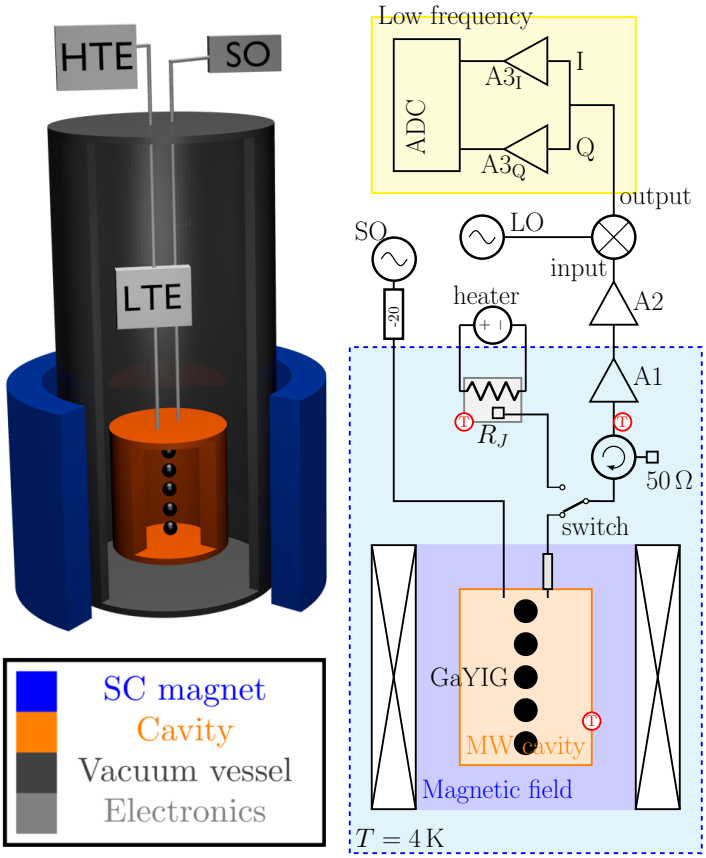


Figure 4.4: *Left* - Simplified scheme of the apparatus showing the high temperature and low temperature electronics (HTE and LTE) and the source oscillator (SO). *Right* - Electronics layout. The blue-dashed line encloses the cryogenic part, the crossed rectangles are the magnet, and the orange rectangle is the cavity with black YIG circles inside. At the top of the cavity are located the sub-critical antenna (left) and the variably-coupled antenna (right). The sub-critical antenna is connected to an attenuator and then to the source oscillator SO, while the other antenna is connected to one of the switch inputs. The other input is the 50 Ω resistor $R_J$ that can be heated with a current generator. The output of the switch is connected to an isolator and then to the amplifiers. The A2 output is down-converted by mixing it with a local oscillator LO. The two outputs, phase $I$ and quadrature $Q$, are fed into the amplifiers $A3_I$ and $A3_Q$, and eventually to the ADC.

to provide the static field. These magnets can reach much higher fields and field uniformity than electromagnets, and the current can be provided by low-voltage high-current supplies. A picture of the cavity inside the SC magnet used for the measurement is reported in Fig. 4.5.

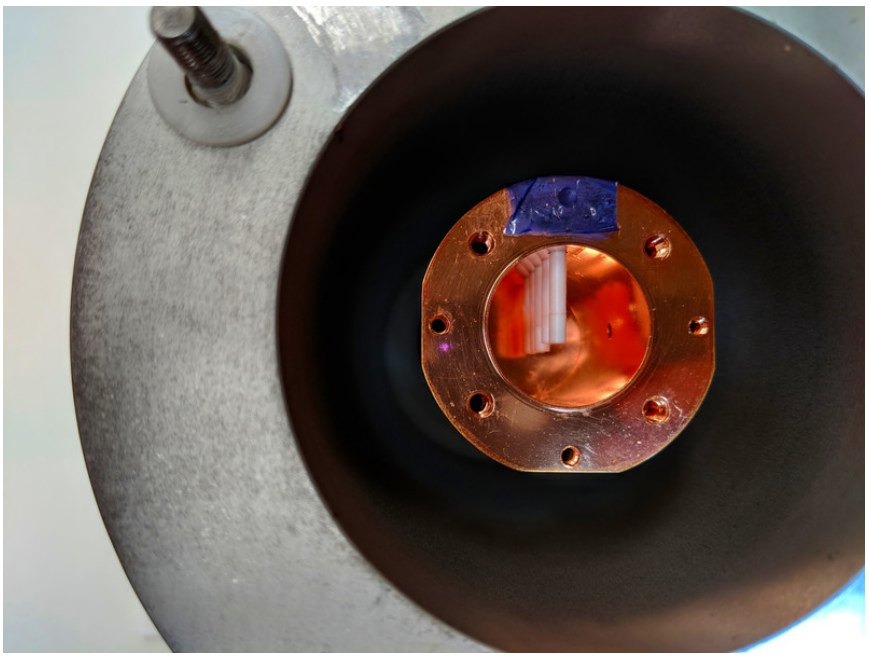

Figure 4.5: Open copper cavity with the five GaYIG PTFE supports inserted inside the SC magnet used for the cryogenic measurements.

### 4.2.1 Multiple YIG spheres in a single copper cavity

The mw resonator is a cylindrical copper cavity TM110 mode with resonance frequency $\omega_c/2\pi \simeq 13.98\,\text{GHz}$ and linewidth $\gamma_c/2\pi \simeq 400\,\text{kHz}$ at liquid helium temperature, measured with a critically coupled antenna. The profile of the cavity is not a regular cylinder, two symmetric sockets are carved into the cylinder to remove the angular degeneration of the normal mode, the maximum and minimum diameters are 26.7 mm and 26.1 mm, and the length is 50.0 mm. The shape of the cavity and of the mode magnetic field are shown in Fig. 4.6. The choice of the TM110 mode has the advantage of having a uniform maximum magnetic rf field along the cavity axis. Its volume can be increased just using a longer cavity without changing the mode resonance frequency. For this mode we calculate a form factor $\xi = 0.52$.

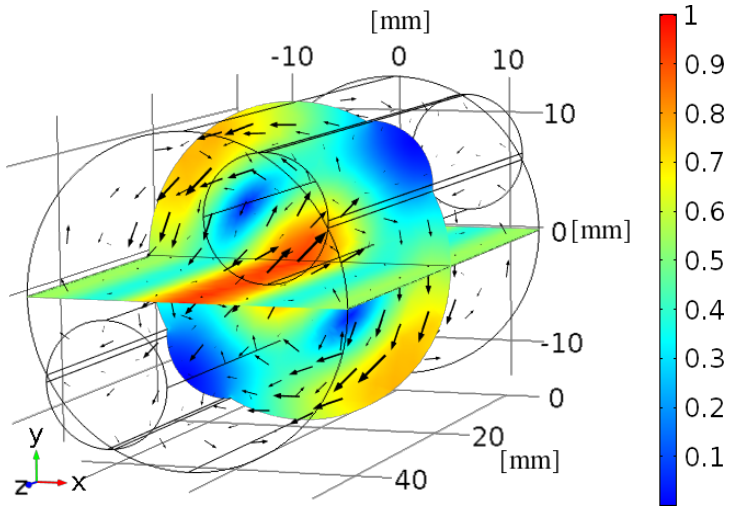


Figure 4.6: Design of the microwave cavity and magnetic field distribution of the TM110 mode (see text for details). The black arrows represent the direction of the magnetic field, and the color is the normalized field amplitude. The GaYIG spheres are placed on the cavity axis at the maximum of the rf magnetic field.

Five GaYIG spheres of 1 mm diameter are placed in the maximum magnetic field of the mode, which lies on the axis of the cavity. The spheres are housed inside a PTFE support large enough to let them rotate in all possible directions, in order to automatically align the GaYIG magnetization easy axis with the external magnetic field. This is crucial for a multi-spheres setup, since if the intrinsic field of the ferrimagnet is not aligned with $B_0$ the Larmor frequencies of the spheres result different, forbidding a coherent coupling of all the YIGs. A simple way is to verify that the spins of the different samples are cooperating is to measure the scaling of $g_{cm}$ with the square root of the number of identical spheres. The total coupling scales with the single spin coupling of Eq. (3.1) and the number of spins as

$$g_{cm} = g_s \sqrt{N_s}\,. \tag{4.2}$$

The scaling is shown in Fig. 4.7 (right) together with the simulated anti-crossing curve (left). The single 2 mm sphere used in the room temperature prototype contains more spins than the five 1 mm spheres used in this setup. However, the aim of this approach is to demonstrate the possibility of using multiple spheres to upscale the system. The amplitude of an external

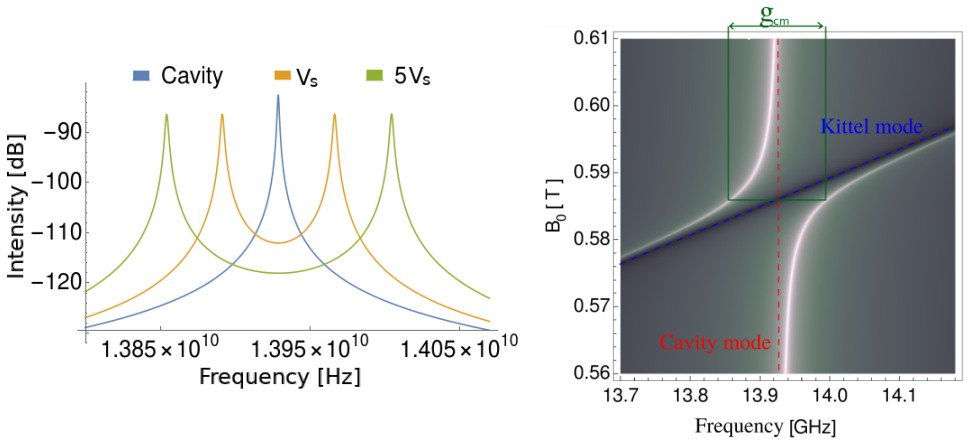


Figure 4.7: Simulation of the HS considered in this setup obtained with the equivalent circuit model presented in Sec. 3.2.3. *Left* - Increased $g_{cm}$ for an increased number of spheres. *Right* - Anticrossing curve of the setup with five spheres. Both the plots represent $S_{21}$ measurements.

magnetic field $B_0$ determines the Larmor frequency of the electrons. The uniformity of $B_0$ on all the spheres must be enough to avoid inhomogeneous broadening of the ferromagnetic resonance. To achieve a magnetic field uniformity $\leq 1/Q_h$, where $Q_h \sim 10^4$ is the quality factor of the hybrid mode, the setup employs a superconducting NbTi cylindrical magnet equipped with a concentric cylindrical NbTi correction magnet. With $B_0 = 0.5\,\mathrm{T}$ the Larmor frequency is $\omega_L \simeq \omega_c$ and thus the full hybridization of the cavity and Kittel modes is achieved. The power supply of the main magnet is a high-precision, high-stability current generator, injecting 15.416 A into the magnet with a precision better than 1 mA, while a stable current generator provides 26.0 A for the correction magnet.

For $f_c \simeq f_L$ the splitted mode frequencies are $f_+ = 14.061\,\mathrm{GHz}$ and $f_- = 13.903\,\mathrm{GHz}$, yielding a splitting $g_{cm}/2\pi = 158\,\mathrm{MHz}$. The coupling $g_{cm}$ scales exactly with $\sqrt{n_s V_s}$, in fact $g_{cm} = \sqrt{5}\,g_1$, where $g_1/2\pi \simeq 71\,\mathrm{MHz}$ is the measured splitting due to a single sphere (see Fig. 4.8, which reports the coupling of a 1 mm sphere at 4 K temperature). This means that all the spins are coherently participating in the material-cavity mode, and ensures that all the spheres' magnetization easy axes are aligned along $B_0$. From $g_{cm}$ it is possible to calculate the effective number of spins in the sample using the relation described by Eq. (4.2), obtaining $n_s = 2.13 \times 10^{28}\,\mathrm{m}^{-3}$, compatible with the YIG spin density. The weakly coupled linewidth is 0.7 MHz,

yielding a critically coupled one of $\gamma_+/2\pi = 1.4\,\text{MHz}$, corresponding to the hybrid modes relaxation times $\tau_- \simeq \tau_+ = 0.11\,\mu\text{s}$.

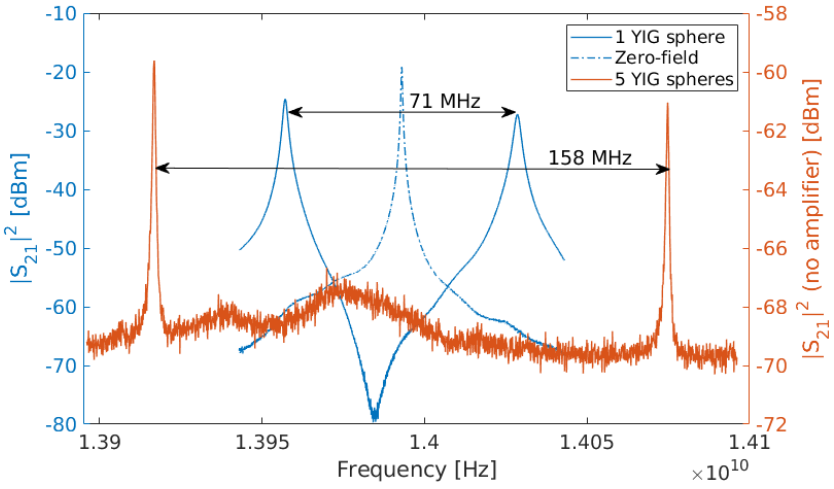


Figure 4.8: $S_{21}$ of a 1 and 5 mm spheres HS. The splittings result $g_1/2\pi = 71\,\text{MHz}$ and $g_5/2\pi = 158\,\text{MHz} = \sqrt{5}\,g_1$, showing coherent coupling of multiple spheres. The two measurements are taken in different conditions.

The system is modeled by means of the equivalent circuit formalism described in Sec. 3.2.3 and the results are reported in Fig. 4.7. It is shown therein that a difference between the material and cavity quality factors can compromise the coupling between the modes. This is not the case of the considered setup, but a smaller effect could be present even for smaller mismatches. To estimate it, it is possible to consider the simplest setup to detect a fluctuation of the magnetization, and compare it with the HS-based magnetometer. The first consists in an antenna critically coupled to the material HO, which collects the axion signal. The HS-based magnetometer is the system already analyzed, i. e. the full circuit of Fig. 3.13. The same axion signal is injected in both the systems, which are set at the same temperature[1]. The difference of the transferred axionic signal power results -0.98 dB, which is the estimated coupling loss in this 4 K prototype [222]. The fraction of transferred power is almost unitary since the mismatch of the two quality factors is small. This will be taken into account when measuring the power outgoing from the hybrid system before converting it to a limit on the axionic field.

[1]The remaining parameters of the considered systems are the ones of Tab. 3.2 and 3.3.

### 4.2.2 Cryogenic rf electronics and data acquisition

The detection electronics consists of an amplification chain which has two inputs, called Input Channel 1 and 2, (IC-1 and IC-2, respectively). Channel 1 measures the signal power, while Channel 2 has calibration and characterization purposes. A cryogenic switch is used to select the desired channel:

**IC-1** - the rf power inside the cavity is collected with a dipole antenna whose coupling to the cavity can be changed using an external micromanipulator, allowing us to switch continuously from weak to over-critical coupling. For optimal measurement conditions, we tune the antenna to critical coupling by doubling the sub-critical linewidth of the selected mode;

**IC-2** - a $50\,\Omega$ termination $R_J$, enclosed in a copper block together with a heater resistance, is used as Johnson noise source. The emitted power can be used to calibrate the noise temperature of the system and the total gain, detailed hereafter.

The detection electronics, as shown in Fig. 4.4, is divided into a liquid helium temperature part (LTE) and a room temperature part (HTE). The collected power is amplified by a HEMT cryogenic low-noise amplifier (A1) with gain $G_{\mathrm{A1}} \simeq 38\,\mathrm{dB}$. To avoid the back-action noise of the amplifier, a cryogenic isolator with 18 dB of isolation is inserted in the chain. The HTE consists of a room temperature HEMT amplifier (A2), with $G_{\mathrm{A2}} \simeq 34\,\mathrm{dB}$, followed by an IQ mixer used to down-convert the signal with a local oscillator (LO). In principle, it is possible to acquire the signal coming from both hybrid modes using two mixers working at $f_+$ and $f_-$. In this simplified scheme it is chosen to work only with $f_+$, thus setting the LO frequency to $f_{\mathrm{LO}} = f_+ - 0.5\,\mathrm{MHz}$ and its amplitude to 12 dBm. The antenna output at the hybrid mode frequency is down-converted in the 0 - 1 MHz band, allowing to efficiently digitize the signal. The phase and quadrature outputs are fed to two low frequency amplifiers ($\mathrm{A3}_{I,Q}$), with a gain of $G_3 \simeq 50\,\mathrm{dB}$ each, and are acquired by a 16 bit ADC sampling at 2 MHz. A weakly coupled dipole antenna is used to inject low power signals and make transmission measurements of the system using a source oscillator, SO. All the apparatus devices are referenced to a GPS disciplined, oven controlled, local oscillator. The measurements are performed at temperatures $T_c \sim T_a \simeq 5.0\,\mathrm{K}$ and $T_r \simeq 5.5\,\mathrm{K}$, as read by the cavity, amplifier and $R_J$ thermometers, respectively.

For the calibration of the system, the load $R_J$ is heated to a temperature $T_r$, as described in Sec. 3.3.1. Using IC-2 it is possible to measure the

Johnson noise of $R_J$ in the temperature range $5 \div 25\,\mathrm{K}$ without significantly heating other parts of the apparatus. The detected power is the one of Eq. 3.29 and the measurement is reported in Fig. 4.9. For this measurement,

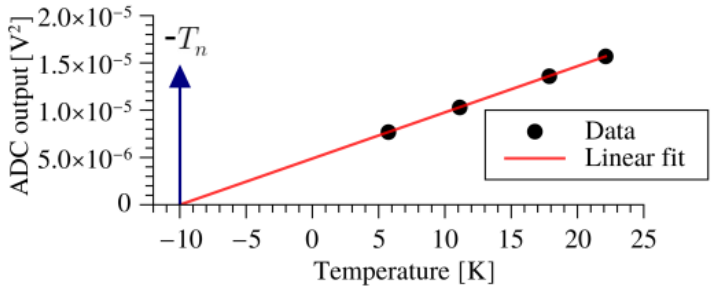


Figure 4.9: Measurement of noise temperature and gain of the detection electronics. The statistical error for each point is smaller than the size of the symbol. In the plot the mean square amplitude of the ADC output is plotted vs $T_r$. The noise temperature at the input of A1 is $10^{L/10} \times T_n = 8.0\,\mathrm{K}$, where $L = -1.0\,\mathrm{dB}$ are the measured losses between $R_J$ and A1.

four collected points are fitted with $q_c(T) = a_c T + b_c$ to obtain the noise temperature $T_n = -b_c/a_c$ and the total gain $G_{\mathrm{tot}} = a_c$. The error of the estimated parameters is less than 1%. This method verifies that the noise of the system changes linearly with the temperature, and that the measured cavity output power at the temperature $T_c$ is given by Eq.(3.29) with $T_r = T_c$, assuming that IC-1 and 2 have the same losses, which is true within 0.2 dB. Typical measured values are $T_n = 9 \div 11\,\mathrm{K}$ and $G_{\mathrm{tot}} = 106 \div 108\,\mathrm{dB}$, at different frequencies around 14 GHz. This procedure ensures the accuracy of the measurement and then, using IC-1, we perform measurements on the hybrid system with the calibrated electronic chain.

The stability of $f_+$ is monitored by injecting with SO an rf probe signal at $f_+ - 0.9\,\mathrm{MHz} = f_{\mathrm{LO}} + 0.1\,\mathrm{MHz}$. The transmitted amplitude of the probe peak is a monitor of the hybrid peak frequency since it changes if $f_+$ drifts. Such amplitude is registered during the whole measurement and is plotted in Fig. 4.10, the frequency stability of an average run is around 3.5%, which is enough for the purposes of this measurement. This variation is presumably due to drifts of the external static magnetic field, since with a $B_0 = 0$ run the corresponding variation results much smaller.

A dedicated DAQ software is used to control the oscillators and the ADC, and verifies the correct positioning of the LO with an automated measurement of the hybrid mode transmission spectrum. The ADC digitizes

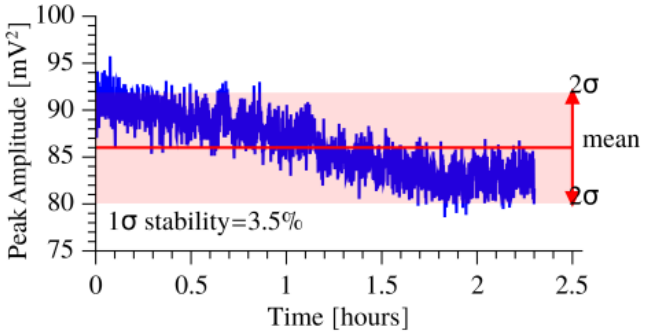


Figure 4.10: Stability of the hybrid mode, measured through the amplitude of a calibration peak injected with SO (see text for further details).

the time-amplitude down-converted signal coming from $A3_I$ and $A3_Q$ and the DAQ software stores collected data binary files of 5 s each. The noise budget of the electronics is reported in Fig. 4.11, to verify that the main noise is due to the amplifier and to the HS. The software also provides a simple

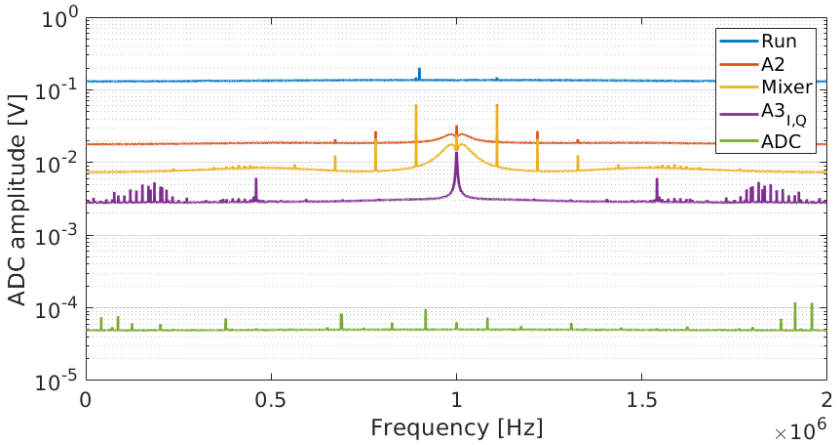


Figure 4.11: Amplitude of the noise introduced by the different parts of the detection chain, from the ADC to a measurement run.

online diagnostic, extracting 1 ms of data every 5 s, and showing its 512 bin FFT together with the moving average of all FFTs. The acquisition control panel and the real-time monitor are shown in the upper and lower part of Fig. 4.12, respectively. The signal is down-converted in its in-phase and quadrature components $\{\phi_n\}$ and $\{q_n\}$, with respect to the local oscillator,

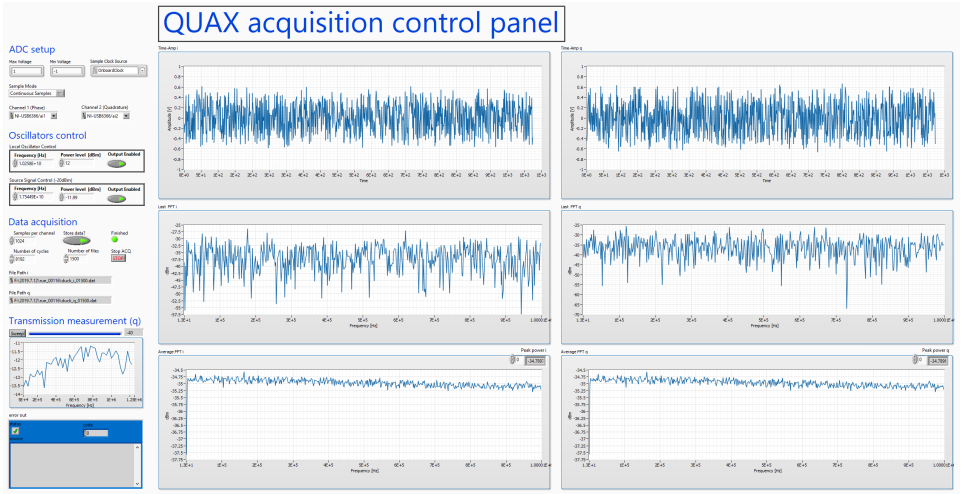


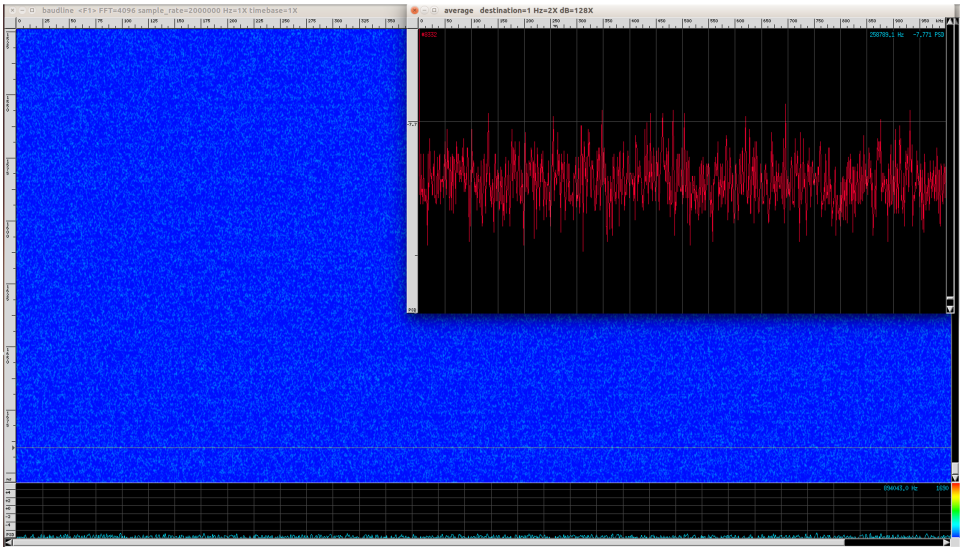

Figure 4.12: *Upper* - Control panel of the DAQ system divided in left and right parts for the in-phase and in-quadrature components acquired by the ADC. From top to bottom the displays are showing the acquired signal as a function of time, the FFT of a subsample of data, and the average of all the FFTs of the ongoing run. *Lower* - The stored data are constantly checked by means of a spectrogram (in blue) and of an averaged FFT (in pink).

that are sampled separately. A complex FFT is applied to $\{s_n\} = \{\phi_n\} + i\{q_n\}$ to get its power spectrum $s_\omega^2$ with positive frequencies for $f > f_{\rm LO}$ and negative frequencies for $f < f_{\rm LO}$. In this experimental setting, the axion signal is mapped almost completely onto the positive frequencies since the hybrid mode linewidth is of order 1 MHz. Using this fact the thermal noise resonance, which is due to the temperature difference between the HS and the isolator, can be measured by subtracting the left part of the spectrum from the right one. The result is compatible with the thermal noise of a HS at slightly higher temperature than the load, as shown in Fig. 4.13. This

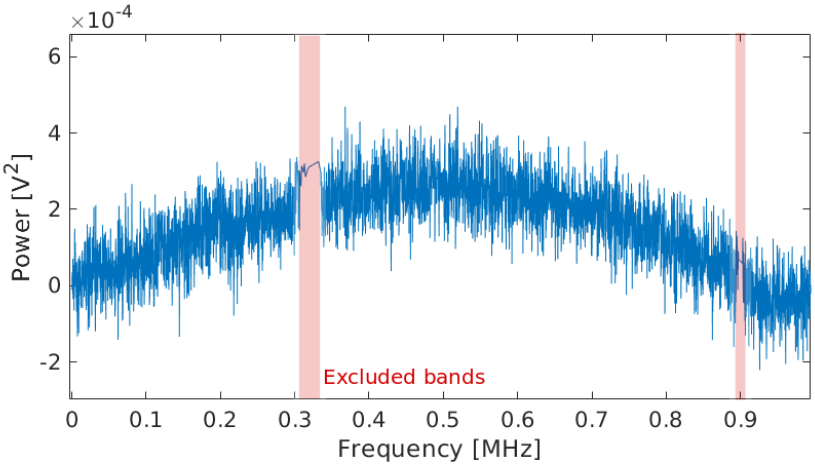


Figure 4.13: Added thermal noise due to the hybrid mode. The spectrum is measured at the ADC output in the band $0 \div 1$ MHz.

last measurement ensures the good coupling of the antenna to the HS and confirms that all the parts of the apparatus work as expected.

### 4.2.3 First limits on the axion-electron coupling

As seen in Chapter 2, the axion wind releases a faint power in a band of $\sim 7$ kHz around $f_a$. This signal can be seen only if $f_a$ falls into the detection bandwidth, which corresponds to the linewidth of the hybrid peak. The expected noise power is given by

$$P_n^{(2)} = 1.48 \times 10^{-18} \left(\frac{T_c + T_n}{5.2\,\mathrm{K} + 10.1\,\mathrm{K}}\right)\left(\frac{\Delta f}{7.0\,\mathrm{kHz}}\right) \mathrm{W}, \tag{4.3}$$

calculated from Eq. (3.29) using the data collected from IC-2. Considering the losses of the system and the gain of the amplifiers, it is shown that the

mean of the measured power is indeed compatible with the expected noise.

Multiple measurements of the effective axion field have been performed as follows. The vacuum vessel containing the system is cooled down to liquid helium temperature and when a proper thermalization is achieved the detection electronics parameters $G_{\rm tot}$ and $T_n$ are measured through IC-2. Then, after switching to IC-1, the magnetic field is set to $B_0$ to 0.5 T to hybridize the cavity and Kittel mode at $f_c \simeq f_L \simeq 14\,\text{GHz}$, and critically couple the antenna with the $f_+$ hybrid mode using the manipulator. Fig. 4.14 reports the analysis of RUN31, which is described hereafter in some details. The ∼2.3 hours of the measurement consist in 2048000 FFTs of 8192 bins each (frequency resolution of 244 Hz), which are square averaged and rebinned to the bandwidth $\Delta f = 7.8\,\text{kHz}$ (256 bins), close to $\Delta f_a$. As explained, only the 128 positive bins of the spectrum is considered and calibrated by setting $s_\omega^2$ to the value of Eq. (3.29). Some frequency intervals of the power

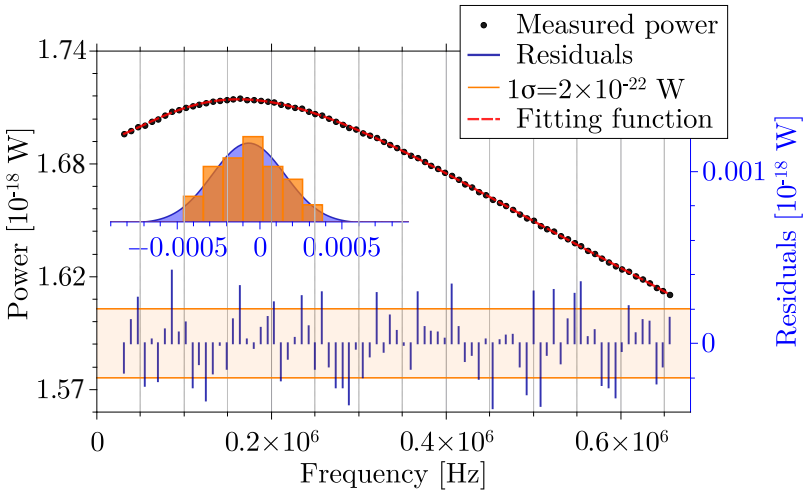


Figure 4.14: Down-converted power spectrum and residuals of RUN31. The black dots are the measured data points and their error is within the symbol dimensions, the red line is a polynomial fit of such points. The residuals are represented in blue and, as an inset, we show them on an histogram. The corrupted intervals are removed.

spectrum are affected by disturbances at the ADC output, and are ignored in the analysis procedure. A polynomial of degree 5 is fitted to the averaged spectrum and the residuals estimated. The averaged spectrum is reported in Fig. 4.14 together with the fitting function. In Fig. 4.14 a plot of the resid-

uals and their histogram is also given. The average value of the residuals is $-4.6 \times 10^{-23}$ W with standard deviation $\sigma_P^{(4\,\mathrm{K})} = 2.2 \times 10^{-22}$ W. The result is compatible with Dicke radiometer equation

$$\sigma_{\mathrm{D}} = k_B T_D \sqrt{\frac{\Delta f}{T_{\mathrm{int}}}} = 2.1 \times 10^{-22} \sqrt{\left(\frac{\Delta f}{7.8\,\mathrm{kHz}}\right)\left(\frac{8280\,\mathrm{s}}{T_{\mathrm{int}}}\right)}\ \mathrm{W}, \tag{4.4}$$

where $t$ is the total integration time and $T_D = T_c + T_n$. This means that the standard deviation of the noise decreases as $1/\sqrt{t}$, at least within the RUN31 time span.

To infer the axion sensitivity of our measurement, two corrections have to be introduced: *(i)* a loss of 0.98 dB (a factor 0.8) at the cavity antenna due to imperfect matching between cavity and axion field (see Sec. 4.2.1); *(ii)* a factor 1/2 to account for the binning search procedure. In fact the maximum power deposited in a single bin is actually $P_{\mathrm{in}}/2$. The correct power standard deviation results in $\sigma'_P = 2\sigma_P^{(2)}/0.8$. The measured rf power is compatible with the modeled noise for every bin and no statistically significant signal consistent with axions was found. The upper limit at the 95% C.L. is $2\sigma'_P = 1.1 \times 10^{-21}$ W. This value can be converted to equivalent axion field with the help of Eq. (4.1), obtaining

$$\begin{aligned} B_m^{(2)} < \left(\frac{P_{\mathrm{out}}^{(2)} = 2\sigma'_P}{4\pi\gamma_e \mu_B n_S f_+ \tau_+ V_s}\right)^{1/2} = 2.6 \times 10^{-17} \Big[\left(\frac{14\,\mathrm{GHz}}{f_+}\right) \times \\ \times \left(\frac{2.13 \cdot 10^{28}/\mathrm{m}^3}{n_S}\right)\left(\frac{0.11\,\mu\mathrm{s}}{\tau_+}\right)\left(\frac{2.6\,\mathrm{mm}^3}{V_s}\right)\Big]^{1/2}\ \mathrm{T}, \end{aligned} \tag{4.5}$$

where all the reported parameters have been explicitly measured. This makes every run highly self-consistent since all the parameters used to extract the limit are checked every single time. The limit holds for the central frequency of the hybrid mode, while for other frequencies the sensitivity have to be normalized: the correct sensitivity is obtained dividing $B_m^{(2)}$ by the normalized amplitude of the hybrid mode Lorentzian. Several measurements have been performed for different cool downs of the setup. Probably due to mechanical instabilities and to the low resolution of the correction magnet power supply, the resulting working frequency $f_+$ slightly changed between the runs, allowing to perform a limited frequency scan over a ∼3 MHz range. The maximum integration time for a 1 MHz band was 6 hours, and no deviations from the $1/\sqrt{t}$ scaling of $\sigma_P$ are found.

These results also represent a limit on the axion-electron coupling constant. Since $B_m$ depends on $g_{aee}$, the explicit form of the effective magnetic

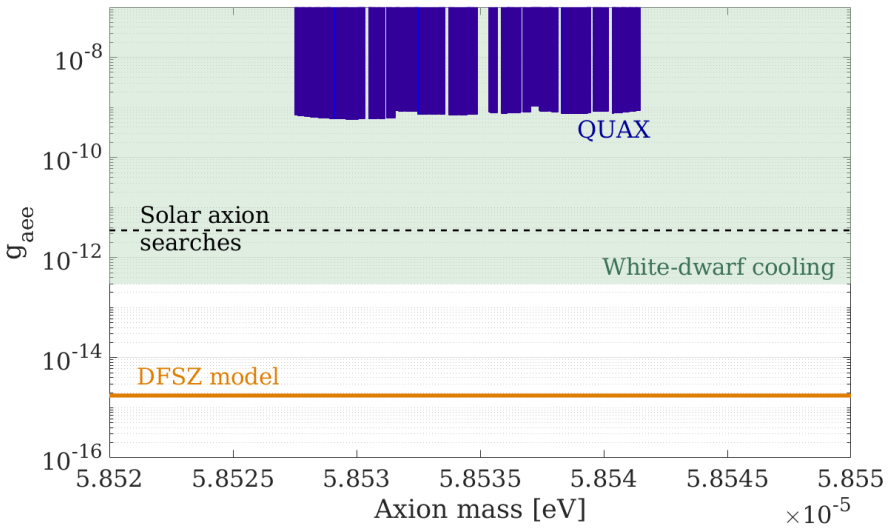


Figure 4.15: Excluded values of the $g_{aee}$ coupling (blue area) compared to its theoretical prediction for the DFSZ axion model (orange line) and a DM density of $0.45\,\mathrm{GeV/cm^3}$. The green shaded area is excluded by white dwarf cooling [238–240], while the black dashed line is the best upper limit obtained with solar axion searches relying on the axio-electric effect [103–109].

field given in Eq. (2.14) can be recast with the help of Eq. (4.1), to The results of this preliminary measurements are far from the sensitivity requirements for a cosmological axion search [see Eq. (2.14)], however they can be used to detect DM Axion-like particles (ALPs) [43]. During the measurement time the DM-wind amplitude was on the maximum of the daily modulation, allowing us to use the collected data to obtain an upper limit on the ALP-electron coupling at the maximum sensitivity. Through Eq. (4.6) we are able to exclude values of the ALP-electron coupling constant for ALP masses given by $f_+$ through Eq. (2.14). The repetition of the analysis procedure for seven measurement runs and averaging together the overlapping bandwidths, produces the plot in Fig. 4.15. The minimum measured value of $g_{aee}$ is $4.9 \times 10^{-10}$, corresponding to an equivalent axion field limit of $1.6 \times 10^{-17}$ T.

$$g_{aee} > \frac{e}{\pi m_a v_a} \sqrt{\frac{2\sigma'_P}{2\mu_B \gamma\, n_a n_S V_s \tau_+}}\,, \tag{4.6}$$

at 95% confidence level.

Using Eq. (4.1), the power released by a DFSZ-axion wind in the five GaYIG spheres of the present prototype is

$$P_{\text{out}}^{(2)} = \frac{P_{\text{in}}^{(2)}}{2} = 1.4 \times 10^{-33} \left(\frac{m_a}{58.5\,\mu\text{eV}}\right)^3 \times \\ \times \left(\frac{n_s}{2 \cdot 10^{28}/\text{m}^3}\right) \left(\frac{V_s}{2.6\ \text{mm}^3}\right) \left(\frac{\tau_h}{0.11\,\mu\text{s}}\right) \text{W}, \tag{4.7}$$

corresponding to a rate $r_a^{(2)} \sim 10^{-10}$ Hz of 14 GHz photons, which is clearly not detectable. To have a statistically significant signal within a reasonable integration time it is mandatory to increase the signal rate, for example in the mHz range, that will give tens counts per day. The present sensitivity to the power deposited in the system by the axion wind maintains an excess photon rate of order 100 photons/s.

The sensitivity of this apparatus is presently limited only by the noise temperature of the system and thermodynamic fluctuations, as it reached the limit of the Dicke radiometer equation. The overall behavior of the apparatus is as expected, and thus the expectations are that the planned upgrades will be effective. These findings indicate the possibility of performing electron spin resonance measurements of a sizable quantity of material inside a cavity cooled down to cryogenic temperatures and is the first measured limit of the coupling between cosmological axions and electrons.

## 4.3 Ultracryogenic quantum-limited prototype

The last stage of the haloscope development described in this thesis is ultra cryogenic quantum-limited version. The laboratory area dedicated to the setup is shown in Fig. 4.16. The latest findings, together with new ones have been used to build a setup which, by implementing positive features, drastically overcomes the previous sensitivity. With respect to the setup of Sec. 4.2, this one increases the axion-deposited power and improves the rf sensitivity. The signal is increased due to a larger material volume constituted by ten YIG spheres of 2 mm diameter, and resulting in a gain factor $\sim 16$ on $P_{\text{in}}$. The new detection electronics employs a JPA like the one described in Sec. 3.3.2, and its quantum-limited noise temperature is close to 0.5 K, roughly a factor 20 better than the ∼10 K of the HEMT. This setup has an operating frequency around 10 GHz due to the JPA working range.

The ultra cryogenic system is an old wet dilution refrigerator by Leiden Cryogenics that has been refurbished as a part of this thesis work. The

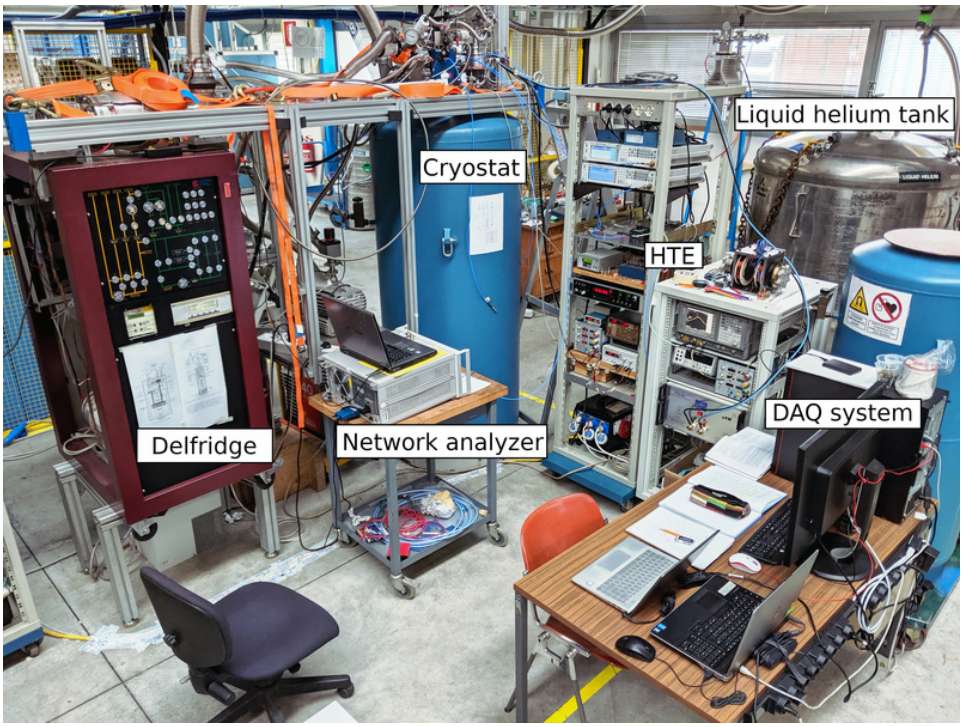


Figure 4.16: Picture of the ultra cryogenic section QUAX laboratory, located at INFN - Laboratori Nazionali di Legnaro near Padua (Italy).

details of the refurbishing are omitted, and consisted mainly in hydraulics and mechanics. The empty fridge reached a base temperature of 16 mK, with a cooling power close to 200 $\mu$W at 100 mK. The diameter of the mixing chamber (MC) plate is close to 7 cm, making it difficult to house the cavity and all the electronics. To increase the available space, the flange of the internal vacuum chamber (IVC) has been replaced with a larger one with four sma feedthroughs for rf cabling. The IVC is now a cylinder of 129 mm diameter and 1 m length. The radiation screen, which is usually attached to the Still plate, has been removed due to the new geometry. Schemes of the electronics, of the mechanical design, and a picture of the apparatus are detailed in Fig. 4.17 and 4.18.

The rf electronics is mounted on the MC, as it is the plate with lower temperature. The IVC is sealed with indium, emptied, leak tested at 77 K and placed inside a cryostat of height 2 m. The cooling down process is reported hereafter in some details. The cryostat is filled with 1400 mm of

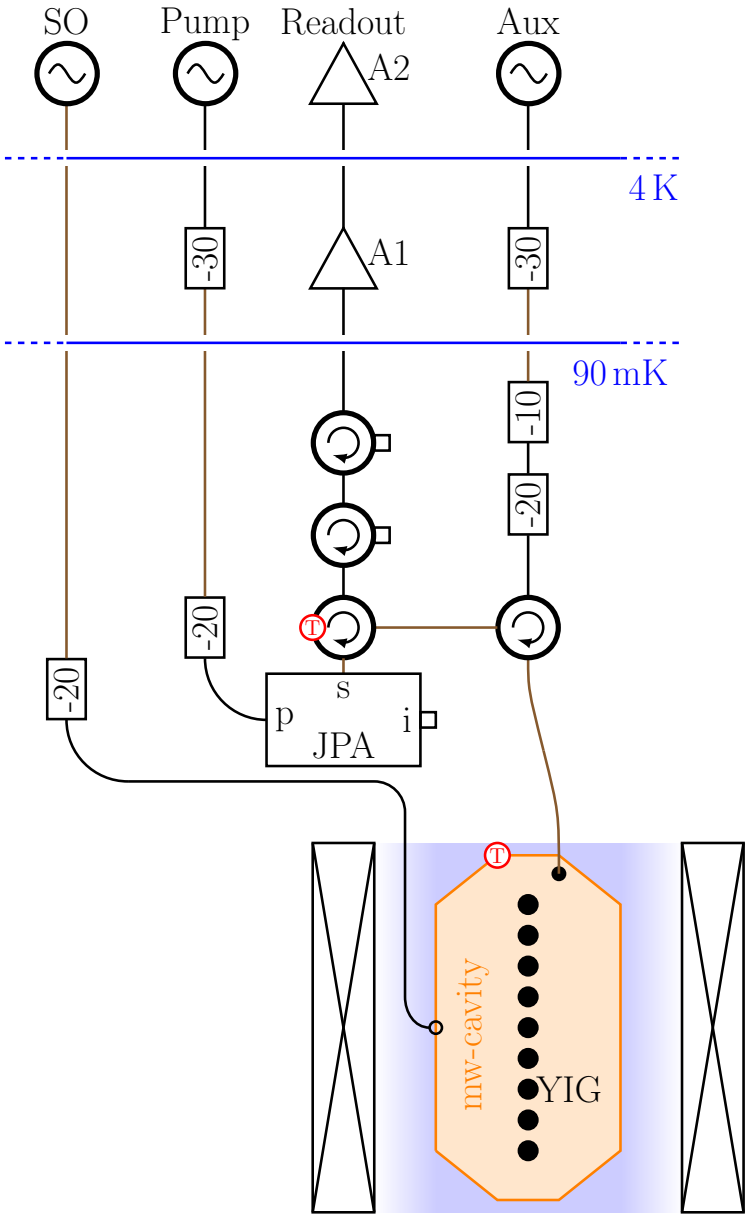


Figure 4.17: Electronic layout of the ultra cryogenic setup. The SC cables are drawn in brown and the low-frequency part of the rf chain is the same as in Fig. 4.4. The temperature in the 90 mK part is not actually uniform.

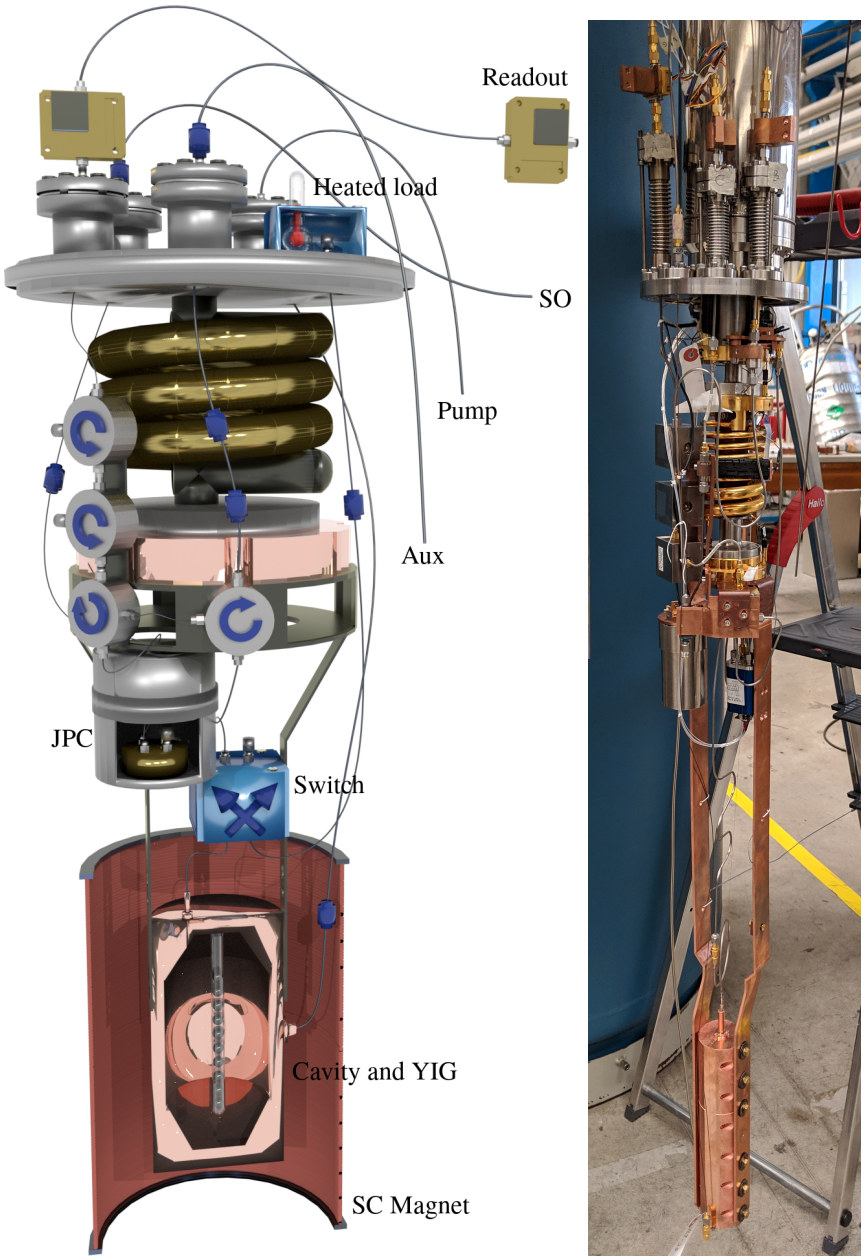


Figure 4.18: Rendered scheme of the setup and picture of the actual configuration. The scheme is not exactly the one of Fig. 4.17 (see text).

liquid helium, enough for covering the IVC and the above electronics (see Fig. 4.17). This allows for the operation of the apparatus for roughly two days. During the filling, 1 mbar of exchange helium is loaded in the IVC for thermalization at 4 K. When the filling is completed, the chamber is pumped for one night to reach a base pressure of $10^{-6}$ mbar. The next day, the circulation of the $^3$He-$^4$He mixture can start, and the system is cooled down to ultra cryogenic temperature. The MC reaches its base temperature when the pressure of the Still is 1 to 2 mbar. With all the electronics and cavity anchored at 90 mK temperature has been reached. The cavity temperature is usually slightly higher, of the order of 120 mK. This is due to the wiring of the antennas and to the thermal conductance. The former is a thermal link with the helium bath, and the latter is reduced due to the distance between cavity and MC. The temperatures are measured with two ruthenium oxide thermometers (for the 1 K pot and for the Still) and two paramagnetic thermometers on the MC and on the cavity, all read by a resistance bridge.

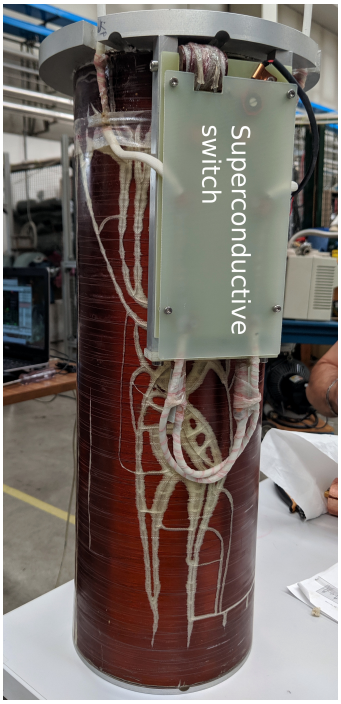


Figure 4.19: The SC magnet used in this setup.

A NbTi SC magnet is placed outside the IVC and immersed in liquid helium. It is mounted to have its axis lying along the mw cavity one, to get the best possible uniformity over the YIG spheres, see Fig. 4.18-left. The inner bore of the magnet is 150 mm and its length is 0.5 m. The magnetic field is uniform up to 7 ppm over a cylinder of 7 cm length and 1 cm diameter at the center of the solenoid, where the magnetic samples are located. The current is supplied by a low-voltage high-current generator developed in the electronic workshop of the Padua University. It is specifically designed to have a stability better than 1 mA. The magnet produces a field of 1 T for a current of 26 A, the maximum field is 2 T. Its circuitry is equipped with a diode system to prevent damages in the case of a quench. A SC switch allows for a persistent operation with SC currents and is shown in Fig. 4.19. To limit the effect of the SC magnet residual field on the SC electronics, there must be a sizable distance between the two. The downside is the reduced thermal conductance aforementioned. A high residual field could compromise the operation of the electronics, and in particular of the

JPA. To further improve the JPA screening a lead shield is placed on it, in addition to the one already described in Sec. 3.3.2. The operating field is about 0.35 T (for a 10 GHz frequency), and the residual field outside the solenoid at the distance of the electronics is of order 10 G, allowing for a proper screening of the SC lead.

A key part of the previous setups was the tunable antenna. Preserving such a feature in this apparatus is not easy. The tuning is realized by a system of pulleys that connects an external manipulator to the antenna with a steel wire. The dipole antenna is the inner part of a NbTi coaxial cable with its outer part removed. It is pushed toward the inside of the cavity with a spring, and the function of the steel wire is to move it in the opposite direction (see Fig. 4.24). The wire is thin to reduce the thermal conductivity, since its upper end is connected to a room temperature manipulator. Most of the rf cabling is done with superconductors. SC cables are useful for two reasons: they have negligible losses when cooled below their transition temperature, and have low thermal conductivity. These cables are drawn in brown in Fig. 4.17, and they are used for critical connections. For example the readout line, from the cavity output to the JPA, needs to have the lowest possible losses since a resistive cable effectively adds noise to the system. A cable with 3 dB losses at the temperature of 2 K adds 1 K of noise temperature to the system.

Initially, a noise calibration similar to the one of the previous prototype was attempted with the scheme of Fig. 4.18 (which is the same of Fig. 3.21 with YIG and magnetic field). However, as mentioned in Sec. 3.3.2, the 4 K Johnson noise largely saturates the amplifier and thus the measurement was not successful. One of the possibilities to overcome this problem is to use a calibrated line which attenuates such noise. A 20 dB attenuator at $\sim$ 100 mK, on the calibration line will produce a 100 mK Johnson noise which adds to the noise of the resistor. For temperatures of the heated resistor between 4 K and 20 K, the added noise is 40 mK to 200 mK. In principle this technique works, but practically it is difficult to implement. Eventually, the chosen setup is the one of Fig. 4.17, and the actual calibration is explained in Sec. 4.3.2.

The next Section, 4.3.1, describes the realization and modeling of the HS of this setup, which is different from the previous ones because of the large quantity of material. A suitable theory is used to model the HS and preserve the consistency of the measurement. Sec. 4.3.2 focuses on the characterization of the JPA in the working conditions, i. e. reading out the HS with the magnetic field turned on. Accuracy and precision of the measurement are checked with the calibration procedure, and the coupling with the

hybrid system is verified. The haloscope operation is in Sec. 4.3.3, which reports how the 2019 QUAX scientific run is performed, presenting details of the scanned mass range, data acquisition and analysis. The results are discussed in Sec. 4.3.4 where the final upper limit on $g_{aee}$ is presented.

### 4.3.1 Coherent couping between material and cavity

A fine result of the previous prototype is that multiple spheres can be coupled to a single cavity mode. The measurements demonstrate that all the spin coherently participate in the interaction, thus the samples are a single oscillator. This is guaranteed by the fact that the static field is uniform over the spheres and that the rf field is degenerate over the axis of the cavity where they are placed. Several tests are performed to understand different features of the system in the light of the two properties mentioned before. To understand the results of the different measurements a simple oscillators model like the one of Sec. 3.2.1 is introduced. Hereafter the photon modes are labeled as $c$ and $d$ while the magnon modes are $m$ and $n$. Since the YIG is a ferrimagnet it has a permanent magnetization, thus if two spheres are too close to each other their magnetization starts interacting. This can be described by introducing two magnon modes that can either have the same resonant frequency or a slightly different one. This is modeled by the hamiltonian

$$\mathcal{H}_{\mathrm{cmn}} = \begin{pmatrix} \omega_c - i\gamma_c/2 & g_{cm} & g_{cn} \\ g_{cm} & \omega_m - i\gamma_m/2 & g_{mn} \\ g_{cn} & g_{mn} & \omega_n - i\gamma_n/2 \end{pmatrix}, \tag{4.8}$$

where $g$ are the couplings between the oscillators, $\omega$ their resonant frequencies and $\gamma$ the dissipation. The autofunction of the system can be calculated as the determinant of

$$\omega\mathbb{I}_3 - \mathcal{H}_{\mathrm{cmn}} = \begin{pmatrix} \omega - \omega_c + \frac{i\gamma_c}{2} & -g_{cm} & -g_{cn} \\ -g_{cm} & \omega - \omega_m + \frac{i\gamma_m}{2} & -g_{mn} \\ -g_{cn} & -g_{mn} & \omega - \omega_n + \frac{i\gamma_n}{2} \end{pmatrix}, \tag{4.9}$$

thus the function used to show the anticrossing curve reads

$$f_{\mathrm{cmn}}(\omega, \omega_m, \omega_n) = \det\left(\omega\mathbb{I}_3 - \mathcal{H}_{\mathrm{cmn}}\right). \tag{4.10}$$

To ideally have a coherent coupling, let the spins of different spheres cooperate and make them indistinguishable, they need to be uncoupled and their resonant frequencies must be the same. These conditions translate

to $g_{mn} = 0$ and $\omega_m = \omega_n$, which clearly can be extended to an arbitrary number of oscillators (in this case, the ten spheres). The cavity used in this measurement has a resonant frequency $\omega_c = 10.7\,\text{GHz}$, the values of $\gamma_c$ and $\gamma_{m,n}$ are set 1 MHz and 2 MHz, respectively, and the magnon-photon coupling is $g_{cm} \sim 180\,\text{MHz}$. These are arbitrary values close to the actual ones used in the test setup.

The interaction between two spheres yields non-zero value of $g_{mn}$, and its effect is to introduce other resonances besides the two of the HS. This effect, shown in Fig. 4.21 (left), needs to be avoided to have control over the system and couple all the spins of the samples to the cavity mode. The sphere production technique described in Sec. 3.1.2 open the possibility of studying spheres of different diameters coupled to the same mode. Some problems arise trying to couple spheres with different diameter to the same mode, since apparently the volume of the sample is linearly related to the offset field as shown in Fig. 4.20. The relation depends on the YIG batch

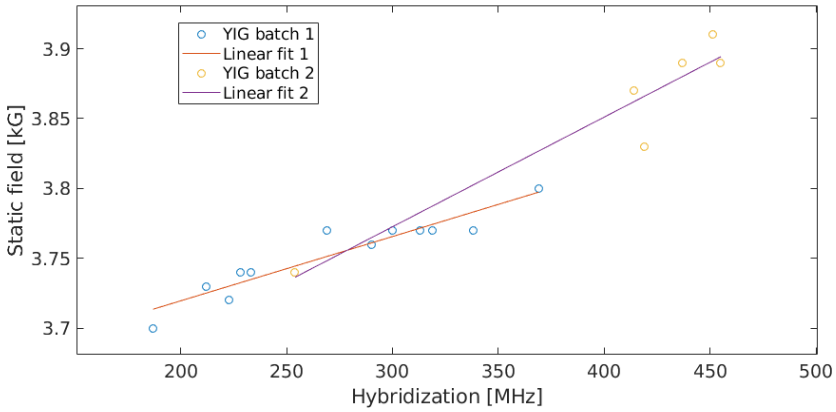


Figure 4.20: Relation between $g_{cm}$ and the full hybridization field. The data are obtained using a 10 GHz cavity, and the peaks splitting is used to measure the volume of the sphere.

that was tested, and is independent on the total number of spins since the same effect is not present with multiple spheres. This is likely due to a geometrical factor affecting the intrinsic field of YIG, but up to now there is no definitive explanation of this observation.

To simulate a sphere with an offset field different from another the autofunction is $f_{\text{cmn}}(\omega, \omega_m) = f_{\text{cmn}}(\omega, \omega_m)|_{\omega_n = \omega_m - \omega_b}$, where $\omega_b = \gamma_e b_0$. The field $b_0$ is small compared to the static $B_0$. From the model it is possible

to estimate the tolerance on $b_0$, and thus on the sphere diameter, needed to preserve a coherent coupling between the spheres. This calculation is

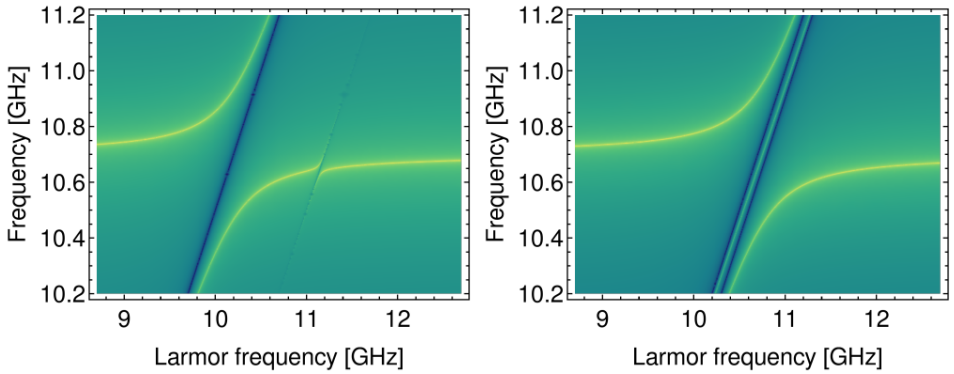


Figure 4.21: Result of the simulation of two magnon oscillators coupled to a single photon oscillator. *Left* - large magnon-magnon coupling. *Right* - effect of two magnon oscillators with slightly different Larmor frequencies.

reported in Fig. 4.21 (right) and shows that the added field must be roughly $b_0 < 10^{-4} B_0$, and thus the diameters must be the same within sub-mm precision.

These constraints are tested with a room temperature setup consisting in a 10.7 GHz cavity with conical endcaps, see Fig. 4.24 and a fused silica pipe holding the YIG spheres. The magnetic field is given by the SC magnet shown in Fig. 4.19 and used in the scientific run. To perform quick tests it is equipped with a room temperature bore allowing the magnet to be in a liquid helium bath during operation. First the minimum separation between two spheres is tested by gradually increasing the distance between them and verifying that a usual anticrossing curve is reproduced. The minimum distance between 2 mm spheres results in 3 mm. A YIG sample then occupies 5 mm of space, and since the cylindrical part of the cavity is 6 cm it can house a maximum of twelve samples. Ten spheres are inserted in the pipe for them not to be too close to the conical part of the cavity. Multiple spheres of different diameters were fabricated and refined to verify that they hybridize with the cavity for the same value of the magnetic field.

Taking these precautions the first tests with ten YIG spheres are performed to obtain the anticrossing curve reported in Fig. 4.22, collected at room temperature. As can be seen the curve is not the usual anticrossing curve, which is also reported in Fig. 4.22. This result is unexpected but can be explained by some simple considerations. First, the central part of

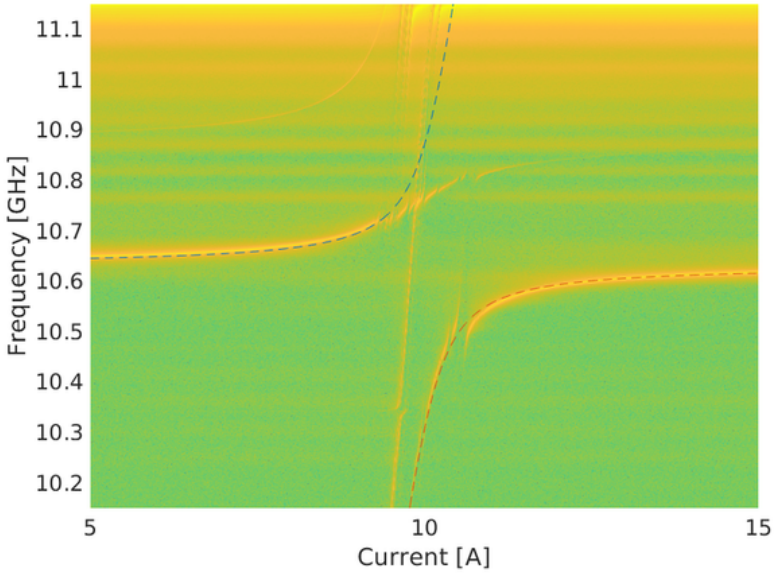


Figure 4.22: Anticrossing curve of the cavity with ten YIG spheres at room temperature. The reported curve is different from usual anticrossings (see for example Fig. 4.7), which is reported in blue and red dashed lines.

the cavity is shaped similarly to the one of Sec. 4.2, thus the shape is not a perfect cylinder but it has two flat surfaces used to remove the angular degeneration of the mode. This creates two modes rotated of $\pi/2$ with different frequencies, in principle one of the two is coupled to the antennas while the other is not. Actually to some extent both of them are coupled, and thus also the second mode is visible in Fig. 4.22 close to 10.9 GHz. This second mode also couples to the material since its maximum magnetic field is on the axis, so it needs to be considered in the model. The oblique mode is likely due to a sphere with a diameter somewhat different from the others', while other disturbances could be related to residual magnon-magnon interaction. By using a model with two photon oscillators (the two cavity modes $c$ and $d$) and two magnon oscillators, the anticrossing curve of Fig. 4.22 is closely reproduced, the hamiltonian is

$$\mathcal{H}_{\mathrm{cdmn}} = \begin{pmatrix} \omega_c - i\gamma_c/2 & g_{cd} & g_{cm} & g_{cn} \\ g_{cd} & \omega_d - i\gamma_d/2 & g_{dm} & g_{dn} \\ g_{cm} & g_{dm} & \omega_m - i\gamma_m/2 & g_{mn} \\ g_{cn} & g_{dn} & g_{mn} & \omega_n - i\gamma_n/2 \end{pmatrix}. \quad (4.11)$$

The same procedure previously used yields the curve of Fig. 4.23. The plot

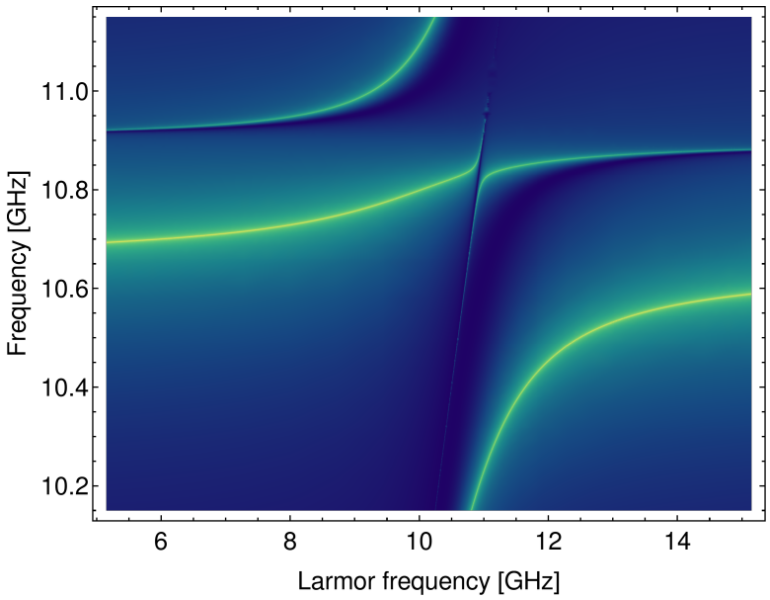


Figure 4.23: Simulation of the anticrossing with two cavity modes coupled to the Kittel mode and one magnon mode which senses an effective field slightly different from the Kittel. See text for further details.

is obtained by tuning the parameters such that they reproduce the experimental curve and it is closely similar to the experimental one. This, together with the previous simulation and experimental results, allows to maintain that the HS under study is correctly represented by this *cdmn*-model.

Remarkably, the lower frequency resonance is almost unaffected by the behavior of the rest of the HS, in the sense that its frequency does not change dramatically, thus it can possibly be safely used for a measurement. In fact, by looking just at the lower hybrid mode, one would notice almost no difference with a normal anticrossing curve. Intuitively this can be expected by thinking that the TM110 mode is a low order mode, at lower frequencies (more than 1 GHz) only the TM010 is present and coupled to antennas and material. However higher order modes, for example TM11$z$, are closer in frequency and become denser the higher the order. In this sense the higher-frequency hybrid mode is not a good choice for the operation of an haloscope, since it could interfere with a number of modes to which the lower-frequency one is immune. This is almost negligible for small couplings, like in the previous prototypes, but starts to be important when it becomes larger, like

in the present case. Relying on this consideration, the measurements of the axion field are done in the frequency range of this lower-frequency mode.

Now that the HS is characterized at room temperature, the same results must be obtained in the delfridge. The setup must ensure a proper ther-

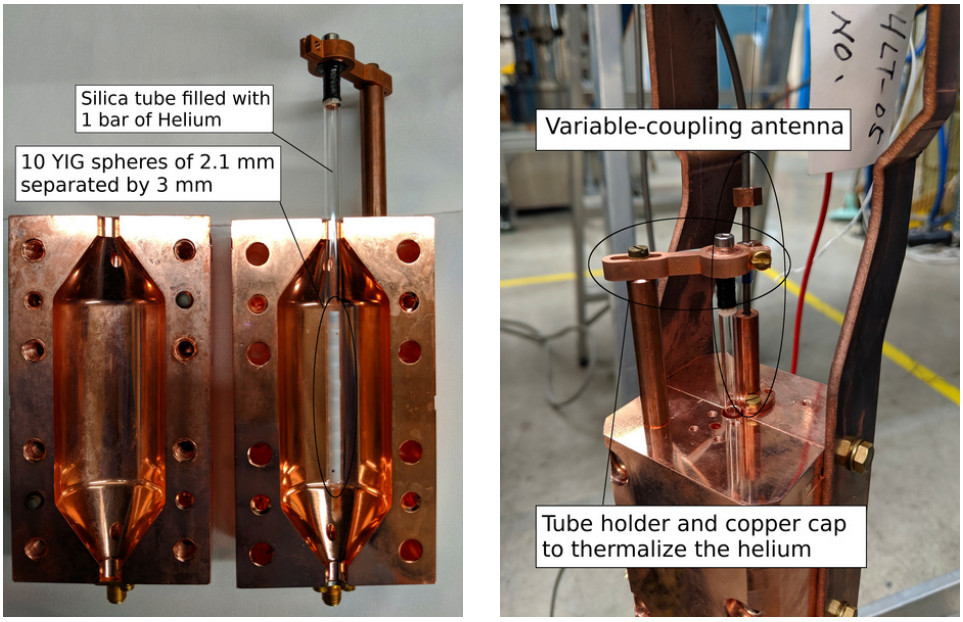


Figure 4.24: *Left* - picture of the pipe with the ten YIG spheres inside and its position inside the resonant cavity. *Right* - support of the pipe and moving antenna with tunable coupling.

malization of the cavity and of the YIG spheres, and it is implemented as shown in Fig. 4.24. The preparation of the fused silica pipe is as follows. A vacuum system (reported in Fig. 4.25) is designed in such a way to empty the pipe from air which is then immersed in a 1 bar helium controlled atmosphere and sealed. This way the pipe is filled with helium, and can be sealed by using a copper plug and Stycast (see Fig. 4.24). First the sealing is tested without the samples by measuring the shift of the TM110 mode of the cavity-pipe system with and without helium. The frequency is measured with the helium-filled pipe, which is then immersed in liquid nitrogen and again placed in the cavity. Re-measuring the same frequency excludes the presence of leaks.

The whole system, constituted by the cavity and the pipe with ten YIG spheres shown in Fig. 4.24 is now ready to be tested at milli-Kelvin temper-

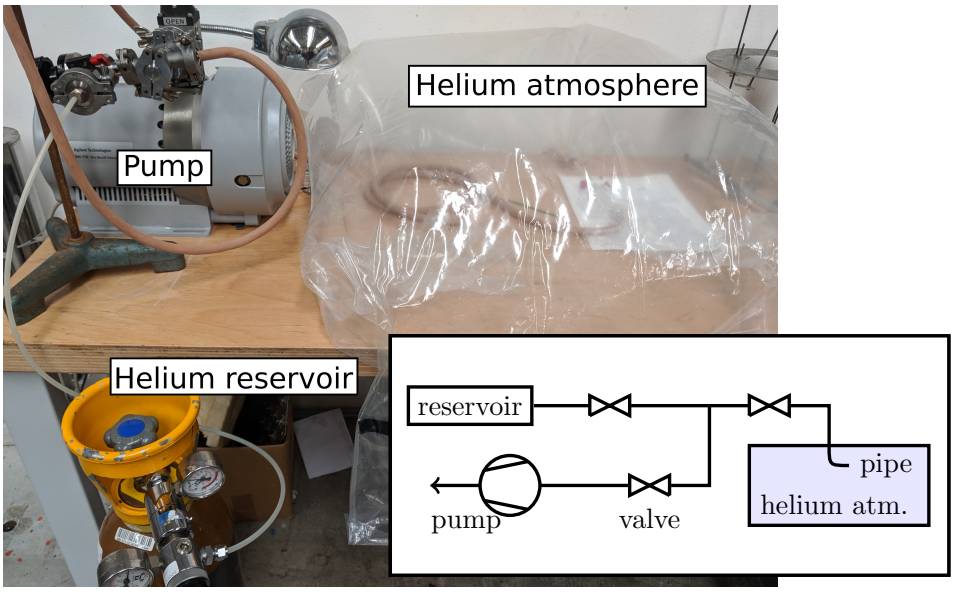


Figure 4.25: Vacuum system used to produce the helium-filled pipe.

atures. The system is cooled down with the procedure described in Sec. 4.3 and the anticrossing curve is measured and reported in Fig. 4.26. Even if more noisy, the plot is not qualitatively different from the room temperature one (Fig. 4.22). Apart from some frequency shifts due to the lower temperature the HS can thus be described with the model aforementioned, preserving the consistency of the measurement. An hint of consistency relies on the value of $g_{cm}$, which is extracted from a fit of the lower hybrid mode resonance frequency on the measured data (reported in Fig. 4.26 with a dashed line). The hybridization results 638 MHz which is compatible with the single 1 mm sphere since $638\,\mathrm{MHz}/\sqrt{8\times 10} = 71\,\mathrm{MHz}$ (see Fig. 4.8). Since the single spin coupling of this cavity is not much different from the one of the 14 GHz cavity (see Sec. 4.2.1), this results indicates that the measured spin density of YIG is consistent both with the previous results and with the values reported in the literature.

The points on the dashed line of Fig. 4.26, where the two oscillators model holds, are in principle suitable for haloscope measurements. This operation range is limited by the bandwidth of the JPC, which will be treated in Sec. 4.3.2, and by the axion deposited power range calculated in Eq. 3.16. For this setup its normalized value $t_{ac}$ is reported in Fig. 4.27 together with the planned frequency range of operation. The overlapping

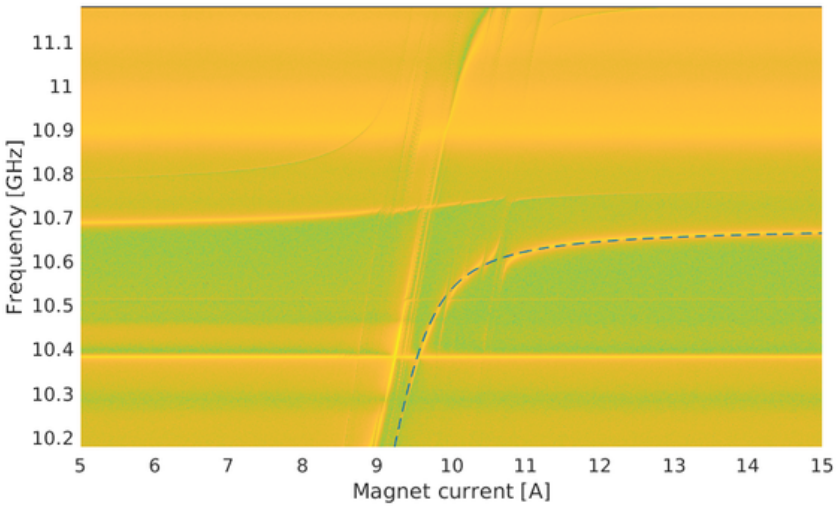


Figure 4.26: Anticrossing curve of the HS at ultra cryogenic temperatures. The result is analogue to the one of Fig. 4.22, and can be consistently described with the model of Fig. 4.23. The dashed line is a fit of the lower hybrid mode resonance frequency.

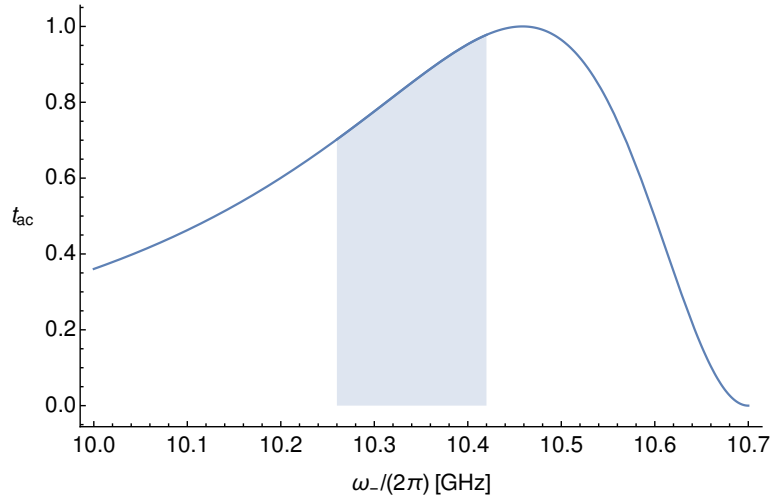


Figure 4.27: Bandwidth of the considered setup, with ten YIG spheres and the copper cavity, as is obtained with Eq. 3.16. The evidenced frequency range is roughly the one covered by the operation of this prototype.

regions between the JPC frequencies and the clean hybrid resonance curves are selected for the measurement. The tuning is made extremely easy by the fact that it is controlled only by means of the external magnetic field, as is shown in Fig. 4.28. A high stability of $B_0$ is necessary to perform long

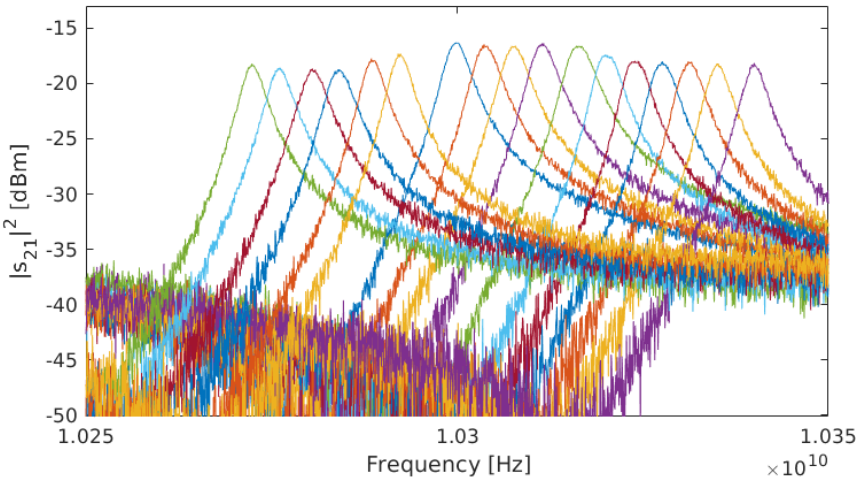


Figure 4.28: Left hybrid resonance tuned by means of the external magnetic field. This frequency range is obtained with a field variation of about 10 mT.

measurements over a single frequency band. This is set by the linewidth of the hybrid mode, which in this case is 2 MHz, and is tuned to cover a range close to 100 MHz. Thanks to the anticrossing curve it is easy to identify the frequency of the correct mode to study. As can be seen in Fig. 4.28 the hybrid mode is not affected by disturbances caused by other modes in a range that largely exceeds ten times its linewidth. These clean frequencies are selected for the measurements whenever it is possible to match them with the working frequencies of the JPC.

### 4.3.2 Operation of the Josephson Parametric Converter

This section characterizes the rf chain used for the measurements, which is based on the JPC described and tested in Sec. 3.3.2. The configuration of the electronics is in Fig. 4.17, and allows the testing of the JPC and the HS. Transmission measurements of the HS can be performed by turning off the JPC (i.e. no bias field and no pump) to reflect the signal on it, the input is the SO line and the output is the readout line. The JPC can be tested

with the help of the Aux line, by uncoupling the antenna from the cavity and reflecting the incoming signal. Some rf is still absorbed at the cavity modes frequency but this does not compromise the measurement. The phase-current characteristics described in Sec. 3.3.2 is collected in working conditions and shown in Fig. 4.29. The external static field does not affect

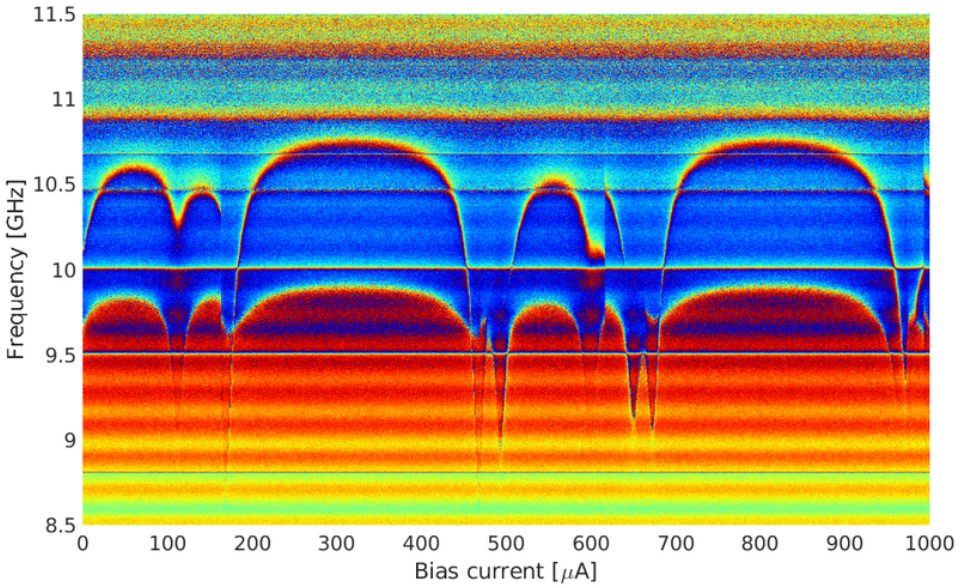


Figure 4.29: Phase-current characteristic of the JPC in the ferromagnetic haloscope configuration. The data are collected with the magnetic field on, and no difference is present between the zero-field characteristics. Horizontal lines are due to the cavity modes.

the resonances of the Josephson ring modulator as no difference has been detected between the measurements with and without field. Runs are performed on both the long lobes, with bias currents $I_b \simeq 170\,\mu$A and $460\,\mu$A at frequencies ranging from 10.26 GHz to 10.42 GHz.

Using the SO line and critically coupling the antenna to the hybrid mode, a signal is injected in the system and read with the whole amplification chain. The first test is to verify the linearity of the JPC (and of the whole chain) using signals of growing intensity until the system saturates. These measurements are reported in Fig. 4.30 and show the linear (left) and saturate (right) behavior of the amplifier. It is possible to calibrate the gain of the JPC by using a signal large enough to be measured with the JPC off but also not to saturate it once it is turned on. This is useful to know

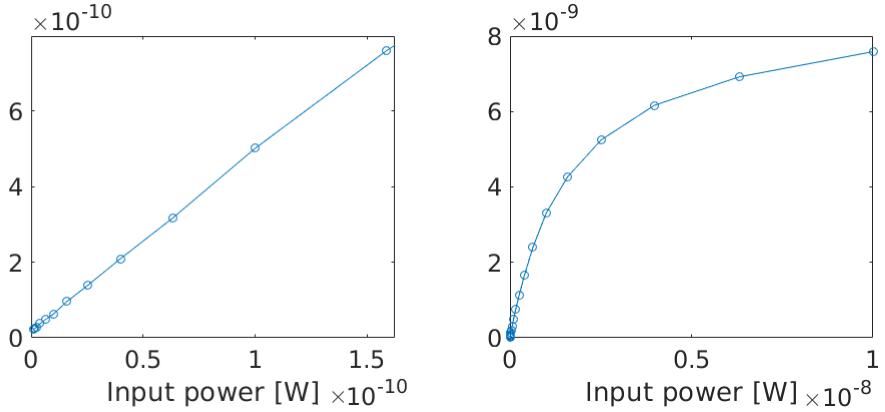


Figure 4.30: Tests of the linearity and of the saturation of the JPC performed with a signal injected by the SO channel.

the gain of the amplifier at the different working points to have a preliminary calibration of the system and to understand whether an output noise with higher amplitude is due to the JPC or to something else. Since the electronics above the 4 K line was already characterized for the previous prototype, the baseline noise with JPC off is roughly the same of Sec. 4.2, and consists in the amplifier noise temperature $T_n^{(\mathrm{hemt})} \simeq 10\,\mathrm{K}$. The measured noise spectra with the JPC turned off is white in a bandwidth of several hundreds of MHz, when the parametric amplifier is turned on its resonance exceeds this noise of roughly 10 dB. Since it is possible to calibrate the gain of the JPC $G_{\mathrm{JPC}} \simeq 20\,\mathrm{dB}$, the amplified noise level can be extracted as $T_n^{(\mathrm{JPC})} = T_n^{(\mathrm{hemt})}/10^{(G_{\mathrm{JPC}}-10\,\mathrm{dB})/10} \simeq 1\,\mathrm{K}$, which is the noise temperature amplified by the JPC. The value of 1 K is reasonable, since a single quantum at this frequency is 0.5 K such noise corresponds to two quanta. Even if this procedure is somewhat correct, it is not a proper calibration of the setup and something better can be done.

Since some problems were encountered in the noise calibration with hot load, the rf setup of Fig. 4.17 is designed to calibrate all the different lines with the help of the variable antenna coupling. By moving the antenna one can arbitrarily choose the coupling to a mode, if it is weakly coupled a signal from the Aux port gets reflected and goes to the JPC. If the antenna is critically coupled to the mode, a signal from SO is transmitted through the cavity and than to the JPC. The critical coupling can be reached by doubling the linewidth of the mode or equivalently by minimizing the reflected signal from the Aux line to the Readout line. The procedure to calibrate all the

lines is:

1. with the weakly coupled antenna or by detuning the mode the losses of the Aux-Readout line $L_{\mathrm{AR}}$ are measured;

2. the antenna is critically coupled to the mode and a signal is sent through the Aux-SO line to get $L_{\mathrm{AS}}$;

3. with the same critical coupling the transmission of the SO-Readot line $L_{\mathrm{SR}}$ is acquired.

At this point a signal of power $A_{\mathrm{in}}$ is injected in the SO line, the fraction of this power getting into the cavity through the weakly coupled antenna is $A_{\mathrm{cal}} = A_{\mathrm{in}} L_{\mathrm{SO}}$. The attenuation of the line can be calculated as $L_{\mathrm{SO}} \simeq \sqrt{L_{\mathrm{SR}} L_{\mathrm{AS}} / L_{\mathrm{AR}}}$, which gives the power collected by the critically coupled antenna. Since $A_{\mathrm{cal}}$ is effectively a calibrated signal, it can be used to measure gain and noise temperature of the Readout line. Different $A_{\mathrm{in}}$ are used to get increasingly large signals to be detected by the JPC-based chain. This measurement results in the plot of Fig. 4.17. This calibration has some minor biases, the first is given by the cable from the cavity to the first circulator which is accounted for two times in the Aux-Readout line. This contribution can be safely neglected as the cable is superconducting, making its losses negligible. Another bias is related by the antenna coupling, which is not perfect. With a proper antenna coupling the reflected signal is reduced of $\sim 10\,\mathrm{dB}$, so there is a bias of a factor 10% intrinsic to the measurement which will be accounted for when calculating the error. As the calibration procedure is long it is not repeated for every run, however no important differences are expected when changing the JPC frequency. As an example a run at 10.409 GHz is considered. The gain of the JPC at this frequency results $G_{\mathrm{JPC}} \simeq 18\,\mathrm{dB}$, and its bandwidth is 8 MHz, the hybrid mode is tuned the its central frequency and the calibration procedure is carried out,resulting in Fig. 4.31. The noise temperature results in $T_n = 1.0\,\mathrm{K}$ and the total gain is $G_{\mathrm{tot}} \simeq 120.4\,\mathrm{dB}$. The value of $T_n$ is compatible with the one estimated previously, and corresponds to two quanta. The total gain is in good agreement with the one of Sec. 4.2 with the added gain of the JPC, even if the different working frequency makes this check not really reliable.

The coupling of the antenna with the hybrid mode is checked for every run. It is controlled by moving the dipole antenna in and out the cavity volume, the critical coupling is reached when the uncoupled linewidth of the mode is doubled. To verify the proper antenna positioning one may rely on

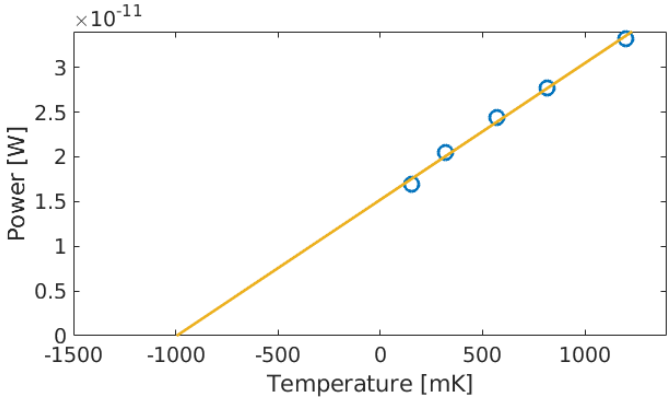


Figure 4.31: Calibration curve of the JPC. The resulting parameters are $T_n \simeq 1.0\,\mathrm{K}$ and $G_{\mathrm{tot}} \simeq 120\,\mathrm{dB}$, which are compatible with the noise temperature estimated in this Section and with the gain of Sec. 4.2.

the fact that depending on the temperature difference between the cavity and a $50\,\Omega$, some power may be absorbed or added to the load thermal noise. This is discussed in Sec. 3.3.2 and in particular in Fig. 3.23, as can be seen the temperature difference is small and so is the power difference. The load under consideration is the hottest between the first JPC isolator and the 20 dB attenuator of the Aux line. The hybrid resonance has a critical linewidth of about 2 MHz, so the depth will not be as narrow as the one of the cavity. In that case the temperature difference is about 10%, which is about 10 mK, and if the temperature of the load and cavity are precisely measured the spectra can be used to get a two-points calibration. The selected calibration procedure was not this one because the temperatures of loads and HS are not easily accessible. With two dedicated thermometers the temperatures of the loads could be measured, but it is not trivial to measure the temperature of the cavity and of the spheres with the needed precision. Since a small temperature difference is expected, the measurement with the antenna coupled to the hybrid mode should be different from the uncoupled one. As reported in Fig. 4.32, there is a difference between the two measurements and it is compatible with the thermal noise of the hybrid mode at a temperature slightly higher then the loads one. The reported measurement is analogue to the one reported in Fig. 4.13 but more noisy. This is due to the fact that the A1 amplifier has a high gain, and thus the added noise of A2 is negligible. This is somewhat true also for the JPC with respect to the noise of A1, but since the parametric amplifier gain is

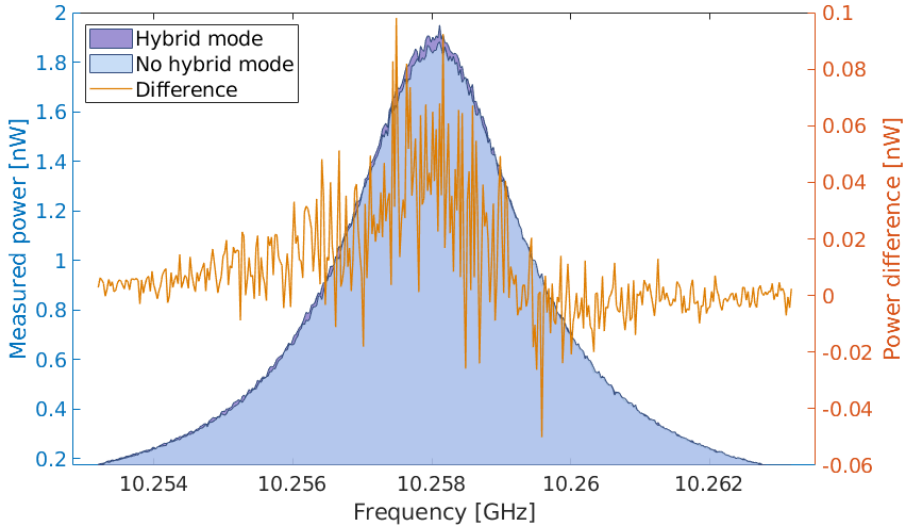


Figure 4.32: Evidence of the HS-added thermal noise over the resonance curve of the JPC.

lower, A1 noise is more important and more integration time is necessary to measure the HS thermal noise. For this reason the measurement is done in a frequency band where the JPC gain is higher (and thus its bandwidth narrower), in order to use a shorter integration time.

### 4.3.3 Data acquisition and analysis

The 2019 QUAX scientific run consists in several measurements in all the common bands between the frequencies of the lower hybrid mode unaffected by disturbances, and the JPC working range. It includes a main large band between 10.26 and 10.37 GHz and a narrower band with overlapping runs around 10.4 GHz. A plot of all the frequencies covered in the different runs is in Fig. 4.33. Before every run a transmission measurement of the hybrid system is used to set the frequency of the left hybrid mode and check the antenna coupling and mode linewidth. A spectrum of the resonance is collected when the measurement run starts, the tuning is shown in Fig. 4.28. At the end of the run another transmission measurement verifies that the conditions did not change. The thermal noise of the system is almost entirely sent to the JPC since all the cables in between are SC. The signal is amplified of $\sim 20$ dB when reflected by the JPC and passes through two

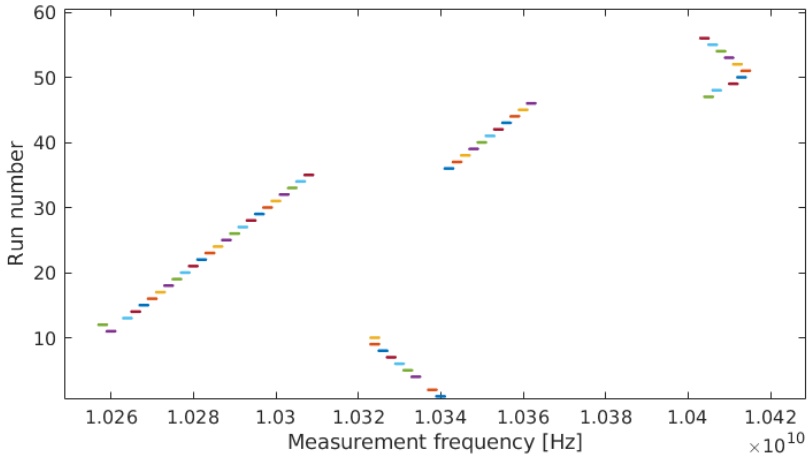


Figure 4.33: Plot of the frequencies bands covered by the different runs.

isolators. Then it passes to the 4 K part of the apparatus where it is further amplified of about 35 dB by A1, which also adds a non-negligible fraction of noise. A further amplification happens at room temperature by the amplifier A2 (with gain $\sim$ 35 dB) and its output goes to the mixer. The LO frequency is set to the central value of the resonance $f_{\mathrm{LO}} = f_h$ and fixes the central frequency of the low-frequency spectrum. Its amplitude is 12 dBm, the down-converted spectrum is further amplified of 50 dB by $A_I$ and $\mathrm{A}_Q$ and acquired by the ADC. The total gain of the amplification chain, as reported in Fig. 4.31, is 120 dB and is compatible with the calculated gain of the amplifier and a realistic estimation of the cables and circulators losses close to 10 dB. The low-frequency chain is the same of the apparatus in Sec. 4.2, the ADC acquires at 2 MHz and a file is saved roughly every 5 s both for the in-phase and in-quadrature components. From each file a subset of data is extracted to monitor each file by producing an FFT, and some online checks include a threshold monitor of the average amplitude, as well as of the peak amplitude, which flags the file if some unexpected large signal is present. Every run includes a header file which saves the frequency of the LO, the average cavity temperature and the length of the measurement.

As is done in the previous prototype, the stability of the measurement is tested by injecting a signal with a large SNR and monitoring its amplitude. Previously the stability was limited by the magnet current generator and by temperature fluctuations (see Fig. 4.10). In this setup it results below the percent level, which is more than enough for its purpose, thanks to

the lower and more stable working temperature and to an extremely stable current generator produced in the Padua University electronic workshop. The signal to analyze is obtained by adding the phase component to the quadrature one, multiplied by the imaginary unit. Its FFT produces a spectrum whose negative (positive) frequencies are below (above) $f_{\mathrm{LO}}$, for a total bandwidth of 2 MHz which contains the whole hybrid linewidth. Some bins are found to be affected by disturbances resulting in systematic noise, but they can be easily removed by analyzing the data with longer FFT. Using 32768 points the single frequency resolution is 61 Hz $\ll \gamma_a$ and thus single bins which do not respect the fluctuation dissipation theorem can be substituted with the average of the ten nearest neighbors. This procedure artificially reduces the variance of the data, but the number of corrupted bins is negligible and so is the effect on the variance. This process does not cut the signal since it affects only known or single bins, while the axion signal is expected to be distributed over many.

For debugging purposes a simulated signal is injected into the analysis code. It is created by generating a high-frequency noise to which are added a simulated axion signal and some disturbances. For creating the in-phase and in-quadrature component it is multiplied by a sine or to a cosine wave, to then extract only one point every $10^4$ and simulate the mixing and down-conversion processes. The FFT of this signal produces a white noise with some peaks (the axion signal plus disturbances), and is eventually integrated. The analysis procedure is verified to remove bad bins and to preserve the signal and SNR.

Thanks to the stability and to the tests on the acquisition and analysis, all the files of a single run can be safely RMS averaged together. The calibration gives a noise temperature $T_n = 1.0\,\mathrm{K}$, which includes all the amplifier noises, the cavity thermodynamic noise, and the losses. This can be used to calibrate the setup by setting the mean value of the FFT to $k_B T_n \Delta f$. As for the calibration errors, the fluctuations of the cavity temperature are of order 10 mK, thus they can change $T_n$ of a fraction close to 1%. A larger contribution is intrinsic to the procedure, which requires the coupling of the antenna to be changed from weak to critical. This is believed to be the larger contribution to the uncertainty of the measurement, and even if in principle this is not a fluctuation it will be used to estimate an error. The fact that the coupling is close to critical is also supported by the thermal noise measurement of Fig. 4.32. The control over this parameter can be estimated by injecting a signal through the Aux port in the weak-coupling position, and then by reducing the reflected amplitude by increasing the coupling. Typically the signal power can be decreased of more than 8 dB,

this value can be used to estimate the larger uncertainty on the coupling resulting in a 16% error.

To estimate the sensitivity to the axion field the resolution bandwidth is set to 5 kHz, which at this frequency is the value producing the best SNR. The spectrum is fitted with a degree five polynomial to extract the residuals, whose standard deviation is the sensitivity of the apparatus in terms of power. It is reported in Fig. 4.34 for every run and, by using the run length, it is compared with the estimated sensitivity obtained with Dicke equation, Eq. 4.4. The measured fluctuations are close to the expectations

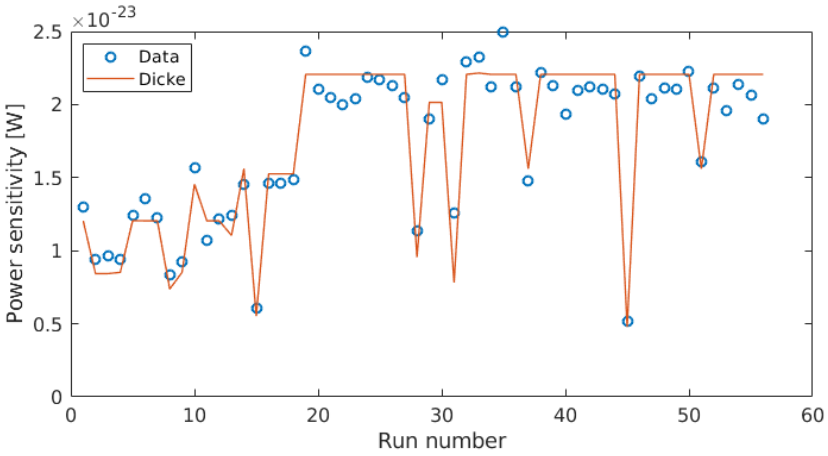


Figure 4.34: Comparison between the expected power sensitivity obtained with Eq. 4.4 and the measured value.

for almost every run, and are always compatible when considering the 16% error which was previously calculated. This shows that the measured power is compatible thermal noise and that the integration is effective over the whole measurement time, since it follows the $1/\sqrt{T_{\text{int}}}$ trend. The best sensitivity reached is $\sigma_P^{(3)} = 5.1 \times 10^{-24}\,\text{W}$ for an integration time of 9.3 h, corresponding to an excess rate $\lesssim 10$ photons/s per bin.

### 4.3.4 Final results

As is discussed in Chapter 2 this setup is a spin-magnetometer, as it is sensitive to variations of the sample magnetization. In this sense, it is interesting to determine the performances of this setup to get some physical intuition on its sensitivity and thus on all the possible phenomena that could be measured. The field sensitivity can be estimated for a field whose coherence

length stretches on all the YIG spheres, and whose linewidth is narrower than the HS one. In the case of the present apparatus the threshold coherence length and time are then 10 cm and 100 ns, respectively. It follows from Eq. 4.1 that

$$\begin{aligned}\sigma_B^{(3)} &= \left(\frac{\sigma_P^{(3)}}{4\pi\gamma_e\mu_B f_-\tau_- n_S V_s}\right)^{1/2} \\ &= 5.5\times10^{-19}\left[\left(\frac{10.4\,\text{GHz}}{f_-}\right)\left(\frac{83\,\text{ns}}{\tau_-}\right)\left(\frac{1.0\times10^{21}\,\text{spins}}{n_S V_s}\right)\right]^{1/2}\text{T},\end{aligned} \tag{4.12}$$

is the minimum effective magnetic field detectable by the spin magnetometer for a unitary SNR. A 0.5 aT sensitivity is remarkable by itself, and shows the high potential of HS-based magnetometers.

The results of the previous section are used to extract a limit on the axion-electron coupling, which is a possible effect that modulates the sample magnetization and produces an excess of photons. Such a field satisfies the conditions previously described and thus can be efficiently tested with the present prototype. The expected power deposited by DM-axions in the HS is increased by a factor five with respect to the previous prototype, see Eq. 4.7, and results

$$P_{\text{out}}^{(3)} = 7\times10^{-33}\left(\frac{m_a}{43\,\mu\text{eV}}\right)^3\left(\frac{n_S V_s}{1.0\times10^{21}\,\text{spins}}\right)\left(\frac{\tau_h}{83\,\text{ns}}\right)\text{W}. \tag{4.13}$$

This is mainly due to the lower working frequency and marginally to the shorter coherence time. The 10.4 GHz photon rate corresponding to this power is $r_a^{(3)} = 10^{-9}$ Hz. By comparing the rate $r_a^{(3)}$ with $\sigma_P^{(3)}/(\hbar\omega_-)$ one obtains that there are ten orders of magnitude to get the sensitivity required to detect the axion, which corresponds to five in terms of field (and thus of coupling constant). As discussed in Chapter 1, even if an instrument is not capable of limiting the QCD-axion parameter space it can still probe the presence of ALPs. These can also constitute the totality of DM and their mass and coupling are unrelated. The present measurements are used to extract a limit on the coupling of ALPs with electrons. No evidence of a signal due to axions has been detected, and the measured spectra are compatible with noise. The $2\sigma$ (95% C. L.) upper limit on the coupling reads

$$g_{aee} > \frac{e}{\pi m_a v_a}\sqrt{\frac{2t_{ac}\times\sigma_P^{(3)}}{2\mu_B\gamma\, n_a n_S V_s\tau_-}}, \tag{4.14}$$

where $t_{ac}$ is a frequency dependent coefficient that takes into account that the axion-deposited power is not uniform in the haloscope operation range,

as is shown in Fig. 4.27. All the experimental parameters used to extract the limits are measured within every run, making the measurement highly self-consistent. The limit on the ALP-electron coupling described by Eq. 4.14 is calculated for every run using the corresponding measured parameters and results in Fig. 4.35. The analysis is repeated by shifting the bins of half

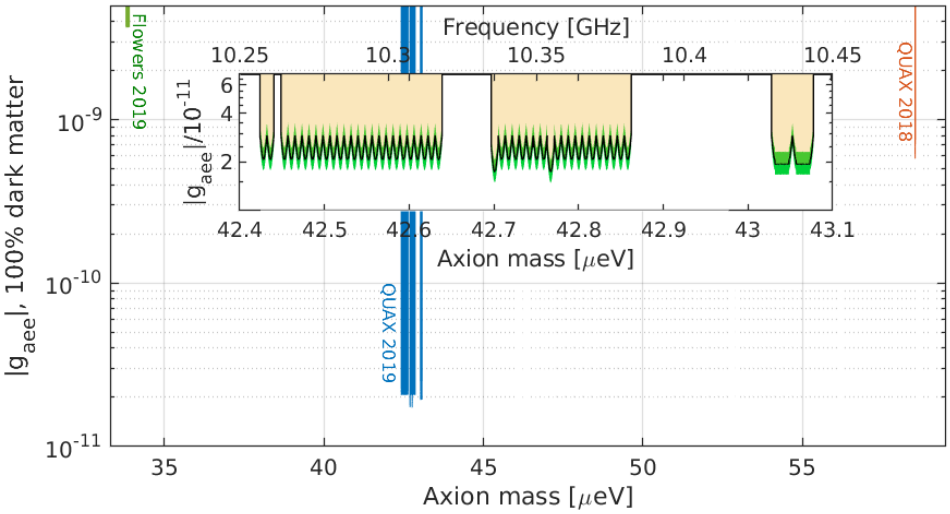


Figure 4.35: Plot of the upper limit produced by the 2019 QUAX scientific run, reported in blue in the main plot. The measured exclusion band is more detailed in the inset, where a green-shaded region shown also shows its error. The limits of the previous QUAX prototype [222] and of [137] are also reported for comparison.

the RBW to exclude the possibility of a signal divided into two bins. The best limit obtained, and corresponding to $\sigma_P^{(3)}$, is $g_{aee} < 1.7 \times 10^{-11}$. The improvement of a longer integration time is not much, since the limit on the coupling scales as $T_{\rm int}^{-1/4}$. To improve the current best limit of a factor 2 the needed integration time is six days.

Fig. 4.35 is also an overview of the present status of spin-based DM-axion searches in the classical QCD window. This last prototype is the one which gave the best results up to now. Except the QUAX prototypes, only another instrument was built to test the same interaction and it is described in Ref. [137]. Here it is not treated because there is no improvement with respect to the schemes described in this thesis. The use of a two-post reentrant cavity [241] increases the single-spin coupling of Eq. 3.1 and thus $g_{cm}$, this improves the tuning range of the haloscope but not the signal. However

the quality factor is roughly ten times worst than the one of cylindrical cavities and compromises the linewidth of the hybrid modes decreasing the sensitivity of the haloscope. In [137] the calculated bandwidth[2] is about 1 GHz but the tested one is ∼35 MHz around a fixed frequency. This feature is thus not exploited and the relative tuning results comparable to the one performed in the QUAX prototype of Sec. 4.2, since it is mainly due to the large hybrid linewidth.

The power sensitivity of this prototype is limited by quantum fluctuations, thus in this sense no linear amplifier is or will be able to improve the haloscope. In future setups only bolometers or quantum counters can yield better results, as is discussed in the next Chapter. Thermodynamic fluctuations are already negligible due to the extremely low working temperature, so it is not necessary to decrease them by orders of magnitude. As the rate of thermal photons of a cavity mode is exponentially decreasing with temperature, the present dilution refrigeration technology is enough to reach the axion-required noise level. As discussed in Chapter 2, to get a rate of axion-induced photons which can be measured in a reasonable amount of time, a much increased quantity of material and a narrower linewidth are required. This setup features 0.05 cc of YIG, such volume must be increased by orders of magnitude to get the required rate. This is also discussed in the next Chapter, and can be achieved by increasing the quantity of material in a single cavity and the number of cavities. The upgrades planned in Sec. 4.2 are implemented and result effective, as the apparatus behaves as expected. No showstoppers were identified so far.

[2]The plots in the reference show a tuning range calculated as a function of the magnetic field, while it should be calculated as a function of the hybrid mode frequency (these two are the projections on the axes of Fig. 3.9).

# Chapter 5

# Further developments

The successful operation of the ultra cryogenic quantum-limited prototype is an important achievement in the development of spin-based axion searches. It demonstrates the possibility of scaling up the setup of orders of magnitude without compromising its sensitivity. Other experiments operated quantum limited setups at high frequencies to search for axion-DM through the Primakoff effect [125, 126, 242–244], the QUAX apparatus reaches similar power sensitivities but is less sensitive to the axion field. This is because the effective interaction volume is not the whole cavity volume but the one of the sample, and because the axion-electron interaction is weaker than the axion-photon one. In this sense the ferromagnetic haloscope is in disadvantage with respect to regular haloscopes. However, there are some peculiarities which make the ferromagnetic haloscope competitive and worth studying, including but not limited to the easy tunability, the possibility to distinguish between different axion models, and its versatility as a detector (discussed in Appendix A).

This Chapter discusses what are the efforts needed to improve the apparatus to get the DFSZ axion sensitivity. As explained throughout the thesis, this can be done in two complementary ways, that are noise reduction and signal improvement. The first one is treated in Sec. 5.2, since no improvement can be obtained with amplifiers and thus quantum counters or bolometers must be exploited. In the same Section a possible design of a mw single photon counter (mw-SPC) is discussed and preliminary results and tests are presented. As for the second one, it is necessary to work on the hybrid system linewidth and number of spins to increase the coherent superposition with the axion field and the interaction probability. These features are discussed in Sec. 5.1, where are also presented some preliminary

evidence that show the different development possibilities.

## 5.1 Maximizing the axion-deposited power

To further increase the axionic signal there are two parameters to work on: the hybrid mode linewidth and the sample spin-density and volume. A cavity with a high enough quality factor was already demonstrated and described in Sec. 3.1.1, but a material with a correspondingly narrow linewidth is not available up to now. Some materials are engineered and studied for their long coherence times. Remarkably, molecular spins have been coupled to microwave resonator to create hybrid quantum systems [194,195,245,246] as the ones of ferromagnetic haloscopes. The downside of such systems is the low spin-density of these samples, with which it is difficult to reach the strong coupling regime with the mw resonator. Among the one tested, the LiFe is the one which has the higher spin density that doubles the one of YIG. The linewidth is nevertheless not as narrow as the YIG one, as is discussed in Sec. 3.1.2. Several ferromagnets and paramagnets have been tested, but eventually the one with the best compromise between spin-density and linewidth is found to be the YIG. There are some evidences in the literature for a narrow YIG linewidth, of the order of 1 MHz [190], also at mK temperatures. In the ultra cryogenic prototype the measured linewidth is of order 2 MHz so some improvement is possible. By baking the spheres it could be possible to further reduce the linewidth to get closer to the desired relaxation time of 1 $\mu$s [134]. These and other techniques related to the sphere production will be the subject of forthcoming R&D tests to develop the next stage of the QUAX experiment.

### 5.1.1 Increased material volume and number of cavities

Considering the spin density of YIG and assuming that a slightly longer relaxation time could be reached, the only parameter that remains to be increased is the material volume. To have a rate of axionic spin-flips which can be measured within a reasonable integration time the volume of the sample must be of order 100 cc. Since the material must be embedded in a resonant cavity there are two main ways to increase its volume, i. e. put more material in a single cavity and increase the number of cavities to be monitored. Both of them are expected to be employed in a 100 cc apparatus and are treated hereafter. The prototype of Sec. 4.2 has five 1 mm spheres, while to the one in Sec. 4.3 has 10 2 mm spheres, this scaling does not introduce extra noise or other unexpected effects on the system.

In principle it is thus possible to further scale up the HS in the same way. The number of spins in the last setup is $10^{21}$ while the needed one is around $10^{24}$, corresponding to $10^4$ 2 mm spheres. As reported in Sec. 4.3, to avoid the sphere-sphere interaction these have to be at a distance of 3 mm so that a single sphere occupies 5 mm of axial space. Preserving the same configuration of the present prototypes, a definitive experiment would need a 50 m long cavity to hold all the spheres. Such a large cavity dimension is difficult to handle, as is the solenoid to provide the static magnetic field. Moreover it is risky to use long cavities because the density of modes close to the TM110 increases with the length, therefore a multiple-cavities approach is foreseen [247]. Many cavities can be read out but a single amplifier by coupling their outgoing signals. With a proper design the use of multiple amplifiers should not increase the overall noise temperature of the system. Still, using simultaneously different amplifiers is a challenging task and it becomes For the sake of the discussion the maximum cavity length is fixed to 1 m, thus fifty of these cavities are needed to reach the 100 cc. These numbers suggest that the volume of material inside a single cavity must be increased, there are different ways to do this as shown for example in Fig. 5.1. A single rod can be placed on the axis of a cylindrical cavity

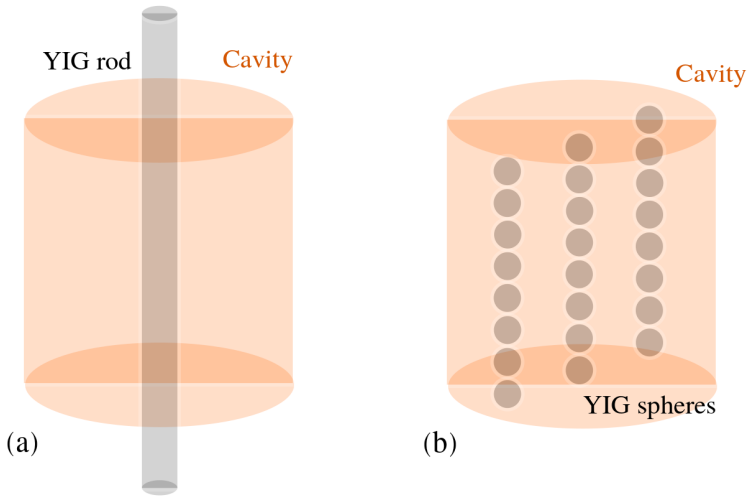


Figure 5.1: Possible ways to increase the volume of material inside a single cavity, (a) a YIG rod which preserves the cylindrical symmetry, and (b) multiple sphere arrays placed in different positions.

instead of multiple spheres, increasing the volume of material and preserving the symmetry. Geometric demagnetization should not affect the linewidth if

the rod is placed on a uniform axial field. It is simpler to build a long cavity with the embedded rod, and the orientation issue is solved by growing the crystal with the easy axis in the direction of the cylinder axis. However, long YIG rods are not commercially available and the crystal growth is rather complicated, making it easier to buy or produce spheres. In the discussed setups the spheres are placed on the axis of the cavity to be on the maximum of the rf magnetic field and at the center of the solenoid. Both these fields are uniform over the sample volume. There are preliminary indications that even if the sample is not placed on a maximum of the rf field, the axionic signal is still transduced through the setup. The setup described in Sec. 3.2.2 is used to test this feature, but no definitive results are available. Until the coupling $g_{cm}$ of a single sphere is larger than the linewidth, it is more likely for a magnon to be converted into a photon. The signal is compromised when the magnon is dissipated in the material, its lifetime is about $1/\gamma_m \simeq 100\,\text{ns}$, but if it is converted to a photon before that the photon can be collected by the antenna. The conversion rate is $g_{cm}$, so if $1/g_{cm} \gg 1/\gamma_m$ the signal is preserved. A large number of spheres could be placed in the cavity in regions other than its axis, allowing a major volume increment. A smaller number of cavities could be more easily implemented in a definitive setup with, say, ten 1 m long cavities.

Some evidences show that the behavior of the HS system with a larger sphere is somehow different than the expected one, as is reported in Fig. 5.2. In fact, measurements of the anticrossing curve at 14 GHz with spheres larger

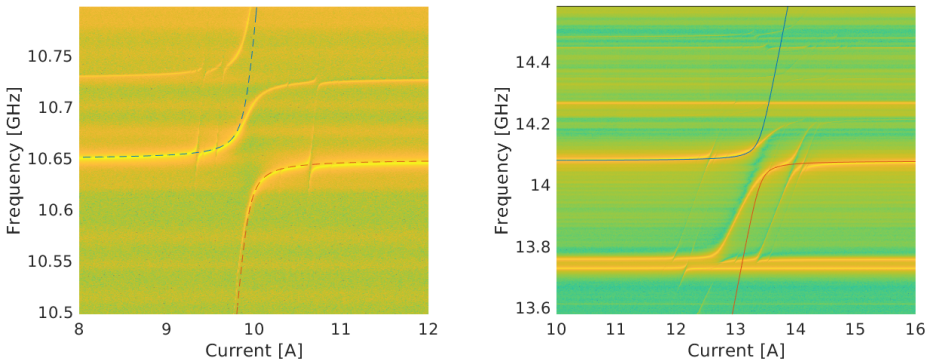


Figure 5.2: *Left* - Anticrossing curve for a single 2.1 mm sphere at 10.7 GHz. *Right* - Anticrossing curve of the same sphere but at 14 GHz. The solid lines represent the expected curve.

than 2 mm exhibit a $B_0$ vs. frequency slope of the Kittel mode which is

different from the Larmor frequency. Even though it is not clear how to interpret the observation, it shows that there is a limit on the dimension of the magnetic sample. The need of a small sample compared to the cavity volume is mentioned in Sec. 2.2.1, and possibly the approximations used are not valid for the 2 mm sphere at 14 GHz. This is not necessarily compromising the signal, but a theoretical understanding of the phenomenon is needed to model the system.

## 5.2 Overcoming the standard quantum limit

The development of a novel microwave detector whose ultimate goal is to operate at the single-photon level is an important objective of different research fields, such as quantum information, meteorology or dark matter searches. It would be important in many applications, for example in quantum measurements and in real-time detection. The former is a key-point for the development of quantum information technologies, while the latter would be important to detect rare events that can be related for example to fundamental physics. However, due to their extremely low energy, the detection of single microwave photons is extremely challenging. To understand the photon-counting capability in the sub-THz range it is necessary to introduce a requirement for the device: the product of the detector's noise equivalent power (NEP) and its response time $\tau$ should not exceed the photon energy $\hbar\omega$. The NEP is the product of the NEP density $k_B T$ (in the thermal noise limited case) and the detector bandwidth $\Delta\omega$. The criterion can be written as

$$k_B T \Delta\omega\tau < \eta_q \hbar\omega, \tag{5.1}$$

where $\eta_q < 1$ is the quantum efficiency factor and takes into account the possibility of a missed photon detection. The detector should be able to count photons at least at the rate determined by its fundamental noise. Because of the frequency-time uncertainty principle applicable to the detection process, the product $\Delta\omega\tau$ cannot be less than $2\pi$, so the photon energy must exceed $k_B T$ in order for photon counting to be possible. In practice the detector's response time is much slower than its inverse bandwidth, forcing the temperature to be lowered down to the mK range to achieve THz and sub-THz photon counting. Practical detectors have a non-zero probability of recording false counts, known as dark counts, which arise either due to the materials properties of the detector, the biasing conditions or the susceptibility to external noise. The dark count rate (DCR) is of crucial importance for single-photon detectors since it acts as its background. An experiment

like a ferrimagnetic haloscope searches for very rare photons and needs to perform real-time measurements, i. e. constantly monitor for a long time period. The DCR needs to be lower for longer measurement times.

To improve the sensitivity of a setup like the one of Sec: 4.3 a SPC is not necessary. In principle, a bolometer with a large number $N_p$ of photons as threshold is better than a quantum-limited amplifier whenever $N_p$/DCR is smaller than the bandwidth of the amplifier $\Delta f$.

### 5.2.1 Microwave single photon counters

An early proposal for single photon detection rely on the interaction of Rydberg atoms with photons in a microwave cavity [248–252]. This interaction adds a photon-number dependent phase to the state, and eventually allows for the measurement of single photons. This technique was already exploited to search for axions by the CARRACK collaboration [253, 254], but is particularly difficult to implement in the considered haloscope scheme. Superconducting nanowires (SSPDs or SNSPDs) offers low dark counts, high efficiency and excellent timing resolution. Such devices are commercially available up to $\sim 1.5\,\mu$m spectral range [255], unfortunately they are hardly sensible to photons in the microwave domain (1 mm - 1 m). Rapid progress has been made in chip-based superconducting systems that allows repeated measurements that give the same eigenvalue (i. e. quantum non demolition). In this sense the detector is completely transparent to the photons and still acquires information about their number [256–260]. Considering for example the scheme of [257], a transmon qubit is coupled to a high-$Q$ storage cavity, whose photon number is to be measured, and to a measurement cavity, optimized for fast qubit readout. This device maps the number of photons onto the qubit state in a single-shot by means of qubit-photon logic gates. The problem associated with these devices is connected with their duty-cycle, since the ultimate goal is to achieve real-time measurements of a low single microwave photon rate. A destructive way to measure microwave photons consists in the use of a bolometer. An emerging highly promising photon-counting technology are single-photon detectors based on proximity Josephson junctions (JJ), which are capable to detect wave packet energy with high-quantum-efficiency in the framework of circuit quantum electrodynamics [261]. A bolometer with this sensitivity, 150 photons of 10 GHz frequency, is already improving the quantum-limited readout.

Remarkably, measurement of itinerant microwave photons has been demonstrated using biased-current JJ [262–264]. In these systems, an incoming photon can drive the transition from a ground state to an excited state,

which will then tunnel into a continuum of states, corresponding to a voltage pulse across the junction. A recent proposal of a mw SPC [265] consists of an underdamped JJ coupled to a coplanar waveguide. The mw radiation, absorbed by the JJ thanks to an adapted line, makes the junction switch from the SC (ground )state to the resistive one, producing the voltage pulse. The switching is not only triggered by the incoming radiation, but also by thermal activation and macroscopic quantum tunneling, which produce false photon counts. The expected axion-induced photon rate is extremely small, for a ferromagnetic haloscope with a large material volume is in the mHz range. To detect these photons the DCR of the SPC must be $\leq$ mHz. To minimize the DCR, the large aluminum JJ is biased with an external magnetic field, the reader is referred to [265] for more details. The promising results of the simulations motivated the experimental measurements. The first chips were fabricated in Chalmers University and tested at Nizhny Novgorod State Technical University. With a zero bias current the spontaneous rate of activation results of order 0.1 mHz. The increase of the current reduces the lifetime of the JJ, but also makes it sensitive to external radiation, as shown in Fig. 5.3. As can be seen, a low spontaneous switching rate can be

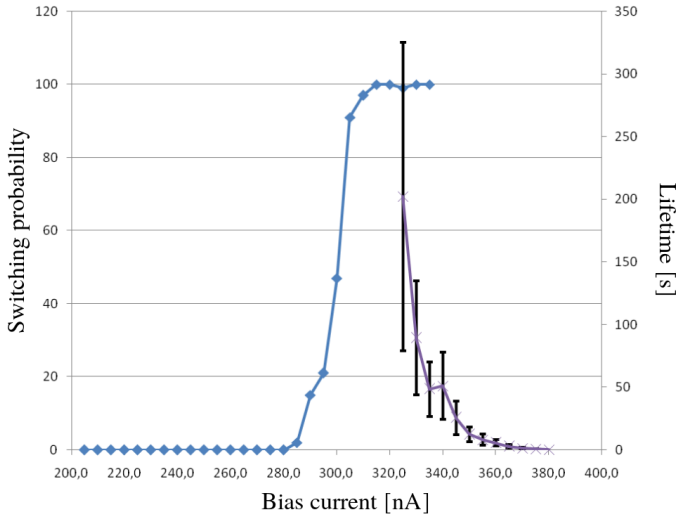


Figure 5.3: Preliminary tests on the Josephson junction. The switching, triggered with an out-of-frequency mw pulse, and the junction lifetime are measured for different bias currents. Credit goes to: Leonid Revin, Andrey Pankratov and Leonid Kuzmin.

obtained even with a bias current. In the reported measurements the JJ is

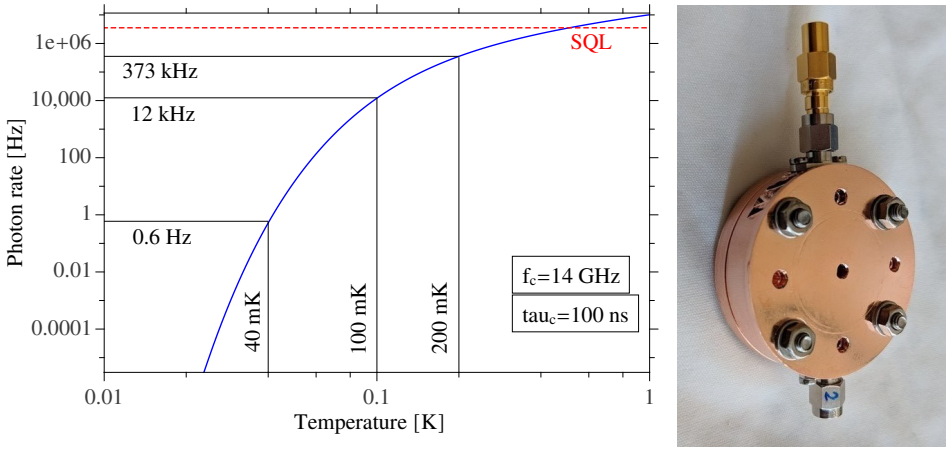


Figure 5.4: *Left* - Calculation of the photon rate produced by a resonant cavity with the parameters reported in figure. *Right* - Photo of the copper cavity to be used for the tests of the SPC.

not coupled to an adapted mw line (i. e. a coplanar waveguide). Simulations of the rf-matching are being performed and the first samples are expected to be fabricated soon. The tests of the SPC prototype are planned to be performed using the thermal noise of a resonant cavity mode as a photon source. The rate $r_n$ reported in Sec. 2.2.1, and derived from Eq. (2.30), is evaluated for the cavity which will be used for the SPC tests in Fig. 5.4. By varying the cavity temperature, $r_n$ changes exponentially, allowing the recording of the DCR at base temperature and of the thermal photons at higher temperatures. The maximum photon-rate that the JJ can detect is close to some kHz, limited by the dead time required to reduce and then increase the bias current to go back to the SC state.

An alternative to SPC is the counting spin-flips induced by axions [266]. This is achieved by coherently coupling a qubit to the magnetic material, to encode the qubit state into the magnon one. Remarkably, a single spin-flip is resolved in a sample with $N_S = 10^{19}$, and somewhat yields a limit on the axion-electron coupling.

## 5.3 Detecting the QCD axion

The development of a SPC would drastically accelerate DM-searches [183, 267]. For a ferromagnetic haloscope, the availability of these new technolo-

gies is the most plausible way to be competitive with standard haloscopes. Nevertheless, a setup with an increased material volume and employing a SPC would have the sensitivity necessary for a QCD-axion search.

Even if constrained by cosmology and astrophysics, the axion parameter-space remains wide for a resonantly-enhanced experiment. Setups like the one of ADMX, which already reached the QCD-axion line, benefit from a SPC since it would greatly increase the scan rate, as the integration time on each axion mass interval gets lower.

In the favored case of a signal detection, its nature can be systematically studied by a ferromagnetic haloscope. The axion signal is persistent, so it will be possible to infer DM properties by using the directionality of the apparatus. This setup is able to test different axion models, measuring separately the axion-photon and axion-electron couplings. In fact, the apparatus also embodies the features of a Sikivie haloscope [121], and can be sensitive to the axion-photon coupling by using a suitable cavity mode.

An experiment reporting the detection of a signal can have its claim confirmed within a short time since, knowing the axion mass, it would be simpler to get to the axion line with dedicated measurements. The discovery of an axionic signal by any mean, would allow multiple experimental groups to test the signal features in different ways, as the proposed detection techniques are several and various [117–119, 129–137].

# Chapter 6

# Conclusions

The scope of this work of thesis is to illustrate the construction and operation of the first ferromagnetic axion haloscope. Such instruments can be used to measure the DM-axion wind which blows on Earth, as this last one is moving through the halo of the Milky Way. The axions interact with the spin of electrons causing spin flips that are, macroscopically, oscillations of a sample magnetization. The models of the isothermal galactic halo and of the axion yield the features of the searched for signal, namely its linewidth, frequency and amplitude. A frequency of 10 GHz, a linewidth of 5 kHz and an amplitude of about $10^{-23}$ T are expected for axion masses of order 40 $\mu$eV. A proper haloscope has a transducer that converts the axion flux into rf power, followed by a sensitive detector to measure it.

For a ferromagnetic haloscope, the transducer consists of a magnetic material containing the electron spins with which the axions interact. In order to maximize the axion-deposited power, the sample should have a large spin density and a narrow linewidth. Several different materials were tested, and the most suitable one is found to be the YIG, a ferrimagnetic insulator that is shaped as a sphere to reduce geometric demagnetization. The axion-induced oscillation of the magnetization can not be collected in a free-field environment because of radiation damping, which broadens the sample linewidth. For this reason, the transducer does not consist in the sole magnetic material but in a photon-magnon (i. e. cavity-material) hybrid system. A mw cavity mode is coherently coupled to the sample's spins by means of a static magnetic field, which tunes the electron's Larmor frequency to the cavity mode frequency. This is implemented using a copper cavity, which is not altered by the static field. This configuration inhibits the radiation damping and allows for $\mu$s coherence times also at high fre-

quencies and with large sample volumes. The system is parametrized as two strongly coupled harmonic oscillators, the cavity photons and the material magnons, weakly coupled to a third one, which is the axion field. Multiple features of the hybrid system, and thus of the haloscope, are studied using two different models. In the first model, a second quantization analysis provides easy access to some of the hybrid system properties. The axion-signal transduction bandwidth is calculated with this model, and experimentally verified with a dedicated setup, employing a laser which illuminates the YIG sphere embedded in a copper cavity. The absorption of the laser light modifies the sample magnetization, as it is assumed would be done by the axion field. The data verifies the model, which can thus be used to compute the operational tuning-range of the haloscope. The second model consists in a system of electrical oscillators, which are a physically intuitive way to describe the setup. A $RL$ loop is added to the three oscillators to account for the antenna. This is used, for example, to understand if it is possible to couple oscillators with different linewidths, or if some limitations occur due to large coupling strengths. It resulted that, to properly transduce the signal, the cavity and material must have similar linewidths. Such downside can be somehow avoided by working in the dispersive regime, i. e. when the electrons Larmor frequency is different from the cavity mode frequency. Nevertheless, to increase the coherence time of the hybrid system both the quality factor of material and cavity have to increase.

The R&D on resonant cavities was successful, as it resulted in the design and test of a superconducting cavity with a high quality factor and working in high magnetic fields. In fact, the correct hybridization of the cavity TM110 mode with a YIG sphere ensures that the magnetic field enters into the cavity, which can therefore be used for haloscope applications. By relying on the Primakoff effect, a measurement of the cavity TM010 mode immersed in a 2 T static field yielded a limit on the axion-photon coupling constant. This measurement opens the way to the building of a new experimental apparatus, a regular haloscope called QUAX-$a\gamma$, which is planned for next year. It aims to reach the QCD-axion line by employing a JPA and an 8 T field at mK temperatures. Photonic-bandgap cavities made of sapphire and copper were also studied with the same aim, and gave promising results. However, since the linewidth of the YIG is not as narrow as the one of these newly developed cavities, it is almost useless to employ them in a ferromagnetic haloscope at this development stage. They should be used with a proper material with a longer relaxation time to increase the hybrid system coherence time.

Following the first room temperature tests of the hybrid system noise,

the first prototype of a ferromagnetic haloscope was operated at liquid helium temperature. Its working frequency is 14 GHz, corresponding to an axion mass of 58 $\mu$eV, the magnon oscillator is made up of five 1 mm diameter YIG spheres and is coupled to the TM110 mode of cylindrical copper resonant cavity. The spheres are positioned along the cavity axis and free to rotate to achieve a full coherent coupling. An antenna with variable coupling is used to collect the hybrid system output, which is monitored to search for axion-deposited extra power. A low-noise HEMT amplifies the output power and adds a noise comparable with thermodynamic fluctuations, for a total system noise temperature of about 10 K. This quantity is calibrated in every run with a heated load which injects a variable known power in the detection chain. The microwave signal is further amplified, down-converted with an heterodyne chain, and finally acquired by an ADC. Thanks to all these features, this setup can be considered an haloscope, and gave the first measured limit of the coupling of DM axions to electrons $g_{aee} \leq 4.9 \times 10^{-10}$. The result is highly self-consistent, as all the parameters used to calculate the limit are measured within the run and can be easily checked.

The apparatus was further improved by lowering the noise temperature of the detection chain and increasing the deposited power. This is obtained with a 90 mK temperature, a quantum-limited JPA with a noise temperature of 0.5 K, and with a material volume increased by a factor 16 by employing ten 2 mm diameter spheres. A dedicated study of the coherent coupling of such a large quantity of material with a single cavity mode is necessary to understand the system behavior. The measured spectra are well characterized by the study, and it is verified that the transduction of the signal is preserved in the working conditions. The study also allows for the measurement of the system parameters needed for the self-consistency of the measurement. A JPA, with a working frequency of 10 GHz, amplifies the signal extracted by a variable coupling antenna as in the previous prototype. The calibration consists in reflection and transmission measurements of all the microwave lines of the setup by means of a monochromatic signal. In this case the antenna coupling gives the larger uncertainty of the measurement, as is actively used in the calibration process. The measured noise temperature is 1.0 K, roughly a factor 10 better than the previous one, and is compatible with the expectations since for 10 GHz it corresponds to two quanta. The bandwidth of a single run is the linewidth of the hybrid mode, close to 2 MHz, but it can be tuned with the external field. The scanned axion-frequencies range from 10.2 GHz to 10.4 GHz, this interval is a factor 100 larger than the one of the previous haloscope. The best limit is obtained with 8 h of integration and gives $g_{aee} \leq 1.7 \times 10^{-11}$ for $m_a \simeq 42.7\,\mu$eV.

The ferromagnetic haloscope measured variation in a sample magnetization, and thus can be configured as a rf spin-magnetometer. It is interesting to calculate what its sensitivity is in terms of an effective magnetic field, to test whether there are other possible applications of the device. With the current parameters, the ultra cryogenic prototype has a SNR = 1 sensitivity of $5.5 \times 10^{-19}$ T for 8 h of integration.

The scalability of all the prototypes is a key part of their design. Longer cylindrical cavities can house more YIG spheres, or a YIG rod. There are some evidences that the transduction of the axion-signal efficiently occurs also if the spheres are not placed along the cavity axis. These two features can be combined to up-scale the sample volume in a single cavity. Multiple cavities can be employed to further increase the spin number, and, in principle, their readout can be performed both by a single device or by multiple ones without increasing the system noise temperature. The power sensitivity of the haloscope can not be further increased by using linear amplifiers, since the employed JPA already reaches the standard quantum limit. Novel mw photon counters, or bolometers sensitive to faint amounts of power, have to be developed as was done for quantum information technology. Existing devices are mostly based on Josephson junctions, and they can be a starting point to develop new ones, suitable for DM searches. The design and first tests of a photon counter based on an underdumped junction gave promising results. The use of a quantum counter is a stimulating possibility for the new apparatuses to be built.

In conclusion, the results of this work demonstrate that it is feasible to detect DM-axions by using a rf spin-magnetometer. The operated setups reached a remarkable sensitivity and no showstoppers have been found so far. Ferromagnetic haloscopes constitute an interesting alternative to Sikivie haloscopes, and in the presence of a signal their combination would be an excellent way to study the axion-wind features. The studies performed for developing such instruments gave interesting results regarding high quality factor cavities, electron spin resonance and the physics of hybrid systems. The spin-magnetometer is a versatile instrument which can test different effects. Its effective field sensitivity is, to present knowledge, a record one, and opens the way to new exciting tests of physics beyond the Standard Model.

# Appendix A

# Versatility of the ferromagnetic haloscope

The ferromagnetic haloscope is essentially a spin-magnetometer. In this sense, it is not only sensitive to DM-axions but to any effect which modulates the magnetization of the sample embedded in the mw cavity. Hereafter three different cases of magnetization-varying effect are considered: neutrino-induced, gravitational waves-induced and electron-EDM -induced. This appendix is meant to report some ideas which are still not consistently developed, and thus should be taken with some mindfulness. To make this section readable independently from the rest of the thesis, the notation is dropped and the symbols are usually redefined.

## A.1 Neutrino induced spin-flips

Hereafter the possibility of using a spin-magnetometer to detect an interaction between electrons and neutrinos is discussed. In particular, the effect of a flux of relic neutrinos on a magnetized sample is considered, similarly to what is done with axions. The major contributions to this section are given by Gianni Carugno, Riccardo Barbieri and Alessandro Bettini, who actively pursued this idea.

Being the neutrino a spin 1/2 lepton as the electron, the interaction cross section which produces an electron spin-flip is expected to be non-zero. Let's consider a relic electron neutrino of Dirac mass $m_\nu$ and only interact via $W$ exchange. The generalization to a realistic case is straightforward but numerically tedious. The amplitude for the scattering to a single polarized

electron is

$$M_{fi} = \frac{-G}{\sqrt{2}}(\bar{e}_f \gamma_\mu e_i)(\bar{\nu}_f \gamma_\mu \nu_i), \tag{A.1}$$

where $G$ is the interaction constant, $e$ and $\nu$ are the electron and neutrino wavefunctions and $\gamma_\mu$ is the vector of Dirac matrices. One has to consider a neutrino $\nu_i$ is polarised in the direction of its 3-momentum and a non-relativistic electron $e_i$ that flips its spin and makes an energy jump $\omega_0 = \gamma_e B_0$. Here, $\gamma_e$ is the electron gyromagnetic ratio, and $B_0$ is a static field, their product is taken equal to $10^{-4}\,\mathrm{eV}$ for numerical purposes. The cross section results

$$\mathrm{d}\sigma = \frac{1}{v_{\nu_i}} \frac{m_\nu}{E_{\nu_i}} |M_{fi}|^2 \mathrm{d}\phi, \tag{A.2}$$

where $v_{\nu_i}$ and $E_{\nu_i}$ are the neutrino's speed and energy, and

$$\mathrm{d}\phi = \frac{1}{4\pi^2} \delta(E_{\nu_i} - E_{\nu_f} - \omega_0) \frac{m_\nu}{E_{\nu_f}} \mathrm{d}^3 p_{\nu_f}. \tag{A.3}$$

The rate of single-electron interaction can be extracted from Eq. (A.2) and (A.3) by using the Fermi-Dirac distribution as

$$R_{e\nu} = \int \frac{\mathrm{d}^3 p_{\nu_i}}{(2\pi)^3} \frac{v_{\nu_i}}{e^{p_{\nu_i}/k_B T} + 1} \mathrm{d}\sigma, \tag{A.4}$$

where $v_{\nu_i} = E_{\nu_i}/p_{\nu_i}$ and $T = 1.7 \times 10^{-4}\,\mathrm{eV}$ is the temperature of relic neutrinos. For a mass $m_\nu < 0.1\,\mathrm{eV}$, the mean velocity of relic neutrinos is bigger than $v_E \simeq 10^{-3}$, the Earth's speed in the rest frame of the galaxy, so $v_E$ can be neglected. To simplify the calculation of the amplitude $M$, for the time being it will be performed in the non-relativistic limit for $m_\nu < 3 \times 10^{-3}\,\mathrm{eV}$ and thus $v_{\nu_i} < 0.2$. In this limit $|M|^2 = G_F^2$, the Fermi constant, so that the rate of Eq. (A.4) becomes

$$R_{e\nu} = G_F^2 \frac{m_\nu}{(2\pi)^3} \int_{p_m}^{+\infty} \frac{p^2 \mathrm{d}p}{e^{p/k_B T} + 1} \sqrt{p^2 - p_m^2}, \tag{A.5}$$

where $p_m = \sqrt{2 m_\nu \omega_0}$ is the minimum incoming neutrino momentum allowed by energy conservation. In the range considered, $3 \times 10^{-3}\,\mathrm{eV} < m_\nu < 0.1\,\mathrm{eV}$, $R_{e\nu}$ is a monotonically decreasing function of the neutrino mass, due to the cutoff of the integral at low momenta, $p_m/k_B T \simeq 8(m_\nu/10^{-2}\,\mathrm{eV})(\omega_0/10^{-4}\,\mathrm{eV})$, that increases with the mass. It results

$$R_{e\nu}(m_\nu = 3 \times 10^{-3}\,\mathrm{eV}) \simeq 10^{-50}\,\mathrm{Hz}. \tag{A.6}$$

Considering a system of $N$ electrons in positions $\mathbf{x}_i$ and spins $\mathbf{s}_i$. The hamiltonian of the non-relativistic interactions with neutrino electrons with position and spins $\mathbf{x}_j$ and $\mathbf{s}_j$, can be written as

$$\mathcal{H}_{e\nu} = \sum_i \mathcal{H}_i = G_F \sum_i (a + b\,\mathbf{s}_i \cdot \mathbf{s}_j)\delta^{(3)}(\mathbf{x}_i - \mathbf{x}_j), \tag{A.7}$$

where $a$ and $b$ are $O(1)$ numbers. The term proportional to $b$ gives the spin-flip interaction. Let's describe the initial state of the electrons approximately as

$$|i\rangle = |\phi_1\rangle\,|\phi_2\rangle \ldots |\phi_i\rangle \ldots |\phi_N\rangle\,, \tag{A.8}$$

where $|\phi_i\rangle$ includes both position and spin dependence. The final state $|f\rangle$ is obtained similarly and the scattering amplitude is

$$A = \langle f|\,\mathcal{H}_{\rangle\nu}\,|\rangle\rangle\,. \tag{A.9}$$

Two different cases can be considered:

- non-coherent interaction - the sum over the single hamiltonians $\mathcal{H}_i$ is outside of the squared term

$$R \propto \sum_i |\,\langle f|\,\mathcal{H}_{\rangle}\,|\rangle\rangle\,|^{\in} \propto \mathcal{N}. \tag{A.10}$$

- Coherent interaction - in this case the sum in the hamiltonian is within the square amplitude,

$$R \propto |A|^2 = |\sum_i \langle f|\,\mathcal{H}_{\rangle}\,|\rangle\rangle\,|^{\in} \propto \mathcal{N}^{\in}. \tag{A.11}$$

  There are strict conditions for this case to verify, and it is still not clear whether the experimental apparatus can match them.

For example, coherent neutron scattering on nuclei is a widely studied phenomenon [268,269], and it demonstrates the dependence of the cross section on the squared number of nucleons. Since nuclei are fermions, this interaction should be analogous to the one of neutrinos with $N$ electrons. Moreover, in heavy dark matter searches, the interaction of WIMPs with nuclei yields a cross section which is proportional to the number of nucleons squared, if the wavelength of the DM particle is larger than the one of the nucleus. More detailed studies have to be performed in this direction, as the $N^2$ dependence would greatly boost the sensitivity to this interaction. For example, considering an ensemble of $10^{24}$ spins (corresponding to roughly 100 cc of YIG) one can calculate that the interaction rate of Eq. (A.6) becomes measurable in the case of a coherent interaction.

## A.2 A GHz gravitational waves detector?

In 2015 the LIGO and Virgo collaborations reported on the detection of the first gravitational wave (GW) [270]. In the present status of gravitational waves searches [271], the highest frequency GW limit reported is 100 MHz [272], while the detected GWs are of order 100 Hz.

It was recently pointed out by A. Ito and collaborators [273] that GHz gravitational waves could excite collective excitations of the magnetization. A spin-magnetometer like the ones described in this thesis, in principle, can be sensitive to such excitation and thus to GHz-GWs. One can start to derive the graviton-magnon interaction from the Dirac equation in a curved spacetime

$$i\gamma^{\hat{\alpha}} e^{\mu}_{\hat{\alpha}} (\partial_\mu + \Gamma_\mu + ieA_\mu)\psi = m_e \psi, \tag{A.12}$$

$$\text{with } e^{\mu}_{\hat{\alpha}} e^{\nu}_{\hat{\beta}} \eta_{\hat{\alpha}\hat{\beta}} = g^{\mu\nu} \tag{A.13}$$

$$\text{and } \Gamma_\mu = \tfrac{1}{2} e^{\hat{\alpha}}_{\nu} \sigma_{\hat{\alpha}\hat{\beta}} (\partial_\mu e^{\nu\hat{\beta}} + \Gamma^{\nu}_{\lambda\mu} e^{\lambda\hat{\beta}}) \tag{A.14}$$

where $\gamma^{\hat{\alpha}}$, $e$, $m_e$, and $A_\mu$ are the Dirac matrices, the electron charge, the electron mass and the vector potential, respectively. The spacetime metric is $g_\mu\nu$, $\sigma_{\hat{\alpha}\hat{\beta}} = [\gamma_{\hat{\alpha}}, \gamma_{\hat{\beta}}]/4$ is a generator of the Lorentz group, and $\Gamma^{\mu}_{\nu\lambda}$ is the Christoffel symbol. The effect of a GW on spins can be treated similarly to the one of an effective magnetic field [274]. In the non-relativistic limit, the spin-field hamiltonian is

$$\mathcal{H}_{\rm s} = -\mu_B (2\delta_{ij} + h_{ij}) \hat{S}^i B^j, \tag{A.15}$$

where $\hat{S}$ is the spin of the electron, $B$ is a magnetic field, and the metric perturbations $h_{ij} \ll 1$ is due to the GW. For a large number of spins $N_s$, the Heisenberg hamiltonian results

$$\mathcal{H}_{N_s} = -\mu_B B_z \sum_i \left[ 2\hat{S}^z_{(i)} + h_{zj} \hat{S}^j_{(i)} \right] - \sum_{i,j} J_{ij} \hat{S}_{(i)} \hat{S}_{(j)}. \tag{A.16}$$

The wavelength of the GW $\lambda_{\rm gw}$ is much larger than the experimental length, thus considering a wave propagating in the $x$-$z$ plane, its wavevector direction is $\hat{k}^i = (\sin\theta, \phi, \cos\theta)$. This effect is remarkably similar to the one of DM-axions described in this thesis, so it could be possibly probed with a ferromagnetic haloscope. The term $h_{ij}$ carries the information on the GW, and may be recast to a form analogous to the one of the axion field in Eq. (3.6). Since $\lambda_{\rm gw}$ is large, the metric perturbation can be expanded in

terms of linear polarization tensors

$$e_{ij}^{\sigma} e_{ij}^{\sigma'} = \delta_{\sigma\sigma'} \;\Rightarrow\; h_{ij}(t) = h^{(+)}(t) e_{ij}^{(+)} + h^{(\times)}(t) e_{ij}^{(\times)} \tag{A.17}$$

$$\text{where } \begin{cases} h^{(+)}(t) = h^{(+)}\big(e^{-i\omega_h t} + e^{i\omega_h t}\big)/2 \\ h^{(\times)}(t) = h^{(\times)}\big(e^{-i(\omega_h t+\alpha)} + e^{i(\omega_h t+\alpha)}\big)/2, \end{cases} \tag{A.18}$$

where $\omega_h$ is the GW frequency and $\alpha$ a phase difference. Explicitly, the polarization tensors are

$$\begin{aligned} e_{ij}^{(+)} &= \frac{1}{\sqrt{2}} \begin{pmatrix} \cos^2\theta & 0 & -\cos\theta\sin\theta \\ 0 & -1 & 0 \\ -\cos\theta\sin\theta & 0 & \sin^2\theta \end{pmatrix}, \\ e_{ij}^{(\times)} &= \frac{1}{\sqrt{2}} \begin{pmatrix} 0 & \cos\theta & 0 \\ \cos\theta & 0 & -\sin\theta \\ 0 & -\sin\theta & 0 \end{pmatrix}. \end{aligned} \tag{A.19}$$

The Primakoff-Holstein transformations of the Heisenberg model yield

$$\begin{cases} \hat{S}_{(i)}^{z} = \frac{1}{2} - \hat{M}_i^{+}\hat{M}_i \\ \hat{S}_{(i)}^{+} = \sqrt{1 - \hat{M}_i^{+}\hat{M}_i}\,\hat{M}_i \\ \hat{S}_{(i)}^{-} = \hat{M}_i^{+}\sqrt{1 - \hat{M}_i^{+}\hat{M}_i}, \end{cases} \tag{A.20}$$

where the bosonic operators satisfy $[\hat{M}_i^{+}, \hat{M}_j] = \delta_{ij}$ and the ladder operators are $\hat{S}_{(j)}^{\pm} = \hat{S}_{(j)}^{x} \pm i\hat{S}_{(j)}^{y}$. Neglecting surface effects, the bosonic operators can be expanded in plane waves which only excite the uniform precession mode, i. e. the Kittel mode

$$\hat{M}_i = \sum_k \frac{e^{ik\cdot r_i}}{\sqrt{N_s}} \hat{m}_k. \tag{A.21}$$

The resulting $\hat{m}$ operators can be used to write the GW-magnon interaction

$$\mathcal{H}_{\mathrm{gw}} = g_{\mathrm{gw}}(\hat{m}^{+} e^{-i\omega_h t} + \hat{m} e^{i\omega_h t}), \tag{A.22}$$

where the effective coupling constant is

$$g_{\mathrm{gw}} = \frac{1}{4\sqrt{2}} \mu_B B_z \sin\theta \sqrt{N_s\big[\cos^2\theta (h^{(+)})^2 + (h^{(\times)})^2 + 2h^{(+)}h^{(\times)}\cos\theta\sin\alpha\big]}. \tag{A.23}$$

Interestingly, a limit on the deposited power as the one obtained with the present prototypes, also yields a limit on $g_{\mathrm{gw}}$, allowing to probe GHz-GW with a rf spin-magnetometer.

If this treatment is found to be correct, an instrument like the one described in Sec. 4.3 improves of two more orders of magnitude the best limit reported in [273], with a strain sensitivity of about $10^{-24}/\sqrt{\text{Hz}}$. This sensitivity level is an interesting band for GWs, and for example can be used to probe the presence of theoretical objects such as gravitational atoms. As the name suggests, these are atoms composed of ultra-heavy particles, with masses of the order of the Planck mass, which are bound thanks to the gravitational interactions. These can be a candidate source of GHz-GW [275], and the quantum-limited haloscope described in this thesis could be already sensitive and exclude some frequency ranges.

## A.3 Electron EDM measurements

As is mentioned in Sec. 2.2, an axion-induced electron EDM may be used to boost the axion signal of a factor $\sim 100$. In this direction a voltage of 1 kV (producing roughly a 1 kV/cm electric field) was applied on the two halves of a mw cavity to test whether some disturbances arise, and no differences have been measured between zero and non-zero fields. The cavity used to perform the test is shown in Fig. A.1.

This setup can also be used with an oscillating electric field to test the presence of a static eEDM. By placing an electron inside static magnetic $\mathbf{B}_0$ and electric $\mathbf{E}_0$ fields, the energy of the system can be described by:

$$\mathcal{H}_{\text{edm}} = -\mu_B \frac{\mathbf{S}}{S} \cdot \mathbf{B}_0 - d_e \frac{\mathbf{S}}{S} \cdot \mathbf{E}_0 \tag{A.24}$$

where $\mu_B$ is the Bohr magneton, $\mathbf{S}$ is the electron spin and $d_e$ is the electron electric dipole moment (eEDM). At present, for the eEDM, only upper limits have been placed, and no direct measurement has been performed: $d_e < 10^{-29}$ e cm [173]. The direction of the electron spin and of the eEDM are normally taken to be parallel. Following Eq. (A.24), the electron spin will have a precession frequency $\omega_S$ given by

$$\omega_S = \gamma_e B_0 + \frac{\hbar d_e}{E_0} = \omega_L + \omega_d, \tag{A.25}$$

where $\gamma_e = g_e \mu_B/\hbar = 2\pi \times 28\,\text{GHz/T}$ is the electron gyromagnetic ratio. Let's now suppose that a modulation of the external field amplitude acts at a certain frequency $\omega_E$. The precession frequency will be time modulated

$$\omega_S(t) = \omega_L + \omega_d \sin(\omega_E t). \tag{A.26}$$

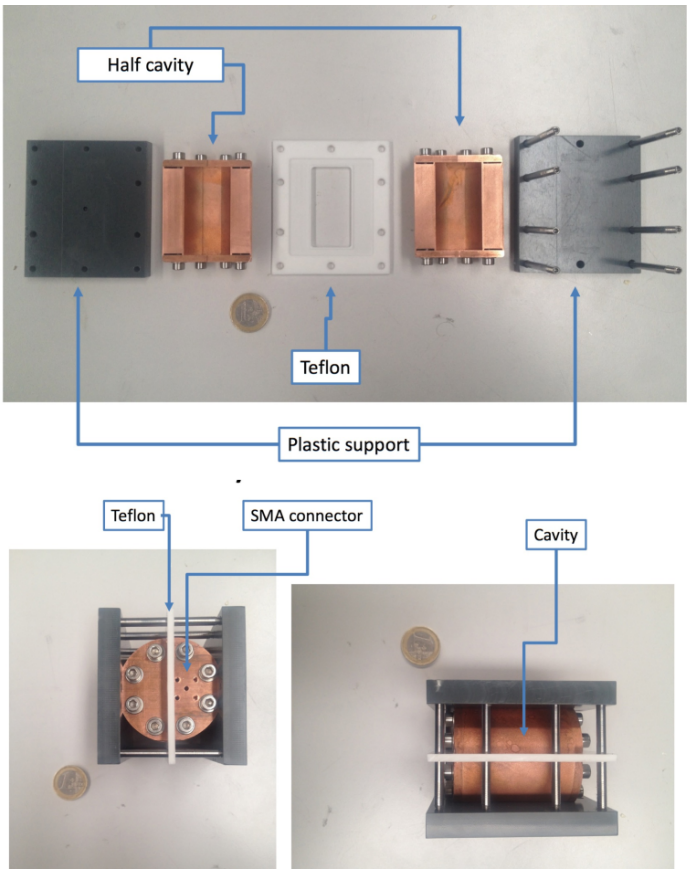


Figure A.1: Microwave cavity cut into two halves to test whether the presence of an electric field somehow compromises the properties of the hybrid system.

If the modulation frequency is within the Larmor linewidth and for small modulation (which is always the case since we are looking for an extremely small effect), this corresponds to a time first derivative of the resonance curve. The resonance is normally described by a Lorentzian function, whose absorption profile is given by

$$A(\omega) = \frac{\gamma B_1 M_0 T_2}{1 + T_2^2(\omega_0 - \omega)^2}, \tag{A.27}$$

where $B_1$ is the probe rf field at frequency $\omega$, $\omega_0$ is the resonance center, corresponding to $\omega_S(t)$, $M_0$ is the magnetization density and $T_2$ is the trans-

verse relaxation time. The above equation is valid below saturation, i.e. for $\gamma^2 B_1^2 T_1 T_2 \ll 1$, with $T_1$ the longitudinal relaxation time. The signal induced by the modulated electric field will appear at $\omega_E$ and its amplitude will be proportional to the first derivative of $A(\omega)$:

$$A'(\omega_S) = \frac{2\gamma B_1 M_0 T_3^2 (\omega_S - \omega)}{[1 + T_2^2(\omega_S - \omega)^2]^2}. \tag{A.28}$$

In order to maximize the derivative, let's put the carrier frequency of the rf field $B_1$ at the half of the Lorentzian maximum, that is $(\omega_S - \omega) = 1/T_2$. At this value we will find that the material transmission is made by a carrier at $\omega_L$ and two sidebands at $\omega_L \pm \omega_d$. By using a mixer tuned to $\omega_L$ it will be possible to down convert this output so that it will have two separate components:

$$S_{\rm dc} = \frac{1}{2}\gamma B_1 M_0 T_2; \tag{A.29}$$

$$S_E(t) = \frac{1}{2}\gamma B_1 M_0 T_2^2 \omega_d \sin(\omega_E t). \tag{A.30}$$

Suppose that the only limiting noise to look for the $S_E$ component is the residual amplitude modulation of the field $B_1$ induced by the signal generator that produces it. Calling $\mathrm{RAM}_B(\omega)$ its relative amplitude, we calculate the signal to noise ratio for the signal as:

$$\mathrm{SNR} = \frac{T_2 d_e E_0}{\hbar\ \mathrm{RAM}_B(\omega)}, \tag{A.31}$$

so we get a sensitivity for the electric dipole moment $d_e$ as:

$$\begin{aligned} d_e &= \frac{\hbar\ \mathrm{RAM}_B(\omega)}{T_2 E_0} \\ &= \left(\frac{\mathrm{RAM}_B(\omega)}{10^{-8}}\right)\left(\frac{10^{-6}\ S}{T_2}\right)\left(\frac{10^3\ \mathrm{V/cm}}{E_0}\right) 6.6\times 10^{-21}\ \mathrm{e\,cm}/\sqrt{\mathrm{Hz}} \end{aligned} \tag{A.32}$$

which is valid for a normal system where the dipole moment of the atom is the same as the one of the electron. An improvement could be foreseen by using molecules which by Shiff theorem have an enhancement of the effect of a single electron as in YbF, where the factor is of order $10^6$. In the literature there is some discussion on this effect on electrons, and it is not clear whether this enhancing will be present [276–278].

It was not explained how the variable electric field could be placed on the sample, but for example a configuration where the magnetic sample is

inside a cut resonant cavity is possible. The two cavity halves would be used as electrodes for the electric field. In general a material in the presence of an external electric field $E_0$ shows an atomic dipole moment induced by the mixing perturbation $V_{\text{mix}} = V_{\text{Stark}} = -d \cdot \mathbf{E}_0$. In this case the interaction energy is however quadratic in the electric field

$$H = -\mathbf{d}_{\text{ind}} \cdot \mathbf{E}_0 \propto E_0^2, \tag{A.33}$$

so it is in general distinguishable from a pure EDM effect which is linear in the external field. In particular, if the external field is time modulated at a frequency $\omega_E$, the effect of electric polarizability will generate a signal at the sidebands $\pm 2\omega_E$. Only in the presence of a static component of the external field a $\omega_E$ term can be generated by the electrical polarizability, but this can be studied experimentally by varying the value of the dc component and taking the residuals in the limit $E_0^{\text{dc}} = 0$.

The experimental arrangement is based on the use of a microwave resonant cavity where an electric field can be superimposed to the ESR magnetic field in the sample. Following Eq. (A.24), the two polarizing fields must be parallel, and thus both orthogonal to the rf field are exciting the Larmor transition. A suitable arrangement is a cylindrical cavity operating in the TM110 mode. By placing a sample in the cavity axis and an external magnetic field $B_0$ along the $\hat{y}$ direction, it is possible to excite the Larmor frequency of the sample. If the cavity is cut in two halves, along the $\hat{x}$ direction, and the halves are separated by a dielectric, then a voltage can be put between the two parts and an electric field will be present oriented again along the $\hat{y}$ direction, i.e. parallel to the magnetic field. A cavity of this type has been already realized, and can be seen in figure A.1. Actually this cavity has the cut along the wrong section, in fact with this cavity the rf magnetic field and the external electric field are parallel, but we need a configuration where these two fields are orthogonal. In principle there are no prescriptions against this, and so we expect that the cavity is working anyway as the one that has been tested that reached a $Q$ factor of about 4000 at the frequency of 14 GHz.

### A.3.1 Sensitivity test

The feasibility of such a scheme is studied by measuring slowly varying fields along the direction of the magnetizing field $\mathbf{B}_0$. A cavity equipped with two coils in the planes orthogonal to the $\mathbf{B}_0$ direction can be used to produce a time varying field

$$\mathbf{B}_0(t) \cdot \hat{y} = B_0 + B_0^v \sin(\omega_v t) \tag{A.34}$$

with the frequency $f_v = \omega_v/2\pi$ in the kHz range.

The microwave cavity is resonant at the frequency of about 10.935 GHz, and contains a 0.5 mm diameter YIG sphere at its center. When placing the cavity inside a static 0.39 T magnetic field, hybridization takes place, and a strong coupling between the cavity and the ferromagnetic resonance of the YIG arises. The main resonance splits in two ones, $f_1 = 10.917$ GHz, and $f_2 = 10.953$ GHz. The pump is on one of the hybrid modes at about its half-width, and consists in an rf signal of suitable amplitude and frequency $f_{\rm rf} = f_1 + \Delta f_1/2$. The system shows maximum transmission through a pair of antennas, one of which is critically coupled. By turning on the variable field $B_0^v$, the transmission of the system shows a main carrier at $f_{\rm rf}$ and two sidebands at $f_{\rm rf} \pm f_v$. The minimum measurable value of $B_0^v$ can be expressed in Hz to be directly compared to the effect of the electric field in equation A.24. The effect $F_{\rm eEDM}$ can be calculated as the one of a typical electric field for a given value of the eEDM. This turns out to be

$$F_{\rm eEDM} = 4.8 \times 10^{-12}{\rm Hz} \left(\frac{E}{10^3 {\rm V/cm}}\right) \left(\frac{d_e}{10^{-29} {\rm e\,cm}}\right) \tag{A.35}$$

having defined the gyroelectric ratio $\gamma_E$ as

$$\gamma_E = \frac{g_e \mu_E}{\hbar} = \frac{g_e d_e S}{\hbar}. \tag{A.36}$$

Of course this is valid for a free electron, in the case of a compound, the atomic or molecular EDM can be boosted through the Schiff theorem up to factors of the order $10^6$, that means that a measurement of a $\mu$Hz frequency amplitude should be made.

In this test set-up the sensitivity is about 10 Hz/$\sqrt{\rm Hz}$ at a frequency of several kHz. The main limitation is not yet clear, but prospects for improvements are expected. Another intermediate step that should be checked soon is the presence of systematics, for example modification of the cavity resonance frequency induced by the force produced between the two cavity halves from the electric field. The electrostatic force $F_{\rm ES}$between the two parts is given by:

$$F_{\rm ES} = \frac{1}{2}\epsilon_0 S \left(\frac{V}{d}\right)^2 \tag{A.37}$$

where $d$, and $S$ are an effective distance and surface respectively, and $V$ is the applied voltage. Due to the quadratic dependence, it should be possible to separate this effect from the searched one. To realize a convincing scheme more efforts are necessary, but these preliminary measurements show a new promising way to test EDMs in hybrid systems.

# Appendix B

# Longitudinal axion detection

This Appendix is temporary omitted because of a pending patent.

# Appendix C

# A testbed for Dicke superradiance?

This Appendix considers the possibility of obtaining the superradiant emission of a spin ensemble coupled to the normal mode of a resonant cavity. In 1954, Dicke [308] demonstrated that a group of $N$ atoms in a single excited energy level and subjected to the same radiation field, must not be treated as independent. If the distance between the $i^{\text{th}}$ and $j^{\text{th}}$ atom is $\mathbf{r}_i - \mathbf{r}_j < \lambda$, where $\lambda$ is the wavelength of the radiation field, one can simplify the transition operator $\sum_i \mathbf{S}_i \to \mathbf{S}$. That is, since the electrons of an energy level are indistinguishable, if one of them decays to the ground state, all the others are doing the same in a time $\propto 1/N$, yielding a power $I \propto N^2$. This process is different from a stimulated emission where a single decaying atom, whose photon triggers all the others, gives an in-phase burst of photons; in this case the power is $I \propto N$. The case of $N$ two-level systems interacting with a single mode radiation field has been considered by Tavis and Cummings [188], who worked out an exact solution to the problem. The work of Dicke has been extended to the case of $\lambda \ll \mathbf{r}_i - \mathbf{r}_j$ and goes under the name of superfluorescence [309]. The system under consideration has many possible experimental realizations [310], these can be a doped crystal subjected to a laser light, qubits coupled to a resonant cavity mode, quantum dots lattices and more.

There is a marked similarity between the original configuration considered by Dicke and a YIG sphere in a resonant cavity. The YIG provides $N$ two level system, spin $\pm\frac{1}{2}$, which are coupled to a single cavity mode, satisfying the condition $\mathbf{r}_i - \mathbf{r}_j < \lambda$. The most direct evidence of hybridization is the anticrossing curve (see for example Fig. 3.2), and when the magnon

frequency $\omega_m$ is equal to the cavity one $\omega_0$ the spectrum shows two resonant modes $\omega_1$ and $\omega_2$, symmetric with respect to $\omega_0$, and the coupling strength can be measured as $g_{21} = \omega_2 - \omega_1$. Let's consider the scheme in Fig. C.1, which represents the simplest energy levels configuration that gives the hybrid resonances spectrum. The ground state is $|g\rangle$, while the two excited

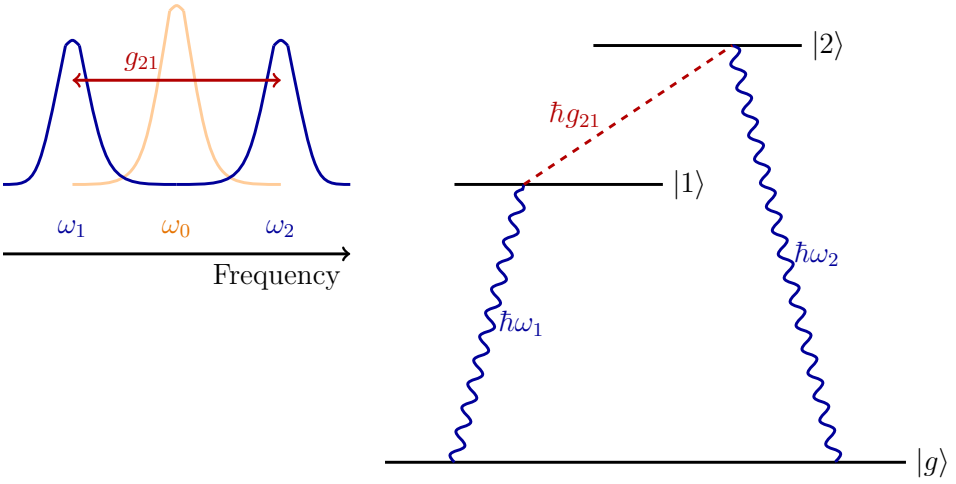


Figure C.1: The left part is the Fourier spectrum. The right part is the energy level scheme which results in the measured hybrid spectrum.

states are $|1\rangle$ and $|2\rangle$. This hybrid system could be a testbed of quantum coherence, and suitable for measuring superradiant effects, but it is still unclear what are the channels through which it can manifest. Further studies are necessary to characterize these energy levels in terms of, i. e., quantum numbers. A correct description of the state could tell which particles $\varphi$ may excite the $1 \to 2$ transition, and thus what physics could be probed with such a system. The $\varphi$-induced transition rate, even if extremely small, could be enhanced by exploiting quantum coherent effects like superradiance.

A preliminary study was carried out to test to which level this transition is not excited. To this aim a pump is used to populate $|1\rangle$, and if an electron is excited to $|2\rangle$, by e. g. a phonon, some extra power should be emitted at the frequency $\omega_2$. A setup similar to the one described in Appendix **??**, in particular in Fig. **??**, is used to test to which level there is no excess signal at $\omega_2$ with a pump at $\omega_1$. With a pump power around 0 dB no extra power was detected above the room temperature thermal noise. If $1 \to 2$ was forbidden for spin-1 bosons (like phonons or photons) but not for scalars, then it may be a suitable probe for scalar particles with energy $\hbar\omega_{21}$ with

a very low electromagnetic and thermal background. This is an intriguing possibility, which would allow the described systems to be the starting point of a new kind of quantum detectors. However, a detailed theoretical analysis is necessary to first understand the behavior of the system.

# Bibliography


[1] F. Zwicky. Die Rotverschiebung von extragalaktischen Nebeln. *Helvetica Physica Acta*, 6:110–127, 1933.

[2] V. C. Rubin, N. Thonnard, and W. K. Ford, Jr. Extended rotation curves of high-luminosity spiral galaxies. IV - Systematic dynamical properties, SA through SC. *Astrophysical Journal*, 225:L107–L111, November 1978.

[3] V. C. Rubin, W. K. Ford, Jr., and N. Thonnard. Rotational properties of 21 SC galaxies with a large range of luminosities and radii, from NGC 4605 /R = 4kpc/ to UGC 2885 /R = 122 kpc/. *Astrophysical Journal*, 238:471–487, June 1980.

[4] Fu, L., Semboloni, E., Hoekstra, H., et al. Very weak lensing in the cfhtls wide: cosmology from cosmic shear in the linear regime. *A&A*, 479(1):9–25, 2008.

[5] Priyamvada Natarajan, Urmila Chadayammuri, Mathilde Jauzac, et al. Mapping substructure in the HST Frontier Fields cluster lenses and in cosmological simulations. *Monthly Notices of the Royal Astronomical Society*, 468(2):1962–1980, 02 2017.

[6] Satoshi Miyazaki, Masamune Oguri, Takashi Hamana, et al. A large sample of shear-selected clusters from the Hyper Suprime-Cam Subaru Strategic Program S16A Wide field mass maps. *Publications of the Astronomical Society of Japan*, 70(SP1), 12 2017.

[7] Masamune Oguri, Satoshi Miyazaki, Chiaki Hikage, et al. Two- and three-dimensional wide-field weak lensing mass maps from the Hyper Suprime-Cam Subaru Strategic Program S16A data. *Publications of the Astronomical Society of Japan*, 70(SP1), 08 2017.

[8] C. Di Paolo, P. Salucci, and J. P. Fontaine. The radial acceleration relation (RAR): Crucial cases of dwarf disks and low-surface-brightness galaxies. *The Astrophysical Journal*, 873(2):106, mar 2019.

[9] Planck Collaboration, Ade, P. A. R., Aghanim, N., et al. Planck 2015 results - xiii. cosmological parameters. *A&A*, 594:A13, 2016.

[10] E. Komatsu, J. Dunkley, M. R. Nolta, et al. Five-year wilkinson microwave anisotropy probe observations: cosmological interpretation. 180(2):330–376, feb 2009.

[11] Matteo Viel, James S. Bolton, and Martin G. Haehnelt. Cosmological and astrophysical constraints from the Lyman $\alpha$ forest flux probability distribution function. *Monthly Notices of the Royal Astronomical Society: Letters*, 399(1):L39–L43, 10 2009.

[12] John A. Peacock, Shaun Cole, Peder Norberg, et al. A measurement of the cosmological mass density from clustering in the 2df galaxy redshift survey. *Nature*, 410(6825):169–173, 2001.

[13] Judd D. Bowman, Alan E. E. Rogers, Raul A. Monsalve, Thomas J. Mozdzen, and Nivedita Mahesh. An absorption profile centred at 78 megahertz in the sky-averaged spectrum. *Nature*, 555:67 EP –, Feb 2018.

[14] Rennan Barkana. Possible interaction between baryons and dark-matter particles revealed by the first stars. *Nature*, 555:71 EP –, Feb 2018.

[15] Katherine Freese, Brian Fields, and David Graff. Death of stellar baryonic dark matter. In Achim Weiss, Tom G. Abel, and Vanessa Hill, editors, *The First Stars*, pages 18–23, Berlin, Heidelberg, 2000. Springer Berlin Heidelberg.

[16] David S. Graff and Katherine Freese. Analysis of a hubble space telescope search for red dwarfs: Limits on baryonic matter in the galactic halo. *The Astrophysical Journal*, 456(1), jan 1996.

[17] Tisserand, P., Le Guillou, L., Afonso, C., et al. Limits on the macho content of the galactic halo from the eros-2 survey of the magellanic clouds. *A&A*, 469(2):387–404, 2007.

[18] Gerard Jungman, Marc Kamionkowski, and Kim Griest. Supersymmetric dark matter. *Physics Reports*, 267(5):195 – 373, 1996.

[19] Giorgio Arcadi, Maíra Dutra, Pradipta Ghosh, et al. The waning of the wimp? a review of models, searches, and constraints. *The European Physical Journal C*, 78(3):203, Mar 2018.

[20] Vasiliki A Mitsou. Overview of searches for dark matter at the LHC. *Journal of Physics: Conference Series*, 651:012023, nov 2015.

[21] Nicolao Fornengo. Status and perspectives of indirect and direct dark matter searches. *Advances in Space Research*, 41(12):2010 – 2018, 2008.

[22] Joerg Jaeckel and Andreas Ringwald. The low-energy frontier of particle physics. *Annual Review of Nuclear and Particle Science*, 60(1):405–437, 2010.

[23] Steven Weinberg. Approximate symmetries and pseudo-goldstone bosons. *Phys. Rev. Lett.*, 29:1698–1701, Dec 1972.

[24] Roberto D. Peccei. *The Strong CP Problem and Axions*, pages 3–17. Springer Berlin Heidelberg, Berlin, Heidelberg, 2008.

[25] Javier Redondo. Axions. http://webtheory.sns.it/ggilectures2019. Lectures given in the "GGI Lectures on the theory of fundamental interactions", GGI Firenze, 7-25 January 2019.

[26] Steven Weinberg. The u(1) problem. *Phys. Rev. D*, 11:3583–3593, Jun 1975.

[27] G. 't Hooft. Symmetry breaking through bell-jackiw anomalies. *Phys. Rev. Lett.*, 37:8–11, Jul 1976.

[28] G. 't Hooft. Computation of the quantum effects due to a four-dimensional pseudoparticle. *Phys. Rev. D*, 14:3432–3450, Dec 1976.

[29] Cumrun Vafa and Edward Witten. Parity conservation in quantum chromodynamics. *Phys. Rev. Lett.*, 53:535–536, Aug 1984.

[30] P. Di Vecchia. G. Veneziano R.J. Crewther and E. Witten. Chiral estimate of the electric dipole moment of the neutron in quantum chromodynamics. *Physics Letters B*, 91(3–4):487, 1980.

[31] Maxim Pospelov and Adam Ritz. Electric dipole moments as probes of new physics. *Annals of Physics*, 318(1):119 – 169, 2005. Special Issue.

[32] Norman F. Ramsey. Electric-dipole moments of particles. *Annual Review of Nuclear and Particle Science*, 32(1):211–233, 1982.

[33] J. H. Smith, E. M. Purcell, and N. F. Ramsey. Experimental limit to the electric dipole moment of the neutron. *Phys. Rev.*, 108:120–122, Oct 1957.

[34] C. A. Baker et al. An Improved experimental limit on the electric dipole moment of the neutron. *Phys. Rev. Lett.*, 97:131801, 2006.

[35] J. M. Pendlebury, S. Afach, N. J. Ayres, et al. Revised experimental upper limit on the electric dipole moment of the neutron. *Phys. Rev. D*, 92:092003, Nov 2015.

[36] R. D. Peccei and Helen R. Quinn. CP conservation in the presence of pseudoparticles. *Phys. Rev. Lett.*, 38:1440–1443, Jun 1977.

[37] Frank Wilczek. Problem of strong p and t invariance in the presence of instantons. *Physical Review Letters*, 40(5):279, 1978.

[38] Steven Weinberg. A new light boson? *Physical Review Letters*, 40(4):223, 1978.

[39] Jihn E. Kim. Weak-interaction singlet and strong CP invariance. *Phys. Rev. Lett.*, 43:103–107, Jul 1979.

[40] Jihn E. Kim. A review on axions and the strong cp problem. *AIP Conference Proceedings*, 1200(1):83–92, 2010.

[41] M.A. Shifman, A.I. Vainshtein, and V.I. Zakharov. Can confinement ensure natural cp invariance of strong interactions? *Nuclear Physics B*, 166(3):493 – 506, 1980.

[42] T. W. Donnelly, S. J. Freedman, R. S. Lytel, R. D. Peccei, and M. Schwartz. Do axions exist? *Phys. Rev. D*, 18:1607–1620, Sep 1978.

[43] C. Patrignani et al. Review of Particle Physics. *Chin. Phys.*, C40(10):100001, 2016.

[44] A. R. Zhitnitsky. The weinberg model of the cp violation and t odd correlations in weak decays. *Sov. J. Nucl. Phys.*, 31:529–534, 1980. [Yad. Fiz.31,1024(1980)].

[45] Michael Dine, Willy Fischler, and Mark Srednicki. A simple solution to the strong cp problem with a harmless axion. *Physics Letters B*, 104(3):199 – 202, 1981.

[46] Michael Dine and Willy Fischler. The not-so-harmless axion. *Physics Letters B*, 120(1):137 – 141, 1983.

[47] Guillermo Ballesteros, Javier Redondo, Andreas Ringwald, and Carlos Tamarit. Unifying inflation with the axion, dark matter, baryogenesis, and the seesaw mechanism. *Phys. Rev. Lett.*, 118:071802, Feb 2017.

[48] Guillermo Ballesteros, Javier Redondo, Andreas Ringwald, and Carlos Tamarit. Standard model—axion—seesaw—higgs portal inflation. five problems of particle physics and cosmology solved in one stroke. *Journal of Cosmology and Astroparticle Physics*, 2017(08):001–001, aug 2017.

[49] Anne Ernst, Andreas Ringwald, and Carlos Tamarit. Axion predictions in so(10) $\times$ u(1)pq models. *Journal of High Energy Physics*, 2018(2):103, Feb 2018.

[50] Yohei Ema, Koichi Hamaguchi, Takeo Moroi, and Kazunori Nakayama. Flaxion: a minimal extension to solve puzzles in the standard model. *Journal of High Energy Physics*, 2017(1):96, Jan 2017.

[51] Lorenzo Calibbi, Florian Goertz, Diego Redigolo, Robert Ziegler, and Jure Zupan. Minimal axion model from flavor. *Phys. Rev. D*, 95:095009, May 2017.

[52] Laurence F Abbott and P Sikivie. A cosmological bound on the invisible axion. *Physics Letters B*, 120(1-3):133–136, 1983.

[53] John Preskill, Mark B. Wise, and Frank Wilczek. Cosmology of the invisible axion. *Physics Letters B*, 120(1):127 – 132, 1983.

[54] Richard Lynn Davis. Goldstone bosons in string models of galaxy formation. *Phys. Rev. D*, 32:3172–3177, Dec 1985.

[55] R.L. Davis. Cosmic axions from cosmic strings. *Physics Letters B*, 180(3):225 – 230, 1986.

[56] S. Chang, C. Hagmann, and P. Sikivie. Studies of the motion and decay of axion walls bounded by strings. *Phys. Rev. D*, 59:023505, Dec 1998.

[57] David H. Lyth. Estimates of the cosmological axion density. *Physics Letters B*, 275(3):279 – 283, 1992.

[58] Michiyasu Nagasawa and Masahiro Kawasaki. Collapse of axionic domain wall and axion emission. *Phys. Rev. D*, 50:4821–4826, Oct 1994.

[59] Leanne D Duffy and Karl van Bibber. Axions as dark matter particles. *New Journal of Physics*, 11(10):105008, oct 2009.

[60] Pierre Sikivie. *Axion Cosmology*, pages 19–50. Springer Berlin Heidelberg, Berlin, Heidelberg, 2008.

[61] David J.E. Marsh. Axion cosmology. *Physics Reports*, 643:1 – 79, 2016. Axion cosmology.

[62] Georg G Raffelt. *Stars as laboratories for fundamental physics: The astrophysics of neutrinos, axions, and other weakly interacting particles*. University of Chicago press, 1996.

[63] Georg G. Raffelt. Astrophysical methods to constrain axions and other novel particle phenomena. *Physics Reports*, 198(1):1 – 113, 1990.

[64] Michael S Turner. Windows on the axion. *Physics Reports*, 197(2):67–97, 1990.

[65] Paolo Gondolo and Georg G. Raffelt. Solar neutrino limit on axions and kev-mass bosons. *Phys. Rev. D*, 79:107301, May 2009.

[66] H. Schlattl, A. Weiss, and G. Raffelt. Helioseismological constraint on solar axion emission. *Astroparticle Physics*, 10(4):353 – 359, 1999.

[67] Javier Redondo. Solar axion flux from the axion-electron coupling. *Journal of Cosmology and Astroparticle Physics*, 2013(12):008–008, dec 2013.

[68] N. Viaux, M. Catelan, P. B. Stetson, et al. Neutrino and axion bounds from the globular cluster m5 (ngc 5904). *Phys. Rev. Lett.*, 111:231301, Dec 2013.

[69] Georg G. Raffelt. Axion constraints from white dwarf cooling times. *Physics Letters B*, 166(4):402 – 406, 1986.

[70] Alejandro H. Córsico, Alejandra D. Romero, Leandro G. Althaus, et al. An asteroseismic constraint on the mass of the axion from the

period drift of the pulsating DA white dwarf star l19-2. *Journal of Cosmology and Astroparticle Physics*, 2016(07):036–036, jul 2016.

[71] J. Engel, D. Seckel, and A. C. Hayes. Emission and detectability of hadronic axions from sn 1987a. *Phys. Rev. Lett.*, 65:960–963, Aug 1990.

[72] Lev B. Leinson. Axion mass limit from observations of the neutron star in cassiopeia a. *Journal of Cosmology and Astroparticle Physics*, 2014(08):031–031, aug 2014.

[73] Jochen Keller and Armen Sedrakian. Axions from cooling compact stars: Pair-breaking processes. *Nuclear Physics A*, 897:62 – 69, 2013.

[74] Armen Sedrakian. Axion cooling of neutron stars. *Phys. Rev. D*, 93:065044, Mar 2016.

[75] Sanghyeon Chang and Kiwoon Choi. Hadronic axion window and the big-bang nucleosynthesis. *Physics Letters B*, 316(1):51 – 56, 1993.

[76] Eduard Massó and Ramon Toldrà. New constraints on a light spinless particle coupled to photons. *Phys. Rev. D*, 55:7967–7969, Jun 1997.

[77] Davide Cadamuro and Javier Redondo. Cosmological bounds on pseudo nambu-goldstone bosons. *Journal of Cosmology and Astroparticle Physics*, 2012(02):032–032, feb 2012.

[78] DN Spergel et al. Wilkinson microwave anisotropy probe (wmap) three year results: implications for cosmology, 2007. *Astrophys. J. Suppl*, 170:377.

[79] Patrick Fox, Aaron Pierce, and Scott Thomas. Probing a qcd string axion with precision cosmological measurements. *arXiv preprint hep-th/0409059*, 2004.

[80] Kyu Jung Bae, Ji-Haeng Huh, and Jihn E Kim. Updating the axion cold dark matter energy density. *Journal of Cosmology and Astroparticle Physics*, 2008(09):005, sep 2008.

[81] Olivier Wantz and E. P. S. Shellard. Axion cosmology revisited. *Phys. Rev. D*, 82:123508, Dec 2010.

[82] Max Tegmark, Daniel J. Eisenstein, Michael A. Strauss, et al. Cosmological constraints from the sdss luminous red galaxies. *Phys. Rev. D*, 74:123507, Dec 2006.

[83] María Beltrán, Juan García-Bellido, and Julien Lesgourgues. Isocurvature bounds on axions revisited. *Phys. Rev. D*, 75:103507, May 2007.

[84] Mark P. Hertzberg, Max Tegmark, and Frank Wilczek. Axion cosmology and the energy scale of inflation. *Phys. Rev. D*, 78:083507, Oct 2008.

[85] J Hamann, S Hannestad, G.G Raffelt, and Y.Y.Y Wong. Isocurvature forecast in the anthropic axion window. *Journal of Cosmology and Astroparticle Physics*, 2009(06):022–022, jun 2009.

[86] Planck Collaboration, Ade, P. A. R., Aghanim, N., et al. Planck 2013 results. xvi. cosmological parameters. *A&A*, 571:A16, 2014.

[87] Planck Collaboration, Ade, P. A. R., Aghanim, N., et al. Planck 2015 results - xiii. cosmological parameters. *A&A*, 594:A13, 2016.

[88] C. Hagmann, S. Chang, and P. Sikivie. Axion radiation from strings. *Phys. Rev. D*, 63:125018, May 2001.

[89] Takashi Hiramatsu, Masahiro Kawasaki, Ken'ichi Saikawa, and Toyokazu Sekiguchi. Production of dark matter axions from collapse of string-wall systems. *Phys. Rev. D*, 85:105020, May 2012.

[90] Masahiro Kawasaki, Ken'ichi Saikawa, and Toyokazu Sekiguchi. Axion dark matter from topological defects. *Phys. Rev. D*, 91:065014, Mar 2015.

[91] Bonati, Claudio, D'Elia, Massimo, Mariti, Marco, et al. Recent progress on qcd inputs for axion phenomenology. *EPJ Web Conf.*, 137:08004, 2017.

[92] Florian Burger, Ernst-Michael Ilgenfritz, Maria Paola Lombardo, Michael Müller-Preussker, and Anton Trunin. Topology (and axion's properties) from lattice qcd with a dynamical charm. *Nuclear Physics A*, 967:880 – 883, 2017. The 26th International Conference on Ultra-relativistic Nucleus-Nucleus Collisions: Quark Matter 2017.

[93] Evan Berkowitz, Michael I Buchoff, and Enrico Rinaldi. Lattice qcd input for axion cosmology. *Physical Review D*, 92(3):034507, 2015.

[94] Szabolcs Borsányi, Z Fodor, J Guenther, et al. Calculation of the axion mass based on high-temperature lattice quantum chromodynamics. *Nature*, 539(7627):69, 2016.

[95] Peter Petreczky, Hans-Peter Schadler, and Sayantan Sharma. The topological susceptibility in finite temperature qcd and axion cosmology. *Physics Letters B*, 762:498–505, 2016.

[96] Giovanni Grilli di Cortona, Edward Hardy, Javier Pardo Vega, and Giovanni Villadoro. The qcd axion, precisely. *Journal of High Energy Physics*, 2016(1):34, Jan 2016.

[97] Paola Arias, Davide Cadamuro, Mark Goodsell, et al. WISPy cold dark matter. *Journal of Cosmology and Astroparticle Physics*, 2012(06):013–013, jun 2012.

[98] Igor G. Irastorza and Javier Redondo. New experimental approaches in the search for axion-like particles. *Progress in Particle and Nuclear Physics*, 102:89 – 159, 2018.

[99] D. M. Lazarus, G. C. Smith, R. Cameron, et al. Search for solar axions. *Phys. Rev. Lett.*, 69:2333–2336, Oct 1992.

[100] Y. Inoue, Y. Akimoto, R. Ohta, et al. Search for solar axions with mass around 1 ev using coherent conversion of axions into photons. *Physics Letters B*, 668(2):93 – 97, 2008.

[101] M. Arik, S. Aune, K. Barth, et al. Search for solar axions by the cern axion solar telescope with $^3$He buffer gas: Closing the hot dark matter gap. *Phys. Rev. Lett.*, 112:091302, Mar 2014.

[102] S Andriamonje, S Aune, D Autiero, et al. An improved limit on the axion–photon coupling from the cast experiment. *Journal of Cosmology and Astroparticle Physics*, 2007(04):010, 2007.

[103] E. Armengaud, Q. Arnaud, C. Augier, et al. Axion searches with the edelweiss-ii experiment. *Journal of Cosmology and Astroparticle Physics*, 2013(11):067, 2013.

[104] E. Aprile, F. Agostini, M. Alfonsi, et al. Erratum: First axion results from the xenon100 experiment [phys. rev. d 90, 062009 (2014)]. *Phys. Rev. D*, 95:029904, Jan 2017.

[105] E. Aprile, F. Agostini, M. Alfonsi, et al. First axion results from the xenon100 experiment. *Phys. Rev. D*, 90:062009, Sep 2014.

[106] Search for solar axions in xmass, a large liquid-xenon detector. *Physics Letters B*, 724(1):46 – 50, 2013.

[107] A. V. Derbin, I. S. Drachnev, A. S. Kayunov, and V. N. Muratova. Constraints on the axion-electron coupling constant for solar axions appearing owing to bremsstrahlung and the compton process. *JETP Letters*, 95(7):339–344, Jun 2012.

[108] Y. S. Yoon, H. K. Park, H. Bhang, et al. Search for solar axions with csi(tl) crystal detectors. *Journal of High Energy Physics*, 2016(6):11, Jun 2016.

[109] D. S. Akerib, S. Alsum, C. Aquino, et al. First searches for axions and axionlike particles with the lux experiment. *Phys. Rev. Lett.*, 118:261301, Jun 2017.

[110] A Payez, J.R Cudell, and D Hutsemékers. New polarimetric constraints on axion-like particles. *Journal of Cosmology and Astroparticle Physics*, 2012(07):041–041, jul 2012.

[111] D Horns and M Meyer. Indications for a pair-production anomaly from the propagation of VHE gamma-rays. *Journal of Cosmology and Astroparticle Physics*, 2012(02):033–033, feb 2012.

[112] J. Biteau and D. A. Williams. The extragalactic background light, the hubble constant, and anomalies: conclusions from 20 years of tev $\gamma$-ray observations. *The Astrophysical Journal*, 812(1):60, oct 2015.

[113] Alessandro De Angelis, Giorgio Galanti, and Marco Roncadelli. Relevance of axionlike particles for very-high-energy astrophysics. *Phys. Rev. D*, 84:105030, Nov 2011.

[114] Melanie Simet, Dan Hooper, and Pasquale D. Serpico. Milky way as a kiloparsec-scale axionscope. *Phys. Rev. D*, 77:063001, Mar 2008.

[115] M. A. Sánchez-Conde, D. Paneque, E. Bloom, F. Prada, and A. Domínguez. Hints of the existence of axionlike particles from the gamma-ray spectra of cosmological sources. *Phys. Rev. D*, 79:123511, Jun 2009.

[116] Asimina Arvanitaki, Masha Baryakhtar, Savas Dimopoulos, Sergei Dubovsky, and Robert Lasenby. Black hole mergers and the qcd axion at advanced ligo. *Phys. Rev. D*, 95:043001, Feb 2017.

[117] M. Ted Ressell. Limits to the radiative decay of the axion. *Phys. Rev. D*, 44:3001–3020, Nov 1991.

[118] Matthew A. Bershady, M. Ted Ressell, and Michael S. Turner. Telescope search for a 3-ev to 8-ev axion. *Phys. Rev. Lett.*, 66:1398–1401, Mar 1991.

[119] Daniel Grin, Giovanni Covone, Jean-Paul Kneib, et al. Telescope search for decaying relic axions. *Phys. Rev. D*, 75:105018, May 2007.

[120] B. D. Blout, E. J. Daw, M. P. Decowski, et al. A radio telescope search for axions. *The Astrophysical Journal*, 546(2):825–828, jan 2001.

[121] P. Sikivie. Experimental tests of the "invisible" axion. *Phys. Rev. Lett.*, 51:1415–1417, Oct 1983.

[122] S. J. Asztalos, R. F. Bradley, L. Duffy, et al. Improved rf cavity search for halo axions. *Phys. Rev. D*, 69:011101, Jan 2004.

[123] L. D. Duffy, P. Sikivie, D. B. Tanner, et al. High resolution search for dark-matter axions. *Phys. Rev. D*, 74:012006, Jul 2006.

[124] S. J. Asztalos, G. Carosi, C. Hagmann, et al. Squid-based microwave cavity search for dark-matter axions. *Phys. Rev. Lett.*, 104:041301, Jan 2010.

[125] N. Du, N. Force, R. Khatiwada, et al. Search for invisible axion dark matter with the axion dark matter experiment. *Phys. Rev. Lett.*, 120:151301, Apr 2018.

[126] B. M. Brubaker, L. Zhong, Y. V. Gurevich, et al. First results from a microwave cavity axion search at 24 $\mu$eV. *Phys. Rev. Lett.*, 118:061302, Feb 2017.

[127] S. DePanfilis, A. C. Melissinos, B. E. Moskowitz, et al. Limits on the abundance and coupling of cosmic axions at $4.5 \leq m_a \leq 5.0\,\mu$ev. *Phys. Rev. Lett.*, 59:839–842, Aug 1987.

[128] Ben T. McAllister, Graeme Flower, Eugene N. Ivanov, et al. The organ experiment: An axion haloscope above 15 ghz. *Physics of the Dark Universe*, 18:67 – 72, 2017.

[129] Petrakou, Eleni and for CAPP/IBS. Haloscope searches for dark matter axions at the center for axion and precision physics research. *EPJ Web Conf.*, 164:01012, 2017.

[130] Allen Caldwell, Gia Dvali, Béla Majorovits, et al. Dielectric haloscopes: a new way to detect axion dark matter. *Physical review letters*, 118(9):091801, 2017.

[131] Dmitry Budker, Peter W. Graham, Micah Ledbetter, Surjeet Rajendran, and Alexander O. Sushkov. Proposal for a cosmic axion spin precession experiment (casper). *Phys. Rev. X*, 4:021030, May 2014.

[132] Antoine Garcon, Deniz Aybas, John W Blanchard, et al. The cosmic axion spin precession experiment (CASPEr): a dark-matter search with nuclear magnetic resonance. *Quantum Science and Technology*, 3(1):014008, dec 2017.

[133] G Ruoso, A Lombardi, A Ortolan, et al. The quax proposal: a search of galactic axion with magnetic materials. *Journal of Physics: Conference Series*, 718(4):042051, 2016.

[134] R. Barbieri, C. Braggio, G. Carugno, et al. Searching for galactic axions through magnetized media: The quax proposal. *Physics of the Dark Universe*, 15:135 – 141, 2017.

[135] Jonathan L. Ouellet, Chiara P. Salemi, Joshua W. Foster, et al. First results from abracadabra-10 cm: A search for sub-$\mu$eV axion dark matter. *Phys. Rev. Lett.*, 122:121802, Mar 2019.

[136] F. Caspers and Y. Semertzidis. Ferrimagnetic resonance, magnetostatic waves and open resonators for axion detection. In *Cosmic axions. Proceedings, Workshop, Upton, USA, April 13-14, 1989*, pages 0173–183, 1989.

[137] Graeme Flower, Jeremy Bourhill, Maxim Goryachev, and Michael E. Tobar. Broadening frequency range of a ferromagnetic axion haloscope with strongly coupled cavity–magnon polaritons. *Physics of the Dark Universe*, 25:100306, 2019.

[138] Klaus Ehret, Maik Frede, Samvel Ghazaryan, et al. New alps results on hidden-sector lightweights. *Physics Letters B*, 689(4):149 – 155, 2010.

[139] R. Ballou, G. Deferne, M. Finger, et al. New exclusion limits on scalar and pseudoscalar axionlike particles from light shining through a wall. *Phys. Rev. D*, 92:092002, Nov 2015.

[140] F Hoogeveen and T Ziegenhagen. Production and detection of light bosons using optical resonators. *Nuclear Physics B*, 358(1):3 – 26, 1991.

[141] P. Sikivie, D. B. Tanner, and Karl van Bibber. Resonantly enhanced axion-photon regeneration. *Phys. Rev. Lett.*, 98:172002, Apr 2007.

[142] Guido Mueller, Pierre Sikivie, D. B. Tanner, and Karl van Bibber. Detailed design of a resonantly enhanced axion-photon regeneration experiment. *Phys. Rev. D*, 80:072004, Oct 2009.

[143] Y. Semertzidis, R. Cameron, G. Cantatore, et al. Limits on the production of light scalar and pseudoscalar particles. *Phys. Rev. Lett.*, 64:2988–2991, Jun 1990.

[144] Della Valle, Federico, Ejlli, Aldo, Gastaldi, Ugo, et al. The pvlas experiment: measuring vacuum magnetic birefringence and dichroism with a birefringent fabry-perot cavity. *Eur. Phys. J. C*, 76(1):24, 2016.

[145] Ephraim Fischbach and Carrick Talmadge. Six years of the fifth force. *Nature*, 356(6366):207–215, 1992.

[146] S. A. Hoedl, F. Fleischer, E. G. Adelberger, and B. R. Heckel. Improved constraints on an axion-mediated force. *Phys. Rev. Lett.*, 106:041801, Jan 2011.

[147] Giles D. Hammond, Clive C. Speake, Christian Trenkel, and Antonio Pulido Patón. New constraints on short-range forces coupling mass to intrinsic spin. *Phys. Rev. Lett.*, 98:081101, Feb 2007.

[148] Wei-Tou Ni, Sheau-shi Pan, Hsien-Chi Yeh, Li-Shing Hou, and Juling Wan. Search for an axionlike spin coupling using a paramagnetic salt with a dc squid. *Phys. Rev. Lett.*, 82:2439–2442, Mar 1999.

[149] A. N. Youdin, D. Krause, Jr., K. Jagannathan, L. R. Hunter, and S. K. Lamoreaux. Limits on spin-mass couplings within the axion window. *Phys. Rev. Lett.*, 77:2170–2173, Sep 1996.

[150] R. C. Ritter, L. I. Winkler, and G. T. Gillies. Search for anomalous spin-dependent forces with a polarized-mass torsion pendulum. *Phys. Rev. Lett.*, 70:701–704, Feb 1993.

[151] B. J. Venema, P. K. Majumder, S. K. Lamoreaux, B. R. Heckel, and E. N. Fortson. Search for a coupling of the earth's gravitational field

to nuclear spins in atomic mercury. *Phys. Rev. Lett.*, 68:135–138, Jan 1992.

[152] E. Fischbach and C.L. Talmadge. *The Search for Non-Newtonian Gravity*. AIP-Press S. Springer New York, 1998.

[153] D. J. Wineland, J. J. Bollinger, D. J. Heinzen, W. M. Itano, and M. G. Raizen. Search for anomalous spin-dependent forces using stored-ion spectroscopy. *Phys. Rev. Lett.*, 67:1735–1738, Sep 1991.

[154] J.M. Daniels and Wei-Tou Ni. A torsion balance search for long-range spin-dependent forces using polarized nuclei. *Physica B: Condensed Matter*, 194–196, Part 1:149 – 150, 1994.

[155] Junyi Lee, Attaallah Almasi, and Michael Romalis. Improved limits on spin-mass interactions. *Phys. Rev. Lett.*, 120:161801, Apr 2018.

[156] N. Crescini, C. Braggio, G. Carugno, et al. Improved constraints on monopole–dipole interaction mediated by pseudo-scalar bosons. *Physics Letters B*, 773:677 – 680, 2017.

[157] B. Frois, V. W. Hughes, and N. De Groot, editors. *The spin structure of the nucleon. Proceedings, International School of Nucleon Structure, 1st Course, Erice, Italy, August 3-10, 1995*, 1997.

[158] A. Airapetian, N. Akopov, Z. Akopov, et al. Precise determination of the spin structure function $g_1$ of the proton, deuteron, and neutron. *Phys. Rev. D*, 75:012007, Jan 2007.

[159] R Barbieri, M Cerdonio, G Fiorentini, and S Vitale. Axion to magnon conversion. a scheme for the detection of galactic axions. *Physics Letters B*, 226(3):357 – 360, 1989.

[160] AI Kakhidze and IV Kolokolov. Antiferromagnetic axion detector. *Zh. Eksp. Teor. Fiz*, 99:1077–1081, 1991.

[161] PV Vorobyov, AN Kirpotin, ME Rovkin, and AP Boldyrev. Ferromagnetic detectors of axions in rf (s-x) band. *arXiv preprint hep-ph/9506371*, 1995.

[162] Lawrence Krauss, John Moody, Frank Wilczek, and Donald E. Morris. Calculations for cosmic axion detection. *Phys. Rev. Lett.*, 55:1797–1800, Oct 1985.

[163] L.D. Landau, E.M. Lifšic, E.M. Lifshitz, et al. *Statistical Physics: Theory of the Condensed State*. Course of theoretical physics. Elsevier Science, 1980.

[164] Michael S. Turner. Periodic signatures for the detection of cosmic axions. *Phys. Rev. D*, 42:3572–3575, Nov 1990.

[165] Michael S. Turner and Frank Wilczek. Positron line radiation as a signature of particle dark matter in the halo. *Phys. Rev. D*, 42:1001–1007, Aug 1990.

[166] Erik W. Lentz, Thomas R. Quinn, Leslie J. Rosenberg, and Michael J. Tremmel. A new signal model for axion cavity searches from n -body simulations. *The Astrophysical Journal*, 845(2):121, 2017.

[167] Peter W. Graham and Surjeet Rajendran. New observables for direct detection of axion dark matter. *Phys. Rev. D*, 88:035023, Aug 2013.

[168] Teng Wu, John W. Blanchard, Gary P. Centers, et al. Search for axionlike dark matter with a liquid-state nuclear spin comagnetometer. *Phys. Rev. Lett.*, 122:191302, May 2019.

[169] Antoine Garcon, John W. Blanchard, Gary P. Centers, et al. Constraints on bosonic dark matter from ultralow-field nuclear magnetic resonance. https://arxiv.org/abs/1902.04644.

[170] Christopher T. Hill. Axion induced oscillating electric dipole moment of the electron. *Phys. Rev. D*, 93:025007, Jan 2016.

[171] V. V. Flambaum, B. M. Roberts, and Y. V. Stadnik. Comment on "axion induced oscillating electric dipole moments". *Phys. Rev. D*, 95:058701, Mar 2017.

[172] Stephon Alexander and Robert Sims. Detecting axions via induced electron spin precession. *Phys. Rev. D*, 98:015011, Jul 2018.

[173] V. Andreev, D. G. Ang, D. DeMille, et al. Improved limit on the electric dipole moment of the electron. *Nature*, 562(7727):355–360, 2018.

[174] Christopher T. Hill. Private communication.

[175] Gary P. Centers, John W. Blanchard, Jan Conrad, et al. Stochastic amplitude fluctuations of bosonic dark matter and revised constraints on linear couplings. https://arxiv.org/abs/1905.13650.

[176] Charles Kittel. *Introduction to Solid State Physics*. Wiley, 8 edition, 2004.

[177] N. Bloembergen and R. V. Pound. Radiation damping in magnetic resonance experiments. *Phys. Rev.*, 95:8–12, Jul 1954.

[178] M.P. Augustine. Transient properties of radiation damping. *Progress in Nuclear Magnetic Resonance Spectroscopy*, 40(2):111 – 150, 2002.

[179] Stanley Bloom. Effects of radiation damping on spin dynamics. *Journal of Applied Physics*, 28(7):800–805, 1957.

[180] Carol Gray Montgomery, Robert Henry Dicke, and Edward M Purcell. *Principles of microwave circuits*. Number 25. Iet, 1948.

[181] J.D. Jackson. *Classical Electrodynamics*. Wiley, 2012.

[182] Martin Frimmer and Lukas Novotny. The classical bloch equations. *American Journal of Physics*, 82(10):947–954, 2014.

[183] S. K. Lamoreaux, K. A. van Bibber, K. W. Lehnert, and G. Carosi. Analysis of single-photon and linear amplifier detectors for microwave cavity dark matter axion searches. *Phys. Rev. D*, 88:035020, Aug 2013.

[184] A. A. Clerk, M. H. Devoret, S. M. Girvin, Florian Marquardt, and R. J. Schoelkopf. Introduction to quantum noise, measurement, and amplification. *Rev. Mod. Phys.*, 82:1155–1208, Apr 2010.

[185] C. Carboni, I. S. Mackenzie, and M. A. H. McCausland. Nuclear magnetic resonance at microwave frequencies. *Hyperfine Interactions*, 51(1):1139–1144, Jun 1989.

[186] Charles Kittel. Interpretation of anomalous larmor frequencies in ferromagnetic resonance experiment. *Phys. Rev.*, 71:270–271, Feb 1947.

[187] M. Sparks and C. Kittel. Ferromagnetic relaxation mechanism for $m_z$ in yttrium iron garnet. *Phys. Rev. Lett.*, 4:232–234, Mar 1960.

[188] Michael Tavis and Frederick W. Cummings. Exact solution for an $n$-molecule—radiation-field hamiltonian. *Phys. Rev.*, 170:379–384, Jun 1968.

[189] Xufeng Zhang, Chang-Ling Zou, Liang Jiang, and Hong X. Tang. Strongly coupled magnons and cavity microwave photons. *Phys. Rev. Lett.*, 113:156401, Oct 2014.

[190] Yutaka Tabuchi, Seiichiro Ishino, Toyofumi Ishikawa, et al. Hybridizing ferromagnetic magnons and microwave photons in the quantum limit. *Phys. Rev. Lett.*, 113:083603, Aug 2014.

[191] Hans Huebl, Christoph W. Zollitsch, Johannes Lotze, et al. High cooperativity in coupled microwave resonator ferrimagnetic insulator hybrids. *Phys. Rev. Lett.*, 111:127003, Sep 2013.

[192] Yutaka Tabuchi, Seiichiro Ishino, Atsushi Noguchi, et al. Coherent coupling between a ferromagnetic magnon and a superconducting qubit. *Science*, 349(6246):405–408, 2015.

[193] Alberto Ghirri, Claudio Bonizzoni, Dario Gerace, et al. Ybco microwave resonators for strong collective coupling with spin ensembles. 106, 03 2015.

[194] Alberto Ghirri, Claudio Bonizzoni, Filippo Troiani, et al. Coherently coupling distinct spin ensembles through a high-$t_c$ superconducting resonator. 93, 05 2016.

[195] Claudio Bonizzoni, Alberto Ghirri, Matteo Atzori, et al. Coherent coupling between vanadyl phthalocyanine spin ensemble and microwave photons: Towards integration of molecular spin qubits into quantum circuits. 7, 10 2017.

[196] Isabella Boventer, Marco Pfirrmann, Julius Krause, et al. Complex temperature dependence of coupling and dissipation of cavity magnon polaritons from millikelvin to room temperature. *Phys. Rev. B*, 97:184420, May 2018.

[197] Michael Harder and Can-Ming Hu. Cavity spintronics: An early review of recent progress in the study of magnon–photon level repulsion. *Solid State Physics - Advances in Research and Applications*, 11 2018.

[198] Khabat Heshami, Duncan G. England, Peter C. Humphreys, et al. Quantum memories: emerging applications and recent advances. *Journal of Modern Optics*, 63(20):2005–2028, 2016.

[199] Gershon Kurizki, Patrice Bertet, Yuimaru Kubo, et al. Quantum technologies with hybrid systems. *Proceedings of the National Academy of Sciences*, 112(13):3866–3873, 2015.

[200] R. Hisatomi, A. Osada, Y. Tabuchi, et al. Bidirectional conversion between microwave and light via ferromagnetic magnons. *Phys. Rev. B*, 93:174427, May 2016.

[201] Caterina Braggio, G Carugno, Marco Guarise, A Ortolan, and G Ruoso. Optical manipulation of a magnon-photon hybrid system. 118, 09 2016.

[202] A. V. Chumak, V. I. Vasyuchka, A. A. Serga, and B. Hillebrands. Magnon spintronics. *Nature Physics*, 11:453 EP –, Jun 2015. Review Article.

[203] Dany Lachance-Quirion, Yutaka Tabuchi, Arnaud Gloppe, Koji Usami, and Yasunobu Nakamura. Hybrid quantum systems based on magnonics. *Applied Physics Express*, 12(7):070101, jun 2019.

[204] Hasan Padamsee, Jens Knobloch, Tom Hays, et al. *RF superconductivity for accelerators*, volume 2011. Wiley Online Library, 2008.

[205] D. Alesini, C. Braggio, G. Carugno, et al. Galactic axions search with a superconducting resonant cavity. *Phys. Rev. D*, 99:101101, May 2019.

[206] Luca Di Luzio, Federico Mescia, and Enrico Nardi. Redefining the axion window. *Phys. Rev. Lett.*, 118:031801, Jan 2017.

[207] I. Stern, A. A. Chisholm, J. Hoskins, et al. Cavity design for high-frequency axion dark matter detectors. *Review of Scientific Instruments*, 86(12):123305, 2015.

[208] D. Di Gioacchino, C. Gatti, D. Alesini, et al. Microwave losses in a dc magnetic field in superconducting cavities for axion studies. *IEEE Transactions on Applied Superconductivity*, 29(5):1–5, Aug 2019.

[209] The saga of yig: Spectra, thermodynamics, interaction and relaxation of magnons in a complex magnet. *Physics Reports*, 229(3):81 – 144, 1993.

[210] R T. Farrar. Spin-lattice relaxation time in yttrium iron garnet. *Journal of Applied Physics*, 29, 03 1958.

[211] E. G. Spencer, R. C. LeCraw, and A. M. Clogston. Low-temperature line-width maximum in yttrium iron garnet. *Phys. Rev. Lett.*, 3:32–33, Jul 1959.

[212] R. C. LeCraw, E. G. Spencer, and C. S. Porter. Ferromagnetic resonance line width in yttrium iron garnet single crystals. *Phys. Rev.*, 110:1311–1313, Jun 1958.

[213] J. F. Dillon. Ferrimagnetic resonance in rare-earth-doped yttrium iron garnet. iii. linewidth. *Phys. Rev.*, 127:1495–1501, Sep 1962.

[214] R. C. LeCraw and E. G. Spencer. Surface-independent spin-wave relaxation in ferromagnetic resonance of yttrium iron garnet. *Journal of Applied Physics*, 30(4):S185–S186, 1959.

[215] Andrew Princep, Russell Ewings, Simon Ward, et al. The full magnon spectrum of yttrium iron garnet. *npj Quantum Materials*, 2, 12 2017.

[216] H.C. Dake. *The Art of Gem Cutting: Including Cabochons, Faceting, Spheres, Tumbling, and Special Techniques*. Gem Guides Book Company, 1987.

[217] Cristiano Ciuti and Iacopo Carusotto. Input-output theory of cavities in the ultrastrong coupling regime: The case of time-independent cavity parameters. *Phys. Rev. A*, 74:033811, Sep 2006.

[218] D.M. Pozar. *Microwave Engineering*. Wiley, 2004.

[219] Emil Zeuthen, Albert Schliesser, Jacob M. Taylor, and Anders S. Sørensen. Electrooptomechanical equivalent circuits for quantum transduction. *Phys. Rev. Applied*, 10:044036, Oct 2018.

[220] L. R. Walker. Resonant modes of ferromagnetic spheroids. *Journal of Applied Physics*, 29(3):318–323, 1958.

[221] P. C. Fletcher and R. O. Bell. Ferrimagnetic resonance modes in spheres. *Journal of Applied Physics*, 30(5):687–698, 1959.

[222] Crescini, N., Alesini, D., Braggio, C., et al. Operation of a ferromagnetic axion haloscope at $m_a = 58\,\mu$eV. *Eur. Phys. J. C*, 78(9):703, 2018.

[223] Athanasios Papoulis and S. Unnikrishna Pillai. *Probability, Random Variables, and Stochastic Processes*. McGraw Hill, Boston, fourth edition, 2002.

[224] T. Mimura. The early history of the high electron mobility transistor (hemt). *IEEE Transactions on Microwave Theory and Techniques*, 50(3):780–782, March 2002.

[225] C. Braggio, G. Bressi, G. Carugno, et al. Characterization of a low noise microwave receiver for the detection of vacuum photons. *Nuclear Instruments and Methods in Physics Research Section A: Accelerators, Spectrometers, Detectors and Associated Equipment*, 603(3):451 – 455, 2009.

[226] B. Yurke, L. R. Corruccini, P. G. Kaminsky, et al. Observation of parametric amplification and deamplification in a josephson parametric amplifier. *Phys. Rev. A*, 39:2519–2533, Mar 1989.

[227] Manuel Castellanos Beltran and K W. Lehnert. Widely tunable parametric amplifier based on a superconducting quantum interference device array resonator. *Applied Physics Letters*, 91:083509–083509, 08 2007.

[228] M. Sandberg, C. M. Wilson, F. Persson, et al. Tuning the field in a microwave resonator faster than the photon lifetime. *Applied Physics Letters*, 92(20):203501, 2008.

[229] Erik A. Tholén, Adem Ergül, Evelyn M. Doherty, et al. Nonlinearities and parametric amplification in superconducting coplanar waveguide resonators. *Applied Physics Letters*, 90(25):253509, 2007.

[230] T. Yamamoto, K. Inomata, M. Watanabe, et al. Flux-driven josephson parametric amplifier. *Applied Physics Letters*, 93(4):042510, 2008.

[231] B. Abdo, O. Suchoi, E. Segev, et al. Intermodulation and parametric amplification in a superconducting stripline resonator integrated with a dc-SQUID. *EPL (Europhysics Letters)*, 85(6):68001, mar 2009.

[232] J. Y. Mutus, T. C. White, R. Barends, et al. Strong environmental coupling in a josephson parametric amplifier. *Applied Physics Letters*, 104(26):263513, 2014.

[233] J. R. Johansson, G. Johansson, C. M. Wilson, and Franco Nori. Dynamical casimir effect in a superconducting coplanar waveguide. *Phys. Rev. Lett.*, 103:147003, Sep 2009.

[234] C. M. Wilson, G. Johansson, A. Pourkabirian, et al. Observation of the dynamical casimir effect in a superconducting circuit. *Nature*, 479:376 EP –, Nov 2011.

[235] Ananda Roy and Michel Devoret. Introduction to parametric amplification of quantum signals with josephson circuits. *Comptes Rendus Physique*, 17(7):740 – 755, 2016. Quantum microwaves / Micro-ondes quantiques.

[236] N. Bergeal, R. Vijay, V. E. Manucharyan, et al. Analog information processing at the quantum limit with a josephson ring modulator. *Nature Physics*, 6:296 EP –, Feb 2010. Article.

[237] N. Roch, E. Flurin, F. Nguyen, et al. Widely tunable, nondegenerate three-wave mixing microwave device operating near the quantum limit. *Phys. Rev. Lett.*, 108:147701, Apr 2012.

[238] Beltrán B Kuster M., Raffelt G. *Axions. Lecture Notes in Physics*. Springer, Berlin, Heidelberg, 2008.

[239] Tiara Battich, Alejandro Córsico, Leandro Gabriel Althaus, and Marcelo Miguel Miller Bertolami. First axion bounds from a pulsating helium-rich white dwarf star. 2016:062–062, 08 2016.

[240] Alejandro H. Córsico, Alejandra D. Romero, Leandro G. Althaus, et al. An asteroseismic constraint on the mass of the axion from the period drift of the pulsating DA white dwarf star L19-2. *JCAP*, 1607(07):036, 2016.

[241] Maxim Goryachev, Warrick G. Farr, Daniel L. Creedon, et al. High-cooperativity cavity qed with magnons at microwave frequencies. *Phys. Rev. Applied*, 2:054002, Nov 2014.

[242] Benjamin M. Brubaker. *First results from the HAYSTAC axion search*. PhD thesis, Yale U., 2017.

[243] C. Boutan, M. Jones, B. H. LaRoque, et al. Piezoelectrically tuned multimode cavity search for axion dark matter. *Phys. Rev. Lett.*, 121:261302, Dec 2018.

[244] Gray Rybka, Andrew Wagner, Kunal Patel, et al. Search for dark matter axions with the orpheus experiment. *Phys. Rev. D*, 91:011701, Jan 2015.

[245] Matteo Atzori, Lorenzo Tesi, Elena Morra, et al. Room-temperature quantum coherence and rabi oscillations in vanadyl phthalocyanine: Toward multifunctional molecular spin qubits. *Journal of the American Chemical Society*, 138(7):2154–2157, Feb 2016.

[246] Dorsa Komijani, Alberto Ghirri, Claudio Bonizzoni, et al. Radical-lanthanide ferromagnetic interaction in a $Tb^{iii}$ bis-phthalocyaninato complex. *Phys. Rev. Materials*, 2:024405, Feb 2018.

[247] Gianpaolo Carosi, Gray Rybka, and Karl van Bibber. *Microwave Cavities and Detectors for Axion Research, proceedings of the 2nd international Workshop*, volume 211. 2018.

[248] M Brune, S Haroche, V Lefevre, JM Raimond, and N Zagury. Quantum nondemolition measurement of small photon numbers by rydberg-atom phase-sensitive detection. *Physical review letters*, 65(8):976, 1990.

[249] M. Brune, F. Schmidt-Kaler, A. Maali, et al. Quantum rabi oscillation: A direct test of field quantization in a cavity. *Phys. Rev. Lett.*, 76:1800–1803, Mar 1996.

[250] M. Tada, Y. Kishimoto, K. Kominato, et al. Single-photon detection of microwave blackbody radiations in a low-temperature resonant-cavity with high rydberg atoms. *Physics Letters A*, 349(6):488 – 493, 2006.

[251] Sébastien Gleyzes, Stefan Kuhr, Christine Guerlin, et al. Quantum jumps of light recording the birth and death of a photon in a cavity. *Nature*, 446(7133):297–300, 2007.

[252] G. Nogues, A. Rauschenbeutel, S. Osnaghi, et al. Seeing a single photon without destroying it. *Nature*, 400(6741):239–242, 1999.

[253] K. Yamamoto, M. Tada, Y. Kishimoto, et al. The rydberg-atom-cavity axion search. In H. V. Klapdor-Kleingrothaus, editor, *Dark Matter in Astro- and Particle Physics*, pages 638–645, Berlin, Heidelberg, 2001. Springer Berlin Heidelberg.

[254] M. Tada, Y. Kishimoto, K. Kominato, et al. Carrack ii — a new large-scale experiment to search for axions with rydberg-atom cavity detector. *Nuclear Physics B - Proceedings Supplements*, 72:164 – 168, 1999. Proceedings of the 5th IFT Workshop on Axions.

[255] Chandra M Natarajan, Michael G Tanner, and Robert H Hadfield. Superconducting nanowire single-photon detectors: physics and applications. *Superconductor Science and Technology*, 25(6):063001, 2012.

[256] D. I. Schuster, A. A. Houck, J. A. Schreier, et al. Resolving photon number states in a superconducting circuit. *Nature*, 445(7127):515–518, 2007.

[257] B. R. Johnson, M. D. Reed, A. A. Houck, et al. Quantum non-demolition detection of single microwave photons in a circuit. *Nat Phys*, 6(9):663–667, Sep 2010.

[258] Kunihiro Inomata, Zhirong Lin, Kazuki Koshino, et al. Single microwave-photon detector using an artificial l-type three-level system. *Nature Communications*, 7(1):12303, 2016.

[259] S. Kono, K. Koshino, Y. Tabuchi, A. Noguchi, and Y. Nakamura. Quantum non-demolition detection of an itinerant microwave photon. *Nature Physics*, 14(6):546–549, 2018.

[260] Jean-Claude Besse, Simone Gasparinetti, Michele C. Collodo, et al. Single-shot quantum nondemolition detection of individual itinerant microwave photons. *Phys. Rev. X*, 8:021003, Apr 2018.

[261] J. Govenius, R. E. Lake, K. Y. Tan, et al. Microwave nanobolometer based on proximity josephson junctions. *Phys. Rev. B*, 90:064505, Aug 2014.

[262] Y.-F. Chen, D. Hover, S. Sendelbach, et al. Microwave photon counter based on josephson junctions. *Phys. Rev. Lett.*, 107:217401, Nov 2011.

[263] G. Oelsner, C. K. Andersen, M. Rehák, et al. Detection of weak microwave fields with an underdamped josephson junction. *Phys. Rev. Applied*, 7:014012, Jan 2017.

[264] E. V. Il'ichev. A microwave photon detector. *Physics of the Solid State*, 58(11):2160–2164, Nov 2016.

[265] L. S. Kuzmin, A. S. Sobolev, C. Gatti, et al. Single photon counter based on a josephson junction at 14 ghz for searching galactic axions. *IEEE Transactions on Applied Superconductivity*, 28(7):1–5, Oct 2018.

[266] Dany Lachance-Quirion, Yutaka Tabuchi, Seiichiro Ishino, et al. Resolving quanta of collective spin excitations in a millimeter-sized ferromagnet. *Science Advances*, 3(7), 2017.

[267] Huaixiu Zheng, Matti Silveri, R. T. Brierley, S. M. Girvin, and K. W. Lehnert. Accelerating dark-matter axion searches with quantum measurement technology. 2016.

[268] T. C. Black, P. R. Huffman, D. L. Jacobson, et al. Precision neutron interferometric measurement of the $nd$ coherent neutron scattering length and consequences for models of three-nucleon forces. *Phys. Rev. Lett.*, 90:192502, May 2003.

[269] K. Schoen, D. L. Jacobson, M. Arif, et al. Precision neutron interferometric measurements and updated evaluations of the $n - p$ and $n - d$ coherent neutron scattering lengths. *Phys. Rev. C*, 67:044005, Apr 2003.

[270] B. P. Abbott, R. Abbott, T. D. Abbott, et al. Observation of gravitational waves from a binary black hole merger. *Phys. Rev. Lett.*, 116:061102, Feb 2016.

[271] Kazuaki Kuroda, Wei-Tou Ni, and Wei-Ping Pan. Gravitational waves: Classification, methods of detection, sensitivities and sources. *International Journal of Modern Physics D*, 24(14):1530031, 2015.

[272] Tomotada Akutsu, Seiji Kawamura, Atsushi Nishizawa, et al. Search for a stochastic background of 100-mhz gravitational waves with laser interferometers. *Phys. Rev. Lett.*, 101:101101, Sep 2008.

[273] Asuka Ito, Tomonori Ikeda, Miuchi Kentaro, and Jiro Soda. Probing ghz gravitational waves with graviton-magnon resonance. 2019.

[274] Charles W. Misner, Kip S. Thorne, and John A. Wheeler. *Gravitation*. Princeton University Press, 2017.

[275] Niklas G. Nielsen, Andrea Palessandro, and Martin S. Sloth. Gravitational atoms. *Phys. Rev. D*, 99:123011, Jun 2019.

[276] Eugene D. Commins, J. D. Jackson, and David P. DeMille. The electric dipole moment of the electron: An intuitive explanation for the evasion of schiff's theorem. *American Journal of Physics*, 75(6):532–536, 2007.

[277] C.-P. Liu, M. J. Ramsey-Musolf, W. C. Haxton, R. G. E. Timmermans, and A. E. L. Dieperink. Atomic electric dipole moments: The schiff theorem and its corrections. *Phys. Rev. C*, 76:035503, Sep 2007.

[278] R. A. Sen'kov, N. Auerbach, V. V. Flambaum, and V. G. Zelevinsky. Reexamination of the schiff theorem. *Phys. Rev. A*, 77:014101, Jan 2008.

[279] R. C. Jaklevic, John Lambe, A. H. Silver, and J. E. Mercereau. Quantum interference effects in josephson tunneling. *Phys. Rev. Lett.*, 12:159–160, Feb 1964.

[280] S. N. Erné, H.-D. Hahlbohm, and H. Lübbig. Theory of rf-biased superconducting quantum interference device for nonhysteretic regime. *Journal of Applied Physics*, 47(12):5440–5442, 1976.

[281] Marco Aprili. The nanosquid makes its debut. *Nature Nanotechnology*, 1(1):15–16, 2006.

[282] R. Kleiner, D. Koelle, F. Ludwig, and J. Clarke. Superconducting quantum interference devices: State of the art and applications. *Proceedings of the IEEE*, 92(10):1534–1548, Oct 2004.

[283] Clarke John and Braginski Alex I. *The SQUID Handbook*. John Wiley & Sons, Ltd, 2005.

[284] I. K. Kominis, T. W. Kornack, J. C. Allred, and M. V. Romalis. A subfemtotesla multichannel atomic magnetometer. *Nature*, 422(6932):596–599, 2003.

[285] I. M. Savukov, S. J. Seltzer, M. V. Romalis, and K. L. Sauer. Tunable atomic magnetometer for detection of radio-frequency magnetic fields. *Phys. Rev. Lett.*, 95:063004, Aug 2005.

[286] Dmitry Budker and Michael Romalis. Optical magnetometry. *Nature Physics*, 3(4):227–234, 2007.

[287] Ya. S. Greenberg. Application of superconducting quantum interference devices to nuclear magnetic resonance. *Rev. Mod. Phys.*, 70:175–222, Jan 1998.

[288] John Clarke, Michael Hatridge, and Michael Mößle. Squid-detected magnetic resonance imaging in microtesla fields. *Annual Review of Biomedical Engineering*, 9(1):389–413, 2007. PMID: 17328671.

[289] Vadim S Zotev, Andrei N Matlashov, Petr L Volegov, et al. SQUID-based instrumentation for ultralow-field MRI. *Superconductor Science and Technology*, 20(11):S367–S373, oct 2007.

[290] T Fedele, H J Scheer, M Burghoff, G Curio, and R Körber. Ultra-low-noise EEG/MEG systems enable bimodal non-invasive detection of spike-like human somatosensory evoked responses at 1 kHz. *Physiological Measurement*, 36(2):357–368, jan 2015.

[291] J-H Storm, D Drung, M Burghoff, and R Körber. A modular, extendible and field-tolerant multichannel vector magnetometer based on current sensor SQUIDs. *Superconductor Science and Technology*, 29(9):094001, jul 2016.

[292] D. Drung, C. Abmann, J. Beyer, et al. Highly sensitive and easy-to-use squid sensors. *IEEE Transactions on Applied Superconductivity*, 17(2):699–704, June 2007.

[293] J-H Storm, P Hömmen, N Höfner, and R Körber. Detection of body noise with an ultra-sensitive SQUID system. *Measurement Science and Technology*, 30(12):125103, sep 2019.

[294] I. M. Savukov and M. V. Romalis. Nmr detection with an atomic magnetometer. *Phys. Rev. Lett.*, 94:123001, Mar 2005.

[295] I.M. Savukov, S.J. Seltzer, and M.V. Romalis. Detection of nmr signals with a radio-frequency atomic magnetometer. *Journal of Magnetic Resonance*, 185(2):214 – 220, 2007.

[296] H. Xia, A. Ben-Amar Baranga, D. Hoffman, and M. V. Romalis. Magnetoencephalography with an atomic magnetometer. *Applied Physics Letters*, 89(21):211104, 2006.

[297] Juho Luomahaara, Visa Vesterinen, Leif Grönberg, and Juha Hassel. Kinetic inductance magnetometer. *Nature Communications*, 5(1):4872, 2014.

[298] I. Baumgart, J.-M. Cai, A. Retzker, M. B. Plenio, and Ch. Wunderlich. Ultrasensitive magnetometer using a single atom. *Phys. Rev. Lett.*, 116:240801, Jun 2016.

[299] S. Forstner, S. Prams, J. Knittel, et al. Cavity optomechanical magnetometer. *Phys. Rev. Lett.*, 108:120801, Mar 2012.

[300] Gianni Di Domenico, Hervé Saudan, Georg Bison, Paul Knowles, and Antoine Weis. Sensitivity of double-resonance alignment magnetometers. *Phys. Rev. A*, 76:023407, Aug 2007.

[301] F. Giazotto and F. Taddei. Hybrid superconducting quantum magnetometer. *Phys. Rev. B*, 84:214502, Dec 2011.

[302] Derek F. Jackson Kimball, Alexander O. Sushkov, and Dmitry Budker. Precessing ferromagnetic needle magnetometer. *Phys. Rev. Lett.*, 116:190801, May 2016.

[303] Tadas Pyragius, Hans Marin Florez, and Thomas Fernholz. Voigt-effect-based three-dimensional vector magnetometer. *Phys. Rev. A*, 100:023416, Aug 2019.

[304] Vladislav Gerginov, F. Silva, and David Howe. Prospects for magnetic field communications and location using quantum sensors. *Review of Scientific Instruments*, 88:125005, 12 2017.

[305] Gian Luca Romani, Samuel J. Williamson, and Lloyd Kaufman. Biomagnetic instrumentation. *Review of Scientific Instruments*, 53(12):1815–1845, 1982.

[306] Karsten Sternickel and Alex I Braginski. Biomagnetism using SQUIDs: status and perspectives. *Superconductor Science and Technology*, 19(3):S160–S171, feb 2006.

[307] T. M. Fortier, C. W. Nelson, A. Hati, et al. Sub-femtosecond absolute timing jitter with a 10 ghz hybrid photonic-microwave oscillator. *Applied Physics Letters*, 100(23):231111, 2012.

[308] R. H. Dicke. Coherence in spontaneous radiation processes. *Phys. Rev.*, 93:99–110, Jan 1954.

[309] R. Bonifacio and L. A. Lugiato. Cooperative radiation processes in two-level systems: Superfluorescence. ii. *Phys. Rev. A*, 12:587–598, Aug 1975.

[310] M. Gross and S. Haroche. Superradiance: An essay on the theory of collective spontaneous emission. *Physics Reports*, 93(5):301 – 396, 1982.